

MOLECULAR SIMULATION OF TUNABLE MATERIALS

**METAL-ORGANIC FRAMEWORKS & IONIC LIQUIDS
THEORY & APPLICATION**

MOLECULAR SIMULATION OF TUNABLE MATERIALS

**METAL-ORGANIC FRAMEWORKS & IONIC LIQUIDS
THEORY & APPLICATION**

Proefschrift

ter verkrijging van de graad van doctor
aan de Technische Universiteit Delft,
op gezag van de Rector Magnificus Prof.dr.ir. T.H.J.J. van der Hagen
voorzitter van het College voor Promoties,
in het openbaar te verdedigen op
vrijdag 13 december 2019 om 10:00 uur

door

Tim Michael BECKER

Master of Science in Chemical Engineering,
RWTH Aachen University, Duitsland
geboren te Aachen, Duitsland.

Dit proefschrift is goedgekeurd door de

promotor: Prof.dr.ir. T.J.H. Vlugt

copromotor: Dr. D. Dubbeldam

Samenstelling promotiecommissie:

Rector Magnificus,	voorzitter
Prof.dr.ir. T.J.H. Vlugt	Promotor, Technische Universiteit Delft
Dr. D. Dubbeldam	Copromotor, Universiteit van Amsterdam

Onafhankelijke leden:

Prof.dr. B. Smit	École Polytechnique Fédérale de Lausanne
Prof.dr. A. Urakawa	Technische Universiteit Delft
Prof.dr. E. Pidko	Technische Universiteit Delft
Prof.dr.ir. S. Keskin	Koç University

Overig lid:

Prof.dr. S. Calero	Universidad Pablo de Olavide
--------------------	------------------------------



This work was sponsored by NWO Exacte Wetenschappen (Physical Sciences) for the use of supercomputer facilities, with financial support from the Nederlandse Organisatie voor Wetenschappelijk Onderzoek (Netherlands Organization for Scientific Research, NWO). TJHV acknowledges NWO-CW for a VICI grant.

Keywords: Metal-Organic Framework, Ionic Liquid, Molecular Simulation, Monte Carlo, Force Field, Polarization, Adsorption, Absorption, Refrigeration

Printed by: Ridderprint BV | www.ridderprint.nl

Copyright © 2019 by T.M. Becker

Cover design by T.M. Becker

ISBN 978-94-6366-215-4

An electronic version of this dissertation is available at

<http://repository.tudelft.nl/>.

„Für meine Familie, auf die ich mich immer verlassen kann.“

CONTENT

1	Molecular simulation for tunable molecular materials	1
1.1	Accurate force fields for MOFs with open metal sites	2
1.2	Ionic liquids for refrigeration	6
1.3	Outline of this thesis	9
2	Introduction to polarizable force fields for porous materials	11
2.1	Introduction	11
2.2	Intermolecular interactions	13
2.3	Methodology	19
2.4	Simulation details	23
2.5	Results and discussion	26
2.6	Conclusions.	29
3	Potential of polarizable force fields for CO₂ in MOF-74	31
3.1	Introduction	31
3.2	Methodology	32
3.3	Simulation details	32
3.4	Results and discussion	34
3.5	Conclusions.	43
4	First principle derived polarizable force field for CO₂ in MOF-74	45
4.1	Introduction	45
4.2	Methodology	46
4.3	Simulation details	48
4.4	Results and discussion	49
4.5	Conclusions.	59
5	Polarizable force fields to model hydrocarbons in MOFs	61
5.1	Introduction	61
5.2	Background.	63
5.3	Simulation details	64
5.4	Results and discussion	65
5.5	Conclusions.	79

6	Molecular simulation to predict the performance of VAR cycles	81
6.1	Introduction	81
6.2	Description of the absorption refrigeration cycle	83
6.3	Predictions of thermodynamic properties	86
6.3.1	Force field	86
6.3.2	Calculation of NH ₃ solubility	86
6.3.3	Calculation of heat capacity	88
6.3.4	Calculation of enthalpy of absorption.	89
6.4	Simulation details	90
6.5	Results and discussion	92
6.5.1	NH ₃ solubility.	92
6.5.2	IL heat capacity.	93
6.5.3	Enthalpy of absorption.	94
6.5.4	Circulation ratio	95
6.5.5	Coefficient of performance	96
6.6	Conclusions.	97
7	Ammonia/ionic liquid based double-effect VAR cycles	99
7.1	Introduction	99
7.2	Properties of working pairs	101
7.2.1	Binary vapor-liquid equilibria	102
7.2.2	Densities and heat capacities	104
7.2.3	Enthalpies.	105
7.3	Cycle configuration and modeling method	106
7.3.1	Double-effect absorption refrigeration cycle	106
7.3.2	Generator-absorber heat exchange cycle	110
7.4	Integrated fishing vessel	110
7.5	Results and discussion	112
7.5.1	Correlation of binary vapor-liquid equilibria.	114
7.5.2	Thermophysical properties	115
7.5.3	Cycle performance	115
7.5.4	Integration of the double-effect vapor absorption cycle with exhaust gas	121
7.5.5	Considerations of feasibility	125
7.6	Conclusions.	127
	Conclusions	129
	Summary	131
	Samenvatting	133

Bibliography	135
Curriculum Vitae	169
List of Publications	171
Acknowledgements	173

1

APPLICATIONS OF MOLECULAR SIMULATION FOR TUNABLE MOLECULAR MATERIALS

Nowadays, materials can be designed on a molecular level to function in a specific way [1, 2]. Examples of tunable molecular materials are Metal-Organic Frameworks (MOFs) [3, 4] and ionic liquids (ILs) [5]. Such materials offer tremendous opportunities [3, 6]. The rational design enables the optimization of material properties for particular applications. Thereby, the performance of some industrially relevant processes can potentially be drastically improved, e.g., fractionating hydrocarbons from crude oil, olefin/paraffin separation, and the separation of greenhouse gases [7–9]. Especially, the replacement of distillation by adsorption processes, which makes up for 10-15% of the world’s energy consumption, can create significant energy savings and reduction in greenhouse gas emissions [10, 11]. To molecularly engineer materials, a fundamental understanding of the molecular behavior and interactions is crucial [5]. In this context, molecular simulation can play an important role [12–14]. Molecular simulation can help to reveal details of molecular behavior that are very challenging to observe experimentally. Moreover, properties of materials can be predicted based on molecular models [15]. The knowledge of these properties is important to assess the applicability for a particular use case and to actively tune materials [16]. Overall, molecular simulation has the potential to extend our understanding of molecular processes and significantly reduce the experimental effort by exclusively selecting very promising materials for actual lab experiments [17]. This is especially beneficial for experiments that are expensive, time-consuming, dangerous,

or at conditions that are difficult to access in the laboratory [15]. In this thesis, two examples in the scope of investigating tunable molecular materials with the help of molecular simulation are discussed. This extract is not intended to provide a complete overview of the topic, however, it can motivate the utilization of molecular simulation and demonstrate advantages and challenges.

In the first part of the thesis (chapter 2-5), the potential of polarizable force fields for MOFs [18] with open metal sites is evaluated. Improving force fields is an important task to enhance the performance of molecular simulation [19] and to enable meaningful predictions. Reliable large scale screening is not feasible without accurate and transferable force fields [17].

The second part (chapter 6 and 7) is more practical and deals with the usage of molecular simulation to estimate the performance of vapor absorption refrigeration (VAR) cycles with NH_3/IL working pairs. The idea is to apply molecular simulation to determine the properties of novel materials and to estimate their performance in relevant processes. The simulation methodology required for VAR cycles is presented and the accuracy for two mixtures is discussed. The development of new processes may be accelerated at lower costs when computational methods are applied to evaluate the performance before conducting lab experiments.

In the following two subsections, these two topics are introduced in detail and aligned with the related literature.

1.1. THE NEED FOR ACCURATE FORCE FIELDS TO DESCRIBE METAL-ORGANIC FRAMEWORKS WITH OPEN METAL SITES

MOFs are a relatively new and versatile type of material with various possible application areas, for instance, in gas separation [20–24], gas storage [25–28], gas and liquid separation [29–34], catalysis [35, 36], sensing [37], drug delivery [38, 39], microelectronics [40, 41], and in biotechnology [42–44]. The general structure of MOFs consists of metal ions or clusters which are connected by organic linkers [45]. In Fig. 1.1, the buildup of MOFs is depicted schematically. In recent years, a tremendous number of new MOFs has been synthesized [18] and an almost infinite number seems to be theoretically possible [46]. By adjusting the combination of metal and organic parts, the properties of MOFs are widely tunable and materials with exceptionally large surface areas can be created [47]. The pore geometry can be customized to enable the separation of gas molecules due to the topology of the MOF [16, 48, 49]. In addition to the geometry, the chemical composition can be tuned to further improve separation performance [49–51]. For example, coordinatively unsaturated metal ions, so-called open metal sites, can be embedded on the surface of the pore structure

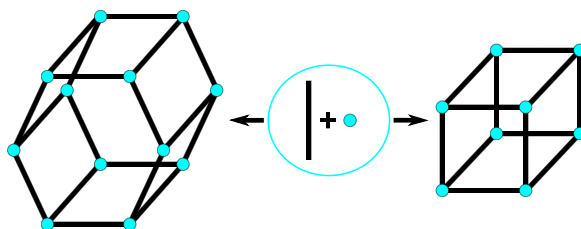


Figure 1.1: Schematic representation of how MOFs are constructed. Metal ions or clusters, and organic linkers are presented in cyan and black, respectively.

[52]. These metal ions are accessible for guest molecules and therefore interact strongly with certain adsorbate molecules [53]. By integrating open metal sites in the framework, the uptake of some adsorbate molecules can be increased significantly [54]. Understanding and predicting the interaction of open metal sites with adsorbates is crucial for the design of new customized adsorbent materials [55]. Besides MOFs with open metal sites, MOFs that undergo structural transitions in response to external influences or adsorption of guest molecules are very interesting for separation processes and biomedical applications [56, 57]. This class of MOFs is called flexible.

A challenge that is inherent with the enormous number of possibilities in the synthesis of MOFs is the selection of the best one for a particular application [16]. Experimental screening of hundreds of thousands of MOFs is impractical. A large effort has been made on developing computational screening approaches to facilitate the selection [46, 58–61]. Today, it is possible to predict adsorption properties for large sets of existing and hypothetical MOFs based on molecular simulation [62, 63]. A prerequisite for this kind of computational screening is a force field that represents the molecular interactions reasonably well for all materials under investigation. Unfortunately, the existing generic force fields do not satisfy this prerequisite for all MOFs [19, 54, 64–68]. Especially, the promising class of MOFs with open metal sites has been shown to be poorly described by generic force fields and research has been focused on developing improved force fields for these materials [16, 66, 69–71]. Similarly to the interactions between open metal sites and guest molecules, MOFs that undergo structural transitions are challenging to describe in molecular simulation [57]. However, the simulation of flexible MOFs would add another level of complexity to an already very challenging problem and is therefore not discussed in this thesis. To illustrate the failure of generic force fields for MOFs with open metal sites, Fig. 1.2 compares experimental measurements from Herm *et al.* [20] to the CO₂ uptake in Mg-MOF-74 calculated from grand-canonical Monte Carlo simulations using the generic UFF force field [72] for Mg-MOF-74 and the TraPPE force field [73]

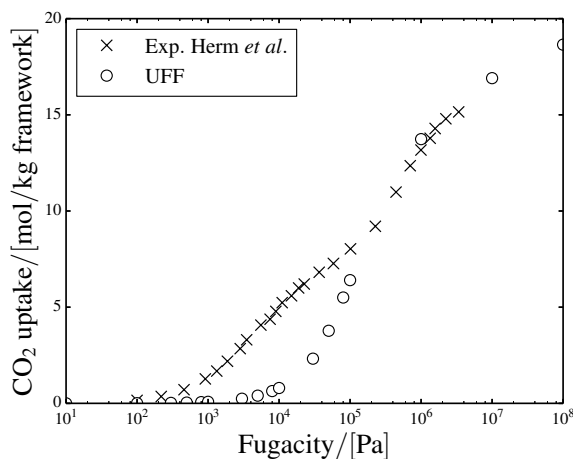


Figure 1.2: Comparison between the experimental adsorption isotherm of CO₂ in Mg-MOF-74 from Herm *et al.* [20] and the simulated one using the UFF force field [72] for Mg-MOF-74 and the TraPPE force field [73] for CO₂ at 313 K.

for CO₂ (i.e., standard generic force fields commonly used for porous materials [68, 74–76]). For low fugacities the calculated CO₂ uptake is considerably lower than the experimentally determined one. The distinct inflection in the experimental adsorption isotherm is not depicted, which suggests that the strong affinity of CO₂ close to the open metal sites is not modeled correctly with the UFF force field. This is typical for MOFs with open metal sites and has been observed for other MOFs [77, 78]. To obtain accurate force fields, several studies have been conducted in which force fields for individual MOFs are matched to interaction energies computed with quantum mechanical methods [51, 66–68, 70, 79–81]. In some of these studies the applicability of the customized force fields was also investigated for MOFs with very similar topology and composition [51, 67, 68]. Borycz *et al.* [76] used this methodology to investigate the influence of exchanging metal ions for a MOF without open metal sites. Addicoat *et al.* [82] designed an extension to the UFF force field to capture the structure of MOFs. Moreover, Vanduyfhuys *et al.* [83] developed a software package called QuickFF to automatically derive force fields for MOFs from ab initio input. The benchmark for new force fields are experimental measurements. Therefore, it is important to keep in mind that adsorption experiments are limited and that some experiments with MOFs are challenging to conduct [84].

The iso-structural M-MOF-74 is well suited to serve as study case to investigate the influence of different metal ions on the adsorption properties of small molecules [53, 68, 85, 86] and thereby further improve force fields. The pore

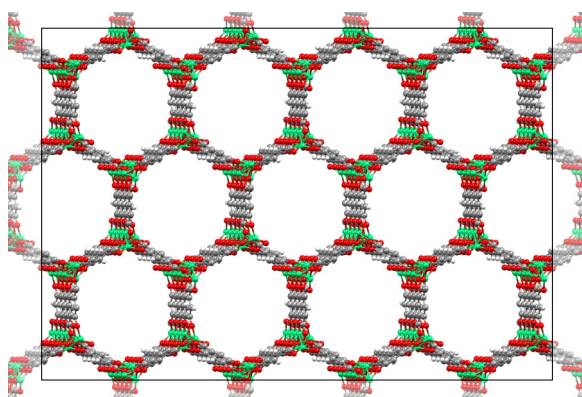


Figure 1.3: Periodic structure of Mg-MOF-74. Mg, C, O, and H atoms are represented in green, gray, red, and white, respectively.

structure of M-MOF-74 is only slightly affected by an exchange of the metal ion while the adsorption of CO_2 varies significantly. The family of M-MOF-74 (where M can be substituted by a variety of first row transition metals or Mg) has been extensively investigated [20, 54, 67, 80, 87–89] due to its large surface area which includes a high density of open metal sites [49]. Zn-MOF-74 was first reported in 2005 [90], and isostructural systems with other metal centers have been subsequently synthesized (Co, Cu, Fe, Mg, Mn, and Ni) [26, 91–95]. M-MOF-74 possesses one-dimensional hexagonal pores with a diameter of around 11 Å [87, 96]. Fig. 1.3 shows the periodic structure of Mg-MOF-74. In recent studies, Mg-MOF-74 has been shown to be a promising candidate for carbon capture [20, 21, 54, 87, 97, 98] and for natural gas sweetening [68] due to its high CO_2 uptake capacity at low partial pressures. In addition, M-MOF-74 offers opportunities to fractionate multicomponent hydrocarbon mixtures [53, 99–103]. M-MOF-74 has been investigated for various gas separations [20, 54, 67, 80, 87, 88]. Among others, experimental studies include adsorption measurements of CO_2 [20, 21, 49, 53, 54, 87, 97, 98], CO [53, 104], CH_4 [53, 85, 99, 101], C_2H_6 [53, 99–101, 105], C_2H_4 [99–101, 105], C_2H_2 [99, 101], C_3H_8 [99–101, 105], C_3H_6 [99–101, 105], Ar [53], O_2 [22], and N_2 [22, 53]. Adsorption sites have been investigated via Neutron and X-ray powder diffraction to determine the binding geometry [49, 85, 106–108]. As complement to experiments, various quantum mechanical studies have been conducted to theoretically investigate adsorption sites [49, 106], adsorption energies [85, 86], and the underlying contributions and mechanisms [50, 55] for a large number of guest molecules. The mechanism of competitive adsorption has been studied by Tan *et al.* [109]. These authors found that kinetic effects can play a significant role in the replacement of ad-

sorbate molecules close to the open metal sites. Molecular simulation has been used to investigate the adsorption at uptakes larger than one guest molecule per open metal site [51, 66, 67, 70, 79–81] and the hopping of guest molecules between open metal sites [110, 111]. Despite the significant progress, it is still a major challenge to accurately capture the change of interaction strength with varying metal ions in M-MOF-74 in molecular simulation. Several simulation studies have already been conducted to reproduce the adsorption of some of the M-MOF-74 structures [51, 66, 67, 70, 79–81]. In these studies, standard interaction potentials are re-parametrized to reproduce guest-host interactions from quantum mechanical calculations. In some quantum mechanical studies it is suggested that guest molecules are polarized in the vicinity of the open metal sites in M-MOF-74 [49–51, 53, 55, 106] and that this interaction contributes to the enhanced CO₂ affinity. Standard force fields do not include this effect directly and separate adjustments of the force field parameters may be necessary for new structures. In this context and due to the observation of polarization in several MOFs [112–114], have polarizable force fields been suggested for porous materials [51, 115–118]. A very limited amount of work exists concerning the development of polarizable force fields for MOFs with open metal sites [117, 119–126]. We anticipate that considering polarization explicitly can help to create force fields that overcome the shortcomings of current generic force fields. In this thesis, we focus on the development of polarizable force fields for MOFs with open metal sites.

1.2. IONIC LIQUIDS FOR REFRIGERATION

Other novel materials that can be customized on a molecular level are ILs [5]. ILs show potential for diverse industrial applications, e.g., as solvents for synthesis [5], catalysts [13], batteries [2], fuel cells [2], cleaning operations [7], as lubricants [7], for carbon capture [127], and for gas and liquid separation [5, 7]. Even today, one of BASF's large scale processes involves an IL [6, 13, 128]. In the BASILTM process, alkoxyphenylphosphine is produced parallel to the IL 1-methylimidazolium chloride. The IL forms a discrete phase, which facilitates the separation in comparison to the initial process without IL. Room temperature ILs are salts with very low melting points [129, 130]. Their large asymmetry hinders packing and therefore prevents crystallization [7]. By combining different anions and cations a huge number of ILs can be created. Fig. 1.4 shows some popular examples of cations and anions that ILs can be built of. Their main advantages are negligible volatility, chemical and thermal stability, and the possibility of tuning their thermodynamic properties by combining varying anions and cations [131–133]. By selecting custom combinations of cations and anions, ILs potentially provide suitable operating conditions for many applications and

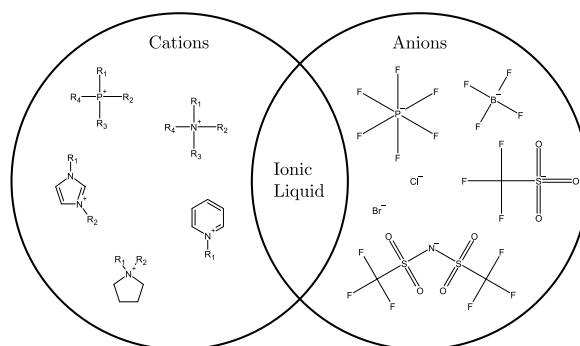


Figure 1.4: Examples of common anions and cations combinations that form ILs.

might offer wider operating ranges leading to better process flexibility [132, 134]. Furthermore, ILs received a lot of attention as "green solvent" due to their very low vapor pressure [2, 128]. The volatility of traditional solvents contributes significantly to industrial emissions that can be connected to climate change, air pollution, and human diseases [7]. Research has been conducted to understand ILs and determine their properties [5, 6]. However, a lot is still unknown about the behavior of ILs and especially about the properties of individual ILs and their mixtures with other components. This knowledge is crucial, because to assess the potential of ILs their properties need to be known. For example, to perform a thermodynamic analysis of absorption processes based on ILs, the miscibility, the heat capacity, and the enthalpy of absorption of the working pairs are required. As an initial step in the development of new absorption based processes, these thermodynamic properties of various ILs and their mixtures need to be evaluated to find the most promising ones [135]. For the vast majority of ILs, the necessary thermodynamic properties (e.g., densities, vapor pressures, heat capacities, refrigerant solubility, etc.) have not been investigated or are experimentally very difficult to access [29, 131, 133, 136, 137]. Moreover, the amount of possible anion-cation combinations is huge [29, 133, 138]. Conducting lab experiments for a large set of ILs is a tedious and, due to the currently high price of ILs, very expensive task. Computer simulations provide a convenient and cheap alternative to predict relevant thermodynamic properties of ILs and to gain a better understanding of the underlying physical behavior [139–143]. A preselection of particularly promising ILs for the design of new absorption processes can be made based on simulations. It is important to note that the molecular model which describes the mixture containing an IL (i.e., the force field) and statistical uncertainties related to the simulation method influence the accuracy of computer simulations. Several studies exist that apply molecular simulation tech-

niques to study ILs [5, 127, 139, 142, 144, 145]. Unfortunately, many challenges do exist, especially for mixtures of ILs with other components. The complex molecular interactions are not easy to capture with standard force fields and the existing force fields are often exclusively validated with the density of pure ILs [146]. Hence, the accuracy of the predictions may affect the quality of the performance predictions of processes using ILs. Moreover, molecular simulation of ILs can be time-consuming which makes the screening of thousands of ILs impossible. The area of application for ILs that is discussed in this thesis is the adsorption refrigeration cycle. Temperature control devices are essential in our society and they are an integral part of many industrial processes [147, 148]. Possible applications of ILs in cooling and heating range from electronic devices [149], food preservation [150], the energy management of buildings [151, 152], to industrial cooling and heating [153]. Hence, refrigeration plays a significant role in improving living conditions [154]. The VAR cycle enables the efficient utilization of low-grade heat, for example, as byproduct of industrial processes or by solar thermal collectors [148, 152, 155–160]. The most widely used fluids in absorption cycles are aqueous solutions of LiBr or NH_3 [132, 160]. The $\text{H}_2\text{O}/\text{LiBr}$ working pair is often applied in room air conditioning [132]. $\text{NH}_3/\text{H}_2\text{O}$ is deployed for sub-zero cooling and free of air infiltration [160]. However, both conventional working pairs are characterized by some inherent drawbacks. The $\text{H}_2\text{O}/\text{LiBr}$ system suffers from problems such as corrosion and crystallization, while the $\text{NH}_3/\text{H}_2\text{O}$ system requires an expensive rectifier to separate the two components [129, 161–163]. ILs have been proposed to overcome some of the problems associated with conventional working pairs [129, 132, 164]. NH_3/ILs working pairs in absorption cycles have received significant attentions in the past decade. Yokozeki and Shifflett [136] reported the first vapor-liquid equilibrium (VLE) data of four NH_3/ILs working pairs. By including measurements and correlations of NH_3/ILs pairs, the performance of eight NH_3/ILs fluids in a SE absorption cycle was compared in Ref. [165]. Most of the studied imidazolium ILs are currently well commercialized. Functional ILs with NH_3 in SE absorption cycles were also investigated. For instance, Chen *et al.* [166] investigated the VLE property of NH_3 with a metal ion-containing imidazolium IL. A thermodynamic performance analysis of a VAR cycle using the studied fluids was conducted in a sequential work by the same authors [167]. Ruiz *et al.* [168] studied certain ammonium ILs. Cera-Manjarres [169] explored six other ILs including imidazolium and ammonium ILs with a hydroxyl group (-OH). By applying more reliable mixing enthalpies and experimental heat capacities, Wang and Infante Ferreira [170] explored the performance of nine NH_3/ILs fluids in SE absorption cycles for heat pump systems. The authors identified promising absorbents which work with NH_3 in absorption cycles under 130 °C heating.

Here, we assess molecular simulation to predict relevant material properties of NH_3/IL mixtures for VAR cycles. NH_3 is chosen as refrigerant due to its low costs, large latent heat [171], and low impact on the environment (zero ozone depletion and global warming potential) [172]. In addition, data for NH_3/IL mixtures are particularly interesting since only a limited amount of experimental measurements exists for these systems [132]. To solve the issue of limited accuracy in a simple and efficient manner, individual force fields are adjusted by comparing the predictions to experimental results.

1.3. OUTLINE OF THIS THESIS

The first part of this thesis summarizes the work related to MOFs. In chapter 2, polarizable force fields for porous materials are introduced in detail. In chapter 3, the potential of polarizable force field is investigated by considering the adsorption of CO_2 in M-MOF-74. On this basis, a predictive polarizable force field for CO_2 in M-MOF-74 is derived from first principle calculations in chapter 4. Finally, opportunities of polarizable force fields to model small hydrocarbons are discussed in chapter 5. The last two chapters contain the work on ILs. First, the accuracy of molecular simulation for three ILs is evaluated in chapter 6. In chapter 7, a simple fix is applied to adjust the force field at conditions that are experimentally available. This adjusted model can then be used to extend the experimental range to conditions that have not been measured.

2

INTRODUCTION TO POLARIZABLE FORCE FIELDS FOR POROUS MATERIALS

This chapter is based on the paper: T. M. Becker, D. Dubbeldam, L.-C. Lin, and T. J. H. Vlugt. Investigating polarization effects of CO₂ adsorption in Mg-MOF-74. *Journal of Computational Science*, 15 (2016) 86-94 [173].

2.1. INTRODUCTION

The acceleration of climate change is one of the big challenges modern society is facing [174]. One of the major causes is the enormous amount of carbon dioxide emitted by power plants, especially coal-fired power plants [58]. Carbon capture and sequestration is a viable near-term solution to mitigate this development [175, 176]. A promising technology in this context is to separate CO₂ from flue gas via solid adsorbents [177]. MOFs have been shown to provide opportunities for this application [176]. In particular, Mg-MOF-74 is of special interest for carbon capture because of its high CO₂ uptake capacity and its favorable selectivity towards carbon dioxide over nitrogen, even in the low pressure region relevant to carbon capture [21]. The framework of Mg-MOF-74 consists of one-dimensional hexagonal pores with a diameter between 11 and 12 Å [87]. Coordinatively unsaturated magnesium ions are embedded into this framework. The strong affinity of Mg-MOF-74 towards CO₂ arises from interactions with the so-called "open metal" sites [107]. Mg-MOF-74 has been extensively studied both experimentally [20, 87] and computationally [54, 67, 80, 88]. In experiments, an inflection

at an absolute uptake of approximately one CO₂ molecule per open metal site is observed. This behavior is associated with the saturation of open metal sites and the subsequent filling of the less favorable centers of the pores [107]. It is a major challenge to quantitatively predict the inflection and the shape of the adsorption isotherm using molecular simulation. Recently, several computational studies have been performed to model such a system [67, 70, 80]. These studies used rather simplified interaction models for guest-host interactions (Buckingham or Lennard-Jones potentials and electrostatic interactions with static partial charges without explicitly accounting for the polarization effect close to the open metal sites). However, polarization has been observed [106] and it has been suggested to contribute to the enhanced CO₂ affinity in Mg-MOF-74 [116]. Our approach is to consider polarization explicitly with a polarizable force field and to compute the CO₂ uptake in grand-canonical Monte Carlo simulations. Polarizable force fields are frequently used in molecular dynamics simulations, e.g., for biological systems [178–180]. However, they are rarely applied in Monte Carlo simulations for guest molecules in solid adsorbents. The reason for this is that in principle, a computationally expensive method is required for every Monte Carlo step [181].

Motivated by the failure of generic force fields, McDaniel *et al.* [120] developed a predictive polarizable force field for CO₂ [119, 120] and CH₄ [121] in several ZIFs and other MOFs. These authors modeled polarization of guest molecules via the shell model [179] while neglecting explicit polarization of the framework. In addition to introducing solely polarization, the interactions between framework and guest molecules were re-parameterized with a non-standard functional form. Good agreement between experiments and computational results was achieved. For the investigated ZIFs, the contribution of polarization was rather small and did not impact the simulation results. However, these authors observed a significant contribution of electrostatics and a shift towards more negative total energies for a large set of other MOFs. To accelerate their simulations for this set of MOFs, a lattice based grand canonical Monte Carlo procedure and coarse grained adsorbate-adsorbate interactions were applied. These simplifications resulted effectively in a pairwise consideration of polarization. The overhead in computational time introduced by polarization slowed the conducted Monte Carlo simulations down by a factor of 2 to 10 in comparison to standard simulations. Furthermore, substantial work concerning polarizable force fields for MOFs with open metal sites has been carried out by the group of Space *et al.* Initially, this group focused on adsorption of H₂ in MOFs with open metal sites [117, 122–125]. Recently, these authors also developed force fields for CO₂ [78, 126, 182] and even small hydrocarbons [126]. To consider polarization, the induced dipole method was applied. While self-polarization of the frameworks

was accounted for implicitly, framework-adsorbate and adsorbate-adsorbate polarization was considered explicitly. The guest molecule H_2 was described by an elaborated 5 site model. The computational results were accurate and showed that considering polarization is crucial for describing the correct adsorption of MOFs with open metal sites. The group showed that polarizable force field predict the energetics, especially for low guest molecule uptakes, better and that these force fields have potential to improve transferability. The computational costs of considering explicit polarization in Monte Carlo simulations, however, was as high as 95% of the total computational time.

We also apply the induced point dipole method to account for polarization additional to repulsion and dispersion interactions with a standard Lennard-Jones interaction potential. To achieve reasonable simulation times, back-polarization is neglected in our simulations. In standard force fields averaged polarization is implicitly accounted for. This contribution needs to be removed from the force field before polarization can be added explicitly. This is regarded for by adjusting the Lennard-Jones energy parameters deployed without polarization. We follow a simple procedure to rescale the Lennard-Jones energy parameters with respect to the assigned atomic polarizabilities. We herein demonstrate that the computed CO_2 adsorption isotherms using the polarizable force field approach are in good agreement with both experimental measurements and previously proposed force fields derived from quantum mechanical calculations, indicating polarization has a crucial role to play. The consideration of polarization in Monte Carlo simulations is also promising for other systems in which polarization is clearly not negligible [178, 183], i.e., water [179], simulations including ions [178, 184], or xylenes [185]. It may lead to more sophisticated force fields and to more physical models with better transferability.

In this chapter, we provide a brief overview of non-bonded intermolecular interactions and on how to account for polarization in molecular simulation. We motivate the necessity of adjusting the potential parameters taken from standard force fields according to polarization (Section 2.2). The simulation details are provided in Section 2.4. We illustrate the procedure on the example of CO_2 adsorption in Mg-MOF-74 and compare the results to simulations with a generic force field and a force field deducted from density functional theory (DFT) [80] (Section 2.5). Our findings are summarized in Section 2.6.

2.2. INTERMOLECULAR INTERACTIONS

An essential component of each molecular simulation is the description of the interactions between atoms and molecules. In general, the contributing interactions arise in some way from the electrostatic interactions between the charge distributions of molecules [186]. Most accurately, these interactions can be com-

puted by quantum mechanical calculations. Unfortunately, these calculations are currently too time consuming to be applied in molecular simulation for large systems. Hence, potential functions are used to describe the interaction energy between atoms and molecules as a function of their positions. Due to increasing computing power, hybrid molecular and quantum mechanical simulations have become feasible for systems with moderate size [187]. In this work, we focus on interactions classically considered in molecular simulation between non-bonded particles that are not involved in chemical reactions. The level of detail and the type of interactions necessary in the simulations depends on the specific system and on the required accuracy of the predictions. To investigate structure-property relations or to screen materials for a certain application, generic force fields like UFF [72] or DREIDING [188] are often chosen. In these cases, the computation time is a crucial factor [187]. To make more accurate predictions, it is often required to deploy interaction potentials that are especially designed to reproduce the behavior of a particular system [73, 187].

Molecular interactions are often divided into short and long range interactions with respect to how fast they decay with the distance between interacting particles. At very small interatomic distances, the electron clouds of atoms overlap, and a strong repulsive interaction arises that determines how close two atoms or molecules can ultimately approach each other. These repulsive interactions are sometimes referred to as exchange repulsion, hard core repulsion, steric repulsion, or, for ions, the Born repulsion. Strictly speaking, repulsive interactions belong to the category of quantum mechanical or chemical forces, and unfortunately there is no general equation for describing their distance dependence. Instead, a number of empirical potential functions have been introduced, all of which appear to be reasonable as long as they have the property of a steeply rising repulsion at small separations. The three most commonly used potentials for describing these interaction are the hard sphere potential, the inverse power-law potential, and the exponential potential [189].

Electrostatic interactions describe Coulombic interaction between charge densities of molecules. In comparison to other interactions, their strength decays slowly with the distance between molecules. This long-range behavior makes the computation more expensive and several methods to compute electrostatic interactions have been proposed, i.e., the Ewald summation technique [15] and its variants like Particle Mesh Ewald [190]. The Wolf method [191, 192] is a computationally less expensive alternative for the Ewald summation. In molecular simulation, electrostatic interactions are usually considered through static partial charges assigned to interaction sites. Higher order multipole interactions can be modeled depending on how the interaction sites are distributed along the molecules. A precise representation requires specification of all non-zero mul-

tipole moments. Electrostatic interactions are strictly pairwise additive, highly anisotropic and can be either repulsive or attractive [193].

Dispersion interactions are significant to the total interactions and present for all systems. They play a role in a host of important phenomena such as adhesion, surface tension, physical adsorption, wetting, the properties of gases, liquids, and thin films, the strengths of solids, the flocculation of particles in liquids, and the structures of condensed macro molecules such as proteins and polymers [194–197]. Dispersion interactions are quantum mechanical in origin. They arise from correlated fluctuations between the motion of electrons. These fluctuations result in a lowering of the energy [186]. Thus, dispersion interactions are attractive. Numerically, dispersion interactions at long ranges can be described by a series in intermolecular separation r [187]. The leading term is power of $1/r^6$, while higher order terms are usually neglected in molecular simulation for computational simplicity [187]. The strength of the dispersion interactions depends on the number of electrons in the outer shell of an atom [198].

Induction interactions result from a distortion of the electron density of a molecule due to an electric field [179], e.g., caused by the charge distribution of another molecule. The difference in the electron density can be captured by adjusted multipole moments. Polarization can induce multipole moments even for spherical particles without static multipole moments [193]. Every change in the electron density again causes an alteration of the electric field. Consequently, the polarization of a system depends on the interactions of the induced and static multipole moments of all molecules in the system [179]. For some systems, the effect of polarization is small and it can be neglected [198]. If this contribution is large, the simplest solution in molecular simulation is modifying the static properties of each molecule to enhance the average interactions. However, this approach results in force fields with poor transferability and it is seldom suitable for systems with highly polarizable molecules like water or for biological systems like proteins or lipids [178].

The most commonly used interaction potential to describe molecular interactions in molecular simulation is the Lennard-Jones potential [15]:

$$U_{\text{LJ}}(r) = 4\epsilon \left[\left(\frac{\sigma}{r} \right)^{12} - \left(\frac{\sigma}{r} \right)^6 \right] \quad (2.1)$$

where ϵ characterizes the energy, σ is the distance scale of the atom or molecule interactions, and r is the interatomic distance. The $1/r^{12}$ term approximates the behavior of the repulsion energy and the $1/r^6$ term represents the behavior of the dispersion energy as a function of the distance between particles. Static charge distributions can be represented as static partial charges and are usually computed via the Ewald summation technique [15]. To reproduce experimental re-

sults the potential parameters and static partial charges are often fitted to experimental data [199, 200]. For instance, the TraPPE force fields for carbon dioxide and nitrogen are calibrated to reproduce vapor-liquid equilibria of the pure components and their mixtures with alkanes [73]. The resulting potential parameters of the Lennard-Jones potential and the static partial charges are effective values, since all occurring interactions are indirectly included in the parametrization. Another approach is to derive the potential parameters from quantum mechanical calculations [67, 70, 80]. Carefully calibrated Lennard-Jones models are usually quite satisfactory and are therefore popular [15, 201]. The model captures the first order effects, but as the fitted parameters are adjustable parameters, also a large portion of the remaining physics is effectively incorporated [178, 179]. As a result, the effective Lennard-Jones potential parameters may not be transferable between diverse molecular systems. The dependency of the charge distribution on the physical state of the system, composition and the fluctuations of the electric field caused by molecular motion can never be fully captured. An effective interaction potential calibrated in an environment of weak polarizability will most likely fail in a highly polarizable system, because it predicts the interaction strength incorrectly. This becomes crucial if polarization effects are strongly localized in a system, e.g., for biomolecular systems, like lipid-bilayers [178] or proteins [179, 183, 202]. In this case, it is inevitable to apply a force field that incorporates this phenomena. Unfortunately, the inclusion of polarization increases the computational costs significantly in Monte Carlo simulations. The effect of polarization has to be evaluated for every interaction site in every simulation step. Due to increasing computational power, now it becomes more feasible to include explicit polarization in molecular simulation [179].

The three most common methods to incorporate polarization in molecular simulation are the fluctuating charge method, the shell model, and the induced point dipole method [180, 203–206]. These methods are additional to the interaction potentials normally applied in molecular simulation (e.g., Lennard-Jones potential and Coulombic interactions with static partial charges).

The fluctuating charge method allows the values of the partial charges assigned to interaction sites to change as a respond to the electric field. Hence, the charges are treated as dynamic properties. Charges can be transferred between interaction sites of a single molecule or even between separated molecules. The electronegativities and chemical hardnesses determine how easily charges can be exchanged from one interaction site to another. For every simulation step, or Monte Carlo trial move, instantaneous values of the partial charges are determined by minimizing the electrostatic energy of the system. In this approach, all order multipoles are considered and no new interactions need to be introduced. The drawback of the method is an artificial restriction of the direction of

the polarization depending on the molecular shape [178, 179], e.g., a linear and rigid representation of a molecular can only transfer charges in the direction of its extent.

In the shell model, exclusively induced dipole interactions are considered and higher order induced multipole moments are neglected. Polarizable sites are described via pairs of charges. One charge is assigned to the nucleus while the other charge is connected to it by a harmonic spring. The values of the charges are kept fixed during the simulation and polarization is obtained via the relative displacement caused by electric interactions with the system. Consequently, there is no charge transfer between molecules. In this method, interactions between the charges of one polarizable site are not calculated. The magnitude of the charges and the value of the spring constant can be related to the polarizability, but they are often treated as tunable variables of the model. The computational costs increase due to the doubling of the electrostatic interaction sites and the requirement of smaller time steps in molecular dynamics simulations. The reduction of the time step size is a necessity because of the division of the atomic mass between the nucleus and the shell charge. Thereby, the mass of the shell charge needs to be small in comparison to the nucleus to enable a rapid respond of its position to the electric field. Accordingly, the size of the time step has to be decreased due to smaller occurring masses [178, 179, 207].

In the induced point dipole method, isotropic dipole-dipole polarizabilities α_i are assigned to interaction sites i . Higher order multipole moments are neglected. Induced dipoles can be calculated for every interaction site as the result of the electrostatic field \mathbf{E}_i . Assuming a linear response for a single isolated point dipole, the induced dipole moment $\boldsymbol{\mu}_i$ can be determined via [179]:

$$\boldsymbol{\mu}_i = \alpha_i \cdot \mathbf{E}_i \quad (2.2)$$

The electric field \mathbf{E}_i is a function of the permanent electric field \mathbf{E}_i^0 caused by the static partial charges, and the induced dipoles of all N interaction sites in the system:

$$\mathbf{E}_i = \mathbf{E}_i^0 - \sum_{j \neq i} \mathbf{T}_{ij} \cdot \boldsymbol{\mu}_j \quad (2.3)$$

where \mathbf{T}_{ij} is the dipole field tensor:

$$\mathbf{T}_{ij} = \frac{1}{r^3} \mathbf{I} - \frac{3}{r^5} \begin{pmatrix} x^2 & xy & xz \\ yx & y^2 & yz \\ zx & zy & z^2 \end{pmatrix} \quad (2.4)$$

Here, \mathbf{I} is the identity matrix, x ($= x_i - x_j$), y ($= y_i - y_j$), z ($= z_i - z_j$) and r are respectively the components and the length of the vector between interaction

sites i and j . In the induced point dipole method, the energy of the induced dipoles U_{ind} has three contributions:

$$U_{\text{ind}} = U_{\text{stat}} + U_{\mu\mu} + U_{\text{pol}} \quad (2.5)$$

U_{stat} is the interaction energy between the permanent electric field and the induced dipoles:

$$U_{\text{stat}} = - \sum_{i=1}^N \boldsymbol{\mu}_i \cdot \mathbf{E}_i^0 \quad (2.6)$$

The energy $U_{\mu\mu}$ results from the interactions among the induced dipoles:

$$U_{\mu\mu} = \frac{1}{2} \sum_{i=1}^N \sum_{j \neq i} \boldsymbol{\mu}_i \cdot \mathbf{T}_{ij} \cdot \boldsymbol{\mu}_j \quad (2.7)$$

The final energy contribution is the polarization energy U_{pol} , which describes the energy necessary to create the induced dipoles by changing the electron distribution:

$$U_{\text{pol}} = \frac{1}{2} \sum_{i=1}^N \boldsymbol{\mu}_i \cdot \mathbf{E}_i \quad (2.8)$$

By inserting Eqs. 2.6, 2.7 and 2.8 into Eq. 2.5 and using Eq. 2.3 to replace \mathbf{E}_i , the relation for U_{ind} reduces to:

$$U_{\text{ind}} = - \frac{1}{2} \sum_{i=1}^N \boldsymbol{\mu}_i \cdot \mathbf{E}_i^0 \quad (2.9)$$

To solve Eq. 2.9 and to compute the energy of the induced dipoles, different techniques have been suggested, i.e., matrix inversion, the extended Lagrangian method, and iteration. The matrix inversion approach is to solve the dependent equations of all N induced dipole moments $\boldsymbol{\mu}_i$ (Eqs. 2.2 and 2.3) simultaneously by forming a matrix, inverting it and subsequently solving Eq. 2.9. However, for N polarizable interaction sites this involves inverting a $N \times N$ matrix at every simulation step. Due to the high computational time of matrix inversions this procedure is not feasible for medium-to-large systems [179]. An alternative approach is to use the extended Lagrangian method. In this approach, each dipole moment is treated as a dynamic quantity with its own mass. Thus, the dipoles follow their own equation of motion in the same way as the atomic positions. The assigned masses have no physical meaning, though they determine the efficiency and accuracy of the simulation [179]. The Lagrangian method is well suited for molecular dynamic simulations, but it is more complicated in Monte Carlo simulations. New Monte Carlo trial moves changing the dipoles were previously designed to tackle this problem [181]. Another approach is to iterate Eq. 2.2

to self-consistency. Typically, this requires between 2 and 10 iterations [179]. A possible initial guess for the electric field is the electric field created by the static charges [179]. This approach can be implemented in a Monte Carlo algorithm without any additional trial moves.

2.3. METHODOLOGY

Force fields describing intermolecular interactions are the foundation of molecular simulation [19, 208]. By definition, molecular simulation represents the behavior of a system for a specified force field. The capability of the force field to describe the true molecular interactions determines its applicability [209]. An additional desirable characteristic of force fields is transferability [19, 82, 83]. Ideally, a force field should be able to describe the experimentally observed behavior for a preferably large set of systems. Generic force field like UFF [72], DREIDING [188], and OPLS [210] have been designed for organic, biological, and inorganic materials [19]. However, if the conditions of the system under investigation vary from the ones the force field was developed for, the resemblance of the real system behavior may be poor [19]. Many studies focus on re-gaging force field parameters to capture experimental behavior [51, 66–68, 70, 79–81, 211]. This approach works well for individual systems [68]. Nevertheless, the transferability of the created force fields is likely to be limited to structures with very similar topology and chemical composition [68]. In addition, new parameters are required for each pairwise interaction and all point charges, because they are all mutually dependent [68]. Repeatedly readjusting force field parameters for every new system is cumbersome. The reason for the limited transferability of this approach could be attributed to the implicit consideration of the interactions that are exceptional for a particular system. Another disadvantage is that the predictive potential of molecular simulation is largely lost when force fields become completely empirical and need to be readjusted for every new system. A more sustainable approach is to develop force fields with a broader applicability due to a physically motivated extension which considers these exceptional interactions. Several studies focus on force field improvement of gas adsorption in MOFs [19, 82, 83]. Unfortunately, a force field with general applicability for the adsorption of small molecules in MOFs does not exist [19]. Especially, the modeling of MOFs with open metal sites represents a challenge [16, 66, 70]. Quantum mechanical calculations of CO₂ adsorption in Mg-MOF-74 suggest that polarization of CO₂ in the vicinity of Mg ions is important and significantly contributes to the interaction energy [49–51, 53, 55, 106]. In contrast, charge transfer between CO₂ molecules and the MOF framework seems to be negligible [49, 55, 212]. Several methods have been proposed for considering polarization in molecular simulation, i.e., the induced dipole method, the fluctuating charge method,

and the shell method (also known as Drude oscillator and charge-on-a-spring model) [180, 203–206, 213]. For molecular dynamics simulations, these methods are well established [118, 178–180]. However, the many-body nature of polarization makes these algorithms more suitable for molecular dynamics simulation in which all molecules are moved in every simulation step. This is in contrast to Monte Carlo simulations in which usually only one molecule is moved [179]. Hence, in MC simulations more steps are required to create independent configurations of the system. Normally, this is unproblematic, since the interactions need to be computed only for the moved molecule. However when considering polarization, the interactions between all molecules change and have to be recomputed due to the many-body nature of polarization for every step. This leads to a less frequent consideration of polarization in MC simulations.

We chose the procedure developed by Lachet *et al.* [185] to mitigate this limitation. A schematic description of the procedure is shown in Fig. 2.1. The energy contribution of polarization has to be computed in every Monte Carlo step. In this way, the difference in polarization energy to the previous configuration can simply be added as another energy term in the acceptance rule of the Monte Carlo algorithm. Higher order induced multipoles are not explicitly incorporated in the induced dipole method. In a similar system, Lachet *et al.* [185] estimated the related error to be less than 5% of the total polarization energy. Special for the procedure of Lachet *et al.* [185] is that it accounts solely for polarization between the framework and adsorbate molecules and that it neglects polarization caused by induced dipoles, so-called back-polarization. Using these assumptions Eq. 2.9 can be rearranged to:

$$U_{\text{ind}} = -\frac{1}{2} \sum_{i=1}^n \alpha_i \cdot |\mathbf{E}_i^0|^2 \quad (2.10)$$

where α_i is the atomic polarizability of interaction site i and n is the number of interaction sites of the moved molecules. The computation of the electric field caused by static partial charges is straightforward [214]. Thereby, an iterative scheme is avoided and the computational costs of the method are drastically reduced. In fact, the computational costs can be similar to simulations without considering explicit polarization. In case of, e.g., a translation trial move of a single molecule only the n interaction sites of this molecule have to be evaluated to determine the change in polarization energy. Lachet *et al.* [185] showed that the error in energy introduced by this assumption is around 6% in a xylene NaY zeolite system. To verify the contribution of back-polarization in Mg-MOF-74, in Fig. 2.2 the total interaction energy of a CO₂ molecule approaching the Mg ion with and without consideration of back-polarization for the developed polarizable force field is compared. The influence of back-polarization increases with decreasing distance between the CO₂ molecule and the metal ion. For the most

```

# conduct Monte Carlo trial move in a system consisting of  $N$  molecules
#
#   move randomly selected molecule  $k$  (randomly select either translation, rotation, regrow)
#
#   compute new energy  $U_k^{\text{new}}$  of molecule  $k$  at its new position. We consider the following terms:
#   (1) induction, (2) Lennard-Jones, (3) electrostatics. The interaction sites of molecule  $k$  are
#   indicated by  $i = 1, 2, 3, \dots, n$  while the interaction sites of all surrounding molecules are
#   indicated by  $j = 1, 2, 3, \dots, m$ .
#
#   (1) compute the contribution of the induction energy  $U_{\text{ind}}$ 
#
#       (a) compute the electric field  $\mathbf{E}_i^\circ$  from the forces caused by static partial charges at the
#           interaction sites of molecule  $k$  at its new position.  $\mathbf{E}_i^\circ = \frac{\mathbf{F}_i}{q_i}$  in which  $\mathbf{F}_i$  is the force
#           on interaction site  $i$  as computed by the Ewald summation technique.
#
#       (b) calculate  $U_{\text{ind}} = -\frac{1}{2} \sum_{i=1}^n \alpha_i \cdot |\mathbf{E}_i^\circ|^2$ 
#
#   (2) compute the contribution of the Lennard-Jones energy  $U_{\text{LJ}}$ 
#
#       (a) calculate  $U_{\text{LJ}} = \sum_{i=1}^n \sum_{j=1}^n 4\epsilon_{ij} [(\frac{\sigma_{ij}}{r_{ij}})^{12} - (\frac{\sigma_{ij}}{r_{ij}})^6]$ , where  $\epsilon_{ij}$  and  $\sigma_{ij}$  are the Lennard-
#           Jones interaction parameters and  $r_{ij}$  is the distance between interaction site  $i$  and  $j$ 
#
#   (3) compute the contribution of the electrostatic energy  $U_{\text{el}}$ 
#
#       (a) calculate  $U_{\text{el}} = \sum_{i=1}^n \sum_{j=1}^n \frac{1}{4\pi\epsilon_0} \frac{q_i q_j}{r_{ij}}$ , where  $q_i$  and  $q_j$  are the charges of interaction
#           site  $i$  and  $j$ , and  $\epsilon_0$  is the electric constant, respectively. In practice, one uses the
#           Ewald summation technique for this step.
#
#   (4) add up all energy contributions  $U_k^{\text{new}} = U_{\text{ind}} + U_{\text{LJ}} + U_{\text{el}}$ 
#
#   accept or reject the Monte Carlo trial move according to  $\exp[-\beta(U_k^{\text{new}} - U_k^{\text{old}})]$ , where  $U_k^{\text{old}}$ 
#   is the energy of molecule  $k$  at its previous position similarly obtained to  $U_k^{\text{new}}$ .  $\beta = \frac{1}{k_B T}$ .

```

Figure 2.1: Schematic description of the procedure of Lachet *et al.* [185] to include the induced point dipole method in a Monte Carlo simulation. In our implementation, the electrostatic energy is computed via the Ewald summation technique and the Lennard-Jones potential is truncated at 12.8 Å. No tail corrections are applied. For insertions and deletions of molecules in the grand-canonical ensemble the procedure is similar and the acceptance rules are listed in Ref. [15].

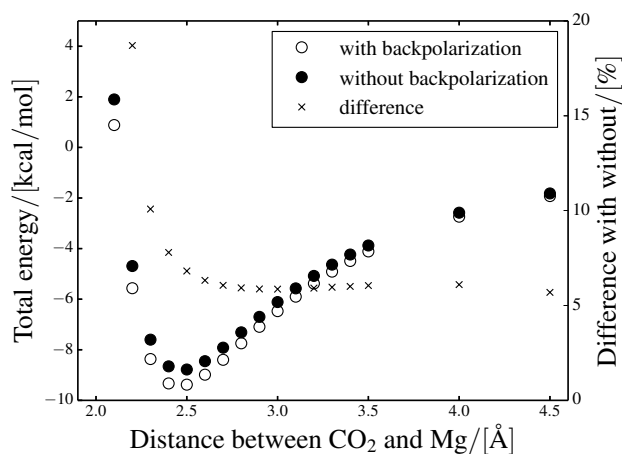


Figure 2.2: Total energy of a single CO₂ molecule in Mg-MOF-74 calculated using the developed polarizable force field as a function of the distance to the open metal site. Comparison between interactions with and without back-polarization.

favorable position at a distance of approximately 2.4 Å between the CO₂ and the magnesium ion, the difference in total energy is approximately 7%. This deviation seems to be acceptable in comparison with the considerable speedup of the simulations. Besides polarization, repulsion and dispersion interactions are considered via a standard Lennard-Jones potential and static charge distributions are modeled via point charges. When explicitly accounting for polarization, one has to ensure that the force field parameters describing the remaining interactions do not include an implicit polarization contribution which would have to be removed. Otherwise, the contribution of polarization would be double counted, once implicitly and once explicitly. The removal of implicit polarization is necessary if a standard force field is used as starting point for the development of a polarizable force field, because current force fields are likely to be calibrated to reproduce certain experimentally observed properties. For example, the TraPPE force fields for CO₂ and N₂ are fitted to reproduce experimental vapor-liquid equilibria of the pure components and their mixtures with alkanes without explicitly considering polarization [73]. Hence, in the fitting of these force fields, all present interactions are indirectly considered and the resulting potential parameters are effective parameters. As starting point for our polarizable force field we use the UFF [72] and the TraPPE force fields [73]. These are standard force fields frequently used for molecular simulation of porous materials [14, 16, 68, 76, 215–217]. To remove the contribution of implicitly considered polarization to the interaction potential, a global scaling parameter λ is applied to all Lennard-Jones energy parameters developed without explicit polarization.

A simple procedure is chosen to verify the applicability of polarizable force fields rather than attempting to perfectly reproducing experimental results. Here, we reduce the Lennard-Jones energy parameters ε_i taken from the UFF and TraPPE force fields with respect to their atomic polarizabilities via:

$$\varepsilon_i^{\text{scaled}} = \varepsilon_i \cdot \frac{(1 + \lambda) - \frac{\alpha_i}{\alpha_{\max}}}{(1 + \lambda) - \frac{\alpha_i}{\alpha_{\max}} \cdot \lambda} \quad (2.11)$$

where α_i and α_{\max} are the atomic polarizabilities of interaction site i and the largest atomic polarizability, respectively. The scaling parameter λ can vary between 0 and 1. Thereby, it is assured that non-polarizable interaction sites ($\alpha_i = 0$) are unchanged and that the potential energy parameters of the atoms with the largest polarizability are reduced the most. The required atomic polarizabilities α_i may be taken from the literature. Many different values for atomic polarizabilities can be found for every atom [185, 198, 218–221]. However, depending on experimental procedure or theoretical assumption the values of polarizabilities can differ significantly [222]. In addition, the local chemical environment affects the polarization behavior and consequently the polarizability of a molecule [220, 221]. Usually, empirical scaling factors are applied to consider differences between gas and condensed phases, whereby different scaling factors are suitable for different classes of molecules [223]. The determination of particular scaling factors often relies on a fitting procedure [224]. Here, a global scaling factor ζ is used to adjust the magnitude of the atomic polarizabilities taken from literature α_i^{lit} with respect to the chosen interaction potential according to:

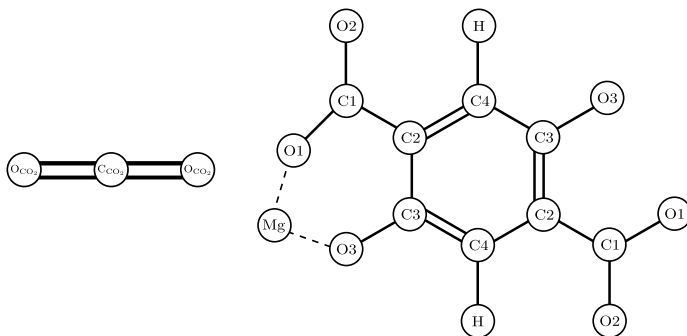
$$\alpha_i = \zeta \cdot \alpha_i^{\text{lit}} \quad (2.12)$$

Thereby, the ratio between the individual atomic polarizabilities is not affected to assure a reasonable relative contribution of polarization between the atoms. This kind of scaling procedure for atomic polarizabilities is frequently used in literature [223, 224] and the scaled polarizabilities adopted in this study have comparable magnitudes to previous molecular simulation studies [117, 184, 185].

2.4. SIMULATION DETAILS

Monte Carlo simulations in the grand-canonical ensemble are conducted to compute the uptake of CO₂ in Mg-MOF-74 for varying pressures of the surrounding gas phase. The simulations were performed using the RASPA software package [225–227]. The atomic structure of Mg-MOF-74 is DFT-based and taken from Dzubak *et al.* [67]. The Lennard-Jones potential is truncated at a cutoff distance of 12.8 Å. No tail corrections are applied. Periodic boundary conditions are used, and the simulation box is composed of multiple unit cells to ensure a distance

Table 2.1: Scaled Lennard-Jones force field parameters and scaled atomic polarizabilities for Mg-MOF-74 and CO₂. The original parameters for Mg-MOF-74 were taken from the UFF force field [72] and the ones for CO₂ are taken from the TraPPE force field [73]. The parameters describing the interactions between framework and adsorbate are adjusted according to Eq. 2.11. Adsorbate-adsorbate interactions are according to the TraPPE force field (*). The atomic polarizabilities are taken from van Duijnen and Swart, and Shannon [218, 219] and scaled with a factor of 0.09. Polarization is only considered between the framework and adsorbate. All molecules are considered to be rigid.



Atom	$\epsilon / k_B / [K]$	$\sigma / [\text{\AA}]$	$\alpha / [\text{\AA}^3]$	Charge / [e]
Mg	55.09	2.69	0.119	1.560
O1	27.93	3.12	0.575	-0.899
O2	27.93	3.12	0.575	-0.752
O3	27.93	3.12	0.575	-0.903
C1	45.80	3.43	0.916	0.900
C2	45.80	3.43	0.916	-0.314
C3	45.80	3.43	0.916	0.456
C4	45.80	3.43	0.916	-0.234
H	21.30	2.57	0.315	0.186
C _{CO₂}	23.40 (27.0*)	2.80	0.916 (-*)	0.700
O _{CO₂}	73.08 (79.0*)	3.05	0.575 (-*)	-0.350

of at least twice the cutoff radius between periodic images. To calculate electrostatic interactions between static partial charges the Ewald summation technique is used. Polarization is considered via the induced point dipole method [179]. Here, the procedure of Lachet *et al.* [185] is applied. To further reduce the simulation time, we use trivial parallelization, i.e., running several simulations concurrently and subsequently averaging over the results to improve statistics. In the past, several approaches have been made to parallel parts of the Monte

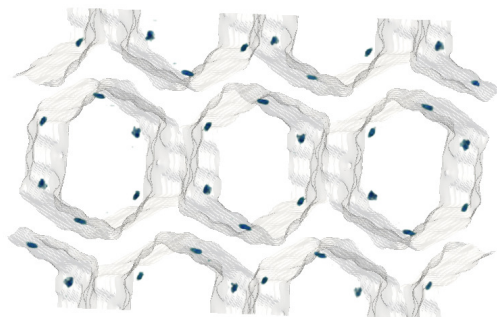


Figure 2.3: Graphic representation of the periodic framework of Mg-MOF-74 with one-dimensional hexagonal channels. The channel surfaces are represented in grey. The blue-green areas show the most favorable adsorption sites of CO_2 which are close to the open metal sites.

Carlo algorithm [228–230]. However, most are not practical anymore due to an increase in the performance of single CPUs. To achieve reasonable energies and CO_2 uptakes in the conducted simulations, we apply a global factor to scale all atomic polarizabilities. The initial values of the atomic polarizabilities are taken from the work of van Duijnen and Swart, and Shannon [218, 219], which provides a large collection of polarizabilities for atoms and molecules. By fitting to the experimentally determined Henry coefficient of CO_2 in Mg-MOF-74, we determine the scaling factor in our simulation to 0.09. In our simulations, polarization is only considered between the framework of Mg-MOF-74 and the adsorbed CO_2 molecules, thus CO_2 - CO_2 interaction parameters are not modified. Framework- CO_2 interaction parameters are calculated via the Lorentz-Berthelot mixing rule from the atomic parameters. We use a simple approach to rescale the Lennard-Jones energy parameters for the interactions between CO_2 and the framework with respect to the assigned atomic polarizabilities. The original parameters for Mg-MOF-74 are taken from the UFF force field [72] and the ones for CO_2 are taken from the TraPPE force field [73]. The Lennard-Jones energy parameter of atom i is adjusted according to Eq. 2.11. By comparing our simulation results to experimental data, we determined λ to be 0.7 ($\alpha_{\max} = 1.591$ which corresponds to the polarizability of methane). All force field parameters are summarized in Table 2.1.

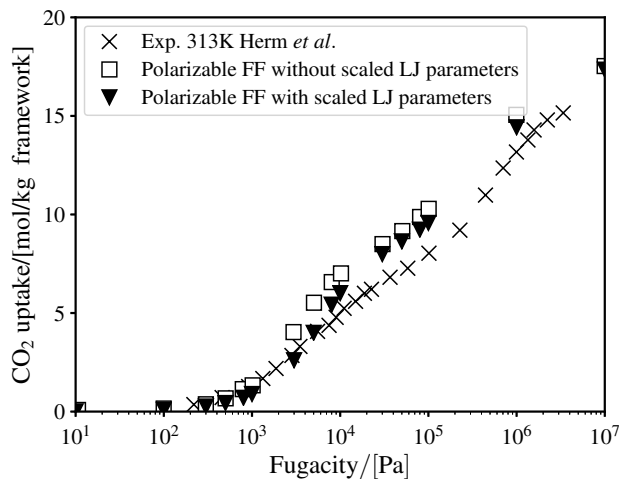


Figure 2.4: Comparison between the experimental adsorption isotherm of CO₂ in Mg-MOF-74 from Herm *et al.* [20] and the simulated ones using polarizable force fields at 313 K. In both simulations, the atomic polarizabilities are taken from van Duijnen and Swart, and Shannon [218, 219] and scaled with a factor of 0.09. The open squares represent the simulation results using the non-scaled Lennard-Jones potential. The adsorption isotherm shown by closed triangles is calculated with a scaling factor $\lambda = 0.7$ for the Lennard-Jones potential. In case of adjusted Lennard-Jones parameters, simulation results are in better agreement with experiments.

2.5. RESULTS AND DISCUSSION

The chosen procedure to scale atomic polarizabilities and to adjust Lennard-Jones energy parameters is divided into two steps. In the first step, Widom test particle insertions are conducted to compute the Henry coefficient of CO₂ in Mg-MOF-74 in the limit of infinite dilution condition [231]. These calculations are computationally relatively cheap. The scaling factor for atomic polarizabilities is adjusted until the predicted Henry coefficient is close to the experimental results. Polarization is of special importance for the low uptake region, where the CO₂ uptake is dominated by the adsorption close to the open metal sites and polarization contributes most. These adsorption sites are shown schematically in Fig. 2.3. The open squares in Fig. 2.4 represent the adsorption isotherm computed with scaled atomic polarizabilities. While in the low pressure region adsorption is already well predicted, the CO₂ uptake in the relatively high pressure region (i.e., larger than 10⁴ Pa) is overestimated. Nevertheless, the overall shape of the adsorption isotherm is in good agreement with experimental measurements. In a second step, the Lennard-Jones energy parameters are adjusted according to Eq. 2.11. Fig. 2.4 shows that this particularly improves the simulation results for intermediate to high pressures. The low pressure region of the adsorption

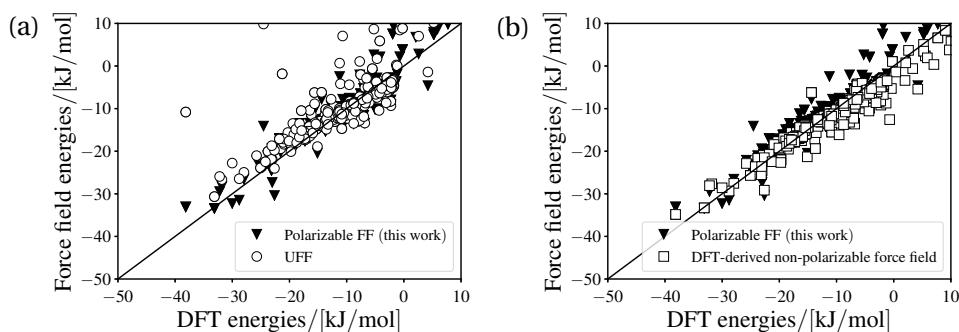


Figure 2.5: CO₂-framework interaction energies for a set of 600 randomly located CO₂ configurations in the accessible volume of Mg-MOF-74. Interaction energies computed in DFT calculations are from Lin *et al.* [80]. The solid line indicates perfect agreement between the force field and DFT energies. (a) Comparison between the polarizable force field and the UFF force field [72]. (b) Comparison between the polarizable force field and the DFT-derived non-polarizable force field of Lin *et al.* (model 3) [80].

isotherm is affected only slightly, because of the higher relative contribution of polarization energy.

To better quantify our polarizable force field for the description of interaction energies between adsorbed CO₂ molecules and the framework of Mg-MOF-74, we compare interaction energies of random CO₂ configurations obtained from DFT calculations with those calculated using the developed polarizable force field. This procedure was previously used by Lin *et al.* [80] to evaluate the quality of force fields. In Fig. 2.5 (a), the comparison of the polarizable force field and the UFF force field is shown. The polarizable force field describes the interaction energies quite adequately, whereas the UFF force field significantly underestimates the interaction energies for a number of configurations, in particular for those with favorable adsorption energies. Fig. 2.5 (b) shows the interaction energies of the polarizable force field and the previously proposed non-polarizable force field derived from DFT calculations (in this work, we compare our results to the model 3 from Lin *et al.* [80]). In the work of Lin *et al.*, the Buckingham potential and electrostatic interactions with static partial charges are used without explicitly accounting for polarization. Both force fields model the interaction energies satisfactorily. However, the DFT-derived non-polarizable force field tends to slightly overestimate the interaction energies (i.e., energetically less favorable region with DFT-computed energies larger than -10 kJ/mol) while the polarizable force field shows the opposite trend. On average and considering only those configurations with interaction energies less than 0 kJ/mol in DFT calculations, the absolute differences between force field-based and DFT-based interaction

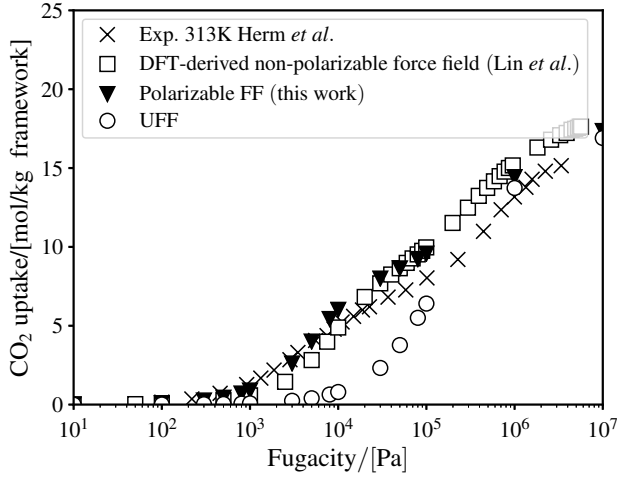


Figure 2.6: Comparison between the experimental adsorption isotherm of CO_2 in Mg-MOF-74 from Herm *et al.* [20] and the ones predicted from molecular simulation at 313 K. The UFF force field [72] cannot reproduce the inflection of the adsorption isotherm and the CO_2 uptake in the low pressures region. The force field previously developed by Lin *et al.* (model 3) [80] derived from DFT calculations can capture the adsorption. The simulations conducted with polarizable force field are in good agreement with the experimental results. The low pressure region and the inflection of the adsorption isotherm are well modeled. The used scaling factor λ for the Lennard-Jones potential is 0.7. The atomic polarizabilities are from van Duijnen and Swart, and Shannon [218, 219] and scaled with a factor of 0.09.

energies are 2.290, 1.673 and 1.537 kJ/mol for the UFF force field, the polarizable force field and the DFT-derived non-polarizable force field, respectively. Another approach to quantify the differences is the Boltzmann-weighted mean deviation (BMD) [80] defined by:

$$\text{BMD} = \frac{\sum_{j=1}^{N_s} |E_{\text{FF},j} - E_{\text{DFT},j}| \exp\left[-\frac{E_{\text{DFT},j}}{k_{\text{B}}T}\right]}{\sum_{j=1}^{N_s} \exp\left[-\frac{E_{\text{DFT},j}}{k_{\text{B}}T}\right]} \quad (2.13)$$

where $E_{\text{FF},j}$ and $E_{\text{DFT},j}$ are the total guest-host interaction energies for configuration j predicted with force field or with DFT calculations, respectively. k_{B} is the Boltzmann constant, and N_s is the total number of sampled configurations. For a chosen temperature T of 300 K, the values of BMD are 21.904, 4.287 and 2.902 kJ/mol for the UFF force field, the polarizable force field, and the DFT-derived non-polarizable force field, respectively. The predicted adsorption isotherms are shown in Fig. 2.6. The experimental adsorption isotherm [20] shows an inflection between 10^4 and 10^5 Pa. The UFF force field cannot reproduce this behavior

and the CO₂ uptake at low pressures that is of direct relevance for carbon capture is largely underestimated. The DFT-derived non-polarizable force field [80] and the polarizable force field both capture the inflection and show significant improvement in the low pressure region. In this region, the CO₂ uptake predicted with the polarizable force field and the DFT-derived non-polarizable force field (i.e., model 3 of Lin *et al.* [80]) are both in good agreement with the experimental data of Herm *et al.* [20]. For higher pressures, all three force fields overestimate the CO₂ uptake compared to the experiments. This overestimation is actually expected, since experimental structures show a certain degree of inaccessibility due to diffusion limitation or defects in the crystal structure [87]. In the limit of high pressures, the guest-host interactions become less important and the adsorption is dominated by the accessible volume for CO₂. The TraPPE force field describes the density per void volume well, because it is designed to reproduce the vapor-liquid equilibria. Therefore, the uptakes of CO₂ predicted using these three models converge in the high pressure region.

2.6. CONCLUSIONS

With the developed polarizable force field, the adsorption of CO₂ in Mg-MOF-74 can be accurately described using molecular simulation. The consideration of polarization results in a force field correctly reproducing the inflection of the adsorption isotherm and the CO₂ uptake in the low pressure region. The quality of the predictions is comparable to a previously DFT-derived non-polarizable force field. The straightforward procedure to adjust atomic polarizabilities and to subsequently re-adjust Lennard-Jones energy parameters should also be applicable in the evaluation of other MOFs with open metal site for a number of gas separation applications, e.g., carbon capture. Moreover, the consideration of explicit polarization in molecular simulation will result in improved physical models, which provide opportunities for better transferability. We motivated the need to re-adjust Lennard-Jones energy parameters that were developed to implicitly account for polarization. A promising aim for the future is the development of a DFT-derived force field that explicitly considers polarization. This approach could result in a fully predictive model with excellent transferability of atomic force field parameters. Such a force field would be of great interest for all systems in which polarization has a significant contribution.

3

POTENTIAL OF POLARIZABLE FORCE FIELDS FOR CO₂ IN MOF-74

This chapter is based on the paper: T. M. Becker, J. Heinen, D. Dubbeldam, L.-C. Lin, T. J. H. Vlugt. Polarizable Force Fields for CO₂ and CH₄ Adsorption in M-MOF-74. *Journal of Physical Chemistry C*, 53 (2017) 4659-4673 [232].

3.1. INTRODUCTION

The society's demand for energy and how it is currently satisfied interweaves strongly with anthropogenic CO₂ emissions and hence to the changing climate [233–235]. It is evident that to maintain present living standards, the energy sector needs to be altered drastically [236]. New environmentally friendly ways of transforming energy have to be implemented on a large scale [237]. This significant change of the energy sector is, however, still years from being fulfilled [176]. New technologies need to be developed and further improved [33]. Near-term measures include the considerable reduction of CO₂ emitted by conventional power plants [174]. To reduce CO₂ emissions of current power plants, CO₂ needs to be separated from, e.g., the flue gas [174, 175]. Besides carbon capture, CO₂ removal is also crucial for other technologies, e.g., the purification of natural gas [238–240]. A promising technology for the efficient separation of large quantities of CO₂ is the separation via solid adsorbents [58, 177]. In this context, MOFs have received substantial attention [48, 176, 241, 242].

In this chapter, we evaluate the potential of explicit polarization to improve

the issue of limited force field transferability using MOFs with open metal sites. In particular, we study the adsorption of CO₂ and CH₄ in M-MOF-74 with M = Co, Cr, Cu, Fe, Mg, Mn, Ni, Ti, V, and Zn. We extend the previously developed polarizable force field for CO₂ in Mg-MOF-74 (compare chapter 2) to structures based on 9 more metal ions and CH₄ without additional fitting parameters. Subsequently, we conduct grand-canonical Monte Carlo simulations, and compare our results to results using other force fields [68, 72] and experiments [21, 49, 68, 85, 87, 212]. Thereby, it is shown that polarizable force fields have potential to improve the transferability of force fields describing porous materials.

3.2. METHODOLOGY

As in chapter 2, scaling of the force field parameters is applied to reproduce the experimental adsorption isotherm for CO₂ in Mg-MOF-74. In a first step, the low fugacity region of the simulated adsorption isotherm and the heat of adsorption for CO₂ in Mg-MOF-74 are tuned by scaling all atomic polarizabilities with ζ (cf. Eq. 2.12). In the low fugacity region CO₂ molecules adsorb close to the open metal sites where polarization interactions are of particular importance. Subsequently, the scaling parameter λ (cf. Eq. 2.11) is adapted to remove the implicit contribution of polarization from the Lennard-Jones potential. Therefore, the value of λ is lowered to match the high fugacity region of the experimentally determined adsorption isotherm. In this region, the center of the channels of Mg-MOF-74 are filled with CO₂ molecules. The locations in the center of the channels are further away from the open metal sites and therefore polarization is less important. By applying this two step procedure, we divide the interaction energy into the underlying physical contributions without using an elaborated approach. For the remaining M-MOF-74 structures and for CH₄, the scaling factors determined for the Mg structure with CO₂ are used. Thereby, the transferability of the approach is investigated. The procedure is chosen to verify if the polarizable force field has the potential to describe the difference between the different metal ions embedded in M-MOF-74.

3.3. SIMULATION DETAILS

Grand-canonical Monte Carlo simulations implemented in the RASPA software package [225, 226] are conducted to compute uptakes and heats of adsorption of CH₄ and CO₂ in different structures of the M-MOF-74 (M = Co, Cr, Cu, Fe, Mg, Mn, Ni, Ti, V, and Zn) family. The uptakes are computed for varying fugacities, for pure components and mixtures at 298 K. DFT-optimized, all atomic MOF structures with atomic charges are taken from Lee *et al.* [86]. In the simulations, the structures are considered to be rigid. Lennard-Jones parameters for CH₄ and

CO₂ are taken from the TraPPE force field [73]. Interactions between guest molecules are not modified and computed concerning to the TraPPE force field. The UFF force field [72] is used for the atoms of M-MOF-74. Cross-interactions are calculated via the Lorentz-Berthelot mixing rule from atomic parameters [243]. All Lennard-Jones energy parameters $\epsilon_i^{\text{scale}}$ used in the simulations are adjusted according to Eq. 2.11 with $\lambda = 0.7$. Thereby, we account for previously implicitly considered polarization. The Lennard-Jones potential is truncated at a cutoff distance of 12.8 Å without tail corrections. To mimic the behavior of the continuous system, i.e., a repetition of identical one-dimensional pores, periodic boundary conditions are applied in all directions (see Fig. 1.3). The simulated system is composed of multiple unit cells to ensure a minimum distance of more than twice the cutoff radius between periodic images. The Ewald summation technique with a relative precision of 10^{-6} is used to calculate electrostatic interactions between static point charges [15]. Explicit polarization is considered via the induced dipole method [179]. Polarization is exclusively considered between the framework and adsorbate molecules. Additionally, back-polarization is neglected to achieve reasonable simulation times. The required atomic polarizabilities α_i are taken from Shannon [218] and van Duijnen and Swart [219] and are scaled with a ζ value of 0.09. All force field parameters are summarized in Tables S1-S11 (Supporting Information of Becker *et al.* [232]). For the comparison with experimental results and simulation results of others we use the Peng-Robinson equation of state to convert pressures to fugacities [244]. The DFT calculations to determine the orbital interaction energy (as explained below) are performed with the Amsterdam Density Functional (ADF) package [245, 246]. The B3LYP-D3 exchange-correlation functional [247–251] is used with a TZP-STO basis set and a large frozen core. A fragment analysis is performed between CO₂ and Mg-MOF-74 to assess the net interaction between these two fragments. Using the energy decomposition analysis scheme by Ziegler and Rauk [252–254], the interaction energy ΔE_{int} between the two fragments is decomposed into:

$$\Delta E_{\text{int}} = \Delta V_{\text{elstat}} + \Delta E_{\text{Pauli}} + \Delta E_{\text{oi}} \quad (3.1)$$

ΔV_{elstat} comprises classical electrostatic interactions between unperturbed charge distributions of the deformed fragments. ΔE_{Pauli} describes the Pauli repulsion energy and corresponds to the destabilizing interactions between occupied orbitals. The Pauli repulsion energy is responsible for steric repulsion. ΔE_{oi} represents the orbital interaction energy which accounts for charge transfer and polarization [245].

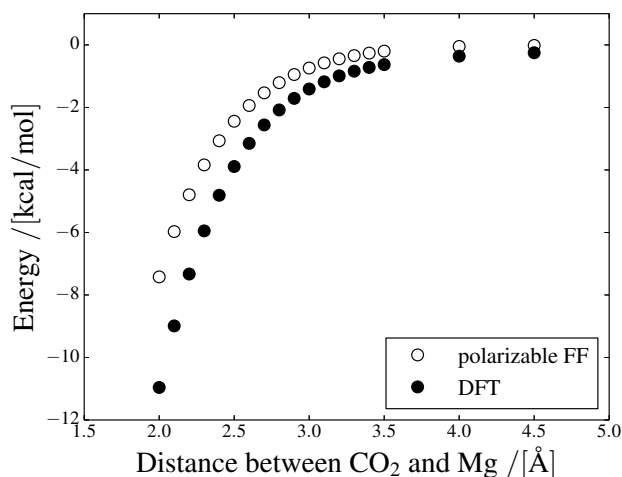


Figure 3.1: Comparison of the polarization energy computed with the developed polarizable force field without considering back-polarization and the orbital interaction energy from DFT calculations as a function of the distance between a CO₂ molecule and the Mg ion.

3.4. RESULTS AND DISCUSSION

As an initial step in the evaluation of the developed polarizable force field, it is important to investigate the role of polarization in the adsorption of guest molecules in M-MOF-74. In Fig. 3.1, we compare the polarization energy of a CO₂ molecule approaching the Mg ion of Mg-MOF-74 estimated with the developed polarizable force field to the orbital interaction energy calculated from ADF. The orbital interaction energy should be a good approximation for the polarization energy, since no reaction is taking place and considerable charge transfer is not expected for very similar configurations of CO₂ inside Mg-MOF-74 [49, 55, 212]. For relevant distances, both methods show a comparable trend for the energy contributions. The most relevant distance between the CO₂ molecule and the Mg ion is where the total energy is the lowest (i.e., 2.3-2.5 Å, as shown in Fig. 2.2). At this distance the polarizable force field predicts that the polarization energy of a single CO₂ molecule in Mg-MOF-74 has a significant contribution of around 30% to the total energy. For larger distances, the contribution of polarization decreases rapidly. In the previous chapter, we investigated the quality of the developed polarizable force field by comparing the total energy of random CO₂ positions inside Mg-MOF-74 with detailed DFT calculations from Lin *et al.* [80]. Thereby, also less favorable positions further away from the Mg ions are probed. These positions are occupied after all open metal sites are saturated. In general, the polarizable force field describes most positions considerably better than the UFF force field and with a quality comparable to a non-polarizable force

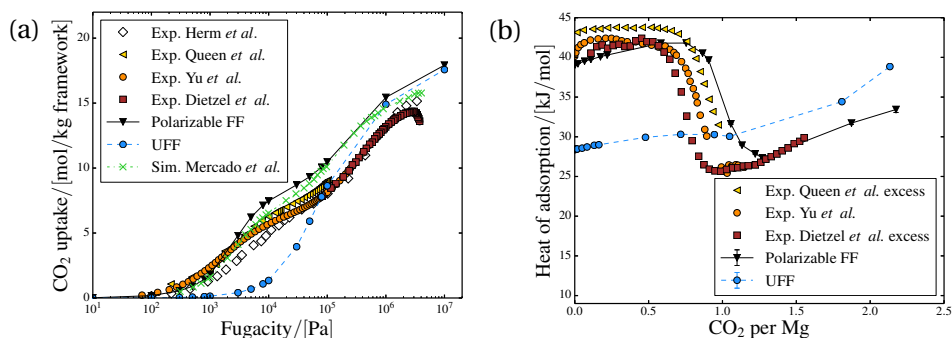


Figure 3.2: Comparison between the experimental results of Herm *et al.* [20] (open), Queen *et al.* [49] (yellow), Yu *et al.* [212] (orange), and Dietzel *et al.* [87] (brown) and simulation results using the developed polarizable force field (black), the UFF force field [72] (blue) and the DFT-derived non-polarizable force field of Mercado *et al.* [68] (green) for CO₂ in Mg-MOF-74. (a) adsorption isotherm at 298 K (Herm *et al.* [20] 313K) (b) heat of adsorption as a function of uptake.

field that has been developed by readjusting the majority of force field parameters [68]. As shown in chapter 2, the scheme applied here is considerably simpler. The resulting adsorption isotherms for CO₂ in Mg-MOF-74 in comparison to experimental measurements, the UFF force field, and the DFT-derived non-polarizable force field of Mercado *et al.* [68] are shown in Fig. 3.2 (a). The simulation results with the polarizable force field clearly display the inflection of the experimental adsorption isotherm. The predicted behavior is significantly better than with the UFF force field. This is expected, because the scaling factors are adjusted to reproduce the experimental data. The overall agreement with the experimental measurements is comparable with the DFT-derived non-polarizable force field of Mercado *et al.* [68]. Both force fields can predict the low fugacity region which is particularly important for carbon capture. For higher fugacities, simulations with all compared force fields predict higher CO₂ uptakes in comparison to the experiments. As pointed out earlier, this can be attributed to the fact that a certain degree of inaccessibility due to diffusion limitation or defects in the crystal structure is inherent with experimental structures [51, 87]. In the limit of very high CO₂ uptakes, the guest-host interactions become less important and the adsorption is dominated by the accessible volume for CO₂ [76]. In the development of the used TraPPE force field the CO₂-CO₂ interactions were adjusted to reproduce the vapor-liquid equilibria and it describes the density per void volume well. Therefore, the uptakes of CO₂ predicted using the polarizable and the UFF force field converge for high fugacities. It should be noted that Mercado *et al.* [68] scaled the calculated CO₂ uptakes with 0.85 to account for inaccessibility of open metal sites. This scaling procedure mainly improves

the agreement between experiments and computations for the high fugacity region. Fig. 3.2 (b) shows the heat of adsorption as a function of CO₂ molecules per metal ion. The distinct inflection of the adsorption isotherm caused by the strong affinity of the CO₂ molecule towards the metal ions is reflected by the change of the heat of adsorption with increasing gas uptake. The calculated heat of adsorption has an inflection at exactly one CO₂ per metal ion. Before and after the rapid decrease at one CO₂ molecule per metal ion, the heat of adsorption increases slightly. This increase can be related to a rise in the total number of adsorbed CO₂ and therefore a larger contribution of CO₂-CO₂ interactions to the total energy. Similarly, the experimental heats of adsorption increase initially. In general, the experimental heats of adsorption have to be regarded with wariness. The heat of adsorption is not measured directly, but calculated at constant loading and averaged over adsorption isotherms at different temperatures according to [212]:

$$-q_{st}/R = \partial(\ln p)/\partial(1/T) \quad (3.2)$$

The temperatures considered vary for all experimental studies. The experimental curves consistently show a drop in the heat of adsorption for lower ratios of the number of guest molecules and metal ions than the simulation results. Different sets of experimental adsorption isotherms show inflections at different uptakes of CO₂. This is another indication for defects in the crystal structure and the blocking of some of the metal ions in the experimental structures. Haldoupis *et al.* [51] further investigated the effect of blocking for Co, Cu, Mn, and Ni based structures. These authors illustrate that varying levels of pore accessibilities can explain the discrepancy between different experimental studies. Especially, the unavailability of open metal sites can explain the drop in the heat of adsorption prior to the complete saturation of these sites. This can be caused by residual solvent molecules binding to the open metal sites. According to Haldoupis *et al.* [51], these residual solvent molecules could reduce the number of accessible open metal sites by 20 to 30%, while only slightly effecting the accessible surface area and the accessible volume. Previously, the good agreement between the experimental BET surface area and pore volume and the theoretical void space in the empty crystal structure made Dietzel *et al.* [87] suggest that their MOF was fully activated. In contrast, Haldoupis *et al.* [51] concluded that a combined effect of crystalline defects and residual solvent molecules is most likely to cause the difference between simulations and experiments. The focus of this study is to evaluate the applicability of a polarizability force field for describing the interactions of guest molecules with different metal ions. In this regard, the consideration of residual solvent molecules and defects does not seem to be crucial. For the remaining M-MOF-74 structures, the parameters adjusted for Mg-MOF-74 and CO₂ are used. Thus, the calculated values are predictions

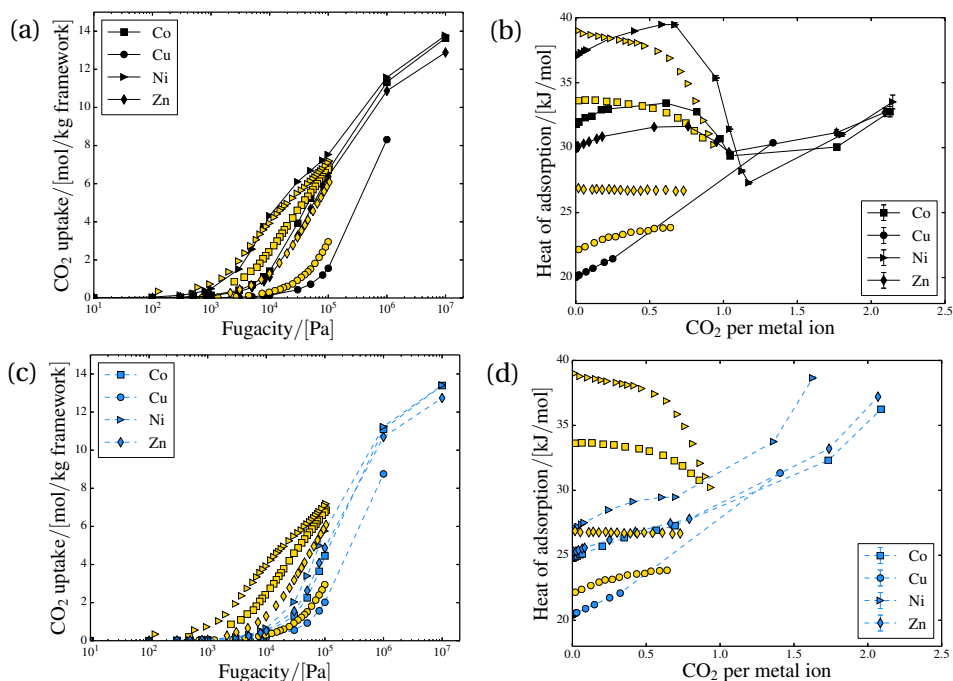


Figure 3.3: Comparison between the experimental results of Queen *et al.* [49] (yellow) and simulation results using the developed polarizable force field (black), and the UFF force field [72] (blue) for CO₂ in the Co (■), Cu (●), Ni (►), and Zn (◆) based structures. (a) and (c) adsorption isotherms at 298 K, (b) and (d) heats of adsorption as a function of uptake.

based on the two global scaling parameters λ and ζ adjusted for Mg-MOF-74. To obtain an overview of the results, we divided the predictions for CO₂ in M-MOF-74 structures into three groups. The first group consists of Co, Cu, Ni, and Zn, the second of Cr, Ti, and V, and the third of Fe, and Mn.

In Fig. 3.3, the computational results for the first group are presented and compared to experimental measurements of Queen *et al.* [49] and the UFF force field. For these structures, the developed polarizable force field is able to describe the experimental measurements well. This is most striking in comparison to the UFF force field which is not able to model the differences between the metal ions. For the polarizable force field, the largest deviations in the adsorption isotherms can be observed for Cu and Co based structures. In agreement with the experimental data, the simulation results for Co and Ni based MOFs show a less distinct inflection for the CO₂ adsorption isotherm than for Mg-MOF-74. The experimental adsorption isotherms for Cu and Zn based structures do not show an inflection for CO₂, which is also accurately predicted in the simulations applying the polarizable force field. The comparison to the experimental results

of Yu *et al.* [212] and the simulation results of Mercado *et al.* [68] can be found in Fig. S2-S11 (Supporting Information of Becker *et al.* [232]). The results of Mercado *et al.* [68] match the experimental adsorption isotherms well. It is worth mentioning that Mercado *et al.* [68] did not perform simulations for Cu-MOF-74. These authors did not develop a force field for Cu-MOF-74, because of an elongation of the unit cell in *c*-direction [86] in comparison to the other M-MOF-74 structures. Although our results for the Cu based structure deviate from the experimental results (compare Fig. 3.3 (a)), the elongation does not seem to be problematic for the general applicability of our approach. The calculated heats of adsorption shown in Fig. 3.3 (b) and Fig. 3.3 (d) have a similar quality as for the Mg based structure. The largest discrepancy between simulation and experiments can be observed for Zn-MOF-74. This is surprising, because the calculated adsorption isotherm agrees very well with experiments and is very similar to the calculated adsorption isotherm for Co-MOF-74 with a similar heat of adsorption curve. Similar to Mg-MOF-74, the heat of adsorption derived from experiments show an inflection significantly before an uptake of one CO₂ molecule per metal ion. As mentioned previously, residual solvent molecules are likely to cause this shift in the heat of adsorption [51], since less open metal sites are accessible. The simulations predict a similar behavior for all structures after all open metal sites are saturated with CO₂. In this region, the CO₂ molecules start to accumulate in the centers of the channels. The geometry of the channels is almost identical for all types of M-MOF-74 and the CO₂ molecules are sufficiently far away from the metal ions to be not significantly affected by polarization. Overall, the polarizable force field seems to have the potential to capture the different degrees of polarizations related to the different metal ions for these 4 structures. Moreover, in contrast to the UFF force field, the polarizable force field is able to predict the correct order of adsorption strength for the Co, Cu, Ni, and Zn based structures.

The computationally predicted adsorption isotherms and heats of adsorption for the second group are compared to the computational results with the UFF force field in Fig. 3.4. For these structures no experimental adsorption measurements are available. To the best of our knowledge these structures belong to the group for which the experimental syntheses is still challenging [89]. The simulations predict a very distinct inflection for the adsorption isotherms of Ti- and V-MOF-74 while the one for Cr-MOF-74 does not show an inflection. The predictions for the Ti and V based structures agree with theoretical predictions of Park *et al.* [45]. These authors expect the structures to have even stronger interactions with CO₂ than Mg-MOF-74 which is supported by our simulations. The trend of the adsorption isotherms for the three MOFs is reflected in the heats of adsorption. The possibility to predict large differences in adsorption also shows that polarizable force fields have the potential to describe such significant dif-

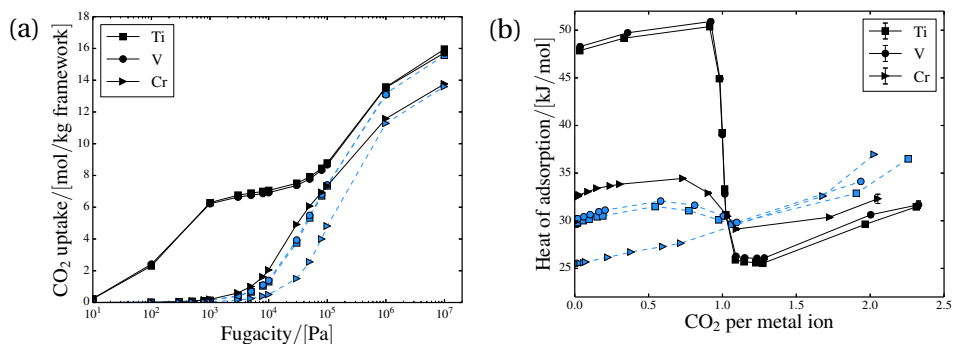


Figure 3.4: Comparison between the simulation results using the developed polarizable force field (black), and the UFF force field [72] (blue) for CO₂ in the Ti (■), V (●), and Cr (►) based structures. (a) adsorption isotherms at 298 K (b) heats of adsorption as a function of uptake.

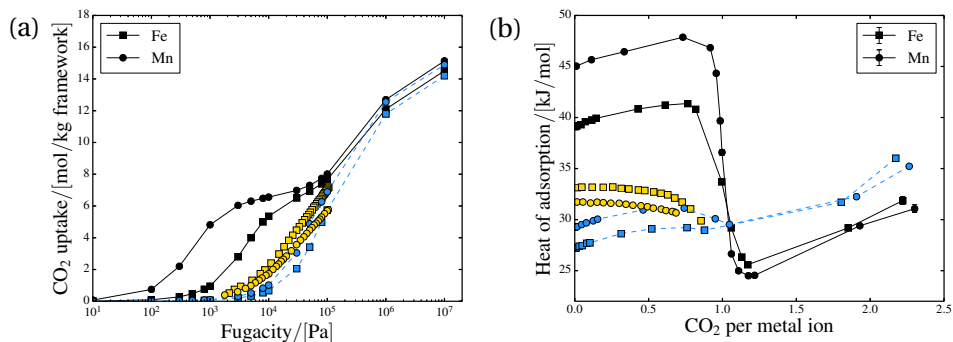


Figure 3.5: Comparison between the experimental results of Queen *et al.* [49] (yellow) and simulation results using the developed polarizable force field (black), and the UFF force field [72] (blue) for CO₂ in the Fe (■), and Mn (●) based structures. (a) adsorption isotherms at 298 K (b) heats of adsorption as a function of uptake.

ferences in the adsorption. Again, the UFF force field predicts a totally different adsorption and a smaller difference between the metal ions (compare Fig. 3.4).

The remaining M-MOF-74 structures are based on Fe and Mn. For these structures, a notably large discrepancy between simulations and experiments is found as shown in Fig. 3.5. The experimental results for the Mn and Fe based structures are very similar. Both structures show weaker interactions between the metal ion and the CO₂ molecules than for the Mg based structure. As can be seen, the developed polarizable force field significantly overestimates these interactions. The UFF force field is able to capture the adsorption better. Several reasons for the overestimation are possible and we feel a combination of different effects is most likely. Interestingly, Mercado *et al.* [68] also failed to obtain a rea-

sonable force field for Mn-MOF-74 based on fitting the interaction potential to quantum mechanical energies. This further suggests that the explanation for the failure could be rather complicated. For example, ferromagnetic effects which are not considered in the polarizable force field may play a more important role for Mn and Fe than for the other structures. Additionally, the initial force field parameters taken from the UFF force field for the two metal atoms could be of particularly bad quality. A comparison between the values for Fe from the DREIDING ($\epsilon/k_B = 27.677$ K, $\sigma = 4.045$ Å) and the UFF force field ($\epsilon/k_B = 6.542$ K, $\sigma = 2.59$ Å) shows the huge difference. Simulations based on the DREIDING parameters result in a totally different prediction of adsorption. This is illustrated by the Henry coefficients of CO₂ in Fe-MOF-74 in the limit of infinite dilution condition [231] which we computed for both sets of force field parameters using Widom test particle insertions [231] (Supporting Information of Becker *et al.* [232]). The sensitivity of the system might also play an important role. In addition, the quality of the selected level of theory for the structure optimization could be better for some of the metal ions than for others [68]. The failure of the polarizable force field to predict the behavior of these two structures needs to be further investigated. Nevertheless, it does not diminish the potential polarizable force fields show for the description of MOFs with open metal sites.

To further verify the applicability of polarizable force fields, grand-canonical Monte Carlo simulations are performed for CH₄ in the M-MOF-74 series. The separation of CO₂ and CH₄ is industrially relevant [240]. Additionally, CH₄ is explicitly chosen to examine the suitability of the polarizable force field to capture the varying influence of different metal ions in M-MOF-74. Both CO₂ and CH₄ have a similar polarizability [219], but show a totally different adsorption in the series of M-MOF-74. Previous studies explain the difference with a combination of electrostatic interactions caused by the permanent quadrupole of CO₂ and polarization [53]. As example, in Fig. 3.6, the predicted adsorption isotherms for CH₄ in Mg, Co, Ni, and Zn based structures are compared to experimental measurements, simulations of Mercado *et al.* [68], and the UFF force field. The data for the remaining structures and the heats of adsorption are provided in Fig. S12-S21 of the Supporting Information of Becker *et al.* [232]. For low fugacities, simulations with the Mn based structure show an unphysical behavior (compare Fig. S17). The DFT-optimized structure of Mn-MOF-74 does not seem to be perfectly symmetrical. Four adsorption sites close to Mn ions are much stronger for CH₄ than the remaining adsorption sites. These adsorption sites are occupied with CH₄ for all fugacities. To investigate this unusual behavior, we conducted Widom test particle insertions to compute Henry coefficients of CH₄ in Mn-MOF-74 in the limit of infinite dilution condition [231] with and without blocking of these 4 adsorption sites. In addition, simulations were performed with Lennard-Jones

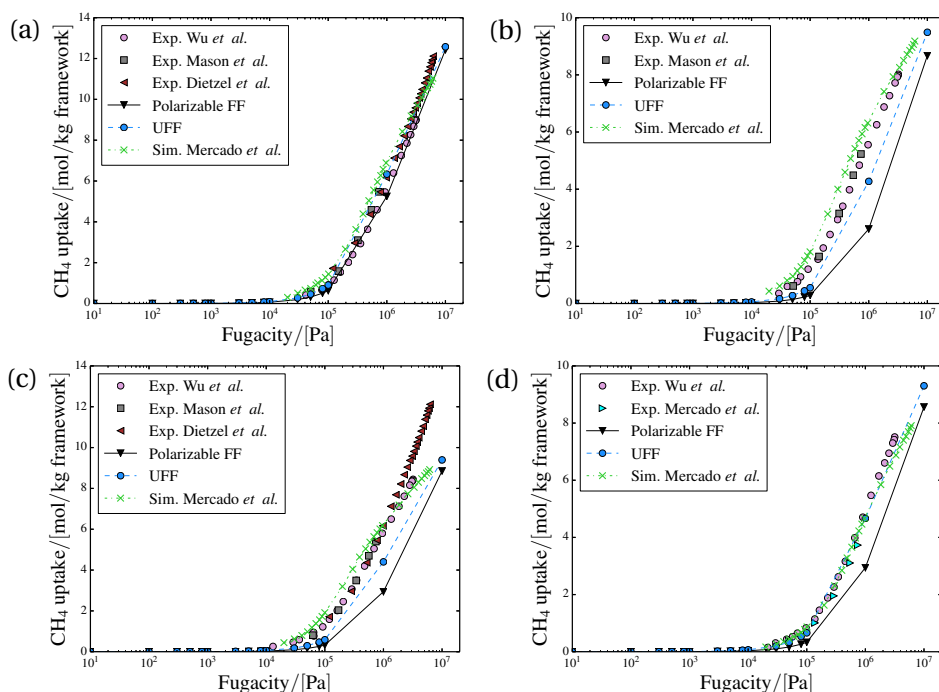


Figure 3.6: Comparison between the experimental results of Wu *et al.* [85] (violet), Mason *et al.* [21] (grey), Dietzel *et al.* [87] (brown), and Mercado *et al.* [68] (cyan) and simulation results using the developed polarizable force field (black), the UFF force field [72] (blue), and the DFT-derived non-polarizable force field of Mercado *et al.* [68] (green) for CH₄. (a) Mg-MOF-74, (b) Co-MOF-74, (c) Ni-MOF-74, (d) Zn-MOF-74.

parameters for Mn from the UFF force field and with parameters for Zn from the DREIDING force field. The results are presented in the Supporting Information of Becker *et al.* [232] and show that the 4 adsorption sites are responsible for the behavior. For DREIDING parameters, the problem does not occur. The locations of the CH₄ molecules are different due to different Lennard-Jones parameters and hence interactions are much smaller. Overall, the UFF force field performs better than the developed polarizable force field for CH₄. The polarizable force field underpredicts the uptake for CH₄. This is due to the very simple and crude procedure to determine the force field parameters. Actually, not a single parameter was adjusted for CH₄. CO₂ and CH₄ have a similar polarizability [219], but CO₂ is modeled with three interaction sides and CH₄ with only one interaction side. Hence, in our force field CH₄ has a larger assigned polarizability than CO₂ and the Lennard-Jones energy parameter for CH₄ is more reduced. Besides, CH₄ is modeled without point charges. It is very reassuring that the

adsorption isotherms of CH₄ computed with the polarizable force field do not show a distinct inflection which is in agreement with experimental results. As expected by Mishra *et al.* [53] and observed in this study, the strong interactions in case of CO₂ are caused by a superposition of static polarity and polarization. Hence, the adsorption of the uncharged CH₄ molecule is far less affected by the different metal ions and a similar behavior is observed for all M-MOF-74 structures. This is correctly captured by the polarizable force field. In addition, the large CH₄ molecules have a larger distance to the metal ions and hence almost no dipole is induced. It would be straightforward to improve the performance of the polarizable force field by introducing a molecule dependent scaling parameter to account for the unequal number of interaction sides. The simulation results of Mercado *et al.* [68] are better than the ones with the UFF force field and the polarizable force field. The experimental adsorption isotherms are well reproduced. However, the same procedure as for CO₂ was performed to fit the force field parameters for all metal ions separately and the CH₄ uptake is scaled with a factor of 0.85 to account for inaccessible open metal sites and blocked pores. In comparison to experimental measurements, the UFF and the polarizable force fields, the curvature of the computed adsorption isotherms for CH₄ of Mercado *et al.* [68] seems to be systematically different. The slope of the adsorption isotherm decreases at much lower fugacities. The reason for this behavior should be investigated to further improve the approach.

Finally, it is possible to make predictions for the adsorption of mixtures of CH₄ and CO₂ with the developed polarizable force field. To measure the gas uptake of mixtures in MOFs is more complicated experimentally and is not often done. Therefore, computational prediction of mixtures are very useful to predict the capability of a material to separate gases. In Fig. 3.7, the predictions of an equimolar mixture of CH₄ and CO₂ are shown for the polarizable force field and compared to predictions based on the UFF force field for Mg-MOF-74 and Zn-MOF-74. For these structures, the single component adsorption isotherms are reproduced reasonably well and therefore the mixture adsorption isotherms are expected to be predicted reasonably. Predictions of mixtures being adsorbed in the other M-MOF-74 structures can be found in Fig. S22-S31 (Supporting Information of Becker *et al.* [232]). Close to the open metal sites the interactions between individual guest molecules with the framework are predominant. Inside the channels, the interactions between CO₂ and CH₄ molecules should be dominant which are reproduced well by the TraPPE force field. Due to the strong interactions for CO₂ with the framework a significantly lower uptake of CH₄ is predicted for Mg-MOF-74 with the polarizable force field. Especially, for low fugacities mainly CO₂ is adsorbed. Only after most of the Mg sites are saturated CH₄ is taken up. In contrast, the UFF force field predicts an uptake of CH₄ even

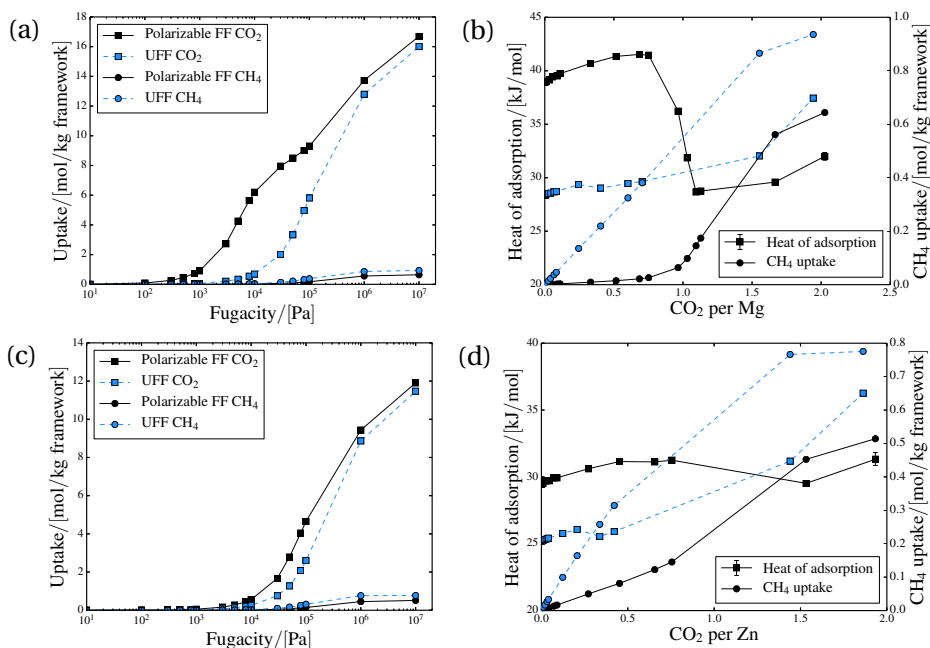


Figure 3.7: Comparison between the simulation results using the developed polarizable force field (black), and the UFF force field [72] (blue) for an equimolar mixture of CO₂ and CH₄ in the Mg (up), and Zn (down) based structures. (a) and (c) adsorption isotherms at 298 K and (b) and (d) heats of adsorption as a function of uptake in Mg-MOF-74 and Zn-MOF-74, respectively.

for very low fugacities. The depicted curves representing heats of adsorption show the released heat for the mixture as a function of CO₂ uptake per metal ion. For Mg-MOF-74, the initial adsorption is very similar to the one for pure CO₂, because initially almost exclusively CO₂ is adsorbed. In contrast, in Zn-MOF-74, CH₄ is already adsorbed for low fugacities. The trend of the heat of adsorption for the mixture deviates from the ones for the pure components. The Zn based structure seems to be less suitable to separate CO₂ from CH₄. The UFF force field predicts an initially larger uptake of CH₄ in comparison to the polarizable force field. This can partially be attributed to smaller interactions between CH₄ and the framework for Zn-MOF-74 with the polarizable force field.

3.5. CONCLUSIONS

The simulations using the developed polarizable force field agree reasonably well with experimental measurements for most of the investigated structures of the M-MOF-74 family. The quality of the predictions for CO₂ is significantly better than with the UFF force field and for most cases comparable to structure

specific force fields developed with more elaborated schemes. The polarization energy computed with the polarizable force field shows a behavior similar to the orbital interaction energy determined from DFT calculations. In principle, these energy contributions should be similar if no reaction and no charge transfer takes place. The conducted procedure of first scaling atomic polarizabilities and subsequently adjusting the Lennard-Jones interaction parameters including implicit polarization is simple and requires relatively little effort. The two global scaling factors used here are exclusively tuned for the Mg based structure and CO₂. Hence, the results for the other structures and CH₄ are predictions. For CH₄, no inflection is observed even so the largest polarizability is assigned to CH₄. The predictions for CH₄ adsorption could be significantly improved by a molecule specific adjustment of the polarizability. The concept of only considering explicit polarization between guest molecules and the framework and neglecting back-polarization seems to be a well suitable approach to study adsorption phenomena in porous materials. The assumptions considerably enhance the computational performance of Monte Carlo simulations while using polarizable force fields. Actually, the computational time can be similar to Monte Carlo simulations without polarizable force field. This is an important assessment, because Monte Carlo simulations are the method of choice for the prediction of adsorption properties in porous materials. Future work will focus on further developing polarizable force fields and to derive a consistent set of parameters from quantum mechanical calculations to avoid fitting to experimental data. We believe that this can lead to force fields with better physical justification and improved transferability. This is crucial for the usage of Monte Carlo simulations for material screening and to make meaningful predictions. Polarizable force fields for Monte Carlo simulations are also promising for other systems with a significant polarization contribution [178, 183], i.e., water [179], systems including ions [178, 184], or xylenes [185].

4

FIRST PRINCIPLE DERIVED POLARIZABLE FORCE FIELD FOR CO₂ IN MOF-74

This chapter is based on the paper: T. M. Becker, L.-C. Lin, D. Dubbeldam, and T. J. H. Vlugt. Polarizable Force Field for CO₂ in M-MOF-74 Derived from Quantum Mechanics. *Journal of Physical Chemistry C*, 122 (2018) 24488-24498 [255].

4.1. INTRODUCTION

In the previous chapters, we verified the potential of polarizable force field for CO₂ in M-MOF-74 by adjusting the force field to reproduce experimental measurements. The applied procedure is based on induced dipoles and has also been successfully applied to model xylenes in NaY zeolite by Lachet *et al.* [185]. The advantage of the procedure is the rapid computational time which is comparable to the time when polarization is not considered. In this chapter, a polarizable force field for CO₂ in M-MOF-74 (M=Co, Fe, Mg, Mn, Ni, Zn) is developed directly from quantum mechanics (QM). Compared to the previous chapters, this procedure is predictive and no prior experiments are necessary. This is of particular interest for hypothetical MOFs [46] that have not been synthesized and no experimental data are available. Adjustments are made to the Lennard-Jones force field parameters of the metal atoms which act as open metal sites. These sites are considered to interact strongly with the guest molecules [67]. The new parameters are determined by reproducing energies computed from DFT calculations. DFT energies for different positions of a CO₂ molecule on paths towards

the interaction sites of the framework are taken from Mercado *et al.* [68] and Lee *et al.* [86]. For Mn-MOF-74, the DFT energies were directly provided by Dr. Kyuho Lee. The details regarding these calculations are analogous to his published work [86]. Similar procedures have been successfully conducted for non-polarizable force fields [67, 68, 80]. Polarization is added to simplify the development of the force field by introducing a model with better physical justification and reducing the number of adjustable variables. Additional parameters to describe the polarizability of interaction sites are assigned according to literature and are not considered adjustable. Simultaneously, explicit polarization might improve the transferability of the resulting force field. The more physical model can potentially lead to a better understanding of the true adsorption.

The detailed procedure on how the polarizable force field is developed from QM is presented in Section 4.2. To investigate the predictive potential of the approach, adsorption isotherms and heats of adsorptions for CO₂ in M-MOF-74 with 6 different metal atoms, i.e., Co, Fe, Mg, Mn, Ni, Zn, are calculated. Subsequently, computational results are compared with experimental results [20, 49, 87, 212]. In comparison to a non-polarizable force field, this approach has the potential to require less adjustable parameters by considering environments with different polarity directly [124, 125, 182]. Moreover, the computational time is comparable to standard Monte Carlo simulations without explicit polarization. We believe that the development of polarizable force fields is a step towards a more realistic description of MOFs and simultaneously to more transferable force fields.

4.2. METHODOLOGY

The development of force fields from QM for MOFs has been the focus of many recent scientific studies [19, 51, 66, 70, 81, 256]. In general, the procedure is based on predicting the potential energy surface from, e.g., DFT [86] or Møller-Plesset perturbation theory [67] and to subsequently optimize the force field parameters in such a way that the potential energy surface is well reproduced. If the force field can describe the correct potential energy surface, it is anticipated to reliably model the adsorption, because locations of single guest molecules and interaction strengths are presumably described well. Of course, assumptions such as the rigidity of the framework and entropic effects may introduce uncertainties. The accuracy of the potential energy surface is determined by the chosen quantum mechanical method [19, 55, 68] and the number of relevant points on the potential energy surface used to describe it. A trade-off between accuracy and computational time has to be made [19]. Different levels of theory, the amount and type of basis sets, and the size of the considered system can affect computational time and accuracy. Here, we chose DFT energies as reference that were

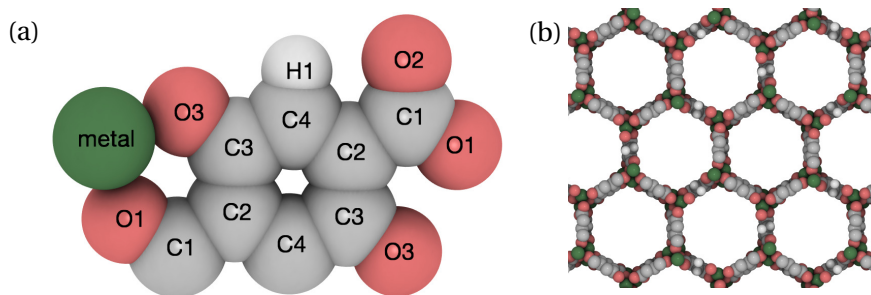


Figure 4.1: (a) Schematic view of the varying atom sites and (b) the framework of Mg-MOF-74. Magnesium, carbon, oxygen, and hydrogen are depicted in green, gray, red, and white, respectively [258].

carefully validated by Lee *et al.* [86]. For the classical force field, it is of particular importance to model the most favorable adsorption sites well, since these sites are dictating the adsorption. As mentioned previously, several studies have been investigating the derivation of force fields from QM to describe adsorption in MOFs [51, 66–68, 70, 79–81]. In these studies Monte Carlo simulations were applied which rarely considered explicit polarizable force fields. Even though polarizable force fields have the potential to improve performance and transferability [117, 122–124]. Here, Monte Carlo simulations are conducted. Explicit polarization is added to the force field via the induced dipole method [178, 179]. Back-polarization is neglected to achieve reasonable simulation times that are in the same order as force fields without considering explicit polarization. The required dipole polarizabilities α_i are taken from literature without being adjusted [218, 257]. More simulation details can be found in chapter 2 and the work of Lachet *et al.* [185]. Lennard-Jones force field parameters of non-metal atoms for M-MOF-74 are assigned according to the UFF force field [72], a generic force field frequently used for the modeling of MOFs [117, 119, 124, 182]. For CO₂, the TraPPE force field is applied which is commonly used to describe CO₂ adsorbed in MOFs [73]. The TraPPE force field describes the VLE of CO₂ well [73]. Polarization is exclusively considered between the framework and guest molecules. Interactions between guest molecules are calculated according to the TraPPE force field. The Lennard-Jones force field parameters of the metal sites are adjusted to reproduce the potential energy surface previously predicted from QM. These metal sites interact strongly with guest molecules and are known to be inadequately modeled by generic force fields [19, 122, 123]. The DFT energies describing the potential energy surface are computed for CO₂ configurations on paths towards atom sites of the MOF frameworks. As an example, Fig. 4.1 provides an overview of the varying atom sites of Mg-MOF-74. The other M-MOF-74 frame-

works are represented analogously. For every M-MOF-74 framework, 9 different atom types can be identified to describe the local environment: the corresponding metal atoms M, three different oxygens O1, O2, O3, four different carbons, C1, C2, C3, C4, and hydrogen, H1. Energy paths are considered towards all atom types besides hydrogen, as in the work of Mercado *et al.* [68] and Lin *et al.* [80]. A grid search is conducted to determine Lennard-Jones force field parameters of the metal atoms. ϵ values and σ values are evaluated ranging from 5.0 to 140.0 K and from 2.4 to 3.3 Å, respectively. For every grid point, the energies predicted from DFT are compared to energies calculated with a polarizable force field for all CO₂ configuration on all energy paths. The objective function used to evaluate the modeling of the total energy on the energy paths towards the various interaction sites is:

$$\min \left(\sum_j^{\text{all paths}} \exp \left[\frac{-E_j^{\text{DFT}}}{k_B \cdot T} \right] \cdot |E_j^{\text{DFT}} - E_j^{\text{MS}}| \right) \quad (4.1)$$

E_j^{DFT} and E_j^{MS} are energies determined via DFT or molecular simulation, respectively, for a CO₂ configuration j on one of the energy paths. k_B is the Boltzmann constant and T the temperature of the conducted molecular simulation (i.e., 298 K). The Boltzmann weight is applied to consider differences in energy and to prioritize more relevant configurations which are lower in energy [19]. The presented approach is straightforward and easy to apply. The aim is to create a predictive polarizable force field that describes the potential energy surface well and can be evaluated with an efficiency comparable to non-polarizable force fields. The effect of polarization is implicitly included in the DFT energies and should be modeled approximately by matching the energies of all energy paths simultaneously while using the induced dipole method in molecular simulation with point polarizabilities taken from literature. Polarizable force fields created in this fashion have the potential to provide improved transferability by considering environments with various polarities [122–124].

4.3. SIMULATION DETAILS

Grand-canonical Monte Carlo simulations as implemented in the RASPA software package [225, 226] are conducted to compute the uptake and heat of adsorption of CO₂ in different structures of M-MOF-74 (M = Co, Fe, Mg, Mn, Ni, Zn). The pure component uptakes are computed for varying fugacities at 298 K up to 10 bar. MOF structures with atomic charges are taken from previous studies [68, 80, 86]. The Ewald summation technique with a relative precision of 10⁻⁶ is used to calculate electrostatic interactions between static point charges [15]. All frameworks are considered as rigid. The Lennard-Jones potential is trun-

cated at a cutoff distance of 12 Å without being shifted and without analytic tail corrections. To mimic a continuous system, periodic boundary conditions are applied. Multiple unit cells are chosen to represent the simulated system and to ensure a minimum distance of more than twice the cutoff radius between periodic images. Lennard-Jones force field parameters for CO₂ are taken from the TraPPE force field [73]. Interactions between CO₂ molecules are not modified and computed based on the original force field. For non-metal atoms of M-MOF-74, Lennard-Jones force field parameters of the UFF force field are assigned [72]. Cross-interactions are calculated via the Lorentz-Berthelot mixing rules from atomic parameters [243]. Explicit polarization is considered via the induced dipole method (cf. Equation 2.10) [185]. Polarization is exclusively considered between the framework and guest molecules. Back-polarization is neglected. The required atomic polarizabilities α_i are taken from Applequist *et al.* [257]. Details on the final force field parameters are listed in the Supporting Information of Becker *et al.* [255]. For the comparison of simulation results with available experimental measurements reported in the literature, the Peng-Robinson equation of state is used to convert pressures to fugacities [244].

4.4. RESULTS AND DISCUSSION

An overview of the results of the grid search is shown in Fig. 4.2 exemplary for Ni-MOF-74. To present the results clearly, the final value of the objective function is scaled between 0 and 1, where 0 represents the lowest and 1 the highest value. The objective function is the sum of the difference in total energy between DFT and molecular simulation weighted by the Boltzmann factor (cf. Equation 4.1). The results of the objective function show that a range of force field parameters for the metal site starting at the upper left corner of Fig. 4.2 and continuing to the lower right corner provides similar agreement between DFT and molecular simulation energies. The results reveal a common problem of force field fitting, namely that the force field parameters can be ambiguous. The lowest value of the objective function can be observed for ϵ of 32.5 K and σ of 2.8 Å for the metal site. The results of the grid search corresponding to the other investigated M-MOF-74 structures illustrate very similar trends and can be found in the Supporting Information of Becker *et al.* [255]. The best found force field parameters together with the value of the corresponding objective function relative to the sum of the objective function for all M-MOF-74 frameworks are summarized in Table 4.1. The parameters for Fe, Mg, and Mn lie on the edge of the parameter space considered in the grid search. However, we observed that enlarging the search range of the grid does not improve the objective function significantly. We decided to continue with the chosen grid which contains a reasonable parameter space. For Mn-MOF-74 and particularly for Mg-MOF-74, the relative values of the objective

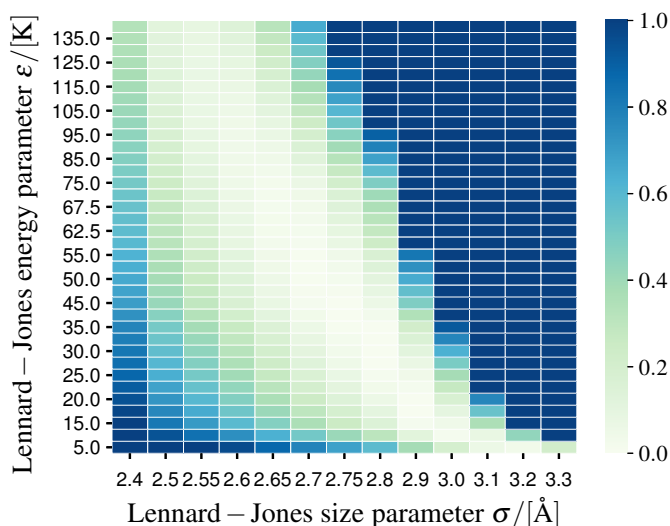


Figure 4.2: Graphic representation of the outcome of the grid search for ϵ and σ of the metal site of Ni-MOF-74. The shown values represent the results of the objective function scaled between 0 and 1. The lowest value of the objective function is represented by 0 while the largest value corresponds to 1.

function are large. Consequently, the description of the CO₂ energy paths for these frameworks seems to be relatively poor in comparison to the other frameworks. In this context, Fig. 4.3 compares the DFT energy paths towards all metal sites. The comparison reveals that the DFT energy path for the Mg site is around 10 kJ/mol lower in energy than for the other metals, while the paths for the Co, Fe, Mn, and Ni based frameworks have a similar lowest energy. This results in a larger value for the objective function of Mg-MOF-74, since the difference in energy is weighted with the Boltzmann factor at 298 K. However, the actual quality of the description of the DFT energy paths for Mg-MOF-74 and the other frameworks is comparable. The case of Mn-MOF-74 is more complicated. The minimum of the Mn energy path is located closer to the framework than for the other metals with similar minimum energy (cf. Fig. 4.3). The large value of the objective function may be a result of the location of the minimum, since the DFT energy paths towards the non-metal interaction sites are comparable for all frameworks. Overall, the chosen objective function suggests that the energy paths are less well modeled for Mn-MOF-74 than for the other frameworks.

In Fig. 4.4 and 4.5, all energy paths for CO₂ towards the various interaction sites of Mn-MOF-74 are compared between the developed polarizable force field and DFT results. It is obvious that the agreement between the DFT energy paths

Table 4.1: Optimal Lennard-Jones force field parameters for the metal sites determined via the grid search. The value of the objective function is provided relative to the sum of objective functions for all frameworks.

Structure	ϵ / [K]	σ / [Å]	Objective function / [%]
Co-MOF-74	30.0	2.75	0.7
Fe-MOF-74	5.0	3.2	0.9
Mg-MOF-74	5.0	3.0	78.7
Mn-MOF-74	5.0	3.1	17.2
Ni-MOF-74	32.5	2.8	2.1
Zn-MOF-74	70.0	2.9	0.4

and the paths obtained with the developed polarizable force field is not perfect. As a result of the grid search, we observed that the Mn and the O1 energy paths cannot be accurately reproduced concurrently. This is important, because both paths are low in energy and therefore crucial for the correct description (cf. Fig. 4.4 (a) and (b)). Interestingly, Mercado *et al.* [68] also experienced difficulties when modeling the adsorption of CO₂ in Mn-MOF-74. These authors did not report a force field for this framework. Besides the comparison between DFT and molecular simulation energies, the underlying energy contributions to the total energy predicted with the polarizable force field are shown. These contributions are polarization energy, electrostatic energy, and Lennard-Jones energy (dispersion and repulsion). A similar energy decomposition is very difficult to achieve in DFT calculations for periodic systems and it is not possible for most available quantum mechanical packages. In the case of Mn-MOF-74, static electrostatic and polarization energies are contributing considerably to the total energy of the Mn and O1 paths, but are less relevant for the other paths. This is expected as the CO₂ molecule is supposed to be polarized in the vicinity of the open metal site [182]. Especially, the repulsive region can not be reproduced accurately by the polarizable force field. The difficulty to model this region could be caused by Lennard-Jones repulsion. Due to overall strong interactions, the energy minima of the energy paths are located close to the framework. At these short distances, the Lennard-Jones contribution of the energy increases too rapidly and dominates the total energy. For example, in case of the optimal position of the CO₂ molecule on the path towards the open metal site, the Lennard-Jones potential is already in the repulsive region (cf. Fig. 4.4 (a)). In addition, static electrostatics and polarization contribute considerably. As a result, a fragile balance between the different energy contributions is created when the binding distance is particularly short. The Lennard-Jones potential was designed rather for computational convenience and especially the repulsive part is non-physical [19] and normally

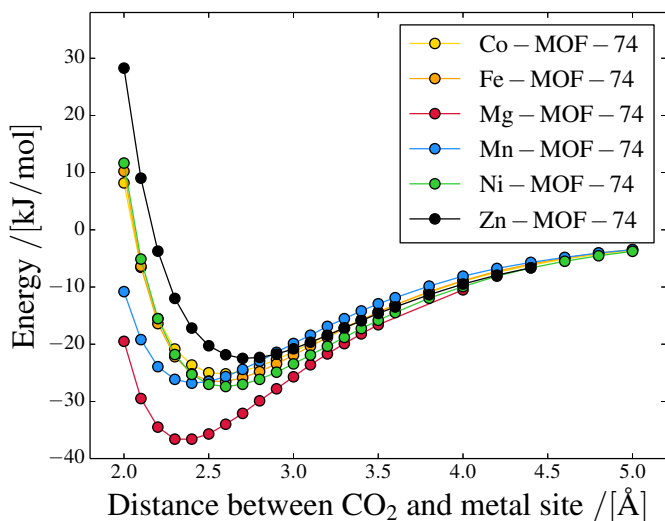


Figure 4.3: DFT energy paths towards the open metal sites for all investigated M-MOF-74 frameworks.

assumed to be modeled poorly [51, 126]. This can lead to inaccuracies in the description, especially for systems with very short binding distances as in the case of MOFs with open metal sites. Another functional form, like in the Buckingham potential which requires an additional fitting parameter, might be closer to reality and therefore more reasonable to describe the repulsion [70]. Finally, it would be beneficial to develop a completely new polarizable force field without any parameters from previous generic force fields [259–262]. Then the balance between the underlying energy contributions could be improved for short binding distances. The energy paths for the other M-MOF-74 frameworks which agree better between DFT and molecular simulation are provided in the Supporting Information of Becker *et al.* [255].

Fig. 4.6 provides an overview of the adsorption isotherms predicted with the developed polarizable force field for all considered M-MOF-74 frameworks and compares the computational results to computational [68] and experimental [20, 49, 87, 212] measurements from various other studies. Overall, the newly designed polarizable force field agrees well with the experimental measurements. Different shapes of the adsorption isotherms can be reproduced by exclusively adjusting Lennard-Jones parameters of metal sites. The agreement is slightly worse than that of the non-polarizable force field of Mercado *et al.* [68]. Somewhat larger deviations can be observed for Co-MOF-74, and Ni-MOF-74. However, to develop their force field, Mercado *et al.* [68] adjusted not only Lennard-

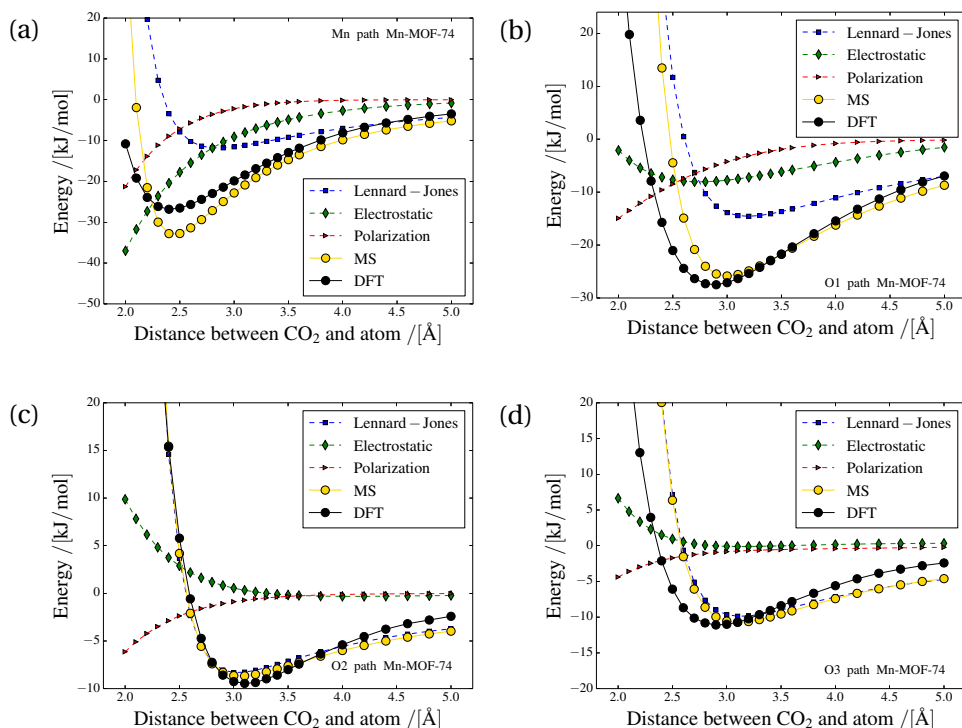


Figure 4.4: Comparison of energy paths towards (a) Mn, (b) O1, (c) O2, (d) O3 for Mn-MOF-74 determined via DFT and molecular simulation with the polarizable force field (MS). Additionally, the different contributions of the molecular simulation energy are shown: Lennard-Jones, static electrostatics, and polarization.

Jones parameters of metal site but of all interaction sites. Thereby, the approach of these authors has more fitting parameters and the potential energy surface can be eventually described better. At the same time, their approach is more elaborate and the resulting force field parameters might be less transferable. In contrast to this work, these authors additionally scaled all adsorption isotherms by a constant factor of 0.85 to account for structural defects. Hence, we are satisfied with the obtained degree of agreement. The computational predictions using the UFF force field cannot describe the experimental data. The adsorption isotherms for frameworks with varying metal ions are predicted to be similar. The larger deviations between experiments and simulations in the adsorption isotherms of Mn-MOF-74 in comparison to the other frameworks might be a consequence of the poor agreement of the energy paths for this framework. As mentioned previously, Mercado *et al.* [68] did not publish a force field for Mn-MOF-74. These authors reported that they could not reproduce the adsorption isotherm even

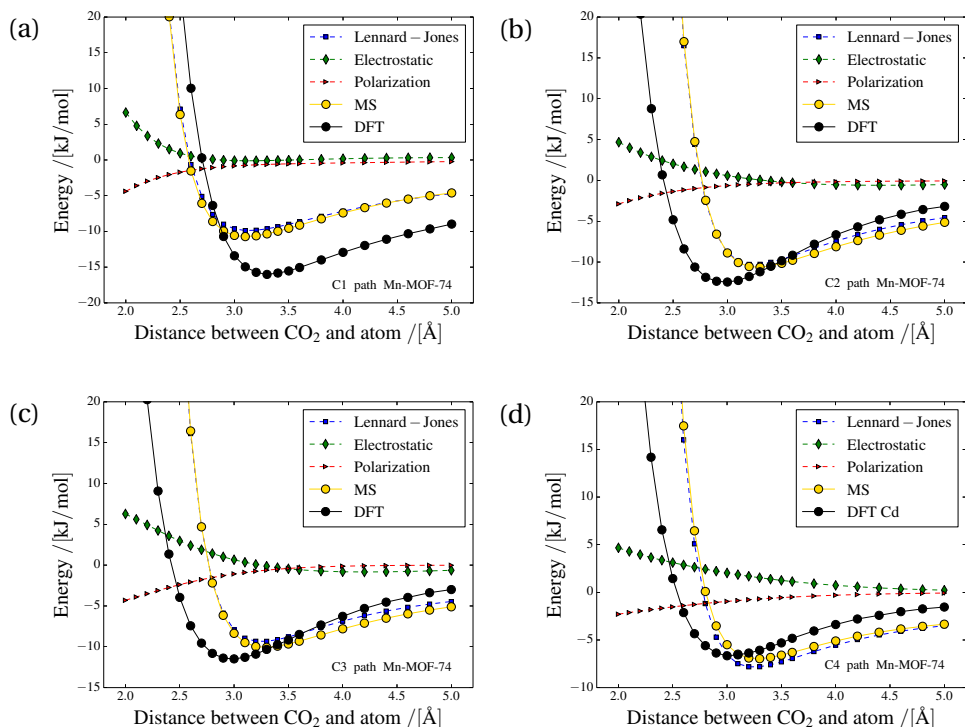


Figure 4.5: Comparison of energy paths towards (a) C1, (b) C2, (c) C3, and (d) C4 for Mn-MOF-74 determined via DFT and molecular simulation with the polarizable force field (MS). Additionally, the different contributions of the molecular simulation energy are shown: Lennard-Jones, static electrostatics, and polarization.

though they could reproduce the energy paths well. The poor agreement could potentially have many causes, e.g., the used atomic structures, the point charge model, or uncertainties in the DFT calculations. To investigate the precise reason is very challenging and beyond the scope of this thesis.

The corresponding comparison of heats of adsorptions for all investigated frameworks are shown in Fig. 4.7. The computational results are compared to heats of adsorptions that are derived from experimental adsorption isotherms via the Clausius-Clapeyron equation [195] by different studies [49, 87, 212]. This method can be sensitive to the specific experimental input [78]. However, in absence of measurements it is the usual benchmark. The computed heats of adsorption follow the trends predicted with the Clausius-Clapeyron equation. The developed polarizable model is able to model the heat of adsorption as a function of the CO₂ uptake. While the overall agreement is good, larger deviations can be observed for the Co, Mn, and Ni based frameworks. These are the

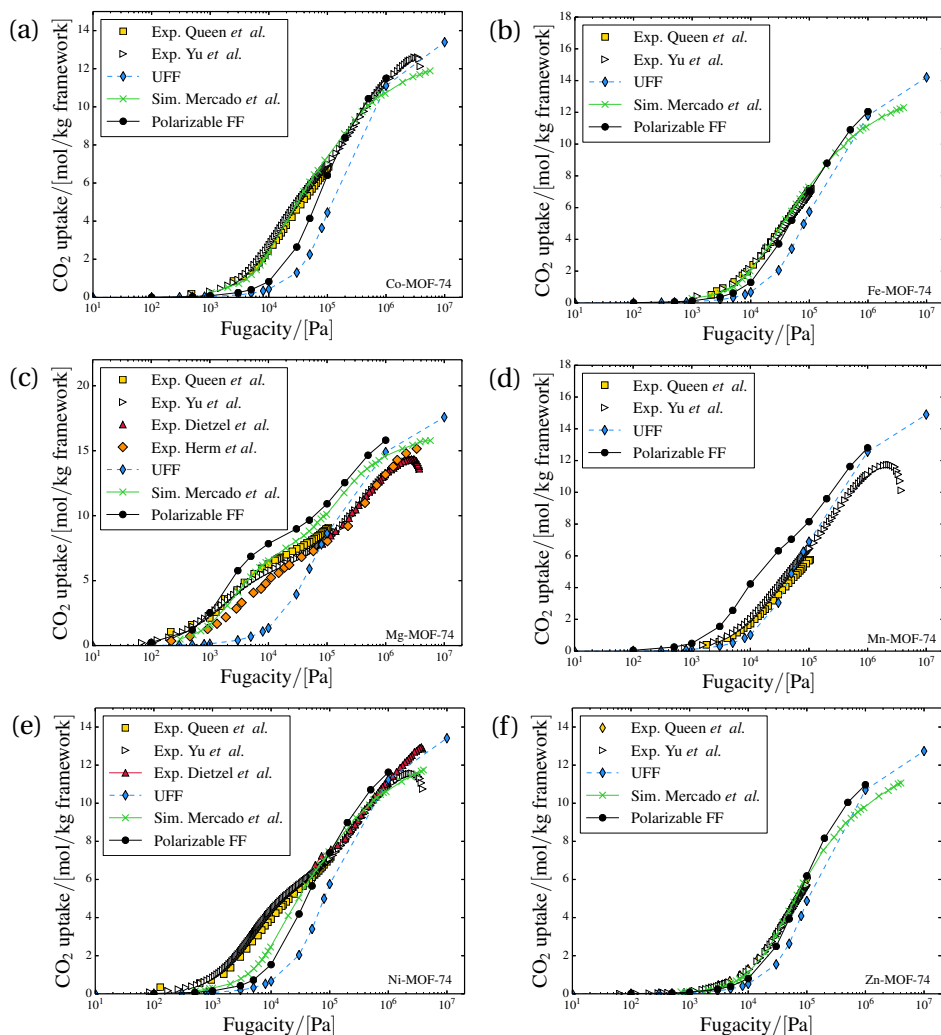


Figure 4.6: Adsorption isotherms for CO₂ in (a) Co-MOF-74, (b) Fe-MOF-74, (c) Mg-MOF-74, (d) Mn-MOF-74, (e) Ni-MOF-74, and (f) Zn-MOF-74 at 298 K. Comparison between the developed polarizable force field, the computational results of Mercado *et al.* [68], simulations performed with the UFF force field [72], and experimental measurement of Herm *et al.* [20], Dietzel *et al.* [87], Yu *et al.* [212], and Queen *et al.* [49].

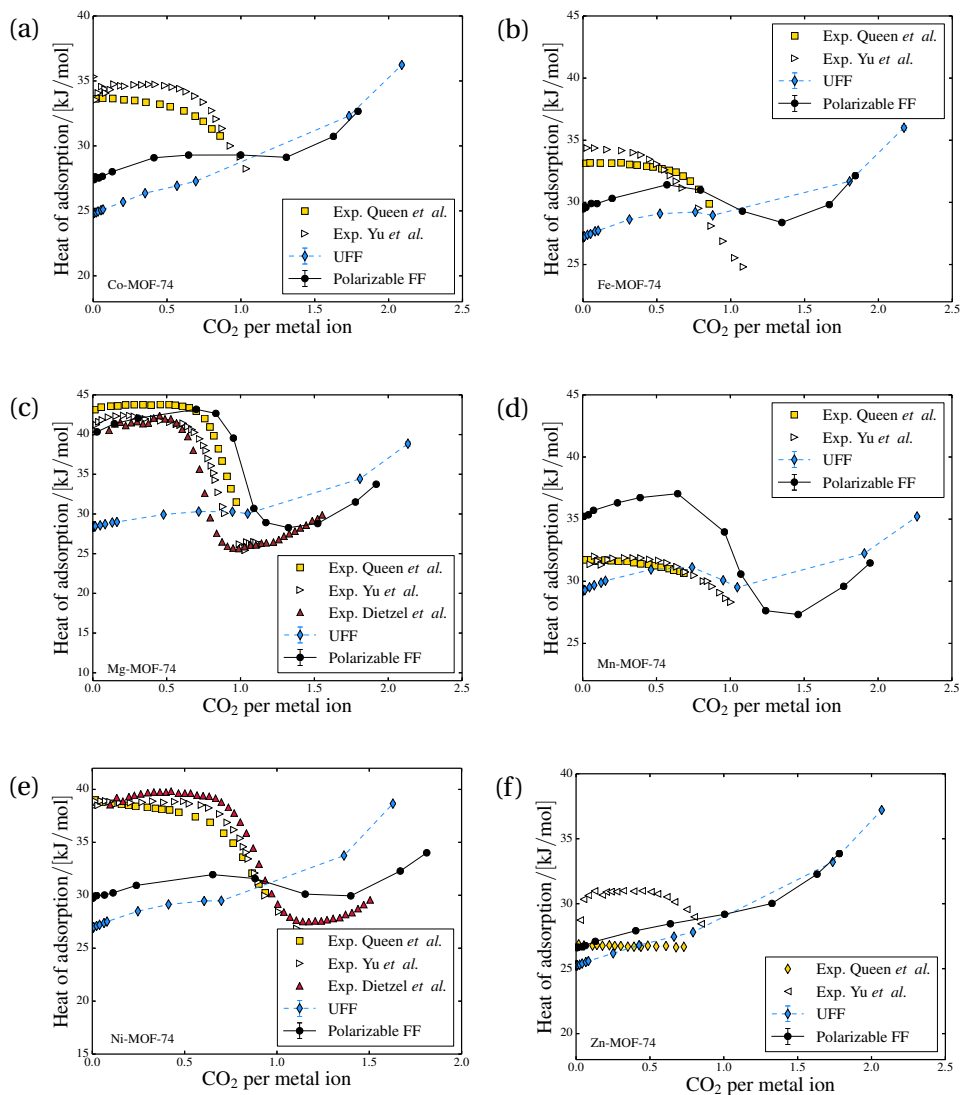


Figure 4.7: Heats of adsorption for CO₂ in (a) Co-MOF-74, (b) Fe-MOF-74, (c) Mg-MOF-74, (d) Mn-MOF-74, (e) Ni-MOF-74, and (f) Zn-MOF74 at 298 K. Comparison between the developed polarizable force field, simulations performed with the UFF force field [72], and results obtained via the Clausius-Clapeyron equation of Dietzel *et al.* [87], Yu *et al.* [212], and Queen *et al.* [49].

Table 4.2: Final Lennard-Jones force field parameters determined via the grid search with charge scaling. The improvement is measured relative to the previous individual objective function without charge scaling (cf. Table 4.1).

Structure	ϵ /[K]	σ /[Å]	f /[-]	Rel. improvement /[%]
Mg-MOF-74	5.0	2.8	0.9	0.196
Mn-MOF-74	105.0	2.4	0.9	0.909

same frameworks that showed deviations for the adsorption isotherms. If the frequently used UFF force field is assigned to the metal sites, the distinct differences between the varying frameworks cannot be modeled.

Although the adsorption is relatively well modeled by the developed polarizable model, further improvement is possible. For Mg-MOF-74 and Mn-MOF-74, the final Lennard-Jones energy parameters are on the lower boarder of the considered grid. Close to the minimum of the total energy of the metal path, the total energy almost exclusively consists of static electrostatic and polarization energy. Hence, Lennard-Jones parameters are favored that contribute only slightly to the total energy of the metal path. As a result, the Lennard-Jones contribution of the metal site to the other energy paths should be small, as well. To further improve the agreement, we have explored the possibility to include charges assigned to framework atoms as fitting parameters in the grid search via a simple scaling. Framework charges are often considered as one of the simulation inputs. However, many different procedures exist to actually fit point charges to the individual interaction sites [263]. Unfortunately, a large sensitivity can be observed for some systems. By reducing the framework charges, the contributions of both the static electrostatic energy and the polarization energy are lowered. The main objective of scaling the point charges is to investigate if the differently determined Lennard-Jones parameters positively influence the overall agreement between DFT and molecular simulation paths. Especially, for the paths that are less influenced by static electrostatic and polarization energy. Consequently, we conducted an additional grid search for Mg-MOF-74 and Mn-MOF-74 in which the point charges and Lennard-Jones parameters of metal ions are varied. Here, all framework charges are scaled with a constant factor f ($q_i^{\text{new}} = q_i^{\text{old}} \cdot f$). We conducted the grid search for f values of 0.95, 0.925, 0.9, 0.85, 0.8, 0.75, and 0.7. The final outcome of this grid search including charge scaling is summarized in Table 4.2. For both frameworks, the best agreement between DFT and molecular simulation energy paths could be achieved for an uniform point charge reduction of 10%. In case of Mn-MOF-74, all energy paths improved. However, the improvement of the objective function relative towards the objective function without charge scaling of Mn-MOF-74 is only 10%. Hence, the modeling of the

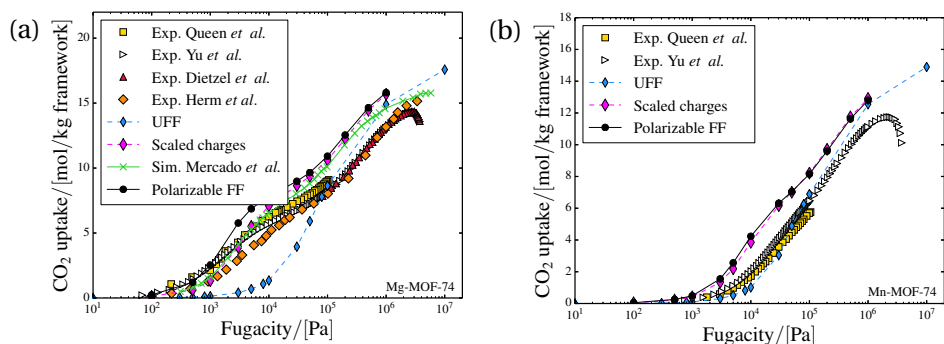


Figure 4.8: Adsorption isotherms for CO₂ with and without charge scaling in (a) Mg-MOF-74, and (b) Mn-MOF-74 at 298 K. Comparison between the developed polarizable force field, the computational results of Mercado *et al.* [68], simulations performed with the UFF force field [72], and experimental measurement of Herm *et al.* [20], Dietzel *et al.* [87], Yu *et al.* [212], and Queen *et al.* [49].

4

energy paths for Mn-MOF-74 is still less accurate than for the other frameworks (cf. Table 4.1). For Mg-MOF-74, the value of the objective function improved by a factor of 5. The improvement results from a better description of the Mg paths. A slight improvement of this path causes a huge change in the objective function, since it is substantially lower in energy than the other energy paths. The other energy paths for Mg-MOF-74 remain approximately the same or in the case of O1 even worsen. All related energy paths with scaled charges for Mg-MOF-74 and Mn-MOF-74 can be found in the Supporting Information of Becker *et al.* [255]. The corresponding adsorption isotherms are shown in Fig. 4.8. The predicted adsorption isotherm for Mg-MOF-74 changes mainly in the low pressure region. Due to the changed parameters, the adsorption isotherm moves closer to the one predicted by Mercado *et al.* [68]. Both adsorption isotherms seem to be acceptable. The one with scaled and the one without scaled charges, are in the range of experimental measurements and the change is rather small. As expected by the rather small improvement in the objective function, the adsorption isotherm for Mn-MOF-74 changes slightly. Still, the agreement between the experimental and predicted adsorption isotherms for Mn-MOF-74 is rather poor. In a related work, Lin *et al.* [80] suggested to not consider the energy paths of the O1 site for the development of a H₂O force field, because the O1 site is located further away from the surface of M-MOF-74. Following this idea, we excluded the energy path for O1 in the evaluation of the grid search for Mn-MOF-74. The best parameters excluding the O1 energy paths for the Mn based framework are $f = 0.9$, $\epsilon = 5.0$ K, and $\sigma = 3.0$ Å. The corresponding energy paths can be found in the Supporting Information of Becker *et al.* [255]. As expected, the energy path towards the

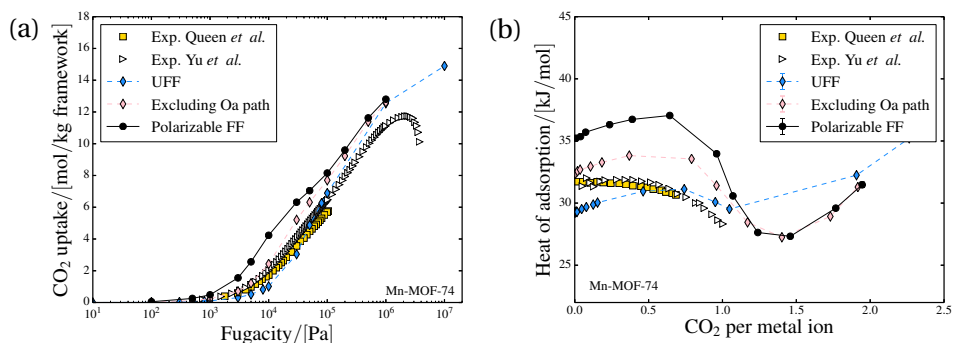


Figure 4.9: (a) Adsorption isotherms and (b) heats of adsorption for CO₂ in Mn-MOF-74 at 298 K with and without considering the O1 energy path in the grid search. Comparison between the developed polarizable force field, the computational results of Mercado *et al.* [68], simulations performed with the UFF force field [72], and experimental measurement of Yu *et al.* [212], and Queen *et al.* [49].

O1 site is less well reproduced than when considering it in the evaluation of the grid search. The description of the Mn energy path is improved even though the repulsion part is still not well reproduced. The computed adsorption isotherm and heat of adsorption predicted with the new parameter set are presented in Fig. 4.9. Apparently, the modeling of the adsorption is improved. Both for the adsorption isotherm as well as for the heat of adsorption. A possible reason may be the improvement in the description of the minimum in the Mn energy path. As mentioned previously, the minimum energy is located closer to the metal site than for the other frameworks with comparable minimum energy. At this distance, the total energy depends strongly on the repulsion in the Lennard-Jones potential of the Mn site. Unfortunately, an improvement caused by the deletion of the O1 energy path in the evaluation of the grid search cannot be observed for the remaining frameworks. Instead, for the other frameworks, the opposite behavior can be observed, the agreement between experimental measurements and computational predictions becomes poorer. This is intuitive, since the energy paths are merely points on the potential energy surface which should in general be described better if more points are considered in the fitting. As suggested by Mercado *et al.* [68], the underlying issue to describe Mn-MOF-74 might be more complicated and further investigations are needed.

4.5. CONCLUSIONS

The presented procedure to derive polarizable force fields is fully predictive. To consider explicit polarization, the induced dipole method is applied. Due to previously introduced simplifications, the computational time is similar to standard

Monte Carlo simulations without considering explicit polarization. The used atomic polarizabilities are taken from literature without further adjustment. No prior experimental data are required for the development. A grid search is conducted to adjust the Lennard-Jones parameters of the open metal sites. The results confirm that the procedure works well and that the experimentally measured adsorption is reproduced. Besides, the procedure is relatively simple and easily transferable to other Metal-Organic Frameworks with open metal sites. By the explicit consideration of polarization in molecular simulation, the contribution of polarization is physically interpretable and can provide further knowledge of the underlying mechanisms of the molecular system. This might help to customize Metal-Organic Frameworks that perform even better for certain applications. Tuning the electrostatic environment could potentially be very useful. The comparison between DFT and molecular simulation energy paths reveals that differences arise mainly in the repulsive region of the Lennard-Jones potential. Typically, this region is badly described by a Lennard-Jones potential. In the case of Metal-Organic Frameworks with open metal sites, it is of more importance than usually, since the guest molecules interact strongly with open metal sites and binding distances are short. Further improvement can be expected when improving the modeling of the repulsive region of the potential. This might be achieved by a more realistic functional form such as the Buckingham potential. For M-MOF-74, significant effects of static electrostatic interactions and polarization can be observed for paths towards the open metal sites and towards the O1 site. The contribution of electrostatics is less for the energy paths towards the other interaction sites. Uniformly adjusting the framework charges together with the Lennard-Jones parameters of the metal sites showed relatively small effects for Mg-MOF-74 and Mn-MOF-74. In contrast, not considering the energy path towards the O1 site could improve the description of the experimentally observed adsorption for Mn-MOF-74. However, for the remaining frameworks the inclusion of the O1 energy path was beneficial. Ultimately, the complete set of force field parameters should be consistently deducted from Quantum Mechanics. A predictive, transferable, and polarizable force field created in this way would be of great value. It would have the potential to improve the understanding of adsorption and to computationally screen Metal-Organic Frameworks for specific applications.

5

OPPORTUNITIES OF POLARIZABLE FORCE FIELDS TO MODEL HYDROCARBONS IN METAL-ORGANIC FRAMEWORKS

This chapter is based on the paper: T. M. Becker, A. Luna-Triguero, J. M. Vicent-Luna, L.-C. Lin, D. Dubbeldam, S. Calero, and T. J. H. Vlucht. Potential of Polarizable Force Fields for Predicting the Separation Performance of Small Hydrocarbons in M-MOF-74. *Physical Chemistry Chemical Physics*, 20 (2018) 28848-28859 [264].

5.1. INTRODUCTION

The separation of light olefins and paraffins is one of the major large scale processes in the petrochemical industry [99, 265]. Light paraffins are mainly used for heating while olefins are important raw chemicals. For instance, the production of polymers requires a high purity of olefins [99]. Conventionally, light hydrocarbons are separated after cracking of long chain hydrocarbons in cryogenic distillation. The product of the cracking at elevated temperatures has to be cooled down to the low boiling points of the light hydrocarbons [266] (e.g., ethane: 184.5 K, propane: 231.1 K [100]). This makes cryogenic distillation a very cost intensive process both energy and investment wise and alternatives have been investigated for decades [267]. A more cost and energy efficient separation

of light hydrocarbons is also crucial for the purification of natural gas [68], which has to be realized economically on a smaller scale [101].

Solid adsorbents can be operated at intermediate temperatures. Thereby, they have the potential to drastically lower the energy required to separate light olefins from paraffins by avoiding the cooling necessary for cryogenic distillation [99, 100, 268–270]. Traditionally, the separation of light olefins via physical adsorption has not been considered promising due to low uptake capacities [267]. This limitation might be surmountable by MOFs. Open metal sites interact more strongly with unsaturated hydrocarbons than with saturated hydrocarbons [271–273]. In an adsorption process, M-MOF-74 has the potential to achieve the high selectivities and large uptakes required by industry [99, 101]. Several experimental studies have been conducted and confirm that M-MOF-74 is indeed able to fractionate multicomponent hydrocarbon mixtures [53, 99–103], as well as other gases [20–22, 53, 54, 85].

5

A recent first-principle simulation study suggests that π bonding, polarization, and strong dispersion interactions between the olefins and the open metal sites are accountable for the high uptake of olefins [102]. In addition, dipole and quadrupole interactions have been demonstrated to play an important role [86, 105]. Molecular simulation offers the possibility to further investigate the underlying mechanisms of the separation [15]. A fundamental understanding can help to rationally design MOFs with customized properties for enhanced performance [120, 126]. However, it is challenging to capture the adsorption of MOFs with open metal sites and further research is required [124, 126, 270, 274]. The main question to address is how to incorporate the enhanced interactions of olefins with open metal sites. From a research perspective, the family of M-MOF-74 is a perfect candidate to examine this question, because the influence of varying cations acting as open metal sites can be investigated using a series of iso-structures [53, 68, 85, 86]. Several molecular simulation studies considering light hydrocarbons in M-MOF-74 have already been conducted [77, 105, 270]. However, generic force fields are known to be inadequate [66, 124, 274, 275] and until now customized force field seem to be the only solution for these systems.

This chapter aims to investigate the potential of polarizable force field to describe the adsorption of ethane, ethylene, propane, and propylene in MOFs with open metal sites. Force fields developed by others [115, 276] which include point charges are used for ethylene and propylene to reproduce the static quadrupole and dipole moments, respectively. The non-iterative induced dipole procedure of Lachet *et al.* [185] is applied to consider polarization explicitly. Point polarizabilities are taken from literature and are added to the atom sites of all investigated molecules. To obtain an unbiased understanding of the potential of polarizable force fields for the description of light olefins and paraffins, no adjust-

ments of the force field parameters are made to further improve results. With the polarizable model, heats of adsorption, binding geometries, and adsorption isotherms are calculated and compared to already existing force fields and experimental data. Subsequently, the influence of individual energy contributions and the effect of different sets of framework charges are discussed. Finally, the performance of the new model including polarization is evaluated, difficulties are reported and possibilities for improvement are highlighted.

5.2. BACKGROUND

The force field development of olefins and paraffins in MOFs with open metal sites is particularly challenging [126, 270, 274]. The model has to describe differences in adsorption for molecules with comparable size and chemical composition [60, 100, 267]. Examples of force fields that are unable to capture the physical difference between olefins and paraffins in MOFs with open metal sites are the TraPPE force field [277] and the force field of Liu *et al.* [278]. A common approach to overcome the limitations of such force fields is to adjust the Lennard-Jones mixing rules between framework and adsorbate. Luna-Triguero *et al.* [77] adjusted the mixing rules and thereby developed a force field which describes the adsorption of light hydrocarbons in M-MOF-74 well. Unfortunately, force fields that are created in this fashion are usually not transferable to other systems [77]. Generic force fields that do not include point charges nor explicit polarization seem to fail in an environment in which localized electrostatic effects occur as in the case of M-MOF-74 [123–125].

A more physically motivated approach to model the difference in adsorption between olefins and paraffins could be to include point charges and explicit polarization [126]. To the best of our knowledge, none of the currently available models considers explicit polarization successfully for these molecules in MOFs [115, 126, 181, 276–278]. Furthermore, many force fields do not take into account the difference in charge distribution between olefins and paraffins explicitly. The polarizability of olefins and paraffins is similar while the permanent multipole moments are much stronger for olefins [100]. It has been suggested that a combined effect between polarization and electrostatics might be crucial to model the adsorption in MOFs with open metal sites and that considering exclusively electrostatics is not sufficient [124, 125]. In molecular simulation most commonly, point charges are assigned to molecules to reproduce multipole moments [263]. These multipole moments can be predicted from QM, determined via experiments, or fitted to reproduce experimental data [263, 279]. For olefins and paraffins, the common approach is to add point charges to olefins, but not for paraffins [115, 276, 280]. Such models are chosen here. Besides the adsorbates, charges need to be considered for the framework of the MOF.

Here, the induced dipole method is adopted [178, 179] to account for polarization. The same additional approximations and assumptions are made as in the previous chapters. Details of the simulation procedure are explained in the work of Lachet *et al.* [185] and in chapter 2. It is important to note that in the work covered in this chapter no fitting parameters are used and that the computational results are pure predictions.

5.3. SIMULATION DETAILS

The RASPA software package [225, 226] is used to conduct grand-canonical Monte Carlo simulations and to compute the absolute uptake of ethane, ethylene, propane, and propylene in several structures of M-MOF-74 (M = Co, Mn, Fe, and Ni). The pure component uptakes are computed for varying fugacities at 318 K and for pressures up to 8 bar. Heats of adsorption at infinite dilution are determined from energy differences in the NVT ensemble [231]. In addition, NVT Monte Carlo simulations are conducted to determine the binding geometry of all adsorbate molecules in M-MOF-74. A simulated annealing procedure is used to find the position corresponding to the global energy minimum. MOF crystal structures for Co-MOF-74, Fe-MOF-74, Mn-MOF-74, and Ni-MOF-74 are taken from Dietzel *et al.* [91], Bloch *et al.* [22], Zhou *et al.* [26], and Dietzel *et al.* [92], respectively, while atomic charges are assigned according to DFT calculations and are taken from the work of Lee *et al.* [86] and Mercado *et al.* [68]. The positions of framework atoms are considered to be fixed. Lennard-Jones parameters for paraffins are taken from the TraPPE force field [277] and for ethylene and propylene from Lahoz-Martín *et al.* [276] and Gutiérrez-Sevillano *et al.* [115], respectively. Interactions between adsorbates are not modified and computed based on the original force fields. Force field parameters of the DREIDING force field are assigned to carbon, oxygen, and hydrogen atoms of M-MOF-74 [188]. Lennard-Jones parameters of Co, Mn, Fe, and Ni are taken from the UFF force field [72]. Cross-interactions are determined via the Lorentz-Berthelot mixing rule [243, 281]. The Lennard-Jones potential is truncated at a cutoff distance of 12 Å without tail corrections. Periodic boundary conditions are applied in all directions to mimic the behavior of a continuous system. The simulated systems are composed of 2x2x4 unit cells to ensure a minimum distance of more than twice the cutoff radius between periodic images. The Ewald summation technique with a relative precision of 10^{-6} is used to calculate electrostatic interactions between static point charges [15]. Explicit polarization is considered via the induced dipole method [179] with additional assumptions introduced by Lachet *et al.* [185]. As noted above, polarization is exclusively considered between the framework and adsorbate molecules. Back-polarization is neglected to achieve reasonable simulation times. The required atomic polarizabilities α_i are taken

from Stout and Dykstra [282]. All force field parameters are summarized in the Supporting Information of Becker *et al.* [264]. For comparison with experimental results and reported simulations results, the Peng-Robinson equation of state is used to convert fugacities to pressures [244].

5.4. RESULTS AND DISCUSSION

To verify how inclusion of polarization influences the description of small hydrocarbons in M-MOF-74, heats of adsorption at infinite dilution, binding geometries, and adsorption isotherms are investigated. The heat of adsorption is a measure of the interaction strength between adsorbates and framework [78, 231]. Here, heats of adsorption at infinite dilution are compared with values derived from experimental adsorption isotherms at different temperatures using the Clausius-Clapeyron equation [100, 195]. Although, heats of adsorption derived from the Clausius-Clapeyron equation are sensitive towards small changes in the adsorption isotherms [78], comparison with the Clausius-Clapeyron equation to assess the quality of molecular simulation in the absence of experimental measurements is useful. To systematically investigate the influence of point charges and explicit polarization, heats of adsorption are calculated with force fields that incorporate these features fully, partially, or not at all. Force fields that neither consider point charges nor polarization are the force field of Liu *et al.* [278] and the TraPPE force field [277]. In the following, the force field that exclusively considers point charges for olefins is named *no polarization* and the one that solely considers explicit polarization is referred to as *no charges*. The force field that considers both charges and polarization is called *pol. force field*. The calculated heats of adsorption for these force fields are presented in Fig. 5.1 for ethane, ethylene, propane, and propylene in (a) Co-MOF-74, (b) Fe-MOF-74, (c) Mn-MOF-74, and (d) Ni-MOF-74. Since no point charges are assigned to paraffins, the force field *no charges* and the force field of Liu *et al.* [278], and *no polarization* and the polarizable force field are equivalent for ethane and propane. The heats of adsorption determined with the Clausius-Clapeyron equation from experiments show strong affinity between the olefins and all investigated M-MOF-74 frameworks [99–101]. The binding energies predicted by Lee *et al.* [86] display larger differences between the individual frameworks. According to the results of these authors, especially the behavior of propane in the different frameworks varies. Here, the computed heats of adsorption show that neither the force field considering solely charges (*no polarization*) nor the one considering solely polarization (*no charges*) can reproduce the experimental trend. The force field of Liu *et al.* [278] and the TraPPE force field [277] show the opposite behavior to experiments, i.e., a higher affinity for paraffins. Adding solely polarization simply increases the interactions for both paraffins and olefins. Moreover, inclusion

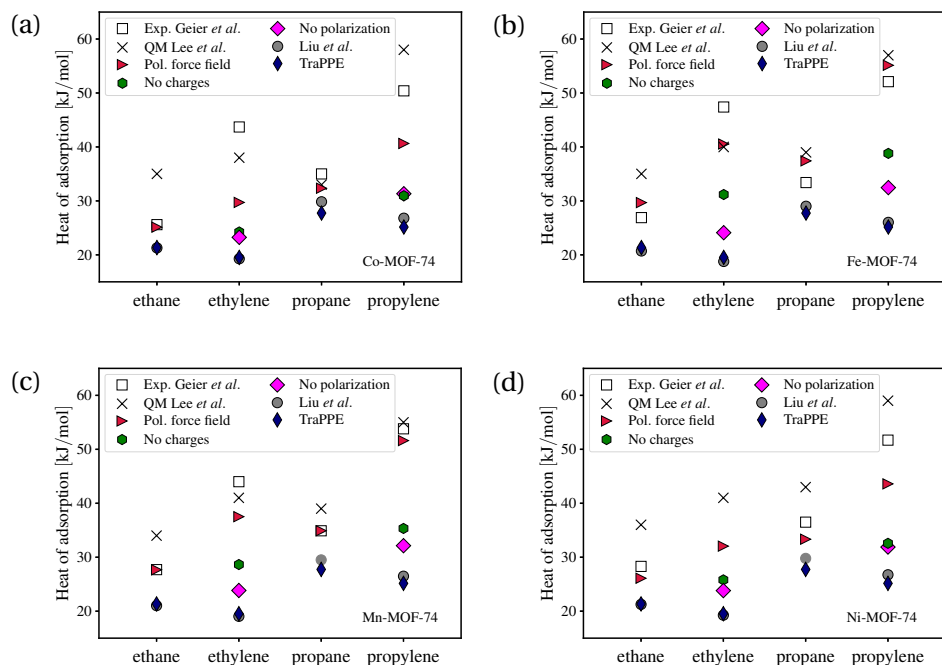


Figure 5.1: Heats of adsorption at infinite dilution calculated using various force fields [277, 278] at 318 K for (a) Co-MOF-74, (b) Fe-MOF-74, (c) Mn-MOF-74, and (d) Ni-MOF-74. The computational results are compared to DFT binding energies from Lee *et al.* [86] and heats of adsorption predicted via the Clausius-Clapeyron equation from experiments by Geier *et al.* [100].

of charges without polarization does not increase the binding affinity of olefins sufficiently to reproduce the expected trend. In sharp contrast to including either point charges or explicit polarization, when considering both, the calculated heats of adsorption follow the experimental trend. A large synergy effect between electrostatic interactions and polarization can be observed. This synergy effect significantly increases the calculated heats of adsorption for olefins. Similar effects have been previously observed by Forrest *et al.* [124] and Pham *et al.* [125]. For the polarizable force field, differences can be observed between Co-MOF-74 and Ni-MOF-74, and Fe-MOF-74 and Mn-MOF-74. In the case of Fe-MOF-74 and Mn-MOF-74, the affinity of the olefins is more pronounced. For Co-MOF-74 and Ni-MOF-74, the polarizable force field predicts lower heats of adsorption for ethylene and propylene in comparison to the predictions from the Clausius-Clapeyron equation. Nevertheless, it is evident that considering polarization together with point charges for olefins significantly improves the capability of the force field to describe heats of adsorption in M-MOF-74. The polarizable force field has the capability to model the larger adsorption strength

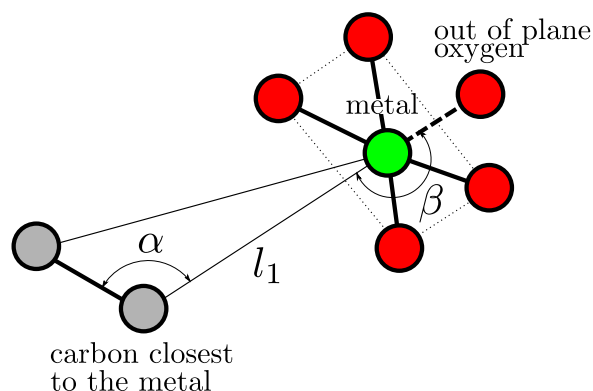


Figure 5.2: Schematic representation of the binding geometry for C2 hydrocarbons within MOF-74. Carbon atoms, the metal atom, and oxygen atoms are colored in grey, green, and red, respectively.

for olefins. No perfect quantitative agreement with experiments can be expected, since the improvement in the description was achieved by simply adding explicit polarization to the model of the adsorbates without further adjusting any force field parameters. Analogously to the observation of Franz *et al.* [126], the predicted energetics for low uptakes seem to be better modeled when considering polarization.

In previous studies of others [86, 99, 270], the stronger binding of olefins over paraffins has been ascribed to interactions between the double bond of olefins and open metal sites of the MOF. Some authors suggest that the double bond of olefins is located parallel to the open metal site, while paraffins bind with one side pointing towards the open metal sites [99, 100]. These adsorption geometries can be examined in molecular simulation. A simulated annealing procedure is conducted to determine the lowest energy binding geometries. The results are compared to geometries predicted in DFT calculations performed by Lee *et al.* [86]. The binding geometry is reported according to Fig. 5.2. Three parameters l_1 , α , and β are used to quantify the binding geometry. l_1 is the distance between the carbon site of the adsorbate closest to the open metal site and the open metal site. α is the angle between the bond of the adsorbate and l_1 , while β is the angle between l_1 and the bond between the open metal site and the out of plane oxygen atom. For C3 hydrocarbons the labeling is analogous, to the exclusion of an additional carbon site that is connected to the carbon site further away from the metal. A schematic representation for C3 hydrocarbons is provided in the Supporting Information of Becker *et al.* [264]. For a binding geometry in which the double bond between the carbons is located parallel to the open metal site, α and β should be approximately 90° and 170° , respectively (expected for olefins

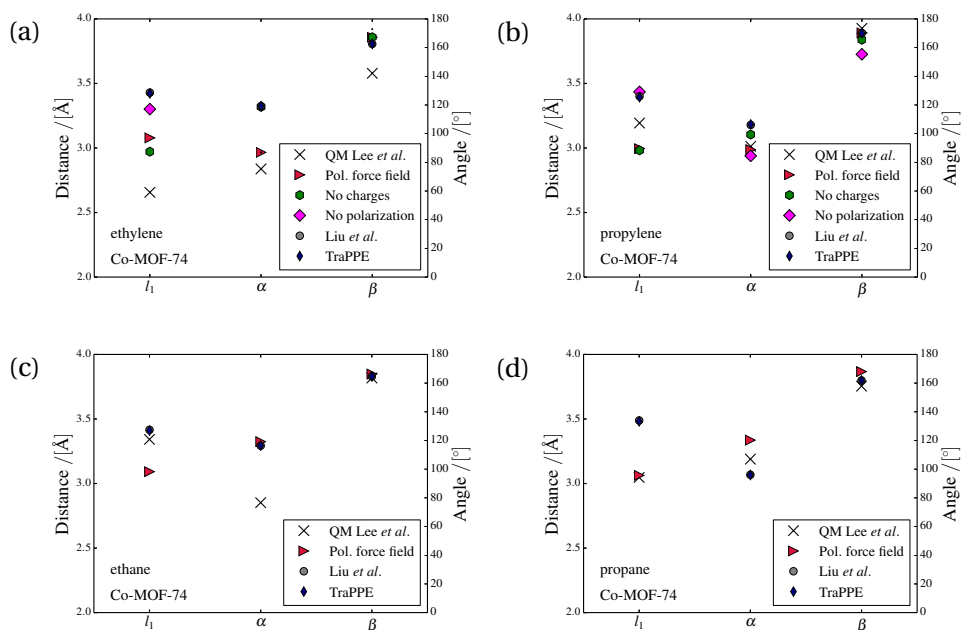


Figure 5.3: Summary of parameters to describe the binding geometry of (a) ethylene, (b) propylene, (c) ethane, and (d) propane in Co-MOF-74. Comparison between several classical force fields [277, 278] and the DFT results of Lee *et al.* [86]. Parameters are defined according to Fig. 5.2.

[99, 100]). If the adsorbate is directed with one side towards the open metal site α should be larger than 90° (expected for paraffins [99, 100]). The determined binding geometries of the lowest energy configurations in Co-MOF-74 are summarized in Fig. 5.3 for (a) ethylene, (b) propylene, (c) ethane, and (d) propane, and compared to lowest energy positions determined in DFT calculations of Lee *et al.* [86]. The geometries determined with the polarizable force field agree well with the previously suggested binding geometries [99, 100]. Distinct differences can be observed between olefins and paraffins. β is close to 170° for all adsorbates, while α is approximately 90° for olefins and 120° for paraffins. This shows that the olefins described by the polarizable force field indeed bind with the double bond parallel to the open metal sites. The force field not considering polarization but including point charges (*no polarization*) predicts very similar angles for the olefins. Hence, point charges for olefins seem to be crucial to model their orientation. For propane, the polarizable force field predicts an α of approximately 120° in agreement with our expectations (one side of the molecule is pointing towards the open metal site). The force field of Liu *et al.* [278] and the TraPPE force field predict configurations for propane in which one bond is arranged parallel to the open metal site. Apparently, the inclusion of polarization influences the

binding geometry of propane positively. Overall, the force fields not considering polarization or without point charges (Liu *et al.* [278], TraPPE [277]) predict binding geometries that vary from the predicted trends for ethylene, propane, and propylene. DFT results of Lee *et al.* [86] for olefins are comparable to the predictions with the polarizable force field. For propane, Lee *et al.* [86] reports that these calculations might have been stuck in a local energy minimum which could explain some deviations. The DFT results suggest that exclusively the distance l_1 is larger for ethane than for ethylene and that the carbon bond of both molecules is located parallel towards the open metal site. Due to a generally high sensitivity of binding geometries towards the applied force field some uncertainties are expected. Issues can easily arise if interactions are strong and adsorbates are located close to the surface of the framework, as for MOFs with open metal sites. The other investigated M-MOF-74 frameworks show a behavior similar to Co-MOF-74. Deviations from the expected configurations can only be observed for propylene in Mn-MOF-74 and propane in Ni-MOF-74. The corresponding Figs. are included in the Supporting Information of Becker *et al.* [264]. It can be concluded that the inclusion of point charges and polarization leads to an improvement in the modeling of the binding geometry. Together with the improvements for heats of adsorption, this is a very reassuring finding, since the description of the adsorption at low uptakes is significantly improved by the polarizable model without introducing any adjustable parameters. These findings verify the need for polarizable force fields.

After considering the adsorption at low uptakes, it is of interest to investigate adsorption isotherms which are influenced by adsorbate-adsorbate interactions and the packing within pores [124]. Computed adsorption isotherms are compared to experimental measurements of Geier *et al.* [100]. These authors provide a complete set of experimental adsorption isotherms for the MOF structures and adsorbates considered. For some MOFs additional experiments are available [99, 101]. As previously shown [77], these experiments agree well with the study of Geier *et al.* [100]. To increase the visibility, exclusively the measurements of Geier *et al.* [100] are presented as comparison. Due to the limited amount of experimental studies, a thorough investigation of the reproducibility of the experimental adsorption isotherms as suggested by Park *et al.* [84] is not possible. Hence, the experimental values should rather be seen as guidelines and not as final target. In Fig. 5.4, the computed adsorption isotherms of ethane are compared to experimental results of Geier *et al.* [100] for (a) Co-MOF-74, (b) Fe-MOF-74, (c) Mn-MOF-74, and (d) Ni-MOF-74 at 318 K. In agreement with the heats of adsorption and the binding geometries, the low pressure region is improved when adding explicit polarization. The uptake at higher pressures is overestimated. This could be due to oversized dispersion interactions

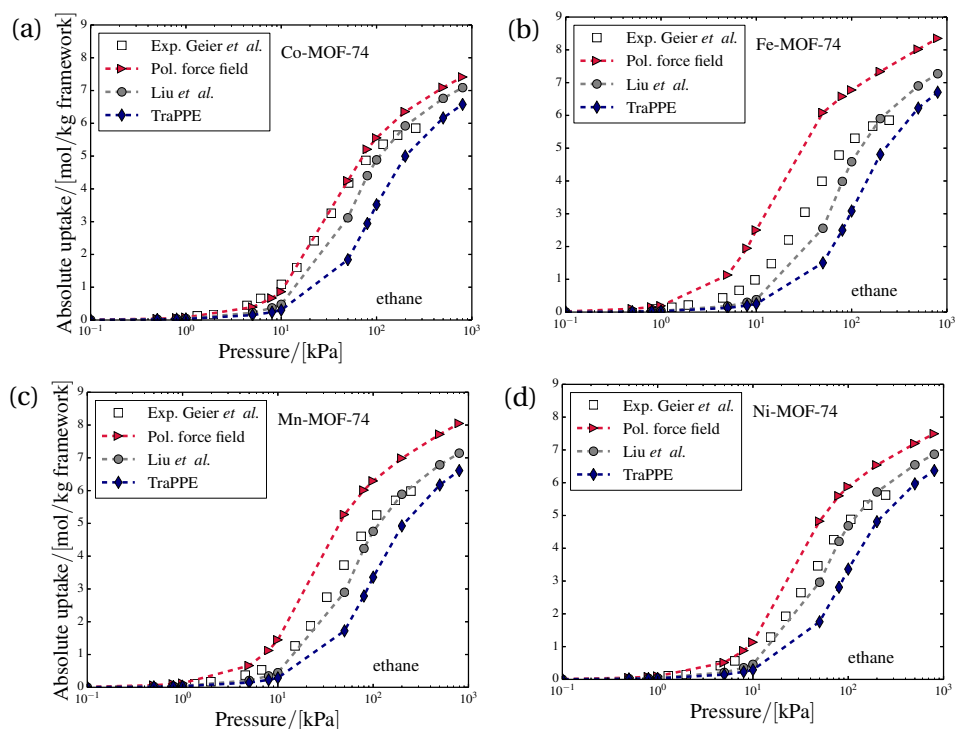


Figure 5.4: Comparison of adsorption isotherms of ethane for (a) Co-MOF-74, (b) Fe-MOF-74, (c) Mn-MOF-74, and (d) Ni-MOF-74 at 318 K between the experimental values of Geier *et al.* [100] and simulation results using the force fields of Liu *et al.* [278], the TraPPE force field [277], and the developed polarizable force field.

of standard force fields and an adjustment of Lennard-Jones parameters might be required for accuracy [126]. However, an overprediction of the uptake at high pressure is frequently observed in molecular simulation and therefore not surprising [116]. Besides the force field, possible reasons can be imperfect crystal structures of the synthesized material or collapsed and blocked cavities in experiments [51, 87]. Adsorption at high pressure is dominated by molecule packing inside the pores and not by specific framework-adsorbate interactions [76, 124]. To describe the packing behavior of molecules, adsorbate-adsorbate interactions are more important than the adsorbate-framework interactions which are influenced by the developed polarizable force field. To achieve a better agreement between experiments and molecular simulation at high pressure many studies apply a constant factor to scale the computational adsorption isotherm [68, 80, 84]. In this study, scaling is avoided to achieve an unbiased evaluation of the potential of polarizable force fields for small hydrocarbons. For ethane, the presented

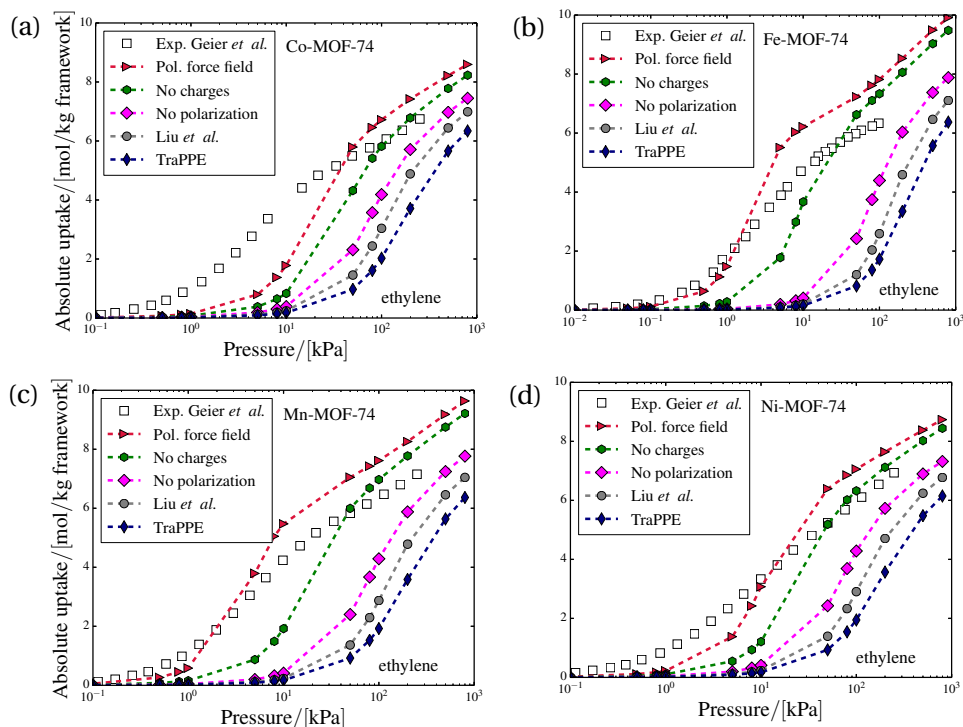


Figure 5.5: Comparison of adsorption isotherms of ethylene for (a) Co-MOF-74, (b) Fe-MOF-74, (c) Mn-MOF-74, and (d) Ni-MOF-74 at 318 K between the experimental values of Geier *et al.* [100] and simulation results using the force field of Liu *et al.* [278], the TraPPE force field [277], a force field without point charges (*no charges*), a force field without polarization (*no polarization*), and the developed polarizable force field.

polarizable force field is created by adding explicit polarization to the TraPPE force field [277]. The TraPPE force field without considering explicit polarization underestimates the uptake in the investigated frameworks. Besides the polarizable force field, the force field of Liu *et al.* [278] performs well. This force field was fitted to reproduce the adsorption of hydrocarbons in zeolites. The conditions in zeolites and MOFs may be similar for paraffins, because these molecules do not interact strongly with open metal sites. Hence, the adjustment for zeolites might result in good agreement for MOFs. If polarization is simply added to the force field of Liu *et al.* [278], the uptake is largely overestimated. The corresponding adsorption isotherms can be found in the Supporting Information of Becker *et al.* [264]. Fig. 5.5 compares the computed adsorption isotherms for ethylene in (a) Co-MOF-74, (b) Fe-MOF-74, (c) Mn-MOF-74, and (d) Ni-MOF-74 with the experimental values from Geier *et al.* [100] at 318 K. For ethylene, the

developed polarizable force field performs the best in all 4 M-MOF-74 frameworks. The force fields without considering polarization fail to predict even the qualitative adsorption. Neither the TraPPE force field [277] nor the force field of Liu *et al.* [278] can capture the behavior of experimentally measured adsorption isotherms. In contrast to ethane, for ethylene the force field of Liu *et al.* [278] performs poorly. The difference could be caused by the strong interactions of olefins with open metal sites. These interactions are not present in zeolites and therefore not captured in the force field of Liu *et al.* [278]. The agreement between the polarizable force field and the experimental results is the poorest for Co-MOF-74. The important low pressure region is underpredicted for Co-MOF-74. This underprediction agrees with the underestimation for the heat of adsorption at infinite dilution of ethylene in Co-MOF-74 (cf. Fig. 5.1). A less pronounced disagreement between experiments and simulations at low pressure can be observed for Ni-MOF-74. Unfortunately, no experimentally derived value for the heat of adsorption is available for ethylene in Ni-MOF-74. For Fe-MOF-74 and Mn-MOF-74, the agreement at low pressure is good while the adsorption at high pressure is overpredicted. Fig. 5.6 shows the computed adsorption isotherms for propane and experimental isotherms of Geier *et al.* [100] for (a) Co-MOF-74, (b) Fe-MOF-74, (c) Mn-MOF-74, and (d) Ni-MOF-74 at 318 K. The observations for propane are very similar to the findings for ethane. The agreement between experiments and simulations is very good for Co-MOF-74, while simulations overestimate the uptake for Fe-MOF-74. For Mn and Ni based frameworks, adsorption at low pressure is well reproduced. With the TraPPE force field [277] the uptake in all frameworks is severely underestimated. In contrast, the force field of Liu *et al.* [278] predicts adsorption well. In Fig. 5.7 the computed adsorption isotherms for propylene in (a) Co-MOF-74, (b) Fe-MOF-74, (c) Mn-MOF-74, and (d) Ni-MOF-74 are compared to experiments of Geier *et al.* [100] at 318 K. The predicted adsorption isotherms for propylene calculated with force fields that do not consider polarization (Liu *et al.* [278], TraPPE [277], and *no polarization*) underestimate the experimental uptake significantly and exhibit different shapes in comparison to experiments. Solely adding point charges to the propylene model does not seem sufficient to depict the correct adsorption. In general, the developed polarizable force field performs better than the other force fields. However, for Fe-MOF-74, the propylene uptake at low pressures is substantially overestimated and the force field considering solely polarization agrees better with experiments. The overestimation for the polarizable force field is in agreement with the overprediction observed for the heat of adsorption of propylene in Fe-MOF-74 (cf. Fig. 5.1). It is difficult to provide any conclusive reason for the overestimation of the propylene uptake in Fe-MOF-74. Fe-MOF-74 seems to be a particularly difficult system to model. Overall, incorporating polarization and

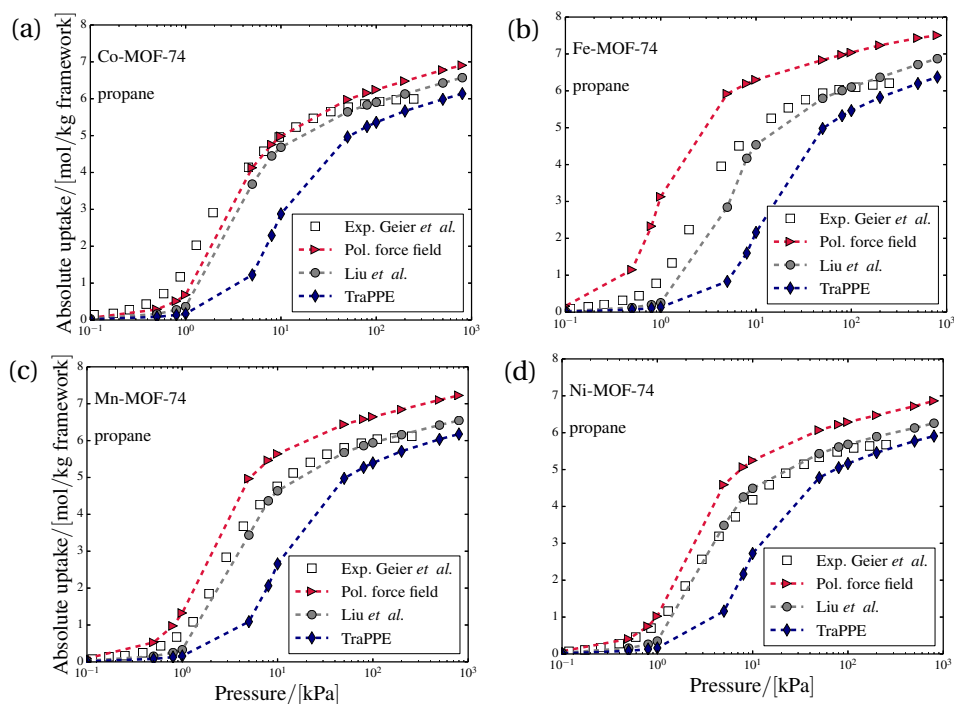


Figure 5.6: Comparison of adsorption isotherms of propane for (a) Co-MOF-74, (b) Fe-MOF-74, (c) Mn-MOF-74, and (d) Ni-MOF-74 at 318 K between the experimental values of Geier *et al.* [100] and simulation results using the force fields of Liu *et al.* [278], the TraPPE force field [277], and the developed polarizable force field.

point charges for propylene notably improves the predictions.

Considering all investigated adsorption isotherms, the potential of polarizable force fields for the description of small hydrocarbons is obvious. Adding polarization helps to model the behavior at low uptakes. Without considering polarization the localized electrostatic environment in MOFs with open metal sites cannot be properly described [123, 124]. Good agreement between some generic force fields and experimental adsorption isotherms could be a result of error cancellation as heats of adsorption and binding geometries are modeled inaccurately [121]. However, even explicit polarization cannot provide quantitative predictions. We note that in this chapter no parameters have been adjusted and therefore, opportunities for further improvements exist. A complete re-parametrization or at least adjustment of the Lennard-Jones parameters, as in chapters 2-4, might be necessary to further enhance prediction accuracy [126]. As noted by Franz *et al.* [126], the development of accurate and transferable force fields for hydrocarbons remains to be challenging. Especially, close to the open

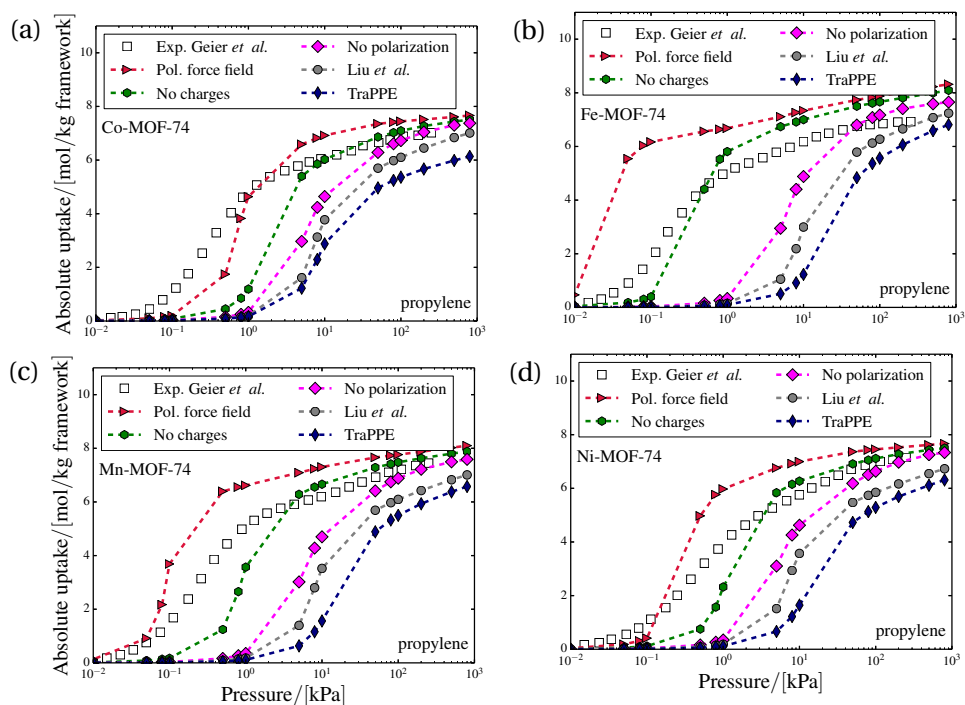


Figure 5.7: Comparison of adsorption isotherms of propylene for (a) Co-MOF-74, (b) Fe-MOF-74, (c) Mn-MOF-74, and (d) Ni-MOF-74 at 318 K between the experimental values of Geier *et al.* [100] and simulation results using the force field of Liu *et al.* [278], the TraPPE force field [277], a force field without point charges (*no charges*), a force field without polarization (*no polarization*), and the developed polarizable force field.

metal site, the energy is low and simulation results may be sensitive to force field parameters that influence the distance and orientation of the adsorbate in this region.

Besides, the Lennard-Jones parameters, the framework charges are an important input in molecular simulation which can influence the location of the adsorbates [126]. To study the influence of varying framework charges, additional simulations are conducted for ethylene in Co-MOF-74 with different point charges. The second set of point charges is computed with the charge equilibration (QEq) method [63, 283]. These charges can be computed quickly, but are usually considered to be less accurate than charges from DFT calculations [263]. Fig. 5.8 shows the calculated adsorption isotherm for ethylene in Co-MOF-74 with point charges from the QEq method in comparison to the previously shown results when applying DFT charges at 318 K. The calculated adsorption isotherm for ethylene in Co-MOF-74 with QEq charges agrees better with

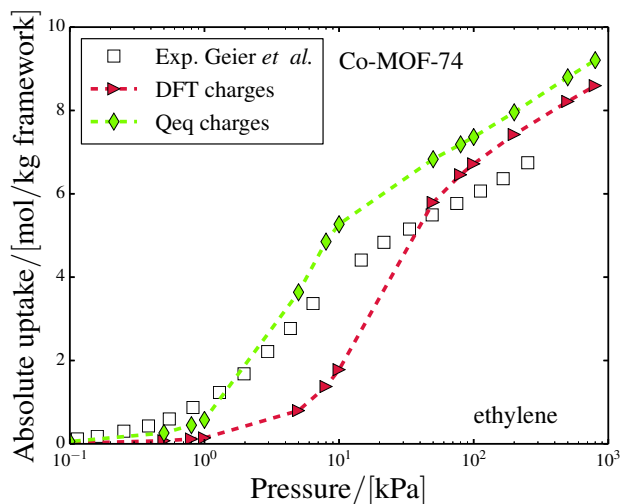


Figure 5.8: Adsorption isotherm for ethylene at 318 K predicted with the developed polarizable force field and charges determined via DFT calculations (\blacktriangleright), and the QEq method (\blacklozenge). Experimental data are from Geier *et al.* [100].

the experiments. This is especially true for lower pressures. The improvement with the QEq charges is rather surprising, since charges from periodic DFT calculations are normally considered to be more accurate [263]. It is important to note that QEq charges did not improve the description of the adsorption for the other investigated frameworks. The large difference in the adsorption isotherms for Co-MOF-74 suggests a large influence of different sets of charges. Such sensitivities towards assigned point charges have been previously observed for polar molecules in similar systems [284–287]. The previously observed issues could be aggravated by polarizable force fields, since explicit polarization depends on the electric field. Computed adsorption isotherms and heats of adsorption for all considered adsorbates in Co-MOF-74 with charges from the QEq method can be found in the Supporting Information of Becker *et al.* [264].

To investigate the detailed differences between the two sets of point charges we computed the energy contributions for an ethylene molecule on a grid inside Co-MOF-74. The Lennard-Jones, electrostatic, and polarization energies of ethylene on a grid with a spacing of 0.1 Å inside the pore of Co-MOF-74 are calculated. For every grid point, 250 approximately uniformly distributed orientations of an ethylene molecule are evaluated. The shown energies represent the Boltzmann average at 318 K of these 250 orientations for every grid point. An energy profile through Co-MOF-74 in z-direction is created via the Widom insertion method [231] to select the plane with the minimum of the Boltzmann average of the total

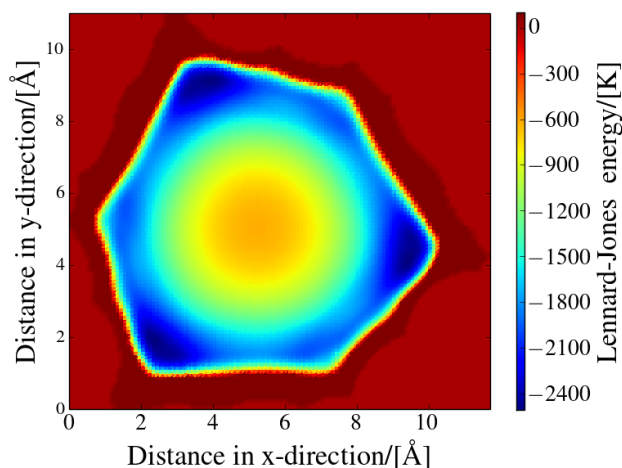


Figure 5.9: Lennard-Jones energies evaluated on a grid with 0.1 \AA spacing on the minimum energy plane in z -direction for ethylene in Co-MOF-74. Grid points for which the total energy (in units of k_B) is larger than 100 K are represented in dark red.

5

energy (Lennard-Jones, electrostatic, polarization). For this plane the energies are calculated on the grid. Fig. 5.9 shows the Lennard-Jones energy calculated on this plane for ethylene in Co-MOF-74. The two investigated sets of charges do not influence the Lennard-Jones energy surface inside the pore of Co-MOF-74. Therefore, the Lennard-Jones energy surface is identical for the two sets of charges. Grid points where the total energy (in units of k_B) is larger than 100 K are represented in dark red. These grid points are very close or on top of the framework and the repulsion part of the Lennard-Jones potential dominates the total energy. The shape of the pore changes along the z -direction and therefore it is not perfectly hexagonal for the shown plane. The open metal sites are located in the 6 corners of the framework. The most favorable adsorption sites are in the vicinity of these sites in the corners of the pore. Three of these open metal sites are located close to the shown plane. Besides the open metal sites, the locations close to the framework are more favorable than the center. With the exception of the repulsive area directly bordering the framework, the Lennard-Jones energy decays as the distance from the surface of the framework increases.

The electrostatic energy calculated with charges from (a) DFT and from (b) the QEq method for the plane with the lowest energy are shown in Fig. 5.10. The energy surface of the electrostatic energy which results from the two different sets of charges varies in the vicinity of the framework. Again, the corners of the pore exhibit the lowest energies. However, the minima for the two sets of charges are located in different corners of the pore. For the DFT charges, the locations of

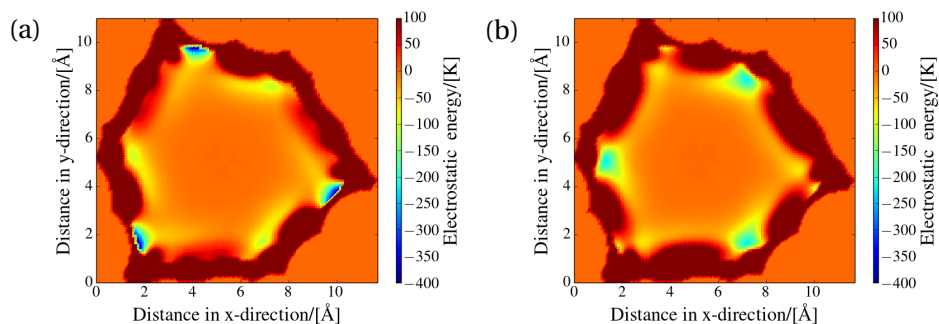


Figure 5.10: Comparison between the electrostatic energies for ethylene in Co-MOF-74 on a grid with (a) DFT charges and (b) charges calculated with the QEq method for the plane of minimum energy. Grid points for which the total energy (in units of k_B) is larger than 100 K are represented in dark red.

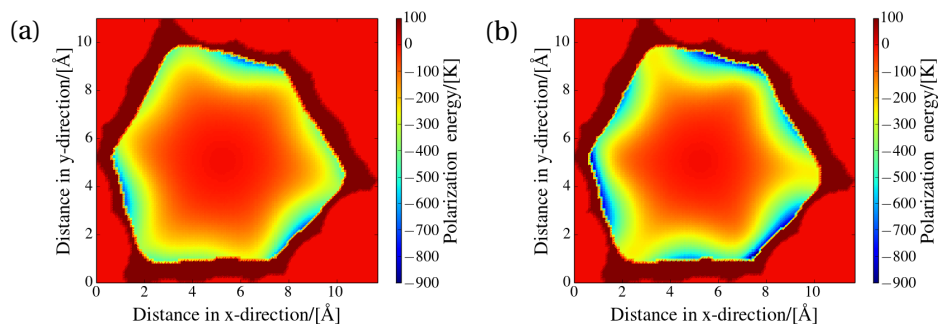


Figure 5.11: Comparison between the polarization energies for ethylene in Co-MOF-74 on a grid with (a) DFT charges and (b) charges calculated with the QEq method for the plane of minimum energy. Grid points for which the total energy (in units of k_B) is larger than 100 K are represented in dark red.

the minima agree with the ones of the Lennard-Jones energy. In contrast to the DFT charges, with the charges from the QEq method, the minima of the static electric energy are predicted to be in the alternating corners. Moreover, the minima of the static electric energy are at lower energies for the DFT charges. Further away from the surface of the framework the static electric energy decays. Therefore, in the center of the pore the influence of static electric interactions is low. For both sets of charges regions of positive energies can be observed close to the framework and between the open metal sites.

In Fig. 5.11, the polarization energy resulting from the electric field created by charges from (a) DFT and from (b) the QEq method is compared for the plane with lowest energy. Despite the difference in the electrostatic energy, the energy surfaces of the polarization energy are similar for both sets of charges. However,

close to the framework the exact values can deviate. Unlike to the electrostatic energy, the polarization energy is always attractive. In addition, the polarization energy declines rapidly and is essentially zero in the center of the pore. This appears reasonable, since polarization is strongly localized. In the vicinity of the surface of the framework the polarization energy is large and it can contribute significantly to the total energy. In this example, the polarization energies can be up to twice as low as the electrostatic energy. It is important to note that the regions of lowest polarization energy border directly on the framework. In the region that is in the close proximity to the framework, the Lennard-Jones energy is already repulsive. Unfortunately, the Lennard-Jones potential was designed rather for computational convenience than for accuracy in the strongly repulsive region [19, 51, 126]. As a consequence, the quality of the force field for this region might not be sufficient. Rapidly increasing and badly modeled repulsion together with large polarization energies might lead to poor modeling. Such difficulties seem to occur where binding distances are short and interactions are very attractive. A beneficial alternative to describe the Lennard-Jones repulsion could be, e.g., the Buckingham potential [68, 119]. Moreover, a complete re-design of the force field could improve results.

5

The total energy for both sets of framework charges for the plane of lowest total energy when (left) exclusively electrostatic energies and (right) additional polarization is considered are presented in Fig. 5.12 for (top row) DFT charges and (bottom row) charges determined using the QEq method [63, 283]. In comparison to solely Lennard-Jones energy (cf. Fig. 5.9), the low energy regions in the corners of the pore are more pronounced when adding point charges to the ethylene model. Especially, the less pronounced local minima in the left, upper right, and lower right corners of the pore are lower in energy (cf. Fig. 5.12 (a) and (c)). If polarizable sites are also added to ethylene, the complete vicinity of the surface of the pore lowers in energy. The difference in energy (in units of k_B) for this region is approximately 300 K. This is a substantial change. Overall, the locations of the minima for both sets of charges agree with the minima of the Lennard-Jones energy and with the location of the open metal sites. The total energies are significantly lower compared to exclusively considering Lennard-Jones energies. It can also be observed that considering polarization in the model may add a large localized contribution to the total energy that can help to describe localized effects. Other non-polarizable classical force fields might fail to describe this behavior [123, 124].

The results show that insights into how polarization contributes to the total energy can help to create a better understanding of adsorption and consequently may be useful to design MOFs with improved capabilities [126]. Interestingly, the different sets of charges do not change the general appearance of the total

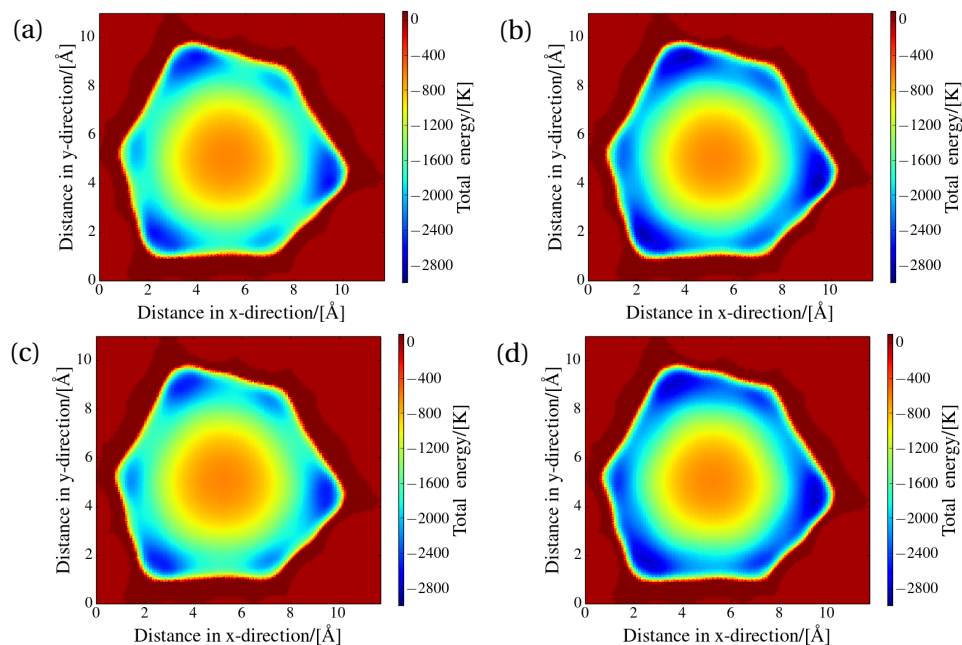


Figure 5.12: Comparison between the total energies for ethylene in Co-MOF-74 on a grid without (left) and with (right) explicit consideration of polarization energy. Energies calculated with (a) and (b) DFT charges and (c) and (d) charges calculated with the QEq method for the plane of minimum energy. Grid points for which the total energy (in units of k_B) is larger than 100 K are represented in dark red.

energy surface. However, for both sets of charges the gradient of total energy close to the open metal sites is very steep which may contribute to the observed sensitivity. The similarity in the total energy surface and the comparison of the adsorption isotherm for ethylene (cf. Fig. 5.8) suggest that differences in the total energy surface lead to large differences in the adsorption. Therefore, an accurate parametrization of the force field parameters may be needed to obtain quantitative agreement between simulations and experiments. The energy surfaces for the maximum energy plane for ethylene show a comparable behavior to the minimum energy plane (can be found in the Supporting Information of Becker *et al.* [264]). Overall, the results show that the choice of charges can have a considerable effect [78, 126, 182].

5.5. CONCLUSIONS

In this chapter, the potential of polarizable force fields to calculate the adsorption of small hydrocarbons in Metal-Organic-Frameworks with open metal sites

has been investigated. Explicit polarization is considered using the induced dipole model. To speed up simulations, additional assumptions introduced by Lachet *et al.* [185] are applied. Atomic polarizabilities are assigned according to literature [282]. Lennard-Jones interactions and point charges were chosen from standard force fields. To test the predictive potential of polarizable force fields, the force field parameters have not been adjusted. In comparison to generic force fields without considering polarization, the description of the adsorption is significantly improved when including polarization explicitly. Computed heats of adsorption at infinite dilution using the polarizable force field are in reasonable agreement with available experimental data and *ab initio* predictions. The experimentally observed trend that olefins interact significantly stronger than paraffins was reproduced. Besides, binding geometries follow the experimentally expected trend, i.e., the double bond of the olefins binds parallel towards the open metal sites, while paraffins point with one side towards the open metal sites. The description of adsorption isotherms for small hydrocarbons is improved as well when including polarization. Even though the agreement for adsorption isotherms is not perfect, the results are very encouraging. It was shown that polarizable force fields have great potential for the modeling of hydrocarbons in Metal-Organic Frameworks with open metal sites. Polarization can help to describe localized effect close to the surface of porous materials. Good predictions for some adsorbates with standard force fields may be a result of error cancellation, since heats of adsorption and binding energies do not match the expected trends. Simulation results are sensitive towards force field parameters that influence the geometry close to the open metal sites with low total values and steep gradients of total energy. Framework charges are such parameters which we explored in more detail. Better models may be expected when the description of repulsion is improved. This part is essential for small binding distances as can be observed in MOFs with open metal sites. A complete re-parametrization of the force field and considering explicit polarization from the beginning should enhance the accuracy and lead to force fields with better transferability.

6

INVESTIGATION OF MOLECULAR SIMULATION TO PREDICT THE PERFORMANCE OF ABSORPTION REFRIGERATION CYCLES WITH AMMONIA - IONIC LIQUID WORKING PAIRS

This chapter is based on the paper: T. M. Becker, M. Wang, A. Kabra, S. H. Jamali, M. Ramdin, D. Dubbeldam, C. A. Infante Ferreira, and T. J. H. Vlugt. Absorption refrigeration cycles with ammonia-ionic liquid working pairs studied by molecular simulation. *Industrial & Engineering Chemistry Research* 57 (2018) 5442-5452 [288].

6.1. INTRODUCTION

In this chapter, we provide a proof-of-principle study to assess the capability of molecular simulation to predict properties for the design of VAR cycles. A multiscale modeling approach to evaluate the accuracy of the prediction on the circulation ratio (f) and the coefficient of performance (COP) of the VAR cycle using two ionic liquids with NH_3 as absorbent is applied. With only minor adjustments, the same approach is applicable to absorption heat pump cycles. On the

smallest scale, quantum mechanical calculations are used to compute the ideal gas heat capacities of ionic liquids. Monte Carlo simulations are conducted to determine residual heat capacity, solubility of the refrigerant in the absorbent, and enthalpy of absorption. These properties are determined by intermolecular interactions and can be described well by Monte Carlo simulations [289]. The computed thermodynamic properties are then used in a developed equilibrium-based cycle model of a single-effect (SE)-VAR cycle. Similar computational based approaches have been developed for vapor-compression cycles [290, 291]. However, simpler molecular models that have been previously fitted to experimental VLE data were applied in these studies. Moreover, different simulation techniques have been used.

Here, we want to introduce the concept for VAR cycles with NH_3/IL working pairs, to explain how the various simulation techniques can be combined to create an initial cycle design, and to assess uncertainties in the performance prediction of the cycle related to the different methods. As exemplary cases, we selected two working pairs, $\text{NH}_3/[\text{emim}][\text{Tf}_2\text{N}]$ and $\text{NH}_3/[\text{emim}][\text{SCN}]$. The IL $[\text{emim}][\text{Tf}_2\text{N}]$ is one of the most studied ILs and extensive experimental data are available [136, 292–294]. This is crucial to validate our approach. The IL $[\text{emim}][\text{SCN}]$ has been proposed as a particularly promising candidate for VAR cycles with NH_3 [165, 170]. Other promising ILs have been suggested, especially ILs containing functional OH groups. Unfortunately, we could not find any reliable force field for this type of ILs. In the traditional approach, experimental measurements are conducted to determine thermodynamic properties of ILs [135]. Afterwards, these experimental measurements can be directly used in the cycle design. Frequently, the available experimental measurements do not cover the complete range of conditions necessary in the cycle model. Hence, equations-of-states (EoSs) or activity coefficient models are fitted to reproduce experimental measurements and are used to extrapolate thermodynamic properties for conditions for which the properties have not been determined directly [170, 295]. This extrapolation may introduce undesired errors. An alternative method to predict thermodynamic properties of mixtures are COSMO-based [133]. However, previous studies suggest that the accuracy of these models is often insufficient for mixtures containing ILs [296, 297]. Especially, for NH_3/IL working pairs the uncertainty can be large [298]. Nevertheless, for the screening of large quantities of ILs less accurate COSMO-based [298] methods seem more suitable due to the advantages in computation time.

This chapter is organized as follows. The first Section presents a brief introduction of the VAR cycle along with the assumptions and the equations used in the cycle description. Subsequently, we provide the background and the methodology to predict the required thermodynamic properties. The third Section pro-

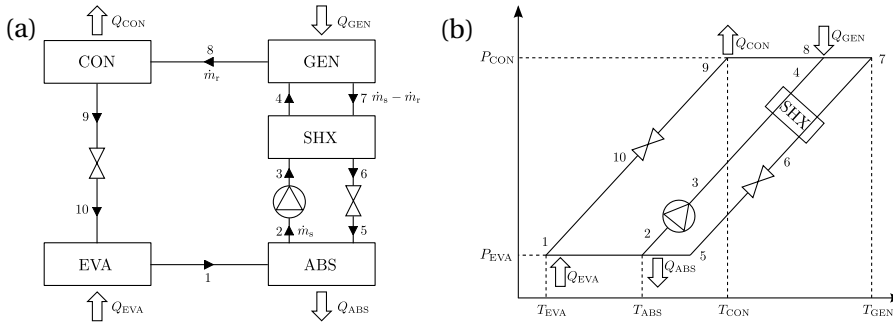


Figure 6.1: (a) Schematic diagram of a SE-VAR cycle. (b) $\ln(P) - 1/T$ diagram of the same VAR cycle. Q_{GEN} , Q_{CON} , Q_{ABS} , and Q_{EVA} are respectively the transferred heat at the generator, the condenser, the absorber, and the evaporator. T_{GEN} , T_{CON} , T_{ABS} , and T_{EVA} are the corresponding temperatures, and P_{CON} and P_{EVA} the pressures. \dot{m}_s and \dot{m}_r are the mass flow rate of the strong NH_3 solution and of the refrigerant.

vides the simulation details for computing the required thermodynamic properties. Section four presents the results for the thermodynamic properties and the thermodynamic performance of the cycle. In the final Section, our findings are summarized.

6.2. DESCRIPTION OF THE ABSORPTION REFRIGERATION CYCLE

A schematic diagram of a SE-VAR cycle is shown in Fig. 6.1 (a). The basic units of the cycle are a generator (GEN), a condenser (CON), an absorber (ABS), and an evaporator (EVA). To illustrate the changes between the different state points Fig. 6.1 (b) shows the relation between vapor pressure ($\ln(P)$) and temperature ($-1/T$). In the EVA, the pure liquid refrigerant (NH_3) is vaporized and provides the cooling load Q_{EVA} . The low-pressure refrigerant at state point 1 enters the ABS and is exothermically absorbed by the weak solution at state point 5 (weak in NH_3) coming from the GEN. Thereby, the weak NH_3 solution is enriched with NH_3 and it becomes the rich solution at state point 2. Here, the redundant heat load Q_{ABS} is released to the surrounding. Before entering the GEN, the rich solution is pumped from state point 2 to a higher pressure level and the temperature is increased in the solution heat exchanger (SHX). In the GEN, the heat load Q_{GEN} is supplied and the refrigerant vapor is released from the rich solution at state point 8. Hence, the concentration of refrigerant in the stream leaving the GEN at state point 7 is reduced. The weak NH_3 solution is cooled in the SHX. Before entering the absorber, the pressure is lowered in an expansion valve. The refrigerant vapor exiting the GEN at state point 8 passes the condenser, where

it is condensed while releasing the condensation heat Q_{CON} to the surrounding. Subsequently, the pressure of the liquid refrigerant at state point 9 is reduced in an expansion valve before the cycle is completed by the liquid refrigerant reentering the EVA. To predict the thermodynamic performance of the SE-VAR cycle with NH_3/IL as working pair, the following assumptions are made to facilitate the calculations:

- The fluid streams are in a steady state.
- The operating pressures of the EVA and the ABS, and likewise, the operating pressures of the GEN and the CON are equal.
- The NH_3 streams leaving the CON and the EVA are saturated liquid and saturated vapor, respectively.
- The solution leaving the GEN is at equilibrium.
- The refrigerant enters the CON as superheated vapor at the end generation temperature.
- The solution leaving the ABS is subcooled by 5 K.
- The pinch temperature of the SHX is set to 5 K.
- Heat, and pressure losses are neglected.
- Throttling is assumed to be an isenthalpic process.
- The power required for pumping is insignificant, and therefore neglected.

Considering these assumptions, the conditions of all state points can be specified. The temperatures T_{EVA} , T_{CON} , T_{ABS} , and T_{GEN} are determined by the heat sources, the surrounding, and the cooling application. The pressures P_{EVA} and P_{CON} are determined by the vapor pressure of pure NH_3 assuming that the IL is nonvolatile. Hence, the conditions of pure NH_3 at state points 1 and 9 are set. The pressures P_{GEN} and P_{ABS} follow directly from the assumption of equal pressures at GEN and CON, and EVA and ABS, respectively. Based on the VLE, the mass fractions of each component at the outlet of the GEN and the ABS (subcooled by 5 K) can be determined for T_{GEN} and T_{ABS} and the corresponding pressure levels P_{GEN} and P_{ABS} . Thereby, the state points 2 and 7 are specified. Between state points 2 and 4, and 7 and 5, the mass fractions of the absorbent do not change ($w_2 = w_3 = w_4$, $w_5 = w_6 = w_7$). Thus, all remaining state points can be determined from energy balances around the SHX and the isenthalpic throttling process. The cycle conditions in this work are: $T_{\text{CON}} = 35^\circ\text{C}$, $T_{\text{ABS}} = 30^\circ\text{C}$,

$T_{\text{EVA}} = 10 \text{ }^\circ\text{C}$, $T_{\text{GEN}} = 74\text{...}120 \text{ }^\circ\text{C}$, $P_{\text{EVA}} = 6.15 \text{ bar}$, and $P_{\text{CON}} = 13.5 \text{ bar}$. The enthalpies of pure NH_3 are directly obtained from Refprop [299] with the Helmholtz energy EoS [300]. For NH_3/ILs mixtures, the enthalpy of the solution \bar{h}_{sol} can be calculated as:

$$\bar{h}_{\text{sol}} = w_{\text{NH}_3} \bar{h}_{\text{NH}_3} + (1 - w_{\text{NH}_3}) \bar{h}_{\text{IL}} + \Delta \bar{h}_{\text{abs}} \quad (6.1)$$

in which \bar{h}_{NH_3} , and \bar{h}_{IL} are the enthalpies of pure NH_3 and IL at the specified conditions, w_{NH_3} is the mass fraction of NH_3 , and $\Delta \bar{h}_{\text{abs}}$ is the enthalpy of absorption of the mixture. The influence of the pressure on the heat capacity and the enthalpy of the liquid IL \bar{c}_p^{IL} can be neglected. Hence, the enthalpy of the pure IL can be determined:

$$\bar{h}_{\text{IL}} = \bar{h}_o + \int_{T_o}^T \bar{c}_p^{\text{IL}} dT \quad (6.2)$$

where \bar{h}_o is the reference enthalpy at an arbitrary reference state for Eq. 6.2 with $T_o = 250.15 \text{ K}$ and $P_o = 1 \text{ MPa}$. Subsequently, it is straightforward to calculate the exchanged heat with the surrounding (see Fig. 6.1):

$$\frac{Q_{\text{EVA}}}{\dot{m}_r} = \bar{h}_1 - \bar{h}_9 \quad (6.3)$$

$$\frac{Q_{\text{ABS}}}{\dot{m}_r} = \bar{h}_1 + f \cdot (\bar{h}_6 - \bar{h}_2) - \bar{h}_6 \quad (6.4)$$

$$\frac{Q_{\text{CON}}}{\dot{m}_r} = \bar{h}_8 - \bar{h}_9 \quad (6.5)$$

$$\frac{Q_{\text{GEN}}}{\dot{m}_r} = \bar{h}_8 + f \cdot (\bar{h}_7 - \bar{h}_4) - \bar{h}_7 \quad (6.6)$$

where Q_{GEN} , Q_{CON} , Q_{ABS} , and Q_{EVA} are, respectively, the heats, the generator, the condenser, the absorber, and the evaporator exchange with the surrounding. \dot{m}_s and \dot{m}_r are the mass flow rate of the strong NH_3 solution and of the refrigerant, respectively, and \bar{h}_i is the specific enthalpy of state point i . The mass balance of the absorbent in the solution yields:

$$\dot{m}_s \cdot w_2 = (\dot{m}_s - \dot{m}_r) \cdot w_5 \quad (6.7)$$

w_2 and w_5 are the mass fractions of the absorbent of the corresponding state points in the cycle. Finally, the performance parameters, i.e., circulation ratio f and the coefficient of performance COP can be determined as:

$$f = \frac{\dot{m}_s}{\dot{m}_r} = \frac{w_5}{w_5 - w_2} \quad (6.8)$$

$$COP = \frac{Q_{\text{EVA}}}{Q_{\text{GEN}}} \quad (6.9)$$

6.3. PREDICTIONS OF THERMODYNAMIC PROPERTIES

6.3.1. FORCE FIELD

MC simulations are performed to calculate the solubility of NH_3 in [emim][Tf_2N] and [emim][SCN], the residual heat capacity of these ILs, and their enthalpies of absorption at various temperatures and pressures. The classical force field developed by Liu *et al.* [29] is used to describe the ILs [131, 137, 139, 289, 301]. It includes intramolecular contributions such as bond-stretching, angle-bending, and torsions. Intermolecular contributions are described with a Lennard-Jones potential and electrostatic interactions are considered via the Ewald summation technique with a relative precision of 10^{-5} [15]. The Lennard-Jones interactions are truncated and shifted at 12 Å. No tail corrections are applied. The Lorentz-Berthelot mixing rules are used to calculate the interactions between unlike atoms [281]. The anion and the alkyl part of the cation of the IL molecules are considered flexible whereas the ring of the cation is rigid. NH_3 is described via the TraPPE force field [302]. The TraPPE force field was developed to reproduce the VLE for pure ammonia and an ammonia-methane mixture [302]. These equilibria can be reproduced very well. Besides, the TraPPE force field has the potential to model hydrogen bonds [302], which is important for NH_3 /[emim] mixtures [139]. The force field parameters are not adjusted and are taken from Liu *et al.* [29], Tenney *et al.* [137] and Zhang and Siepmann [302]. The used force fields to describe ILs are summarized in the Supporting Information of Becker *et al.* [288].

6.3.2. CALCULATION OF NH_3 SOLUBILITY

The osmotic ensemble is well suitable to calculate the solubility of gases in non-volatile liquids such as ILs [137, 144]. In this ensemble, the temperature, the pressure, the fugacity of the solute, and the number of solvent molecules are fixed. The fugacity and the hydrostatic pressure are coupled via the Peng-Robinson EoS applied for NH_3 . The volume of the system and the number of solute molecules fluctuate. In equilibrium, the number of solute molecules in the system determines the solubility. A representation of a simulated system is shown in Fig. 6.2. An inherent difficulty of a fluctuating number of solute molecules (NH_3) is the insertion of additional molecules into already dense systems. To overcome this issue, Shi and Maginn [303] proposed the Continuous Fractional Component Monte Carlo method. In this method, the system consists of whole molecules and a fractional one. Insertion and deletion Monte Carlo trial moves of the solute are achieved by scaling the intermolecular interactions (Lennard-Jones and Coulombic) of the fractional molecule. The scaling parameter λ can range between 0 and 1. $\lambda = 0$ signifies that the fractional molecule does not interact with the surroundings, whereas $\lambda = 1$ implies that the fractional molecule has full in-

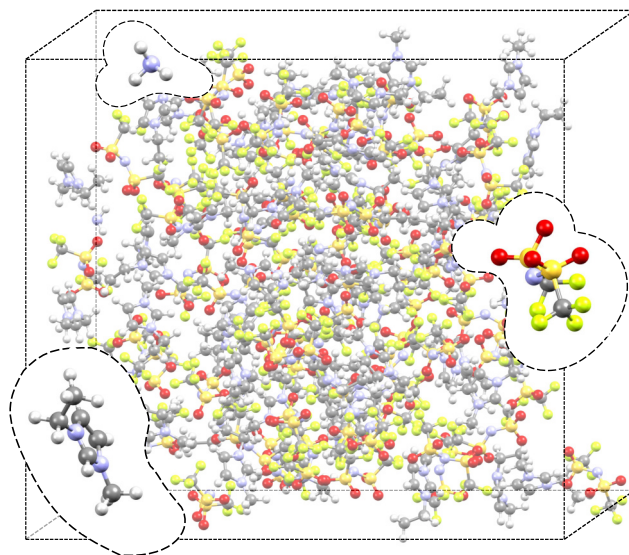


Figure 6.2: Representation of the simulated system consisting of NH_3 , $[\text{emim}]^+$, and $[\text{Tf}_2\text{N}]^-$. Exemplary, one representation of each type is enlarged and marked by dashed lines. White, red, gray, purple, yellow, and green spheres represent hydrogen, oxygen, carbon, nitrogen, sulfur, and fluorine atoms, respectively.

teractions with the surrounding molecules. In the Monte Carlo algorithm, trial moves for thermalization and trial moves to change the value of λ are included. If λ is changed to a value larger than 1 the molecule is completely inserted and a new fractional molecule is added to the system with $\lambda = \lambda - 1$. If λ is changed to a value smaller than 0 the molecule is removed and a random molecule is chosen as the new fractional one with $\lambda = 1 + \lambda$. This method significantly facilitates the insertion of molecules in dense systems [226]. The fractional molecule and its surrounding can slowly adjust while λ is changed and thus the interactions are gradually switched on. Thereby, the probability of successful insertions increases. To ensure an uniform sampling of the scaling parameter λ , the Wang-Landau scheme [304] is applied during equilibration to determine a biasing function $W(\lambda)$. The advantage of the Wang-Landau scheme is that it does not require any former knowledge of the biasing function. For more details on computing solubilities with the Continuous Fractional Component Monte Carlo method, the reader is referred to Shi and Maginn [139, 145, 303] and Vlught and co-workers [144, 167, 305, 306].

In this chapter, we compare solubilities computed from Monte Carlo simulations with the non-random two-liquid (NRTL) model which was fitted to reproduce the experimental data of Yokozeki and Shiflett [136, 165]. In the range of

experimental data, the NRTL model describes the experiments very well. Consequently, the calculated solubilities are compared to the NRTL model at the exact cycle conditions. Details of the NRTL model and the fitted parameters can be taken from Wang and Infante Ferreira [170].

6.3.3. CALCULATION OF HEAT CAPACITY

The heat capacity describes how much the temperature of a system changes if a certain amount of heat is added. The heat capacity at constant pressure C_P is defined as:

$$C_P(T, P) = \left(\frac{\partial \langle H \rangle}{\partial T} \right)_P \quad (6.10)$$

where T , P , and $\langle H \rangle$ are the temperature, the pressure, and the average enthalpy computed in the NPT ensemble, respectively. The enthalpy is defined as

$$H = U^{\text{intra}} + U^{\text{inter}} + K + PV \quad (6.11)$$

U^{intra} and U^{inter} are the intramolecular and the intermolecular contributions to the potential energy, respectively, K is the kinetic energy, and V is the volume of the system. The average enthalpy can be expressed as the sum of two separate contributions, i.e., the ideal gas enthalpy and the residual enthalpy [301]:

$$\langle H \rangle = \langle H^{\text{ig}} \rangle + \langle H^{\text{res}} \rangle \quad (6.12)$$

$$H^{\text{ig}} = U^{\text{intra}} + K + Nk_B T \quad (6.13)$$

$$H^{\text{res}} = U^{\text{inter}} + PV - Nk_B T \quad (6.14)$$

where $\langle H^{\text{res}} \rangle$ is the ensemble average of the residual enthalpy, N is the number of molecules the system comprises, and k_B is the Boltzmann constant. The ensemble average of the ideal gas enthalpy $\langle H^{\text{ig}} \rangle$ is defined as the sum of the intramolecular energy U^{intra} , the kinetic energy K , and the PV term which can be replaced with $Nk_B T$ according to the ideal gas law. Consequently, the total heat capacity can be split into an ideal gas and a residual part by differentiating the two enthalpy contributions individually:

$$C_P(T, P) = C_P^{\text{ig}}(T) + C_P^{\text{res}}(T, P) \quad (6.15)$$

$$C_P^{\text{ig}}(T) = \left(\frac{\partial \langle H^{\text{ig}} \rangle}{\partial T} \right)_P \quad (6.16)$$

$$C_P^{\text{res}}(T, P) = \left(\frac{\partial \langle H^{\text{res}} \rangle}{\partial T} \right)_P \quad (6.17)$$

Here, it is assumed that the ensemble average of the ideal gas enthalpy is independent of the residual enthalpy [301]. The splitting of the heat capacity is

convenient, because intramolecular potentials used in force field-based molecular simulation may result in large deviations for the ideal part of the heat capacity [301]. The causes of these deviations are the overestimated of the vibrational energy due to the harmonic oscillator approximation and the negligence of off-diagonal coupling terms [301]. Likewise, it is unfavorable to use quantum mechanical calculations to predict the residual contribution of the heat capacity due to rapidly increasing computational costs for systems containing more than a single molecule or ion. Therefore, a separate calculation of the ideal and residual terms is advantageous. The derivative of the residual enthalpy with respect to temperature can be determined from fluctuations of thermodynamic variables throughout the simulations. In this work, the procedure of Lagache *et al.* [307] is applied:

$$\begin{aligned} C_P^{\text{res}} &= \left(\frac{\partial \langle H^{\text{res}} \rangle}{\partial T} \right)_P \\ &= \frac{1}{k_B T^2} [\langle U^{\text{res}} \hat{H} \rangle - \langle U^{\text{res}} \rangle \langle \hat{H} \rangle + P(\langle V \hat{H} \rangle - \langle V \rangle \langle \hat{H} \rangle)] - Nk_B \end{aligned} \quad (6.18)$$

The configurational enthalpy

$$\hat{H} = H - K \quad (6.19)$$

differs from the enthalpy H by not including the kinetic energy K . The ideal contribution to the heat capacity can be reliably predicted from ab initio electronic structure calculations [301]. Therefore, quantum mechanical calculations of isolated ions are performed where only intramolecular interactions are considered. The combination of both computational methods has been successfully applied to predict the heat capacity of ILs and other molecules [29, 131, 137, 289, 301, 307–309].

The results of this simulation based approach are compared to experimental data of Paulechka *et al.* [310] and Navarro *et al.* [311] for [emim][Tf₂N] and [emim][SCN], respectively. These experimental results are fitted to a polynomial function to describe the temperature dependency of C_P^{IL} .

6.3.4. CALCULATION OF ENTHALPY OF ABSORPTION

The enthalpy of absorption $\Delta \bar{h}_{\text{abs}}$ can be calculated from Monte Carlo simulations following the procedure of Shi and Maginn [139]. Eq. 6.1 can be rearranged to:

$$\Delta \bar{h}_{\text{abs}} = \bar{h}_{\text{sol}} - w_{\text{NH}_3} \bar{h}_{\text{NH}_3} - (1 - w_{\text{NH}_3}) \bar{h}_{\text{IL}} \quad (6.20)$$

Three separate Monte Carlo simulations at the same conditions are necessary to compute $\Delta \bar{h}_{\text{abs}}$: one for the enthalpies of the solution (\bar{h}_{sol}), one for NH₃ (\bar{h}_{NH_3}),

and one for the IL (\bar{h}_{IL}). Here, the enthalpies of pure NH_3 and the ILs are computed from simulations in the NPT ensemble whereas the enthalpy of the solution is computed from simulations in the osmotic ensemble, simultaneously with the solubility of NH_3 . The specific enthalpies in both ensembles are calculated via $\bar{h} = \bar{u} + P\bar{v}$, where \bar{u} is the specific energy and \bar{v} is the specific volume. The enthalpies of pure NH_3 and the ILs are computed at T and P corresponding to the condition of the mixture. Note that at the conditions chosen for the cycle design, pure NH_3 is in the gaseous state.

There are no experimental data for the enthalpy of absorption available for NH_3/IL mixtures. Therefore, the mixing enthalpy $\Delta\bar{h}_{\text{mix}}$ derived from EoS or activity coefficient models has to be used in the traditional cycle design. To compare the enthalpy of absorption computed from Monte Carlo simulations with the mixing enthalpy obtained from EoSs or activity coefficient models with the liquid state as reference, the latent heat $\Delta\bar{h}_{\text{lat}}$ of pure NH_3 at the same T and P has to be subtracted:

$$\Delta\bar{h}_{\text{abs}} = \Delta\bar{h}_{\text{mix}} - w_{\text{NH}_3}|\Delta\bar{h}_{\text{lat}}| \quad (6.21)$$

The latent heat of NH_3 is taken from Refprop [299, 300]. Here, the calculation results are compared with the predictions of the Redlich-Kwong-EoS (RK-EoS) and mixing rules based on experimental VLE data using:

$$\Delta\bar{h}_{\text{mix}} = -w_{\text{NH}_3}\bar{h}_{\text{NH}_3}^{\text{res}} - (1 - w_{\text{NH}_3})\bar{h}_{\text{IL}}^{\text{res}} + \bar{h}_{\text{sol}}^{\text{res}} \quad (6.22)$$

where $\bar{h}_{\text{NH}_3}^{\text{res}}$, $\bar{h}_{\text{IL}}^{\text{res}}$, and $\bar{h}_{\text{sol}}^{\text{res}}$ are the residual enthalpies for NH_3 , the IL, and the solution at liquid state, respectively. The detailed procedure and the necessary critical parameters and binary interaction parameters are explained in the work of Yokozeki and Shiflett [136, 165]. Wang *et al.* [312] showed that the RK-EoS performs well in comparison to other EoS models, activity coefficient models, and the Clausius-Clapeyron equation. It is also possible to predict mixing enthalpies directly from the NRTL model. However, the NRTL model is not recommended for determining mixing enthalpies due to a purely empirical temperature dependency of the fitting parameters [165, 312].

6.4. SIMULATION DETAILS

Molecular simulations are performed with the RASPA software package [225, 226]. In RASPA, the number of Monte Carlo steps conducted during every cycle is equal to the total number of molecules considered in the simulation with a minimum of 20 Monte Carlo steps per cycle. The total number of simulation cycles is divided into five blocks. The provided statistical uncertainty in the computed properties is the standard error calculated from the standard deviation of the block averages.

The solubility of NH_3 in $[\text{emim}][\text{Tf}_2\text{N}]$ and $[\text{emim}][\text{SCN}]$ is computed by conducting Monte Carlo simulations in the osmotic ensemble. NH_3 molecules are inserted or removed via the Continuous Fractional Component Monte Carlo technique [226, 303]. A production run of 5 million cycles is performed. Simulations are performed with 52 and 70 IL molecules for $[\text{emim}][\text{Tf}_2\text{N}]$ and $[\text{emim}][\text{SCN}]$, respectively. Three different Monte Carlo trial moves with an equal probability are considered for the ILs: translational, rotational, and configurational-bias to account for different configurations of the molecules. For NH_3 , translational, rotational, and λ trial moves are considered with an equal probability. The probability of a volume change trial move is 1%.

The calculation of the heat capacity is divided in two parts. Quantum mechanical calculations with the Gaussian software package [313] are performed to determine the ideal gas part of the heat capacity. In these calculations the isolated ions $[\text{emim}]$, $[\text{Tf}_2\text{N}]$, and $[\text{SCN}]$ are considered. Possible conformers are analyzed using molecular mechanics with the Merck molecular force field [314] and the results are compared to literature [315]. Paulechka *et al.* [315] concluded that the B3LYP functional [247–250] with a 6-31+G(2df,p) basis set is adequate for calculation of the frequencies of $[\text{emim}]$ and $[\text{Tf}_2\text{N}]$ which is also chosen here. First, the geometry is optimized and subsequently, a frequency analysis is performed. A scaling factor of 0.965 is applied to scale the calculated vibrational frequencies consistent with the NIST database [316]. In the NIST database [316], these kind of well-established scaling factors are tabulated to improve the agreement between QM and experiments for different basis sets and levels of theory. To compute the residual part of the heat capacity of the pure ILs, MC simulations in the NPT ensemble are conducted. For $[\text{emim}][\text{Tf}_2\text{N}]$ and $[\text{emim}][\text{SCN}]$, simulations are performed with 55 and 70 molecules, respectively. After reaching equilibrium, between 22 and 24 million MC cycles are conducted to compute the residual heat capacity according to Eq. 6.18. Again, translational, rotational, and configurational-bias Monte Carlo trial moves with equal probability are considered for the ILs and the probability of a volume change trial move is 1%.

For the enthalpy of absorption, the energies for NH_3/IL mixtures are computed in the osmotic ensemble simultaneously with the NH_3 solubility. For pure ILs, energies are computed from simulations in the NPT ensemble together with the residual heat capacity. Additional, NPT simulations at the same conditions are conducted for pure NH_3 . These simulations are performed with 160 molecules. First the systems are equilibrated, and then continued for 10^5 production cycles. Translational and rotational Monte Carlo trial moves with an equal probability are considered for NH_3 . Volume change trial moves have a probability of 1%.

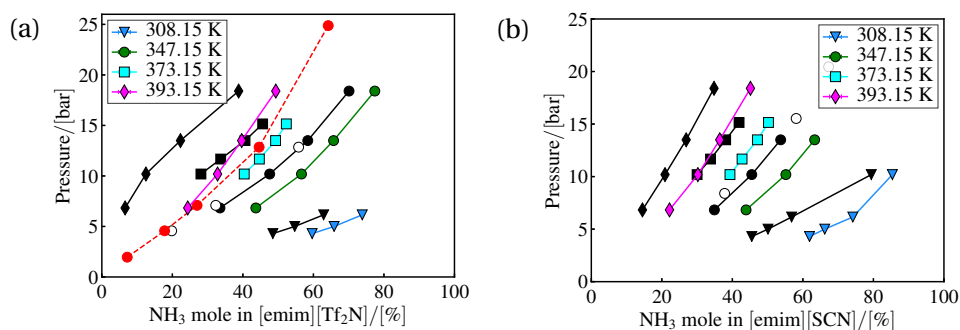


Figure 6.3: Computed NH₃ solubilities (blue/green/cyan/magenta) in (a) [emim][Tf₂N] and (b) [emim][SCN], compared to solubilities calculated with the NRTL model (black), experimental data (open), and simulation results of Shi and Maginn [139] (red) at 308.15 K (▼), 347.15 K (●), 373.15 K (■), and 393.15 K (◆). The determined standard error is smaller than the size of the symbols.

6.5. RESULTS AND DISCUSSION

6.5.1. NH₃ SOLUBILITY

In accordance with the conditions occurring in the VAR cycle, the solubility of NH₃ is computed in [emim][Tf₂N] and [emim][SCN] at 308.15 K, 347.15 K, 373.15 K, and 393.15 K for pressures between 4 bar and 19 bar. The computed results for [emim][Tf₂N] and [emim][SCN] are shown in Fig. 6.3 (a) and Fig. 6.3 (b), respectively. The simulation results (colored) are compared to the NRTL model (black). Results of experimental measurements are shown exemplarily as open symbols. The predictions of the Monte Carlo simulations are in qualitative agreement with the NRTL model. The comparison between experimental and simulation results shows that the high solubility of NH₃ in the two ILs and the influence of temperature and pressure are reproduced. The average relative deviation between the NRTL model and Monte Carlo simulations is 17-28% for [emim][Tf₂N], and 20-29% for [emim][SCN], whereby our Monte Carlo simulations predict a higher solubility of NH₃ in the ILs than the NRTL model. The relative deviations decrease at higher pressures indicating that the force field performs better at higher loadings of NH₃. At higher loadings of NH₃, NH₃-NH₃ interactions become more important. The TraPPE force field of NH₃ is designed for VLE data and describes these interactions well. The magnitude of the deviations observed between computed values and experimental results is comparable with the work of Shi and Maginn [139] and Urukova *et al.* [317] who also computationally investigated highly soluble gases in ILs. Shi and Maginn [139] also computed the absorption of NH₃ in [emim][Tf₂N]. For comparison, one of the absorption isotherms computed by these authors is shown in Fig. 6.3 (a) (dashed line). The force field of [emim][Tf₂N] used in this work is almost identical to the one used by

Shi and Maginn [139]. The only difference is that Shi and Maginn [139] considers the IL completely flexible. However, their force field describes NH_3 with smaller charges and a smaller Lennard-Jones energy parameter. These differences in the description of NH_3 result in a poorer prediction of the VLE of pure NH_3 . In contrast to our results, these authors underpredict the solubility of NH_3 in $[\text{emim}][\text{Tf}_2\text{N}]$. This suggests that NH_3/IL interactions play a major role. Deviations in the predicted solubility can be ascribed to the applied force fields. Hence, improvements in the force field parameters are required. Nevertheless, Monte Carlo simulations can be used to predict thermodynamic properties at high temperatures and pressures which are otherwise difficult to determine experimentally [291]. A recently published COSMO-RS study reports an average under-prediction of 34% for vapor pressures of a large set of NH_3/IL mixtures [298]. However, these authors did not provide detailed conditions which makes a direct comparison impossible. Experimental solubilities of NH_3 in $[\text{emim}][\text{Tf}_2\text{N}]$ have been measured up to 347.6 K. Using the NRTL model to extrapolate the solubility results in a change of the curvature of the absorption isotherm for 393.15 K (see Fig. 6.3 (a)). This change in curvature is not expected since the nature of the physical interactions between the IL and NH_3 should remain similar. Therefore, the change in curvature might be an artifact of the extrapolation using the NRTL model. Hence, we recommend caution when using the NRTL model to extrapolate experimental data. For the extrapolation of experimental data, the qualitative behavior predicted by Monte Carlo simulations may be more reliable [291].

6.5.2. IL HEAT CAPACITY

The total heat capacity for $[\text{emim}][\text{Tf}_2\text{N}]$ and $[\text{emim}][\text{SCN}]$ is obtained by summing up the ideal gas part and the residual part (Eq. 6.15). In Fig. 6.4, the computed and experimental heat capacities [292, 293, 310, 311, 318] are compared as functions of temperature. The computed values for both ILs are in agreement with experimental data. Average deviation between the experimental and the computed heat capacities are around 4% and 2.5% for $[\text{emim}][\text{Tf}_2\text{N}]$ and $[\text{emim}][\text{SCN}]$, respectively. For temperatures from 303.15 K to 333.15 K, the residual heat capacity is computed at 6.1505 bar (evaporation pressure) while for temperatures from 343.15 K to 393.15 K, it is computed at 13.508 bar (condensation pressure). The experimental uncertainty is large which is depicted by the high degree of scatter between the different experimental data sets. For usage in the cycle model, the computed heat capacities are fitted to a quadratic polynomial in temperature. The resulting parameters are shown in Table 6.1. Subsequently, the enthalpies of the pure IL at different cycle conditions can be calculated from Eq. 6.2.

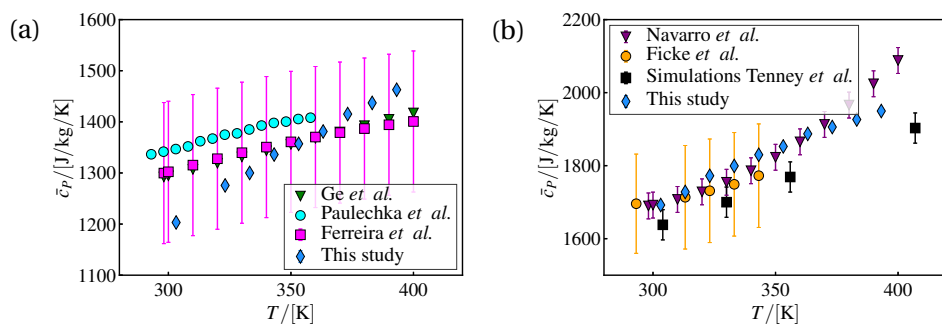


Figure 6.4: Comparison between computed total heat capacities (blue), computational results of Tenney *et al.* [137] (black), and experimental measurements of Ge *et al.* [293] (green), Paulechka *et al.* [310] (cyan), Ferreira *et al.* [292] (magenta), Navarro *et al.* [311] (purple), and Ficke *et al.* [318] (orange) for (a) [emim][Tf₂N] and (b) [emim][SCN].

Table 6.1: Parameters used to fit the polynomial describing the temperature dependency of the heat capacity ($\bar{c}_p^{\text{IL}} = a + bT + cT^2$) to our simulation results.

ILs	a / [J kg ⁻¹ K ⁻¹]	b / [J kg ⁻¹ K ⁻²]	c / [J kg ⁻¹ K ⁻³]
[emim][Tf ₂ N]	-429.51	7.338	$-6.429 \cdot 10^{-3}$
[emim][SCN]	-552.20	10.947	$-1.167 \cdot 10^{-2}$

6.5.3. ENTHALPY OF ABSORPTION

The computed enthalpies of absorption from Monte Carlo simulations are reported in Table 6.2 and compared to the results obtained from the RK-EoS. The enthalpies of absorption computed from Monte Carlo simulations show a consistent trend and are negative for all computed conditions. The determined absolute values increase as the temperature decreases and as the concentration of NH₃ increases. This behavior signifies attraction between the ILs and NH₃, which is consistent with the results reported by Shi and Maginn [139]. Enthalpies of absorption from Monte Carlo simulations are consistently larger than the ones from the RK-EoS. In addition, the EoS predicts positive heats of absorption for [emim][SCN] and temperatures higher than 373 K. Without experimental data, it is difficult to comment on the accuracy of the obtained data and further experiments are necessary. However, it is known that it is problematic to describe the phase behavior of polar nonvolatile compounds such as ILs with a cubic EoS [319]. Hence, the enthalpies of absorptions predicted from molecular simulation might be more reliable.

Table 6.2: Enthalpies of absorption at different cycle conditions computed from Monte Carlo simulations and the RK-EoS (Eqs. 6.21 and 6.22).

ILs	T /[K]	P /[bar]	Monte Carlo sim.		RK-EoS	
			w_{NH_3} /[kg kg ⁻¹]	$\Delta\bar{h}_{\text{abs}}$ /[kJ kg ⁻¹]	w_{NH_3} /[kg kg ⁻¹]	$\Delta\bar{h}_{\text{abs}}$ /[kJ kg ⁻¹]
	308.15	6.15	0.1086	-144.2±9	0.0688	-63.27
[emim]	347.15	13.15	0.0766	-94.6±12	0.0576	-42.87
[Tf ₂ N]	373.15	13.15	0.0404	-51.5±17	0.0290	-15.98
	393.15	13.15	0.0277	-28.7±7	0.0123	-4.61
	308.15	6.15	0.2235	-293.8±3	0.1159	-94.42
[emim]	347.15	13.15	0.1480	-184.9±5	0.1045	-58.67
[SCN]	373.15	13.15	0.0822	-99.4 ±6	0.0580	-0.78
	393.15	13.15	0.0544	-54.7 ±6	0.0357	22.71

6.5.4. CIRCULATION RATIO

The circulation ratio f is defined as the ratio between the mass flow rate of the strong NH₃ solution leaving the absorber and the mass flow rate of refrigerant (see Eq. 6.8). The value of f depends solely on the solubility of NH₃ in the absorbent. It is an important performance parameter as it is directly related to size and cost of equipment [170]. The calculated values for f as a function of T_{GEN} following from Monte Carlo simulations and the NRTL model for both ILs are compared in Fig. 6.5. Deviations between the circulation ratio predicted from the NRTL model and from Monte Carlo simulations can be observed. The average deviation for NH₃/[emim][Tf₂N] is 50% and 67% for NH₃/[emim][SCN]. The reason for these deviations is the discrepancy in the calculated NH₃ solubility (see Eq. 6.8). This deviation is particularly important for low-end generation temperatures. At these temperatures, the solubility of NH₃ in the ILs is very high (above 60 mole %). Hence, the mass flow rate of the IL in comparison to NH₃ is relatively low. This results in a sensitivity of f towards changes in the solubility of NH₃. For both ILs, the simulations overestimate the solubility of NH₃ and therefore predict lower mass fractions of ILs. As T_{GEN} increases, the mass fraction of the ILs in the weak solution increases and f decreases to a nearly constant value at high-end generation temperatures. A high circulation ratio raises the generation heat input according to Eqs. 6.6. Therefore, it is not recommended to operate a VAR cycle at low T_{GEN} .

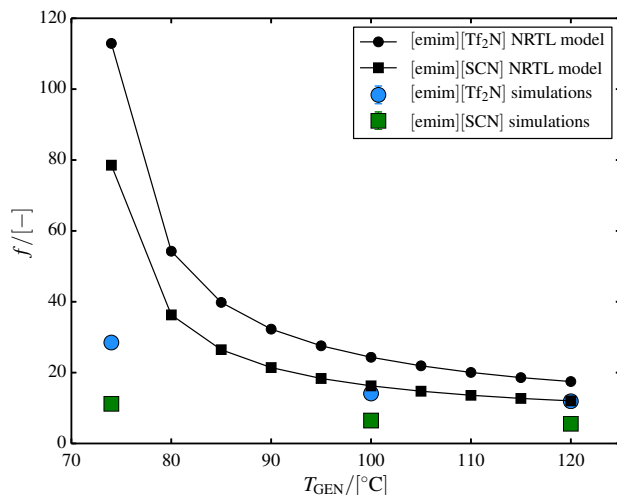


Figure 6.5: Comparison between f calculated with NH_3 solubilities from Monte Carlo simulations (colored) and from the NRTL model (black) for [emim][Tf₂N] (●) and [emim][SCN] (■). The cycle conditions in this work are: $T_{\text{CON}} = 35^\circ\text{C}$, $T_{\text{ABS}} = 30^\circ\text{C}$, $T_{\text{EVA}} = 10^\circ\text{C}$, $T_{\text{GEN}} = 74\text{--}120^\circ\text{C}$, $P_{\text{EVA}} = 6.15\text{ bar}$, and $P_{\text{CON}} = 13.5\text{ bar}$.

6.5.5. COEFFICIENT OF PERFORMANCE

Fig. 6.6 shows the comparison between the COP calculated from simulations (Monte Carlo simulations and quantum mechanical calculations) and the traditional approach (NRTL/EoS model) for both working pairs as a function of T_{GEN} . A different trend of the COP can be observed for both approaches. The COP predicted from simulations is almost constant over the whole range of considered end generation temperatures. In contrast, the COP based on the NRTL/EoS model increases rapidly with T_{GEN} for low temperatures. This behavior results from a strong temperature dependency of the circulation ratio for low T_{GEN} (see Fig. 6.5). For our simulations, a smaller value of f than for the NRTL model is predicted for both ILs. A smaller f decreases the required heat input for the generator (see Eq. 6.6) and therefore has a favorable impact on the COP , which explains the larger COP for the simulation approach for low T_{GEN} . However, for high T_{GEN} , the larger enthalpy difference predicted from simulations between the solutions entering (state point 4) and leaving (state point 7) the generator affects the COP even more (see Table 6.2) and results in smaller COP s for the computational approach. The difference in the heat capacity predicted from simulations and measured experimentally is rather small and is therefore not causing significant changes in the COP prediction. For the COP , the average deviation between the two approaches is 32% and 38%, for NH_3 /[emim][Tf₂N]

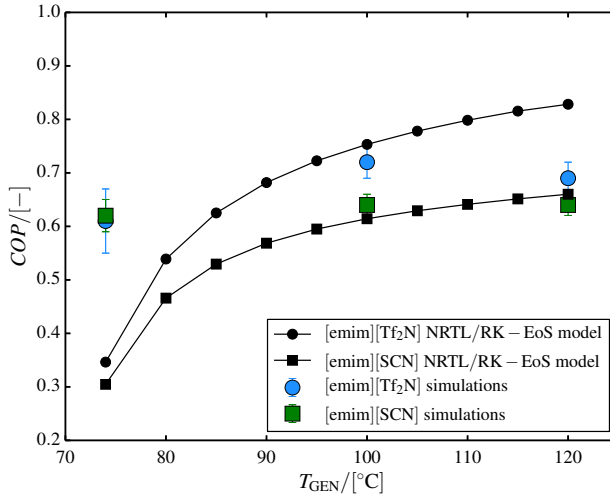


Figure 6.6: Comparison between the COP calculated from simulations (colored) and from the NRTL/EoS model (black) for [emim][Tf₂N] (●) and [emim][SCN] (■). The cycle conditions in this work are: $T_{CON} = 35^\circ\text{C}$, $T_{ABS} = 30^\circ\text{C}$, $T_{EVA} = 10^\circ\text{C}$, $T_{GEN} = 74\text{--}120^\circ\text{C}$, $P_{EVA} = 6.15\text{ bar}$, and $P_{CON} = 13.5\text{ bar}$.

and NH₃/[emim][SCN], respectively. Overall, the results show that, for the investigated cycle model, NH₃/[emim][Tf₂N] performs better than NH₃/[emim][SCN] for a preset T_{GEN} . This statement is true for both NRTL/EoS model and simulations.

6.6. CONCLUSIONS

It has been shown that computational predictions of thermodynamic properties from Monte Carlo simulations along with quantum mechanical calculations can be used to predict the performance of a SE-VAR cycle. The approach has been demonstrated for NH₃/[emim][Tf₂N] and NH₃/[emim][SCN]. For these working pairs solubility, heat capacity, and enthalpy of absorption are computed at various cycle conditions. Subsequently, the circulation ratio f and the coefficient of performance COP are determined with a developed model of the cycle. The only prerequisite for the simulation based approach is a force field describing the interactions between the absorbent and the ions of the ionic liquids, as well as the intramolecular interactions of the ions. The determined thermodynamic properties and performance parameters are compared to a NRTL/EoS model which is fitted to experimental data. Average deviations in COP between the traditional and the simulation based approach of 32% and 38%, for NH₃/[emim][Tf₂N] and NH₃/[emim][SCN], respectively, were observed. For the circulation ratio f , the

average deviations between the traditional and the simulation based approach are around 50% for $\text{NH}_3/[\text{emim}][\text{Tf}_2\text{N}]$ and 67% for $\text{NH}_3/[\text{emim}][\text{SCN}]$. The observed deviations are mainly due to discrepancies of the enthalpies of absorption predicted with the RK-EoS and with simulations, and the overprediction of the solubilities of NH_3 in the ILs by Monte Carlo simulations. These results show that accurate force fields for the investigated working pairs are crucial. To enable the systematic computational screening of working pairs for VAR cycles, this issue needs to be further addressed. Two major problems are worth mentioning concerning the traditional approach. First, the extrapolation with the NRTL model of the NH_3 solubility in the investigated ionic liquids to temperatures higher than experimentally measured is questionable. Deviations in the solubility can significantly influence f and thereby the COP . Second, the absence of experimental data for the enthalpy of absorption introduces a considerable uncertainty for the predicted enthalpy of absorption. Therefore, an error of unknown magnitude exists for this thermodynamic property. This error can also have a significant impact on the COP . Simulation techniques show potential to mitigate these issues. They can play an important role in the prediction of thermodynamic properties for conditions under which experiments are challenging to perform (such as high temperatures and high pressures) and the prediction of mixture properties (such as the enthalpy of absorption). We feel that the presented computational approach seems to be a reasonable choice in the complete absence of experimental data.

7

AMMONIA/IONIC LIQUID BASED DOUBLE-EFFECT ABSORPTION REFRIGERATION CYCLES DRIVEN BY WASTE HEAT FOR COOLING IN FISHING VESSELS

This chapter is based on the paper: M. Wang, T. M. Becker, B. Schouten, T. J. H. Vlugt, and C. A. Infante Ferreira. Ammonia/ionic liquid based double-effect vapor absorption refrigeration cycles driven by waste heat for cooling in fishing vessels. *Energy Conversion and Management*, 174 (2018) 824-843 [320].

7.1. INTRODUCTION

Global warming is a critical issue that impacts our society. According to the International Maritime Organization [291], maritime transport emits around 1000 million tons of carbon dioxide (CO₂) annually and is responsible for about 2.5% of global greenhouse gas emissions along with 15% and 13% of global NO_x and SO_x emissions. Fishery is a major part of the maritime transport sector. Vessels for pelagic seas usually demand refrigeration plants, which consume fuel or electricity onboard [321]. The refrigeration plant is one of the largest electricity consumers onboard of fishing vessels, typically using 50% of the total power [322]. Diesel engines are normally used for propulsion and on-board electricity generation in trawlers. The engines also produce a significant amount of waste

heat [323]. A study by MAN Diesel & Turbon LTD [324] shows that a large 2-stroke marine diesel engine may waste 50% of total fuel energy and that 25.5% of this total energy is wasted through exhaust gas (250 - 500 °C) [321].

Heat activated VAR cycles provide opportunities to recover waste heat and use it to cool down fish and onboard space. Fernández-Seara *et al.* [325] designed, modeled, and analysed a gas-to-thermal fluid waste heat recovery system based on an ammonia/water ($\text{NH}_3/\text{H}_2\text{O}$) cycle for onboard cooling applications. Cao *et al.* [326] carried out a study on a water/lithium bromide ($\text{H}_2\text{O}/\text{LiBr}$) VAR cycle powered by waste heat for space cooling in a cargo ship. In their study, the cooling COP is 0.6 and an electricity-based coefficient of performance (COP) could be up to 9.4. Thereby, fuel consumption and CO_2 emission for the cooling system are reduced by 62%. Recently, Salmi *et al.* [323] modeled both a $\text{H}_2\text{O}/\text{LiBr}$ SE-VAR cycle and a $\text{NH}_3/\text{H}_2\text{O}$ refined cycle for cooling on a bulk carrier ship with waste heat recovered from exhaust gases, jacket water and scavenge air cooler. The VAR cycle has a theoretical potential to save 70% of electricity in comparison to a compression air-conditioning system. They also pointed out that the $\text{H}_2\text{O}/\text{LiBr}$ cycle is more efficient (COP of 0.75-0.85) and $\text{NH}_3/\text{H}_2\text{O}$ is more suitable for below-freezing-point cooling (COP of 0.5).

Exhaust gases seem to be the best source of waste heat onboard to drive absorption chillers, even though they cannot be cooled down below 167 °C to avoid sulfur corrosion [323]. At temperatures above 150 °C, double-effect vapor absorption refrigeration (DE-VAR) cycles, in which the refrigerant is generated twice, are able to achieve higher thermal efficiencies by taking advantage of the higher temperature of the heat sources [327]. Usually, these cycles utilize the working pair $\text{H}_2\text{O}/\text{LiBr}$, which cannot meet the demand of below-freezing-point cooling. With $\text{NH}_3/\text{H}_2\text{O}$, the DE-VAR cycle is not feasible on fishing vessels due to the need of rectifiers which introduce a higher complexity.

To use exhaust gas at higher temperatures for below-freezing-point cooling onboard, NH_3 in combination with an IL is proposed as working pair for the use in DE-VAR cycles. Previous studies of NH_3/IL working pairs were conducted at temperature and pressure ranges suitable for SE-VAR cycles. The DE-VAR cycle requires VLE data at higher temperatures and higher pressures, which have not been measured experimentally. Previously, Wang and Infante Ferreira [328] investigated nine NH_3/ILs working pairs in DE absorption cycles for application in refrigeration and heat pump systems. The used VLE properties were obtained by simply extrapolating the ones at temperatures and pressures available for SE-VAR cycles. Schouten [329] used the same extrapolated properties for a DE-VAR cycle in a series design. We showed in the previous chapter that molecular simulation is able to predict relevant thermophysical properties for temperatures and pressures applied in SE-VAR cycles, but also pointed out that improved force

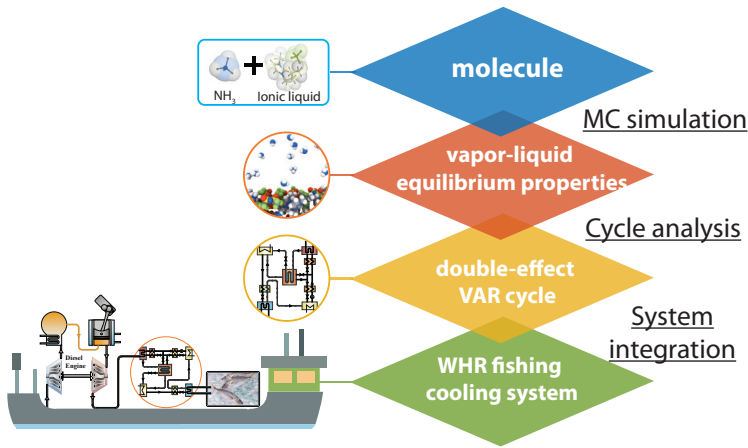


Figure 7.1: Outline showing the different simulation scales considered in this study.

fields are needed for an accurate prediction of the cycle performance.

In this chapter, a DE-VAR cycle in parallel configuration which is driven by heat recovered from diesel engines using NH_3/IL working pairs is proposed for refrigeration applications in fishing vessels. A multi-scale method is applied to study its performance, from a molecular level to a system integration level, as shown in Fig. 7.1. First, an adjusted force field is used in Monte Carlo simulations to predict VLE properties in high temperature and high pressure conditions of the three selected NH_3/IL working pairs. Together with the experimental VLE and heat capacities, the VLE data are correlated and mixture enthalpies are predicted. These thermophysical properties are then used for the evaluation of the DE-VAR cycle. After considering practical concerns, a case study based on a real vessel operating in high-latitude conditions is carried out to check the techno-economic feasibility of the integrated system in practice.

7.2. PROPERTIES OF WORKING PAIRS

The ILs under consideration are $[\text{emim}][\text{SCN}]$, $[\text{bmim}][\text{BF}_4]$, and $[\text{emim}][\text{Tf}_2\text{N}]$. Previously, the corresponding NH_3/IL working pairs were identified showing higher *COPs* than $\text{NH}_3/\text{H}_2\text{O}$ in SE absorption cycles [170]. Additionally, these ILs are commercialized, their thermophysical properties, and the required force fields are accessible. Hence, these ILs are selected for further study.

7.2.1. BINARY VAPOR-LIQUID EQUILIBRIA

For the three studied NH_3/IL working pairs, experimental VLE data measured by Yokozeki and Shiflett [136, 165] only cover the conditions suitable for SE-VAR cycles. To extend the VLE data of these fluids for DE-VAR cycles at higher temperatures and pressures, Monte Carlo simulations are conducted. The data from experimental sources together with simulated ones are correlated with the NRTL model for usage in the studied cycle.

MONTE CARLO SIMULATIONS

Molecular simulation is a powerful tool to predict the behavior of materials [15]. In this type of simulation, thermodynamic properties are computed based on force fields which describe interactions between molecules [281]. Comparable to the NRTL model, these force fields are often developed by correlating experimental data. However, the potential to predict properties outside the correlated data is often better than with traditional models and hence molecular simulation can be used to extend existing experimental data [131]. Here, Monte Carlo simulations were performed to obtain solubility data of NH_3 in 3 different ILs at higher temperatures than measured experimentally.

As shown in the previous chapter, the osmotic ensemble [144] can be applied to compute the uptake of gases in ILs. Thereby, the temperature, the pressure, the number of solvent molecules, and the fugacity of the solute are fixed, while the volume of the system, and the number of solute molecules can fluctuate. Here, the Continuous Fractional Component Monte Carlo method is applied to insert and delete solute molecules [139, 144, 145, 167, 303, 305, 306]. After the equilibration phase, the total amount of solute molecules in the system determines the gas uptake at the chosen conditions. The details of the conducted simulations can be found in the previous chapter.

All force fields considered in this work are taken from literature. The force fields for ILs are from Tenney *et al.* [137] (for cation $[\text{emim}^+]$ and anion $[\text{SCN}^-]$), Liu *et al.* [29] (for cation $[\text{bmim}^+]$ and anion $[\text{Tf}_2\text{N}^-]$), and Canongia Lopes and Pádua [330] (for anion $[\text{BF}_4^-]$). For NH_3 , the TraPPE force field is used [302]. In the simulations, parts of the cations and NH_3 molecules are considered to be rigid while the alkyl part and anions are flexible. A summary of force field parameters is provided in the Supporting Information of Wang *et al.* [320]. The Ewald summation technique with a relative precision of 10^{-5} [15] is used to calculate electrostatic interactions. Lennard-Jones interactions are truncated and shifted at 12 Å without applying tail corrections. Polarization is not explicitly considered in the simulations. The simulations are conducted with the RASPA software package [225, 226].

Unfortunately, commonly used force fields do not predict the solubility of

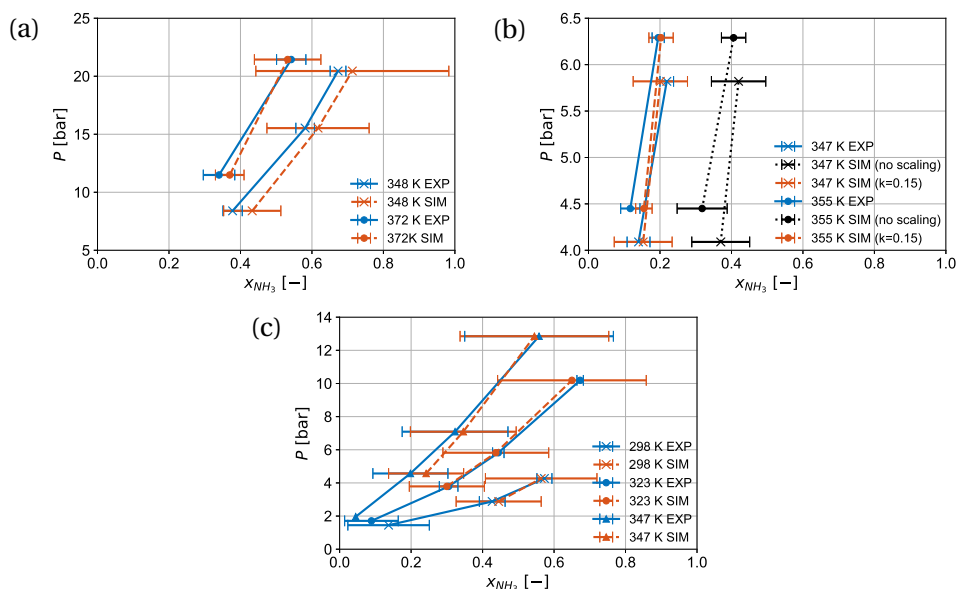


Figure 7.2: Comparison between the simulated (SIM) and experimental (EXP) VLE data [136, 165] for the working pairs: (a) NH_3 /[emim][SCN], (b) NH_3 /[bmim][BF_4] and (c) NH_3 /[emim][Tf_2N]. The shown error bars of the simulated data represent the 95% confidence interval.

NH_3 in ILs accurately (cf. chapter 6). To overcome this limitation, the binary mixing rule of the Lennard-Jones energy parameters, ϵ , between NH_3 and ILs in Monte Carlo simulations has been scaled to fit the experimental solubility for available conditions. The applied mixing rule is:

$$\epsilon = k \cdot \sqrt{\epsilon_{\text{NH}_3} \cdot \epsilon_{\text{IL}}} \quad (7.1)$$

By adjusting ϵ , the interaction strength between NH_3 and the ILs is changed. Different interaction strengths between the molecules were tested to find the one that predicts the best behavior in regard to the experimental data. The applied scaling parameter, k , is respectively 0.78, 0.15, and 0.78 for [emim][SCN], [bmim][BF_4] and [emim][Tf_2N]. To validate the quality of the adjusted force field, a comparison between the computed solubilities (dashed curves) with the adjusted force fields and the experimental data [136, 165] (solid curves) is provided in Fig. 7.2. In the case of [bmim][BF_4] (Fig. 7.2 (b)), the computed solubility without adjusting force field is shown (dotted curves). It can be observed that the qualitative trend of the gas uptake of these simulations is similar, while the absolute values are significantly overestimated. After the scaling of the mixing rule, the simulation results agree well with the experimental data for all investigated ILs and for varying temperatures. The average 95% confidence interval

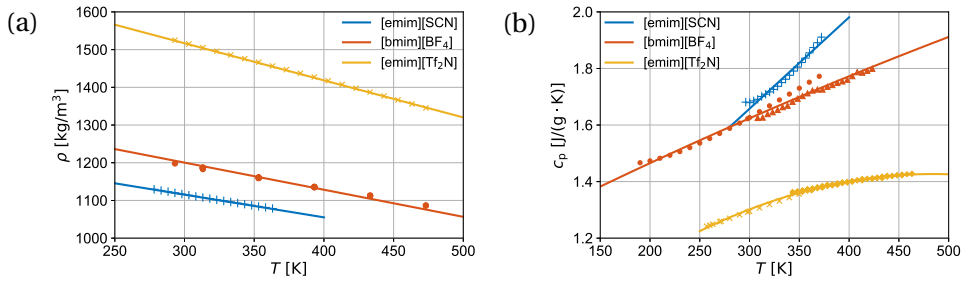


Figure 7.3: Experimental data and the correlations of (a) densities [318, 331, 332], and (b) heat capacities [292, 310, 311, 333, 334] of the three studied ILs.

for the computed solubilities used in the cycle calculations for [emim][SCN], [bmim][BF₄], and [emim][Tf₂N] is 2.8%, 1.7%, and 2.9%, respectively.

CORRELATION OF VAPOR-LIQUID EQUILIBRIA

The NRTL model has been shown as a suitable model to correlate and predict VLE of ILs-based working pairs [312]. The experimental vapor pressures of binary NH₃/IL systems have been regressed to the NRTL model as explained by Wang and Infante Ferreira [170]. Subsequently the operating concentrations of solutions can be determined. The form of the NRTL model can be found in Wang and Infante Ferreira [170]. Note that for data points at temperatures above the critical point of NH₃, an extrapolation of the vapor pressure equation is used for an easy processing of the data [167]. In particular, an extrapolation of the Antoine equation is applied.

7.2.2. DENSITIES AND HEAT CAPACITIES

Densities of pure [emim][SCN], [bmim][BF₄] and [emim][Tf₂N] have been reported by Ficke *et al.* [318], Matkowska and Hofman [331], Tariq *et al.* [332] respectively. Specific heat capacities of [emim][SCN] are from the work of Navarro *et al.* [311]. The combined data reported by Paulechka *et al.* [333] and Nieto de Castro *et al.* [334] are used for the specific heat capacities of [bmim][BF₄]. For [emim][Tf₂N], the data of specific heat capacities were reported by Paulechka *et al.* [310] and Ferreira *et al.* [292] for different temperature ranges. These data are plotted in Fig. 7.3, as functions of temperature. Correlations of the data are listed in Table 7.1. Currently, densities and heat capacities of the studied NH₃/IL mixtures have not been reported. Eq. 7.2 provides a general form of ideal solution properties, which is based on weighted average of properties from both components:

$$M_{\text{sol}} = w_{\text{NH}_3} M_{\text{NH}_3} + w_{\text{IL}} M_{\text{IL}} \quad (7.2)$$

Table 7.1: Molecular weights (M_w) and correlations of relevant thermophysical properties for the 3 investigated ILs at 1 bar * (Densities [318, 331, 332] and heat capacities [292, 310, 311, 333, 334]).

IL	M_w [kg/kmol]	ρ [kg/m ³]	c_p [kJ/(kg·K)]
[emim][SCN]	169.25	$\rho = 1296 - 0.602 \cdot T$	$c_p = 0.6882 + 0.0032 \cdot T$
[bmim][BF ₄]	226.02	$\rho = 1416 - 0.719 \cdot T$	$c_p = 1.119 + 1.83 \cdot 10^{-3} \cdot T - 4.879 \cdot 10^{-7} \cdot T^2$
[emim][Tf ₂ N]	391.31	$\rho = 1812 - 0.984 \cdot T$	$c_p = 0.5644 + 3.56 \cdot 10^{-3} \cdot T - 3.674 \cdot 10^{-6} \cdot T^2$

* T in K.

The equation is used to estimate densities and heat capacities for the investigated mixtures. The applied simplification is verified with the density data of six NH₃/IL mixtures reported by Cera-Manjarres [169]. The maximum relative deviation is 6.5%. Moreover, the equation for the heat capacities has been verified with data of H₂O/[mmim][DMP] from Dong *et al.* [163]. In their case, the relative deviation is smaller than 4% [170]. The applicability of the equation has also been checked by the authors for the H₂O/[emim][DMP] solution, for predicting the solution enthalpy and cycle performance. No obvious difference has been observed in comparison to using the heat capacity of the real solutions [312].

7.2.3. ENTHALPIES

The enthalpy of pure NH₃ is directly obtained from NIST's Refprop [335]. For a saturated solution at T , P and with a NH₃ mass fraction of w_{NH_3} , the total enthalpy of the solution, $h_{\text{sat}}^{\text{sol}}$ is provided by,

$$h_{\text{sat}}^{\text{sol}}(T, P, w_{\text{NH}_3}) = w_{\text{NH}_3} h_{\text{NH}_3}(T) + w_{\text{IL}} h_{\text{IL}}(T) + \Delta h_{\text{mix}}(T, P, w_{\text{NH}_3}) \quad (7.3)$$

where enthalpies of NH₃ are chosen at its saturated liquid state for cases below the critical temperature. For temperatures above the critical point of NH₃, the ideal gas enthalpy is added to the enthalpy at the critical point, following the work of Chen *et al.* [167]:

$$h_{\text{NH}_3}(T) |_{T > T_c} = h_{\text{NH}_3}(T_c) + \int_{T_c}^T c_{p,\text{ig}}^{\text{NH}_3} dT \quad (7.4)$$

For the ILs, enthalpies are calculated based on their pure heat capacities c_p^{IL} ,

$$h_{\text{IL}}(T) = h_0(T_0) + \int_{T_0}^T c_p^{\text{IL}} dT \quad (7.5)$$

The experimental mixing enthalpy Δh_{mix} used in Eq. 7.3 has not been reported for the studied NH₃/IL working pairs. For an alternative NH₃/IL working pair, the authors have quantified this term using various thermodynamic models [312].

The calculation has shown that the exothermic effect of mixing NH_3 and IL is less than that of mixing H_2O and IL. Furthermore, it has been shown that neglecting Δh_{mix} does not significantly change the total enthalpy and the COP in a SE-VAR cycle with NH_3/IL working pairs [312]. Therefore, in the following calculations, the effect of the mixing enthalpy is neglected.

For solutions at subcooled conditions T , P and w_{NH_3} , enthalpies can be obtained by subtracting the subcooled part from the corresponding saturated solution,

$$h_{\text{sub}}^{\text{sol}}(T, P, w_{\text{NH}_3}) = h(T_{\text{sat}}, P, w_{\text{NH}_3}) - \int_T^{T_{\text{sat}}} c_p^{\text{sol}} dT \quad (7.6)$$

7.3. CYCLE CONFIGURATION AND MODELING METHOD

In the following Section, the configuration and modeling method of the studied DE-VAR cycle are presented. Besides, an alternative choice, the generator-absorber heat exchange (GAX) cycle with $\text{NH}_3/\text{H}_2\text{O}$, is introduced for the sake of comparison. The GAX cycle is promising in combination with high temperature heat sources [327].

7.3.1. DOUBLE-EFFECT ABSORPTION REFRIGERATION CYCLE

Fig. 7.4 depicts a schematic representation of a double-effect absorption system in parallel configuration. The main feature of the parallel DE-VAR cycle is that the strong solution (strong in refrigerant NH_3), pumped from the absorber (ABS), is divided into two parallel streams after being heated in the solution heat exchanger (SHX1). The two sub-streams are heated in two generators (GENs) to generate refrigerant vapor: One sub-stream is heated in the high pressure generator (HG) by the external heat source at a high temperature. In the HG, superheated refrigerant vapor is generated which continues to the high pressure condenser (HC). The second sub-stream is heated in the low pressure generator (LG) to generate more refrigerant vapor. The heat is supplied by condensation of the superheated refrigerant vapor in the HC. The HC and LG are coupled in an intermediate heat exchanger (iHX). Key state points of the solutions are illustrated qualitatively in both $\ln P$ - $(-1/T)$ and $h-w$ diagrams in Fig. 7.5. Cycle 5-8-9-11a-11-13-5 shows the sub-stream passing the HG and cycle 5-7c-11b-11-13-5 represents the other sub-stream passing the LG. The distribution ratio (DR) is the ratio of the mass flow of the solution passing the HG and the total mass flow:

$$DR = \frac{\dot{m}_8}{\dot{m}_5} \quad (7.7)$$

To create an integrated model for the thermodynamic analysis of the DE-VAR cycle, several assumptions are made to simplify the calculations:

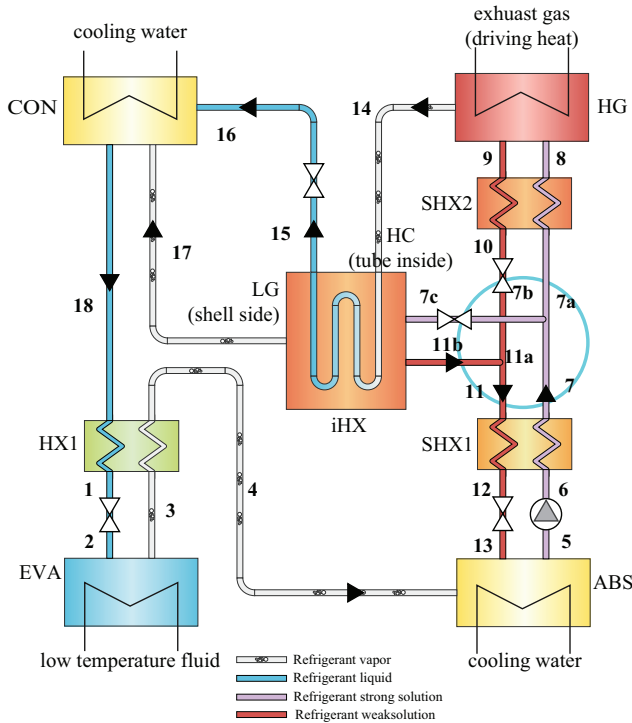


Figure 7.4: Schematic diagram of the studied DE-VAR cycle in parallel configuration. A non-volatile absorbent absorbs refrigerant in the absorber (ABS). The solution is then split and pumped to the high and low pressure generators (HG and LG) to generate refrigerant vapor. The blue circle identifies the parallel sub-streams leaving and returning the ABS. The refrigerant vapor generated in the HG is used to heat the LG. The two refrigerant streams are mixed in the condenser (CON) and continue through the valve and the evaporator (EVA) to generate the cooling effect.

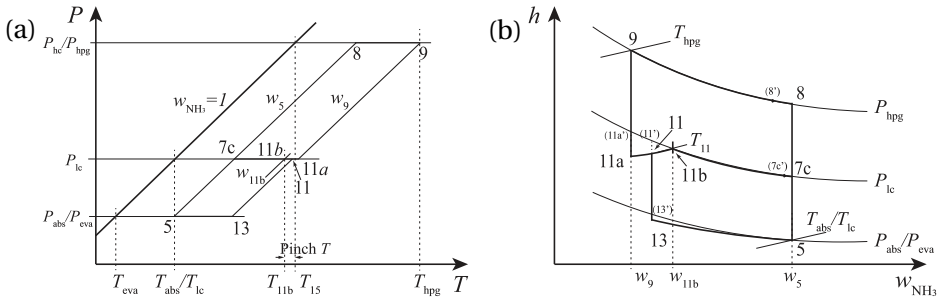


Figure 7.5: The state points (referring to Fig 7.4) of the solution stream plotted in (a) a $\ln P - (-1/T)$ diagram and (b) a $h - w$ diagram. State points 11, 11a and 13 which share the same pressure and mass fraction with state points 11', 11a', and 13', respectively, are at subcooled conditions. For state points 7c and 8 a possibility of refrigerant boil off exists. The portions of saturated solutions are denoted as 7c' and 8', respectively.

- The system operates in a steady state.
- The operating pressures of the absorber and the evaporator are identical, and similarly, the pressure of each generator is equal to its directly linked condenser.
- In the outlets of the two condensers and the evaporator, the refrigerant streams are in a saturated liquid or saturated vapor state, respectively. The solutions are in equilibrium state while leaving the two generators and the ABS.
- The pinch temperature of the SHXs is assumed as 10 K. The pinch temperature of the iHX is set to 5 K. The effectiveness of the HX1 is assumed to be 75%.
- Heat losses and pressure losses are neglected.
- Throttling is an isenthalpic process.

For each component shown in Fig. 7.4, the mass, species and energy balances are implemented. For instance, for the ABS shown in Fig. 7.4, the balances are:

$$\dot{m}_4 + \dot{m}_{13} = \dot{m}_5 \quad (7.8)$$

$$\dot{m}_4 + w_{13} \dot{m}_{13} = w_5 \dot{m}_5 \quad (7.9)$$

$$\dot{m}_4 h_4 + \dot{m}_{13} h_{13} = \dot{m}_5 h_5 + \dot{Q}_{\text{abs}} \quad (7.10)$$

The power consumption of the solution pump, \dot{W}_p , can be calculated by,

$$\dot{W}_p = \frac{\dot{m}_5}{\rho_{\text{sol}}} \frac{P_{\text{hpg}} - P_{\text{eva}}}{\eta_p} \quad (7.11)$$

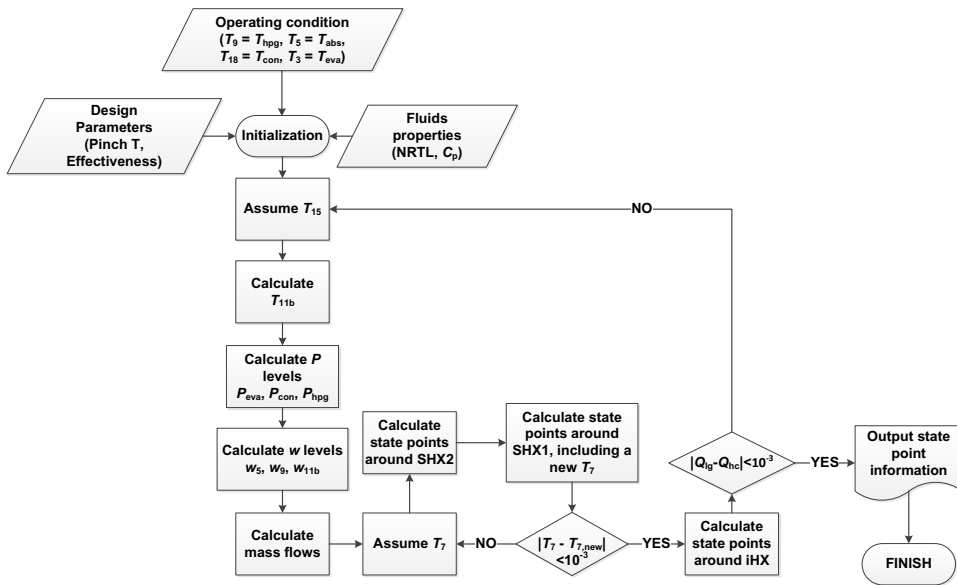


Figure 7.6: Flow-chart for the thermodynamic modeling of the DE-VAR cycle in parallel configuration. Mass, species and energy balances are applied for each component. Iterations of T_{15} and T_7 are implemented to close energy balances of the iHX and the two SHXs.

The calculation procedure for the cycle is illustrated in Fig. 7.6. The temperature of state point 7, which is between two SHXs, is obtained iteratively by closing the energy balances of both SHXs. Another iteration is required to determine the temperature of state point 15, which can be calculated based on the energy balance of the iHX. The coefficient of performance, COP , of a cycle for cooling is defined as,

$$COP = \frac{\dot{Q}_{\text{eva}}}{\dot{Q}_{\text{hpg}} + \dot{W}_{\text{p}}} \quad (7.12)$$

The circulation ratio, f , is defined as the ratio between the mass flow of the pump stream and the mass flow of refrigerant. f can be obtained via mass and species balances around the ABS,

$$f = \frac{\dot{m}_5}{\dot{m}_4} = \frac{1 - w_{13}}{w_5 - w_{13}} \quad (7.13)$$

This model was previously validated by Vasilescu and Infante Ferreira [336] for an air-conditioning application with a LiBr/H₂O working pair.

7.3.2. GENERATOR-ABSORBER HEAT EXCHANGE CYCLE

NH₃/H₂O GAX cycles have been claimed to be suitable for applications with a heat source at high temperatures [327]. As shown in Fig. 7.7, the promising thermal performance of this cycle is achieved by coupling the heat between partial sections of the GEN and the ABS. A perfect operation of the GAX cycle relies on the accurate identification of temperature profiles of sections in ABS and GEN where the heat can be coupled. This kind of heat coupling is difficult to achieve in practice. However, the GAX cycle represents “a compelling theoretical possibility” [327]. Therefore it is used as a benchmark to compare the DE-VAR cycle with. The modeling of the GAX cycle is based on the method introduced by Herold *et al.* [327]. During the heat coupling, both the available heat in the ABS and the required heat in the GEN can be obtained through mass and energy balances, by assuming that solution and vapor streams are in counter-current flow. The heat that is transferred in the GAX cycle is the minimum between the available and required heat of vapor generation. The rectifier is analyzed as an ideal device that produces vapor with 99.5% NH₃.

7.4. INTEGRATED FISHING VESSEL

A trawler vessel is taken into consideration for the following case studies. The required cooling capacity in this vessel is provided by the refrigeration seawater plant (RSW), chilled water plant (CWP), and freezing plant (FP). Currently, the plants are all configured with vapor compression refrigeration systems. The RSW and CWP apply NH₃ as refrigerant, while the FP is a NH₃/CO₂ cascade system (NH₃ is used in the high temperature circuits). The technical characteristics

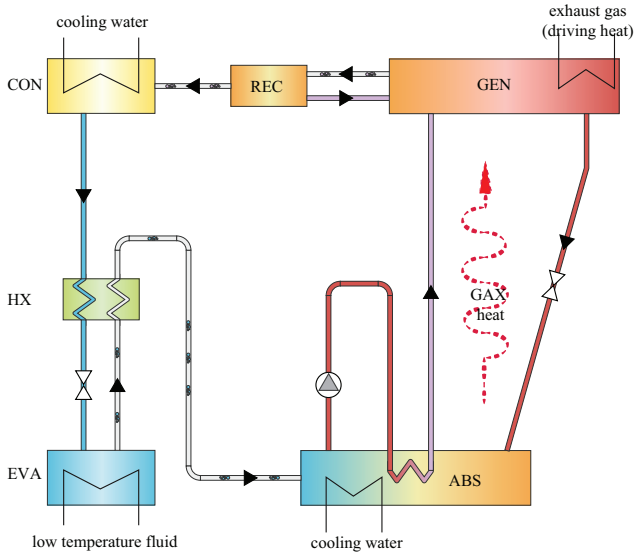


Figure 7.7: Schematic diagram of a standard NH₃/H₂O GAX cycle [327]. The main feature of the GAX cycle is that the final stages of its ABS have higher temperatures than the flow in the first stages of the GEN. The heat from the ABS is recycled to heat up later stages in the GEN. The weak NH₃/H₂O solutions absorb NH₃ vapors from the EVA and experience an internal heat recycling in the ABS before they are pumped into the GEN. Vapors leaving the GEN are mixtures of NH₃/H₂O, which are purified in the rectifier (REC). NH₃ vapor is treated similarly as in the DE-VAR cycle to generate the cooling effect.

Table 7.2: Cooling capacities, temperatures and power consumptions of the refrigeration plants (RSW, CWP and the NH₃ circuits of FP) used in the studied trawler vessel, for two typical climate situations.

	\dot{Q}_{eva} [kW]	T_{eva} [°C]	\dot{W} [kW]	
RSW plant	2·1416	-5	2·414	32 °C heat sink
CWP	2·880	-5	2·222	
FP (NH ₃ circuits)	2·900	-5	2·253	
RSW plant	2·1556	-5	2·271	16 °C heat sink
CWP	2·954	-5	2·152	
FP (NH ₃ circuits)	-	-	-	

Table 7.3: Typical operating modes of the fishing vessel, main engine loads, and the corresponding flow and temperature of the exhaust flue gas.

Operation mode	Duration per year [hour]	Main engine load [-]	Exhaust gas flow [kg/s]	T of exhaust gas [°C]
Mode 1 Fishing with production	5400	90%	15	340
Mode 2 Fishing without production	400	90%	15	340
Mode 3 Sailing to fishing zone and pre-cooling	320	70%	12	326.5
Mode 4 Placing or retrieving nets, pumping fish on board	1200	40%	8.75	307.4
Mode 5 Unloading or out of service	1440	0%	-	-

are listed in Table 7.2. It is investigated if the proposed IL-based DE-VAR cycle has the potential to replace the current plants entirely or partially. Scavenge air, jacket water, and exhaust gas are among the main waste heat sources from the diesel engines as illustrated in Fig. 7.8. The heat released via the exhaust gas takes up approximately 50% of total wasted heat [324]. Here, the exhaust gas after the turbine is used. The studied ship is equipped with a Wärtsilä diesel engine of type 12V38 for propulsion [337]. The properties of the exhaust gas are shown in Fig. 7.9, which is copied from the official project guide [337]. Note that the data for an operation under 40% load are based on extrapolations. Operations of the engine can be classified into five typical modes, which are listed in Table 7.3. Corresponding exhaust gas properties are identified from Fig. 7.9.

7.5. RESULTS AND DISCUSSION

Following the proposed multi-scale method, the results of the property level, cycle level, and integrated system level are discussed in this Section.

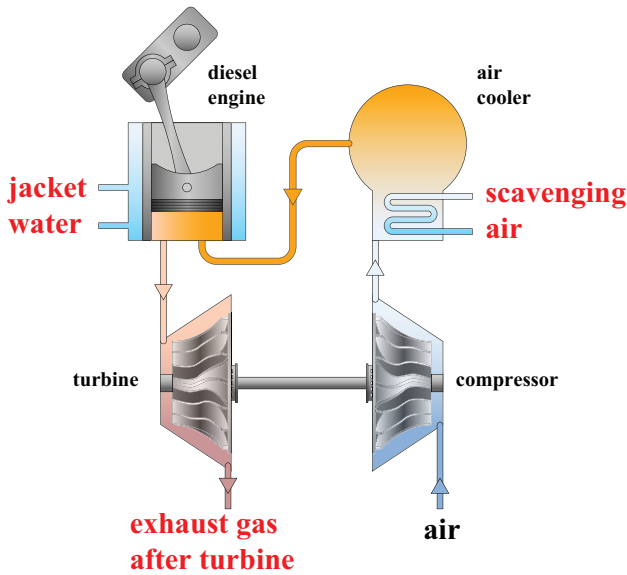


Figure 7.8: Main waste heat sources of a two-stroke diesel engine: Scavenge air is used to cool down the compressed air before entering the engine. Jacket water is applied to maintain the temperature of the engine where the combustion of fuels takes place. Exhaust gas, a mix of air and fuel at high temperature, is released with 50% of the total waste heat.

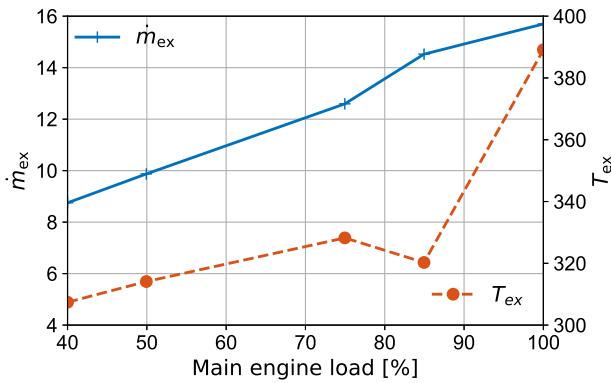


Figure 7.9: Exhaust gas flow and temperature (after the turbine) of the studied diesel engine 12V38 for different engine loads [337]. The solid curve denotes the flow rate of the exhaust gas and the dashed curve denotes its temperature after the turbine.

Table 7.4: Fitted interaction parameters used for the NRTL model (following the same notations as in Ref. [170]) for the studied NH_3 /IL working pairs.

IL	α [-]	$\tau_{12}^{(0)}$ [-]	$\tau_{12}^{(1)}$ [K]	$\tau_{21}^{(0)}$ [-]	$\tau_{21}^{(1)}$ [K]
[emim][SCN]	-0.0320	-20.18	4342.10	11.07	-2084.20
[bmim][BF ₄]	-0.0001	-481.23	2740.10	456.75	-2297.27
[emim][Tf ₂ N]	-0.0024	-107.90	8969.70	82.95	-5276.93

7.5.1. CORRELATION OF BINARY VAPOR-LIQUID EQUILIBRIA

The experimental VLE data and the ones from Monte Carlo simulations are plotted together in Fig. 7.10 for the three studied NH_3 /IL working pairs. The fitted

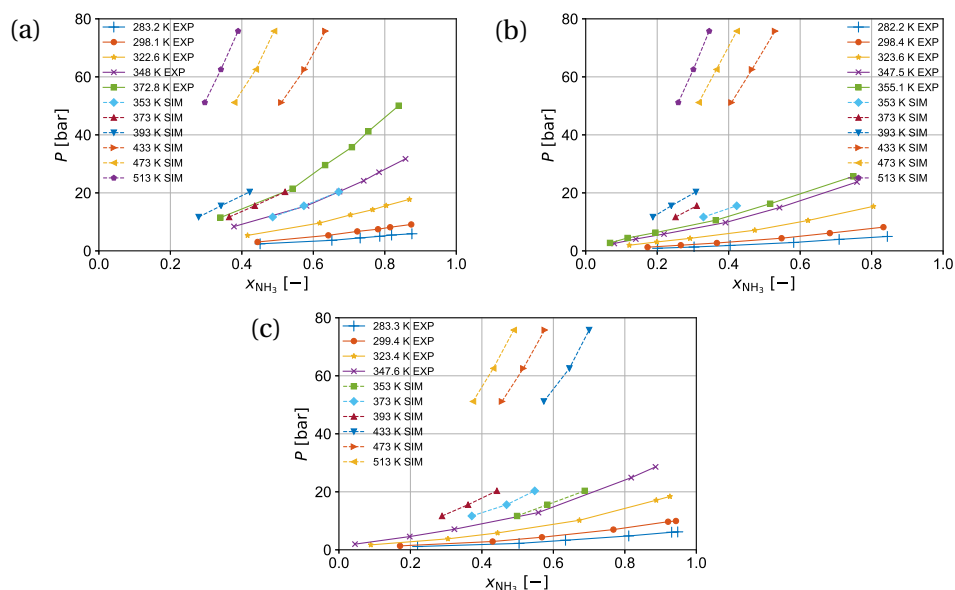


Figure 7.10: VLE data of working pairs (a) NH_3 /[emim][SCN], (b) NH_3 /[bmim][BF₄] and (c) NH_3 /[emim][Tf₂N]. Solid curves denote (EXP) experimental data from Yokozeki and Shiflett [136, 165], dashed curves the (SIM) simulated results of this work.

parameters of the NRTL model based on the shown data are listed in Table 7.4. These parameters follow the same notations introduced in Ref. [170]. Based on the NRTL model, predicted vapor pressures of the three studied fluids are presented in Fig. 7.11. To show the influence of the additional data provided by Monte Carlo simulations, results are compared with and without the inclusion of the computed data. Vapor pressures shown in Figs. 7.11 (a), 7.11 (c), and 7.11 (e) are obtained by exclusively fitting experimental VLE data at low temperatures

and low pressures (interaction parameters can be found in Ref. [170]). The vertical and horizontal dashed lines represent temperature and pressure boundaries of experimental data, respectively. The other three diagrams are based on both experimental and computed VLE data. In every diagram of Fig. 7.11, NH₃ fractions cover the conditions applied in the DE-VAR cycle. Vapor pressures fitted only with VLE data at low temperatures and low pressures (Figs. 7.11 (a), 7.11 (b), and 7.11 (c)) show linear behavior inside the experimental temperature and pressure ranges. However, outside of the range of the experimental data, the vapor pressures increase rapidly with an increase of temperature. This behavior fails to follow the physical basis indicated by the Clausius-Clapeyron equation (Eq. 7.14):

$$\frac{d \ln P}{d(1/T)} = - \frac{\Delta h}{R\Delta Z} \quad (7.14)$$

where Z is the compressibility factor. According to the Clausius-Clapeyron equation, the vapor pressures should be approximately linear, because the term $-\Delta h/(R\Delta Z)$ depends only slightly on temperature [338]. The nonlinear shape of the vapor pressure curves is pronounced at relatively low NH₃ mass fractions, which are crucial for the studied cycle. The detailed influence of using exclusively the experimental based VLE properties on estimating the cycle performance is discussed in Section 7.5.3. By including computed data (right-hand side), the trends of vapor pressures, especially for cases with low NH₃ fractions at high temperatures, become more reasonable. This indicates that the computed data help to improve the description of the behavior. The reasonable extension of VLE data for NH₃/IL mixtures, confirms the added value and need for Monte Carlo simulations to extend the range of VLE properties of NH₃/IL mixtures.

7.5.2. THERMOPHYSICAL PROPERTIES

Based on the methods discussed in Section 7.2, diagrams for the studied working pairs are created. These diagrams can be used to easily determine properties needed for thermal applications including VAR cycles. The corresponding diagrams are provided in the Appendix of Wang *et al.* [320].

7.5.3. CYCLE PERFORMANCE

With the thermophysical properties, the performance of the DE-VAR cycle can be predicted. In the following Section, influences of operation conditions, different sources of properties, and the comparison with the GAX cycle is presented.

INFLUENCE OF VARYING OPERATION CONDITIONS

Parametric studies are carried out to explore the performance of the DE-VAR cycle for different operating conditions. The investigated parameters are the DR ,

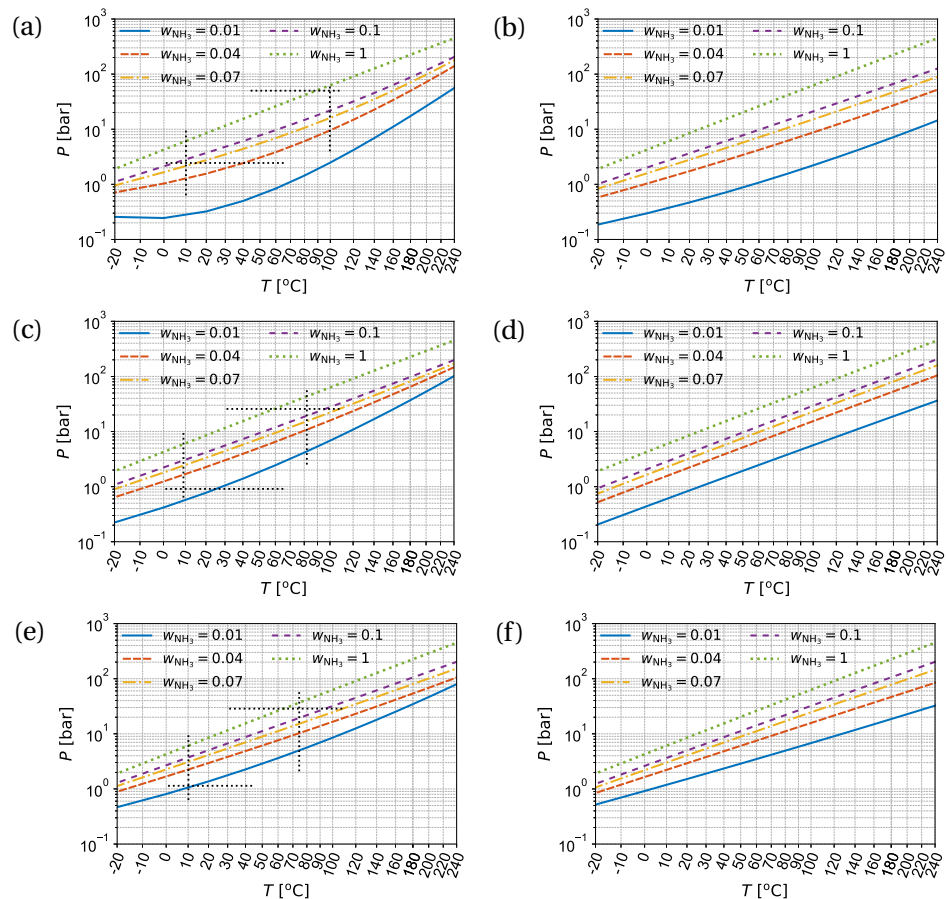


Figure 7.11: Comparison of vapor pressures generated only using (EXP) the experimental VLE data and (SIM) the ones using the experimental and simulated VLE data for the studied NH_3/IL working pairs: (a) $\text{NH}_3/[\text{emim}][\text{SCN}]$ (EXP [165]), (b) $\text{NH}_3/[\text{emim}][\text{SCN}]$ (EXP [165] + SIM) (c) $\text{NH}_3/[\text{bmim}][\text{BF}_4]$ (EXP [136]), (d) $\text{NH}_3/[\text{bmim}][\text{BF}_4]$ (EXP [136] + SIM), (e) $\text{NH}_3/[\text{emim}][\text{Tf}_2\text{N}]$ (EXP [136]), (f) $\text{NH}_3/[\text{emim}][\text{Tf}_2\text{N}]$ (EXP [136] + SIM). Vertical and horizontal dashed lines represent temperature and pressure boundaries of EXP data.

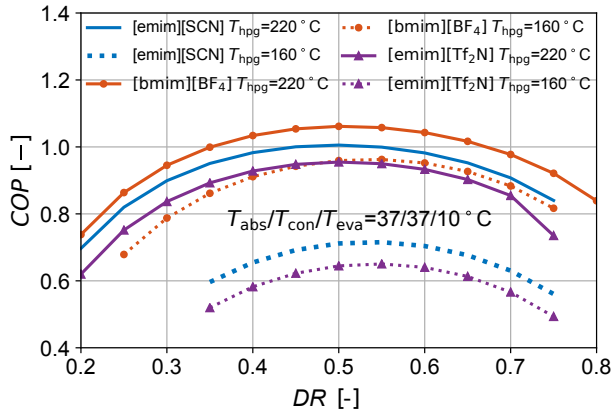


Figure 7.12: Influence of the distribution ratio on the coefficient of performance of the DE-VAR cycle with working pair $\text{NH}_3/[\text{emim}][\text{SCN}]$, $\text{NH}_3/[\text{bmim}][\text{BF}_4]$, and $\text{NH}_3/[\text{emim}][\text{Tf}_2\text{N}]$. The performance is calculated at T_{hpg} of 220 or 160 °C. $T_{\text{abs}}/T_{\text{con}}/T_{\text{eva}}$ are kept constant at 37/37/10 °C.

the temperature of the heat source, the cooling temperature and the temperature of the environment. As shown in Fig. 7.12, optimum performances for different conditions (heat source temperature, T_{hpg} , of 160 and 220 °C, respectively) of the three working pairs are obtained when the DR s are close to 0.5. This indicates that two sub-streams which are comparable in flow are preferable. This would allow for simplifications in constructing pipelines and controlling valves in a real system. In the following calculations, the value of DR will be kept constant at 0.5.

Fig. 7.12 also indicates that a higher temperature of the heat source, T_{hpg} , contributes to a better performance for the studied conditions. Similar trends can be observed for the other cases in Figs. 7.13 (a) and 7.13 (b) for which the cooling temperature, T_{eva} , is at a relatively low level or the heat sink temperatures, T_{con} and T_{abs} , are at a relatively high level. However, when T_{eva} is higher and T_{con} or T_{abs} is lower, an increase of T_{hpg} can lead to constant trends of the COP . This is, for instance, the case in Fig. 7.13 (a), when T_{eva} is 10 °C for the working pair $\text{NH}_3/[\text{bmim}][\text{BF}_4]$. A decreasing trend can also be observed in Fig. 7.13 (b), when T_{eva} is 0 °C, for the same working pair. Figs. 7.13 (a) and 7.13 (b) indicate that lower temperatures of the cooling demand lead to an inferior performance for all working pairs. Moreover, for the same operating condition, $\text{NH}_3/[\text{bmim}][\text{BF}_4]$ performs better than the other two working pairs.

The influence of the temperature of the seawater on the performance can be understood by comparing Figs. 7.13 (a) and 7.13 (b). Fig. 7.13 (a) applies for cases in which the seawater temperature is 32 °C, corresponding to an application in tropical areas. In this case, the temperature of the side of the working

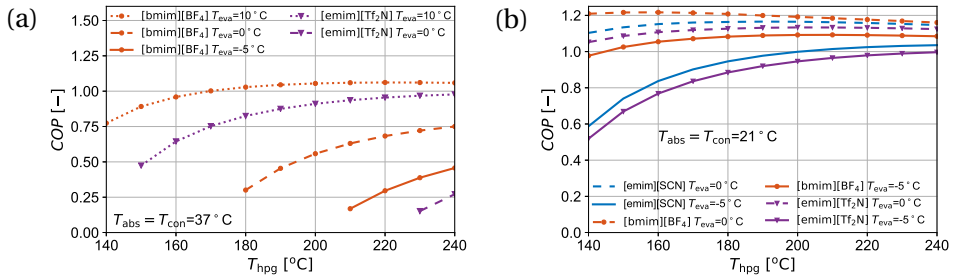


Figure 7.13: Influence of cooling temperature, T_{eva} , on the coefficient of performance of the DE-VAR cycle with working pairs $\text{NH}_3/[\text{emim}][\text{SCN}]$ (smooth curves), $\text{NH}_3/[\text{bmim}][\text{BF}_4]$ (●) and $\text{NH}_3/[\text{emim}][\text{Tf}_2\text{N}]$ (▼) for applications in: (a) tropical areas ($T_{\text{con}} = T_{\text{abs}} = 37^\circ\text{C}$) and (b) high-latitude areas ($T_{\text{con}} = T_{\text{abs}} = 21^\circ\text{C}$).

pair is 5 K higher than the cooling medium, the seawater ($T_{\text{abs}} = T_{\text{con}} = 37^\circ\text{C}$). Fig. 7.13 (b) corresponds to an application in high-latitude areas, for instance, the North Sea adjoining the Netherlands, where the seawater temperature is on average 16°C ($T_{\text{con}} = T_{\text{abs}} = 21^\circ\text{C}$). The comparison of Figs. 7.13 (a) and 7.13 (b) shows that both working pairs have higher performances at lower T_{abs} and T_{con} . For the application in tropical areas, the DE-VAR cycle with working pairs $\text{NH}_3/[\text{emim}][\text{SCN}]$ and $\text{NH}_3/[\text{emim}][\text{Tf}_2\text{N}]$ cannot operate at a cooling temperature of -5°C . $\text{NH}_3/[\text{bmim}][\text{BF}_4]$ does not show very promising performance, either. Hence, the following analysis is focused on high-latitude areas.

The DE-VAR cycle with NH_3/IL working pairs shows similar performances, in respect to the operating pairs conditions, as the cycle with the traditional $\text{H}_2\text{O}/\text{LiBr}$ working pair [339] or other investigated working pairs, such as $\text{NH}_3/\text{LiNO}_3$ [340].

INFLUENCE OF VARYING VAPOR-LIQUID EQUILIBRIA ON THE CYCLE PERFORMANCE

To investigate the influence of excluding the simulated VLE data, the DE-VAR cycle with $\text{NH}_3/[\text{bmim}][\text{BF}_4]$ in the condition of $T_{\text{hpg}}/T_{\text{abs}}/T_{\text{con}}/T_{\text{eva}} = 240/37/37/-5^\circ\text{C}$ is studied. Relevant parameters which can help to indicate the influences of different VLE sources on the cycle performance are listed in Table 7.5. NH_3 mass fractions of state point 5 (solution outlet of the ABS), 11b (solution outlet of the LG) and 9 (solution outlet of the HG) are determined by temperatures and pressures at saturated conditions. NH_3 fractions estimated based on solely extrapolating experimental VLE data are lower than those based on VLE data including simulation data. Exclusively for state point 5, the differences are negligible. From state point 5 to 11b and to 9, temperatures and pressures increase. The deviation of saturated NH_3 fractions from the one obtained including simulation data show an increasing trend.

The two streams with a NH_3 mass fractions of w_9 and w_{11b} are mixed before

Table 7.5: Comparison of the effect of different VLE properties sources for $\text{NH}_3/[\text{bmim}][\text{BF}_4]$ on the DE-VAR cycle performance at the condition of $T_{\text{hpg}}/T_{\text{abs}}/T_{\text{con}}/T_{\text{eva}} = 240/37/37/-5^\circ\text{C}$ ($DR = 0.5$).

Relevant parameters	EXP [136] VLE (Fig. 7.11 (c))	EXP [136] + SIM VLE (Fig. 7.11 (d))
w_5 [-]	0.0387	0.0383
w_{11b} [-]	0.0245	0.0290
w_9 [-]	0.0064	0.0285
w_{13} [-]	0.0156	0.0287
f [-]	42.49	101.72
specific \dot{Q}_{eva} [kJ/kg]	1158.32	1158.32
specific \dot{Q}_{hpg} [kJ/kg]	1204.01	1638.62
specific \dot{W}_p [kJ/kg]	321.80	772.49
COP [-]	0.759	0.480

state point 13. Consequently, state point 13 shows a lower value of NH_3 fraction when calculated without using the simulated VLE data. Due to the underestimation of the change in NH_3 fraction between state points 5 and 13, the circulation ratio, f , which is based on w_{13} and w_5 (Eq. 7.13), is lower than the one obtained using the simulated VLE. This results in a lower pump flow.

In terms of cycle performance, specific heat duties and pump power are listed in Table 7.5, as well. They are the corresponding heat and power loads for 1 kg/s refrigerant flow. The estimated demands of heat and pump power by using exclusively experimental VLE data are underestimated compared with the ones using simulation data. This is consistent with the underestimation of the circulation ratio. As a result, the COP is significantly overestimated.

COMPARISON WITH THE GENERATOR-ABSORBER HEAT EXCHANGE CYCLE

Fig. 7.14 shows how the COP of a GAX cycle changes with the temperature of the heat source, T_{gen} , at the condition of $T_{\text{abs}}/T_{\text{con}}/T_{\text{eva}} = 21/21/-5^\circ\text{C}$. Due to missing thermophysical properties of the $\text{NH}_3/\text{H}_2\text{O}$ mixture [335], the calculated performance of the GAX cycle can only be obtained for T_{gen} below 170°C . It can be seen in Fig. 7.14 that for T_{gen} below 116°C , there is no possibility for heat coupling. Thus, the GAX cycle performs as a single-stage cycle, showing a decreasing trend with rising T_{gen} . Above 116°C , the solid curve indicates the performance of the ideal GAX cycle, which is increasing as T_{gen} rises. The GAX cycle is entitled “ideal” because the calculation of it is based on the perfect heat coupling between ABS and GEN. Hence, the solid curve shows the upper limit of the GAX cycle. The dotted curve represents the results of the single-stage (or SE) $\text{NH}_3/\text{H}_2\text{O}$ VAR cycle, which provides the lower limit of the GAX cycle if the heat is not perfectly coupled. A practical system is supposed to perform between these two limits. The dashed curve represents the average of these two limits, which is

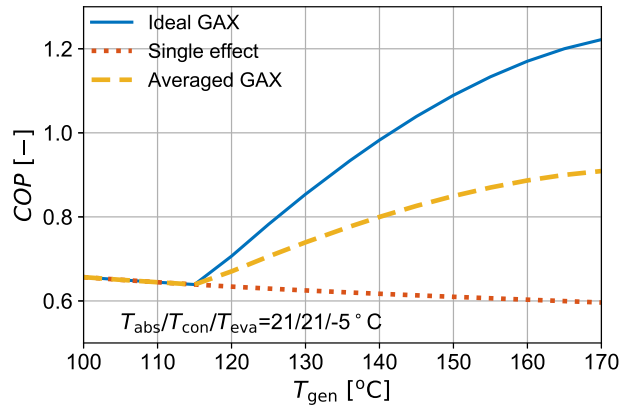


Figure 7.14: Comparison of the performance between the ideal $\text{NH}_3/\text{H}_2\text{O}$ GAX cycle and the single-stage $\text{NH}_3/\text{H}_2\text{O}$ cycle at various T_{gen} ($T_{abs}/T_{con}/T_{eva} = 21/21/-5^\circ\text{C}$). The solid curve indicates the “ideal” GAX performance and the dotted curve indicates the “degraded” GAX, i.e., the SE cycle. The dashed curve denotes the estimated performance of a real system.

an estimation of the actual performance.

Fig. 7.15 shows a comparison of the performance of the $\text{NH}_3/\text{H}_2\text{O}$ GAX cycle and the DE-VAR cycle with $\text{NH}_3/[\text{bmim}][\text{BF}_4]$ and $\text{NH}_3/[\text{emim}][\text{SCN}]$ at the condition of $T_{abs} = T_{con} = 21^\circ\text{C}$, suggesting an application at high-latitude areas. T_{eva} is set to -5 and 0°C . The temperature of the driving heat is varied to investigate its influence. Note that the performance of the GAX cycle is represented by the average value between the ideal GAX and the normal SE-VAR cycle performance. The performance of the GAX cycle for T_{gen} above 170° is based on extrapolation. As shown in Fig. 7.15, the GAX cycle is able to reach a high performance even when the driving temperature is relatively low. With increasing T_{gen} , the performance of this cycle is increasing less rapidly. The DE-VAR cycle with $\text{NH}_3/[\text{emim}][\text{SCN}]$ shows a poor performance around 150°C for a -5°C cooling application. After a sharp initial increase, COP values of the DE-VAR cycle increase only slightly when T_{hpg} is above 180°C . The COP value of the proposed cycle with $\text{NH}_3/[\text{bmim}][\text{BF}_4]$ is approximately 10% higher than that of the averaged GAX cycle when they are driven by heat at 200°C . In the higher temperature range, these two cycles show a similar performance. Advantages of the proposed DE-VAR cycle applying ILs are that there is no special need for a control strategy of the internal heat coupling, and the utilization of the ILs prevents the need for rectification of the refrigerant flow.

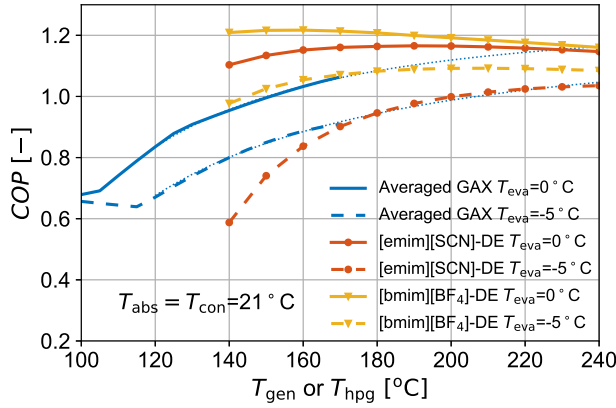


Figure 7.15: Comparison of the performance of the DE-VAR cycle with working pairs $\text{NH}_3/[\text{bmim}][\text{BF}_4]$, $\text{NH}_3/[\text{emim}][\text{SCN}]$ and the $\text{NH}_3/\text{H}_2\text{O}$ GAX cycle at condition $T_{\text{abs}} = T_{\text{con}} = 21^\circ\text{C}$. Smooth curves indicate the performance of the GAX cycle and the dotted curves are extrapolations of their trend lines. The solid curves denote the performance of cooling at $T_{\text{eva}} = 0^\circ\text{C}$ and the dashed curves denote the performance of cooling at $T_{\text{eva}} = -5^\circ\text{C}$.

7.5.4. INTEGRATION OF THE DOUBLE-EFFECT VAPOR ABSORPTION CYCLE WITH EXHAUST GAS

Direct heat exchange is assumed between the exhaust gas and the strong NH_3/IL solution. DE-VAR cycles are designed for high temperature applications and a direct coupling can take full advantage of the high temperature exhaust gas. Thus, the waste heat recovery (WHR) exchanger, i.e., the flue gas cooler, also plays the role of high pressure generator.

RECOVERABLE HEAT AND CORRESPONDING COOLING CAPACITIES

For the exhaust gas stream associated with the WHR heat exchanger applied in typical modes, the inlet temperature, $T_{\text{ex}}^{\text{in}}$, and the flow rate, \dot{m}_{ex} , are listed in Table 7.3. The outlet temperature, $T_{\text{ex}}^{\text{out}}$, cannot be cooled down below 167°C to prevent sulfur corrosion [323]. With these constraints, the driving heat of the DE-VAR cycle is the recovered heat from the exhaust gas, \dot{Q}_{whr} , which is expressed as,

$$\dot{Q}_{\text{whr}} = c_p^{\text{ex}} \dot{m}_{\text{ex}} (T_{\text{ex}}^{\text{in}} - T_{\text{ex}}^{\text{out}}) \quad (7.15)$$

where the specific heat of the exhaust gas, c_p^{ex} , is taken as $1.08 \text{ kJ}/(\text{kg} \cdot \text{K})$ [341].

In the design phase, a pinch temperature of 10 K is assumed in this HX. T_8 cannot be below 157°C to prevent corrosion problems. The value of T_8 is also influenced by the operation of the cycle. Hence, the pumped flow, which is easy to adjust by changing the pump settings, is studied to explore its influence on the cooling capacity and on the performance of the heat recycling.

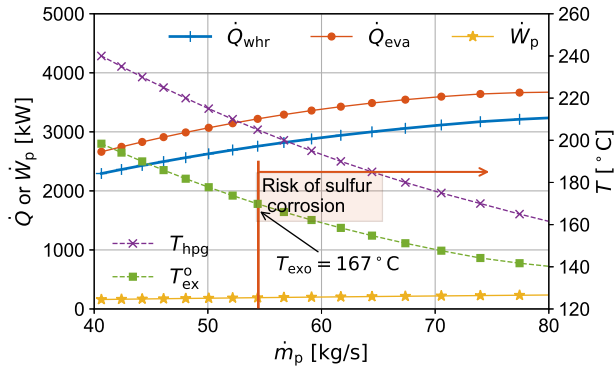


Figure 7.16: Influence of the designed pump flow, \dot{m}_p , on operating parameters of the exhaust gas driven DE-VAR cycle with $\text{NH}_3/[\text{bmim}][\text{BF}_4]$. The case is based on a 90% diesel engine load, in high-latitude areas for a -5°C cooling temperature. Note that for pump flows above 54.4 kg/s, the exhaust gas might condensate and cause sulfur corrosion.

Fig. 7.16 depicts a case in which the inlet exhaust gas stream is at 340°C and 15 kg/s (which corresponds to the majority of operating cases: mode 1 and 2 in Table 7.3), in high-latitude areas ($T_{\text{abs}} = T_{\text{con}} = 21^\circ\text{C}$) with $T_{\text{eva}} = -5^\circ\text{C}$ cooling application. In the proposed DE-VAR cycle, a higher driving temperature leads to a higher T_{g} (cf. Fig. 7.4). To maintain a constant temperature difference for the heat transfer between the exhaust gas and the solution, a higher $T_{\text{ex}}^{\text{out}}$ is required. Accordingly, the exhaust gas has a smaller temperature range over which it can be cooled and a smaller waste heat can be recovered. While a higher driving temperature also results in a higher COP . These dependencies influence the cooling capacity \dot{Q}_{eva} (round symbols), and lead to an initial increase, and then to a constant value as a function of pump flow.

However, for the studied case, when the pump flow of the solution, \dot{m}_p , is higher than 54.4 kg/s, the exhaust gas cannot be cooled below 167°C as shown in Fig. 7.16. Even though cooling and performances of heat recovery would be better in this range, the DE-VAR cycle cannot be operated due to the risk of sulfur corrosion. Therefore, the optimum performance is achieved at a pump flow of 54.4 kg/s. The corresponding cooling capacity is 3220 kW.

Table 7.6 summarizes operating parameters and optimum cooling performance when using the DE-VAR cycle with the studied working pairs for different engine loads. The cooling capacity of the exhaust gas-driven DE-VAR cycle with $\text{NH}_3/[\text{bmim}][\text{BF}_4]$ is always larger than 1518 kW in the high-latitude environment. This is the largest cooling capacity among the three studied working pairs. For an engine load of 90%, the cooling capacity with $\text{NH}_3/[\text{bmim}][\text{BF}_4]$ is 3220 kW. For most of the operating conditions, this working pair has the potential to

Table 7.6: The optimum cooling performance (\dot{Q}_{eva}), corresponding recovered waste heat (\dot{Q}_{whr}), DE-VAR cycle performance (f and COP , \dot{m}_p , and \dot{W}_p), and operating conditions ($T_{\text{ex}}^{\text{in}}$, $T_{\text{ex}}^{\text{out}}$, T_8 , and T_{hpg}) for different diesel engine loads with $\text{NH}_3/[\text{emim}][\text{SCN}]$, $\text{NH}_3/[\text{bmim}][\text{BF}_4]$, and $\text{NH}_3/[\text{emim}][\text{Tf}_2\text{N}]$ in high latitude areas.

Engine load	$\text{NH}_3/[\text{emim}][\text{SCN}]$			$\text{NH}_3/[\text{bmim}][\text{BF}_4]$			$\text{NH}_3/[\text{emim}][\text{Tf}_2\text{N}]$		
	90%	70%	40%	90%	70%	40%	90%	70%	40%
$T_{\text{ex}}^{\text{in}} [^\circ\text{C}]$	340	326.5	307.4	340	326.5	307.4	340	326.5	307.4
$T_{\text{ex}}^{\text{out}} [^\circ\text{C}]$	170.4	170.4	170.4	169.8	169.8	169.8	179.6	179.6	179.6
$T_8 [^\circ\text{C}]$	160.4	160.4	160.4	159.8	159.8	159.8	169.6	169.6	169.6
$T_{\text{hpg}} [^\circ\text{C}]$	190	190	190	205	205	205	200	200	200
$f [-]$	28.7	28.7	28.7	20.4	20.4	20.4	22.8	22.8	22.8
$COP [-]$	0.977	0.977	0.977	1.092	1.092	1.092	0.946	0.946	0.946
$\dot{m}_p [\text{kg/s}]$	69.8	51.4	32.9	54.4	40.1	25.6	94.5	69.2	43.9
$\dot{W}_p [\text{kW}]$	257	189	121	191	141	90	257	188	120
$\dot{Q}_{\text{whr}} [\text{kW}]$	2748	2023	1295	2756	2030	1300	2599	1904	1208
$\dot{Q}_{\text{eva}} [\text{kW}]$	2936	2162	1383	3220	2372	1518	2701	1979	1255

substitute at least one of the RSW plants in the studied fishing vessel (Table 7.2). The solution pump flow, \dot{m}_p , of $\text{NH}_3/[\text{bmim}][\text{BF}_4]$ is lower than the ones of the other two pairs.

SPECIFICATION OF STATE POINTS

The details of the state points for the studied case (conditions $T_{\text{hpg}}/T_{\text{abs}}/T_{\text{con}}/T_{\text{eva}} = 205/21/21/-5$ °C) for $\text{NH}_3/[\text{bmim}][\text{BF}_4]$ in the DE-VAR cycle, are listed in Table 7.7. Due to the pressure drop in the valve and heating in the SHXs, NH_3 vapor may be generated in state points 7c and 8 [170]. However, only small amounts of NH_3 vapor are created before entering the generators. As shown in Table 7.7, the results of NH_3 fractions and specific enthalpies of these two state points are close to the bulk streams (saturated solution with NH_3 vapor). Specific enthalpies of the bulk stream are obtained via,

$$h^{\text{sol}}(T, P, w_{\text{NH}_3}) = (1 - q) h_{\text{sat}}^{\text{sol}} + q h^{\text{V}} \quad (7.16)$$

where, $h_{\text{sat}}^{\text{sol}}$ and h^{V} are the specific enthalpies for the saturated solution part and the vapor part, respectively. q is the quality, which is identified as,

$$q = \frac{w - w_{\text{sat}}}{1 - w_{\text{sat}}} \quad (7.17)$$

Qualities and saturated NH_3 fractions of these two state points are additionally listed in the footnote of Table 7.7.

Table 7.7: State points of the DE-VAR cycle (conditions $T_{\text{hpg}}/T_{\text{abs}}/T_{\text{con}}/T_{\text{eva}} = 205/21/21/-5$ °C) run with $\text{NH}_3/[\text{bmim}][\text{BF}_4]$ ($DR = 0.5$, $\dot{m}_p = 54.4$ [kg/s]).

State point	\dot{m} [kg/s]	T [°C]	P [bar]	w_{NH_3} [-]	h^* [kJ/kg]
1	2.67	10.6	8.85	1	146.90
2	2.67	-5.0	3.55	1	146.90
3	2.67	-5.0	3.55	1	1353.86
4	2.67	14.5	3.55	1	1402.69
5	54.40	21.0	3.55	0.0766	79.38
6	54.40	21.0	39.53	0.0766	82.37
7	54.40	57.2	39.53	0.0766	148.41
7a	27.20	57.2	39.53	0.0766	148.41
7b	27.20	57.2	39.53	0.0766	148.41
7c **	27.20	57.2	8.85	0.0766	148.41
8 **	27.20	159.8	39.53	0.0766	393.02
9	25.57	205.0	39.53	0.0179	411.84
10	25.57	67.2	39.53	0.0179	151.64
11	51.73	70.1	8.85	0.0290	160.09
11a	25.57	67.2	8.85	0.0179	151.64
11b	26.16	72.9	8.85	0.0399	168.34
12	51.73	31.0	8.85	0.0290	90.64
13	51.73	31.0	3.55	0.0290	90.64
14	1.63	205.0	39.53	1	1791.27
15	1.63	77.9	39.53	1	485.50
16	1.63	21.0	8.85	1	485.50
17	1.04	72.9	8.85	1	1517.54
18	2.67	21.0	8.85	1	195.73

* Specific enthalpies are calculated based on an arbitrarily chosen reference state of $T = -23$ °C and $P = 10$ bar.

** At state points 7c and 8, the NH_3 may boil off from the solution. Saturated fractions and qualities of state points 7c and 8 are: $w_{\text{sat}}^{7c} = 0.0672$, $q_{7c} = 0.01$. $w_{\text{sat}}^8 = 0.0384$, $q_8 = 0.04$.

7.5.5. CONSIDERATIONS OF FEASIBILITY

The above studied IL-based working pairs show a promising technical performance for the DE-VAR cycle at high-temperature applications. Before implementing the cycle, thermal stabilities of the investigated ILs and the potential economic benefits must be considered.

THERMAL STABILITY

It has been reported that imidazolium ILs have high thermal stabilities [342]. The short and long-term thermal stabilities of [emim][SCN] have been studied by Navarro *et al.* [311]. Liu *et al.* [343] investigated short and long-term thermal stability of [bmim][BF₄]. Feng *et al.* [344] also carried out thermal analysis of [bmim][BF₄]. Heym *et al.* [345] measured the thermal decomposition of [emim][Tf₂N]. The work of Villanueva *et al.* [346] included the long-term stabilities of [emim][Tf₂N]. The key findings of these studies are summarized in Table 7.8. It can be seen that the thermal stabilities of [bmim][BF₄] and [emim][Tf₂N] are better than that of [emim][SCN] regarding both short and long-term stability. The two ILs have also been classified into the group of “most stable” ILs by Cao and Mu [342]. The conducted long-term tests have shown the applicability of [bmim][BF₄] below 250 °C. [emim][SCN] has shown obvious mass loss above 160 °C and for this reason it cannot be applied in DE-VAR cycles.

ECONOMIC AND ENVIRONMENTAL BENEFITS

It can be concluded that the proposed DE-VAR cycle with NH₃/[bmim][BF₄] is promising for the application in high-latitude areas. An accurate estimation of the initial cost and the system size relies on a thorough understanding of the heat and mass transfer of the newly-proposed working pairs and further investigation is required. Nevertheless, the operational costs can be estimated based on the analysis in this study. Table 7.9 shows two options of replacing RSW plants with the proposed exhaust gas driven DE-VAR cycle. The first option is to replace only one RSW plant. The exhaust gas for all 5 operating modes of the engine (Mode 1-5 shown in Table 7.3) is able to drive the proposed DE-VAR cycle to produce the equivalent cooling capacity of one RSW. For this operating time (7320 hour per year), a saved primary energy can be obtained via the difference in power consumption of the proposed system and the existing compression one, which is 4.77 TJ/year. If the CO₂ emission of diesel oil is taken as 778 g/kWh_e [347], the CO₂ emission during fishing can be reduced by 1031 tons/year. Option 2 concerns replacing two RSW plants with one DE-VAR cycle. In this option, the DE-VAR cycle is able to provide an equivalent cooling capacity of two RSW plants only when the engine operates at a load of 90%. For an operating time of 5800 hours/year, the saved energy is 7.33 TJ/year and the corresponding reduced CO₂ emission is 1633.5 tons/year.

Table 7.8: Summary of thermal stabilities of the studied ILS [311, 343–346].

	[emim][SCN] [311]	[bmim][BF ₄]	[emim][Tf ₂ N]
T_{onset}^*	525.5 (5 K/min) 538.6 (10 K/min) 553.7 (20 K/min)	630 K (10 K/min) [343]	692 K (10 K/min) [345]
long-term stability	≥ 433.2 K for 48 hours: obvious mass loss	513 K for 5 hours: No obvious mass loss [343].	533 K for 5 hours: mass losses rates ≥ 2% [346].
	≤ 393.2 K for 48 hours: no obvious mass loss	Mass losses rates 1.30% and 2.60% for 453 K and 573 K, for 10 hours. No change in Fourier Transform Infrared Spectroscopy analysis [344].	

* T_{onset} is an extrapolated and reproducible temperature that denotes a point at which the weight loss begins. A graphic explanation can be found from literature, for instance, Navarro *et al.* [311].

Table 7.9: Economic and environmental benefits of replacing refrigeration seawater plants with the proposed system applied in high-latitude areas.

	in substitute of	operating hours [hrs/year]	saved energy [TJ/year]	reduced CO ₂ [tons/year]
Option 1	RSW-1	7320	4.77	1030.8
Option 2	RSW-2	5800	7.56	1633.5

7.6. CONCLUSIONS

A waste heat recovery cooling system is proposed which uses ammonia/ionic liquid mixtures as working pairs in a double-effect vapor absorption refrigeration (DE-VAR) cycle. A multi-scale analysis is carried out to study its performance in a fishing vessel. The analysis includes Monte Carlo simulation to predict vapor-liquid equilibria at high temperatures and pressures, thermodynamic modeling for cooling cycle analysis, and system evaluation when integrated with engine exhaust gas. Based on the work, the following conclusions can be drawn:

- Monte Carlo simulations are capable to extend the vapor-liquid equilibrium data of the working pairs. The inclusion of the computed solubilities improves the quality of the extension with the NRTL model to high temperature and pressure conditions in comparison to solely using experimental data obtained at low temperatures and pressures.
- The ranking of the coefficient of performance (*COP*) for the three studied ILs within NH₃-based DE-VAR cycle is: [bmim][BF₄] > [emim][SCN] > [emim][Tf₂N]. The best candidate achieves a *COP* above 1.1 for -5 °C cooling in a fishing vessel operating in high-latitude areas.
- The DE-VAR cycle shows an approximately 10% higher performance than the GAX cycle with NH₃/H₂O for applications with high temperature driving heat.
- Because of stability problems at high temperatures, [emim][SCN] is not suitable for high-temperature applications of a double-effect vapor absorption refrigeration cycle.
- The proposed system with NH₃/[bmim][BF₄] can provide the cooling capacity of one refrigeration seawater (RSW) plant for all operating modes of the diesel engine, when driven by its exhaust gas (*COP* of 1.1, cooling capacity of 1518 kW). Thereby, 4.8 TJ of energy can be saved and 1030 tons of CO₂ emission can be avoided annually per fishing vessel. Alternatively, the proposed system can provide the cooling capacity of two RSW plants

for most of the operating modes (cooling capacity of 3200 kW). Annually saved energy and reduced CO₂ emissions are 7.6 TJ and 1635 tons, respectively.

CONCLUSIONS

The opportunities for molecular simulation in the context of tunable materials are numerous. Molecular simulation can be used to improve the understanding of how materials function and additionally predict material properties that are relevant to assess the performance for applications. However, many challenges do exist. Better and transferable force fields are needed to enable the accurate screening of a multitude of materials. Besides, simulation methodologies need to be optimized for speed to allow the screening within a reasonable amount of time.

Concerning Metal-Organic Frameworks, the presented work shows that polarizable force fields are indeed promising. This is especially true for Metal-Organic Frameworks with open metal sites like M-MOF-74. It has been shown that the assumptions first made by Lachet *et al.* [185] to describe xylenes in NaY zeolite can be used for rigid Metal-Organic Frameworks. These assumptions significantly speed up the induced dipole method for Monte Carlo simulations and lead to simulation times that are comparable to non-polarizable force fields. Despite the assumptions, the polarizable force field is able to model differences in adsorption in M-MOF-74 depending on the choice of metal ion. The computational speed and the improved accuracy make this type of force field particularly interesting for the screening of large sets of Metal-Organic Frameworks in Monte Carlo simulations. This is a reassuring result, since non-polarizable generic force fields frequently fail to describe the adsorption in Metal-Organic Frameworks. Many existing generic force fields used for Metal-Organic Frameworks are rather old and there is an urgent need for improvement. Metal-Organic Frameworks offer opportunities for a variety of applications and the selection of the best one for a particular application is highly relevant for research and industry. Polarizable force fields for which consistent parameters are derived from quantum mechanics may offer further improvement for the description of Metal-Organic Frameworks in respect to accuracy and transferability. A next step in further developing the presented procedure to account for polarization could be to extend it for flexible Metal-Organic Frameworks. Only if the procedure can be applied to rigid and flexible frameworks, is it applicable for comprehensive screening studies which explore the complete space of Metal-Organic Frameworks. These screening studies would allow for an efficient selection process of Metal-Organic Frameworks for specific applications and thereby enable the exploitation of the

potential of Metal-Organic Frameworks to improve processes and save energy.

For ionic liquids, simulation methods exist which apply molecular simulation to predict thermodynamic properties that are relevant to calculate the performance of industrial process, e.g., absorption refrigeration cycles. The case study which was conducted as part of this thesis showed that properties of ionic liquids predicted by molecular simulation may show large uncertainties. This again has a significant impact on the accuracy of the performance prediction of the absorption refrigeration cycle. The results also reveal that standard methods, e.g., equation of states or activity coefficient models, which are often used to correlate experimental data may fail outside of the experimental range and are therefore afflicted with large uncertainties, as well. Similar to Metal-Organic Frameworks, the work conducted in this thesis depicts that current force fields are not suitable to model all ionic liquids satisfactory. Especially, for mixtures of ionic liquids with other components better force fields are required to allow for meaningful predictions. Efficient force field fitting can help to extend the range of experimental data for individual ionic liquids. As shown in this thesis, the use of molecular simulation to extend the experimental data range seems to be more reliable than other methods. This finding was confirmed by investigating three ionic liquid based mixtures as working pairs in double-effect vapor absorption cycles for the application in fishing vessels. A very relevant example, because it requires solubility data at higher temperatures than are experimentally available. To improve the accuracy of molecular simulation of ionic liquids, more effort has to be done. Besides the insufficient accuracy, simulations are computationally too expensive. Only if the accuracy increases and the computational time decreases can molecular simulation be readily applied to ionic liquids and its mixtures with other components.

SUMMARY

Undoubtedly, materials that can be tuned on a molecular level offer tremendous opportunities. However, to understand and customize such materials is challenging. In this context, molecular simulation can be helpful. The work presented in this thesis deals with two types of materials, Metal-Organic Frameworks and Ionic Liquids, and the study with molecular simulation to determine their potential for specific gas separations. For the prediction of their behavior and relevant materials properties with molecular simulation, force fields of sufficient quality are required.

The work in this thesis concerning Metal-Organic Frameworks focuses on force fields for frameworks that include open metal sites. Generic force fields, e.g., UFF and DREIDING, fail to describe this class of Metal-Organic Frameworks. Here, we investigate the potential of polarizable force fields for an improved description of such systems. Polarizable force fields are introduced and their usage for the description of Metal-Organic Frameworks with open metal sites is investigated. The potential of polarizable force fields is confirmed. This is done by applying the induced dipole method for the adsorption of CO_2 and CH_4 in M-MOF-74 ($M = \text{Co, Cr, Cu, Fe, Mg, Mn, Ni, Ti, V, Zn}$). By varying the type of metal ion (M), different degrees of adsorption strength can be achieved. In contrast to generic force fields that do not explicitly consider polarization, it is shown that polarizable force fields are able to capture the difference in adsorption in M-MOF-74 depending on the metal ion. The required force field parameters are fitted to reproduce experimental adsorption data for CO_2 in Mg-MOF-74. Identical scaling parameters are used for the other metal ions without further adjustment. Subsequently, force field parameters for CO_2 in M-MOF-74 ($M = \text{Co, Fe, Mg, Mn, Ni, Zn}$) are derived from energies determined via DFT calculations. A grid search in which DFT energies on paths towards interaction sites of the framework are compared to energies from molecular simulation is conducted. To reproduce the DFT energies, exclusively the Lennard-Jones force field parameters of metal sites of M-MOF-74 are customized. For other interaction sites, Lennard-Jones force field parameters of the UFF force field are used. Atomic polarizabilities are taken from literature. The developed force field describes the adsorption behavior significantly better than standard non-polarizable force fields. Finally, the potential of polarizable force field for Metal-Organic Frameworks with open metal sites is verified for small hydrocarbons. For this purpose simulations with and without

polarizable force field are conducted for ethane, ethylene, propane, and propylene in M-MOF-74 (M = Co, Fe, Mn, Ni). The force field parameters are taken from literature without adjustment. Overall, the polarizable force field performs better than standard non-polarizable force fields. Especially, the description of energies and binding geometries at low uptakes of guest molecules is improved.

For ionic liquids, the usability of molecular simulation to predict material properties for adsorption refrigeration cycles is investigated. The methodology to compute heat capacity, heat of absorption, and solubility of gas molecules in liquids is presented. Subsequently, these properties are calculated for [emim][Tf₂N]/NH₃ and [emim][SCN]/NH₃ mixtures and used for the performance prediction of an adsorption refrigeration cycle. It is observed that the accuracy of molecular simulation for the investigated mixtures is not sufficient to make reasonable performance predictions and that better force fields are necessary. Due to these findings, the force field mixing rules between the ionic liquids [emim][Tf₂N], [emim][SCN], [bmim][BF₄] and NH₃ are adjusted to reproduce available experimental data. Afterwards, the customized force field is applied to predict the solubility of NH₃ for temperatures higher than the experimental range. The solubility of NH₃ at high temperatures is necessary to evaluate the performance of double-effect vapor absorption refrigeration cycles.

SAMENVATTING

Materialen die op moleculaire schaal kunnen worden afgestemd op hun toepassing bieden mogelijkheden om producten en processen te verbeteren. Het is een uitdaging om de eigenschappen van dergelijke materialen te begrijpen en aan te passen. In dat geval kunnen moleculaire simulaties nuttig zijn. Het onderzoek in dit proefschrift behandelt twee soorten materialen: Metal-Organic Frameworks en Ionic Liquids. In dit proefschrift worden moleculaire simulaties gebruikt om hun toepasbaarheid voor gasscheidingen te bepalen. Voor de voorspelling van hun gedrag en materiaaleigenschappen met behulp van moleculaire simulatie zijn betrouwbare krachtvelden nodig.

Het werk in dit proefschrift richt zich op krachtvelden voor Metal-Organic Frameworks met open metal sites. Generieke krachtvelden, zoals UFF en DREIDING, beschrijven de interacties van geadsorbeerde moleculen met Metal-Organic Frameworks onvoldoende. In dit proefschrift onderzoeken we het gebruik van polariseerbare krachtvelden voor een betere beschrijving van dergelijke systemen. In het bijzonder worden polariseerbare krachtvelden gebruikt voor de beschrijving van Metal-Organic Frameworks met open metal sites. De potentie van deze polariseerbare krachtvelden wordt aangetoond. Dit wordt gedaan door gebruik te maken van de zogenaamde induced dipole method voor de adsorptie van CO₂ en CH₄ in M-MOF-74 (M = Co, Cr, Cu, Fe, Mg, Mn, Ni, Ti, V, Zn). Door het type metaalion (M) te veranderen kunnen verschillende adsorptiesterken worden bereikt. In tegenstelling tot generieke krachtvelden die niet expliciet rekening houden met polarisatie, zijn polariseerbare krachtvelden in staat om het verschil in adsorptie in M-MOF-74 te beschrijven afhankelijk van het metaalion. De krachtveldparameters zijn aangepast zodanig dat experimentele adsorptiegegevens voor CO₂ in Mg-MOF-74 worden gereproduceerd. Dezelfde parameters worden gebruikt voor de andere metaalionen. Vervolgens worden krachtveldparameters voor CO₂ in M-MOF-74 (M = Co, Fe, Mg, Mn, Ni, Zn) bepaald via energieën uit DFT-berekeningen. Een grid search wordt uitgevoerd waarbij DFT-energieën op paden naar interactiesites van het framework worden vergeleken met energieën uit moleculaire simulaties. Om de DFT-energieën te reproduceren zijn alleen de Lennard-Jonesparameters van de metal sites in M-MOF-74 aangepast. Voor de andere interacties worden de Lennard-Jones parameters van het UFF-krachtveld gebruikt. De atomaire polariseerbaarheden zijn afkomstig uit bestaande literatuur. Het hier ontwikkelde krachtveld beschrijft het adsorptie-

gedrag aanzienlijk beter dan de standaard niet-polariseerbare krachtvelden. Als laatste wordt de toepasbaarheid van een polariseerbaar krachtveld voor Metal-Organic Frameworks met open metal sites bestudeerd voor kleine koolwaterstoffen. Hiervoor worden simulaties mét en zonder polariseerbaar krachtveld uitgevoerd voor ethaan, ethyleen, propaan en propyleen in M-MOF-74 (M = Co, Fe, Mn, Ni). De krachtveldparameters worden zonder aanpassingen uit literatuur gehaald. In het algemeen behaalt het polariseerbare krachtveld betere resultaten dan de standaard niet-polariseerbare krachtvelden. Vooral de waarden van energieën en bindingsgeometrieën bij lage belading van gastmoleculen zijn beter.

Voor Ionic Liquids wordt het gebruik van moleculaire simulatie onderzocht om materiaaleigenschappen voor absorptiekoelcycli te voorspellen. De methode om de warmtecapaciteit, absorptiewarmte en de oplosbaarheid van gasmoleculen in vloeistoffen te berekenen wordt geïntroduceerd. Daarna worden deze eigenschappen berekend voor mengsels van [emim][Tf₂N]/NH₃ en [emim][SCN]/NH₃ en gebruikt voor de voorspelling van de prestatie van absorptiekoelcycli. De precisie van moleculaire simulatie voor de onderzochte mengsels is niet voldoende om de prestaties nauwkeurig te bepalen: er zijn betere krachtvelden nodig. Daarom worden de regels voor het combineren van de krachtvelden van de Ionic Liquids [emim][Tf₂N], [emim][SCN], [bmim][BF₄] en NH₃ aangepast om de experimentele resultaten te reproduceren. Dit aangepaste krachtveld wordt gebruikt om de oplosbaarheid van NH₃ bij temperaturen hoger dan de experimentele temperaturen te voorspellen. De oplosbaarheid van NH₃ bij hoge temperaturen is nodig om de prestaties van koelcycli met double-effect dampabsorptie te bestuderen.

BIBLIOGRAPHY

BIBLIOGRAPHY

- [1] M. E. Davis, *Ordered porous materials for emerging applications*, *Nature* **417**, 813 (2002).
- [2] M. Armand, F. Endres, D. R. MacFarlane, H. Ohno, and B. Scrosati, *Ionic-liquid materials for the electrochemical challenges of the future*, in *Materials For Sustainable Energy: A Collection of Peer-Reviewed Research and Review Articles from Nature Publishing Group* (World Scientific, 2011) pp. 129–137.
- [3] C. Wang, D. Liu, and W. Lin, *Metal-organic frameworks as a tunable platform for designing functional molecular materials*, *Journal of the American Chemical Society* **135**, 13222–13234 (2013).
- [4] Q.-G. Zhai, X. Bu, C. Mao, X. Zhao, L. Daemen, Y. Cheng, A. J. Ramirez-Cuesta, and P. Feng, *An ultra-tunable platform for molecular engineering of high-performance crystalline porous materials*, *Nature Communications* **7**, 13645 (2016).
- [5] H. Weingärtner, *Understanding ionic liquids at the molecular level: Facts, problems, and controversies*, *Angewandte Chemie International Edition* **47**, 654–670 (2008).
- [6] N. V. Plechkova and K. R. Seddon, *Applications of ionic liquids in the chemical industry*, *Chemical Society Reviews* **37**, 123–150 (2008).
- [7] J. F. Brennecke and E. J. Maginn, *Ionic liquids: Innovative fluids for chemical processing*, *AIChE Journal* **47**, 2384–2389 (2001).
- [8] B. Li, H.-M. Wen, Y. Cui, W. Zhou, G. Qian, and B. Chen, *Emerging multifunctional metal-organic framework materials*, *Advanced Materials* **28**, 8819–8860 (2016).
- [9] D. S. Sholl and R. P. Lively, *Seven chemical separations to change the world*, *Nature* **532**, 435–437 (2016).
- [10] J. L. Humphrey, *Separation process technology* (McGraw-Hill, 1997).

- [11] O. R. N. Laboratory, *Materials for Separation Technologies. Energy and Emission Reduction Opportunities* (United States. Department of Energy. Office of Energy Efficiency and Renewable Energy, 2005).
- [12] S. T. Meek, J. A. Greathouse, and M. D. Allendorf, *Metal-organic frameworks: A rapidly growing class of versatile nanoporous materials*, *Advanced Materials* **23**, 249–267 (2011).
- [13] G. G. Eshetu, M. Armand, H. Ohno, B. Scrosati, and S. Passerini, *Ionic liquids as tailored media for the synthesis and processing of energy conversion materials*, *Energy & Environmental Science* **9**, 49–61 (2016).
- [14] S. Keskin, J. Liu, R. B. Rankin, J. K. Johnson, and D. S. Sholl, *Progress, opportunities, and challenges for applying atomically detailed modeling to molecular adsorption and transport in metal-organic framework materials*, *Industrial & Engineering Chemistry Research* **48**, 2355–2371 (2009).
- [15] D. Frenkel and B. Smit, *Understanding Molecular Simulation (Second Edition)* (Academic Press, San Diego, 2002).
- [16] Y. J. Colón, D. Fairen-Jimenez, C. E. Wilmer, and R. Q. Snurr, *High-throughput screening of porous crystalline materials for hydrogen storage capacity near room temperature*, *Journal of Physical Chemistry C* **118**, 5383–5389 (2014).
- [17] Y. J. Colón and R. Q. Snurr, *High-throughput computational screening of metal-organic frameworks*, *Chemical Society Reviews* **43**, 5735–5749 (2014).
- [18] J. R. Long and O. M. Yaghi, *The pervasive chemistry of metal-organic frameworks*, *Chemical Society Reviews* **38**, 1213–1214 (2009).
- [19] H. Fang, H. Demir, P. Kamakoti, and D. S. Sholl, *Recent developments in first-principles force fields for molecules in nanoporous materials*, *Journal of Materials Chemistry A* **2**, 274–291 (2014).
- [20] Z. R. Herm, J. A. Swisher, B. Smit, R. Krishna, and J. R. Long, *Metal-organic frameworks as adsorbents for hydrogen purification and precombustion carbon dioxide capture*, *Journal of the American Chemical Society* **133**, 5664–5667 (2011).
- [21] J. A. Mason, K. Sumida, Z. R. Herm, R. Krishna, and J. R. Long, *Evaluating metal-organic frameworks for post-combustion carbon dioxide capture via*

- temperature swing adsorption*, Energy & Environmental Science **4**, 3030–3040 (2011).
- [22] E. D. Bloch, L. J. Murray, W. L. Queen, S. Chavan, S. N. Maximoff, J. P. Bigi, R. Krishna, V. K. Peterson, F. Grandjean, G. J. Long, B. Smit, S. Bordiga, C. M. Brown, and J. R. Long, *Selective binding of O₂ over N₂ in a redox-active metal-organic framework with open iron(II) coordination sites*, Journal of the American Chemical Society **133**, 14814–14822 (2011).
- [23] S. Couck, J. F. M. Denayer, G. V. Baron, T. Rémy, J. Gascon, and F. Kapteijn, *An amine-functionalized MIL-53 metal-organic framework with large separation power for CO₂ and CH₄*, Journal of the American Chemical Society **131**, 6326–6327 (2009).
- [24] T. M. McDonald, J. A. Mason, X. Kong, E. D. Bloch, D. Gygi, A. Dani, V. Crocella, F. Giordanino, S. O. Odoh, W. S. Drisdell, B. Vlasisavljevič, A. L. Dzubak, R. Poloni, S. K. Schnell, N. Planas, K. Lee, T. Pascal, L. F. Wan, D. Prendergast, J. B. Neaton, B. Smit, J. B. Kortright, L. Gagliardi, S. Bordiga, J. A. Reimer, and J. R. Long, *Cooperative insertion of CO₂ in diamine-appended metal-organic frameworks*, Nature **519**, 303–308 (2015).
- [25] N. L. Rosi, J. Eckert, M. Eddaoudi, D. T. Vodak, J. Kim, M. O’Keeffe, and O. M. Yaghi, *Hydrogen storage in microporous metal-organic frameworks*, Science **300**, 1127–1129 (2003).
- [26] W. Zhou, H. Wu, and T. Yildirim, *Enhanced H₂ adsorption in isostructural metal-organic frameworks with open metal sites: Strong dependence of the binding strength on metal ions*, Journal of the American Chemical Society **130**, 15268–15269 (2008).
- [27] Y. Peng, V. Krungleviciute, I. Eryazici, J. T. Hupp, O. K. Farha, and T. Yildirim, *Methane storage in metal-organic frameworks: Current records, surprise findings, and challenges*, Journal of the American Chemical Society **135**, 11887–11894 (2013).
- [28] D. J. Collins and H.-C. Zhou, *Hydrogen storage in metal-organic frameworks*, Journal of Materials Chemistry **17**, 3154–3160 (2007).
- [29] H. Liu, E. Maginn, A. E. Visser, N. J. Bridges, and E. B. Fox, *Thermal and transport properties of six ionic liquids: An experimental and molecular dynamics study*, Industrial & Engineering Chemistry Research **51**, 7242–7254 (2012).

- [30] H. Wu, Q. Gong, D. H. Olson, and J. Li, *Commensurate adsorption of hydrocarbons and alcohols in microporous metal organic frameworks*, *Chemical Reviews* **112**, 836–868 (2012).
- [31] M. Shah, M. C. McCarthy, S. Sachdeva, A. K. Lee, and H.-K. Jeong, *Current status of metal-organic framework membranes for gas separations: Promises and challenges*, *Industrial & Engineering Chemistry Research* **51**, 2179–2199 (2012).
- [32] J.-R. Li, J. Sculley, and H.-C. Zhou, *Metal-organic frameworks for separations*, *Chemical Reviews* **112**, 869–932 (2011).
- [33] K. Sumida, D. L. Rogow, J. A. Mason, T. M. McDonald, E. D. Bloch, Z. R. Herm, T.-H. Bae, and J. R. Long, *Carbon dioxide capture in metal-organic frameworks*, *Chemical Reviews* **112**, 724–781 (2012).
- [34] A. U. Czaja, N. Trukhan, and U. Muller, *Industrial applications of metal-organic frameworks*, *Chemical Society Reviews* **38**, 1284–1293 (2009).
- [35] J. Lee, O. K. Farha, J. Roberts, K. A. Scheidt, S. T. Nguyen, and J. T. Hupp, *Metal-organic framework materials as catalysts*, *Chemical Society Reviews* **38**, 1450–1459 (2009).
- [36] D. J. Xiao, E. D. Bloch, J. A. Mason, W. L. Queen, M. R. Hudson, N. Planas, J. Borycz, A. L. Dzubak, P. Verma, K. Lee, F. Bonino, V. Crocell, J. Yano, S. Bordiga, D. G. Truhlar, L. Gagliardi, C. M. Brown, and J. R. Long, *Oxidation of ethane to ethanol by N_2O in a metal-organic framework with coordinatively unsaturated iron(II) sites*, *Nature Chemistry* **6**, 590–595 (2014).
- [37] L. E. Kreno, K. Leong, O. K. Farha, M. Allendorf, R. P. V. Duyne, and J. T. Hupp, *Metal-organic framework materials as chemical sensors*, *Chemical Reviews* **112**, 1105–1125 (2012).
- [38] P. Horcajada, C. Serre, M. Vallet-Regí, M. Sebban, F. Taulelle, and G. Férey, *Metal-organic frameworks as efficient materials for drug delivery*, *Angewandte Chemie International Edition* **45**, 5974–5978 (2006).
- [39] R. C. Huxford, J. D. Rocca, and W. Lin, *Metal-organic frameworks as potential drug carriers*, *Current Opinion in Chemical Biology* **14**, 262–268 (2010).
- [40] S. Kitagawa, R. Kitaura, and S.-i. Noro, *Functional porous coordination polymers*, *Angewandte Chemie International Edition* **43**, 2334–2375 (2004).

- [41] C. N. R. Rao, S. Natarajan, and R. Vaidhyanathan, *Metal carboxylates with open architectures*, *Angewandte Chemie International Edition* **43**, 1466–1496 (2004).
- [42] A. McKinlay, R. Morris, P. Horcajada, G. Férey, R. Gref, P. Couvreur, and C. Serre, *BioMOFs: Metal-organic frameworks for biological and medical applications*, *Angewandte Chemie International Edition* **49**, 6260–6266 (2010).
- [43] J. D. Rocca, D. Liu, and W. Lin, *Nanoscale metal-organic frameworks for biomedical imaging and drug delivery*, *Accounts of Chemical Research* **44**, 957–968 (2011).
- [44] P. Horcajada, R. Gref, T. Baati, P. K. Allan, G. Maurin, P. Couvreur, G. Férey, R. E. Morris, and C. Serre, *Metal-organic frameworks in biomedicine*, *Chemical Reviews* **112**, 1232–1268 (2012).
- [45] J. Park, H. Kim, S. S. Han, and Y. Jung, *Tuning metal-organic frameworks with open-metal sites and its origin for enhancing CO₂ affinity by metal substitution*, *Journal of Physical Chemistry Letters* **3**, 826–829 (2012).
- [46] C. E. Wilmer, M. Leaf, C. Y. Lee, O. K. Farha, B. G. Hauser, J. T. Hupp, and R. Q. Snurr, *Large-scale screening of hypothetical metal-organic frameworks*, *Nature Chemistry* **4**, 83–89 (2012).
- [47] T. F. Willems, C. H. Rycroft, M. Kazi, J. C. Meza, and M. Haranczyk, *Algorithms and tools for high-throughput geometry-based analysis of crystalline porous materials*, *Microporous and Mesoporous Materials* **149**, 134–141 (2012).
- [48] J. L. Rowsell and O. M. Yaghi, *Metal-organic frameworks: a new class of porous materials*, *Microporous and Mesoporous Materials* **73**, 3–14 (2004).
- [49] W. L. Queen, M. R. Hudson, E. D. Bloch, J. A. Mason, M. I. Gonzalez, J. S. Lee, D. Gygi, J. D. Howe, K. Lee, T. A. Darwish, M. James, V. K. Peterson, S. J. Teat, B. Smit, J. B. Neaton, J. R. Long, and C. M. Brown, *Comprehensive study of carbon dioxide adsorption in the metal-organic frameworks M₂(dobdc) (M=Mg, Mn, Fe, Co, Ni, Cu, Zn)*, *Chemical Science* **5**, 4569–4581 (2014).
- [50] R. Poloni, K. Lee, R. F. Berger, B. Smit, and J. B. Neaton, *Understanding trends in CO₂ adsorption in metal-organic frameworks with open-metal sites*, *Journal of Physical Chemistry Letters* **5**, 861–865 (2014).

- [51] E. Haldoupis, J. Borycz, H. Shi, K. D. Vogiatzis, P. Bai, W. L. Queen, L. Gagliardi, and J. I. Siepmann, *Ab initio derived force fields for predicting CO₂ adsorption and accessibility of metal sites in the metal-organic frameworks M-MOF-74 (M=Mn, Co, Ni, Cu)*, Journal of Physical Chemistry C **119**, 16058–16071 (2015).
- [52] S. R. Caskey, A. G. Wong-Foy, and A. J. Matzger, *Dramatic tuning of carbon dioxide uptake via metal substitution in a coordination polymer with cylindrical pores*, Journal of the American Chemical Society **130**, 10870–10871 (2008).
- [53] P. Mishra, S. Edubilli, B. Mandal, and S. Gumma, *Adsorption characteristics of metal-organic frameworks containing coordinatively unsaturated metal sites: Effect of metal cations and adsorbate properties*, Journal of Physical Chemistry C **118**, 6847–6855 (2014).
- [54] A. O. Yazaydin, R. Q. Snurr, T.-H. Park, K. Koh, J. Liu, M. D. LeVan, A. I. Benin, P. Jakubczak, M. Lanuza, D. B. Galloway, J. J. Low, and R. R. Willis, *Screening of metal-organic frameworks for carbon dioxide capture from flue gas using a combined experimental and modeling approach*, Journal of the American Chemical Society **131**, 18198–18199 (2009).
- [55] R. Poloni, B. Smit, and J. B. Neaton, *CO₂ capture by metal-organic frameworks with van der Waals density functionals*, Journal of Physical Chemistry A **116**, 4957–4964 (2012).
- [56] S. Henke, A. Schneemann, A. Wütscher, and R. A. Fischer, *Directing the breathing behavior of pillared-layered metal-organic frameworks via a systematic library of functionalized linkers bearing flexible substituents*, Journal of the American Chemical Society **134**, 9464–9474 (2012).
- [57] A. Schneemann, V. Bon, I. Schwedler, I. Senkowska, S. Kaskel, and R. A. Fischer, *Flexible metal-organic frameworks*, Chemical Society Reviews **43**, 6062–6096 (2014).
- [58] L.-C. Lin, A. H. Berger, R. L. Martin, J. Kim, J. A. Swisher, K. Jariwala, C. H. Rycroft, A. S. Bhowm, M. W. Deem, M. Haranczyk, and B. Smit, *In silico screening of carbon-capture materials*, Nature Materials **11**, 633–641 (2012).
- [59] J. Kim, R. L. Martin, O. Rübél, M. Haranczyk, and B. Smit, *High-throughput characterization of porous materials using graphics processing units*, Journal of Chemical Theory and Computation **8**, 1684–1693 (2012).

- [60] J. Kim, L.-C. Lin, R. L. Martin, J. A. Swisher, M. Haranczyk, and B. Smit, *Large-scale computational screening of zeolites for ethane/ethene separation*, *Langmuir* **28**, 11914–11919 (2012).
- [61] J. Kim, M. Abouelnasr, L.-C. Lin, and B. Smit, *Large-scale screening of zeolite structures for CO₂ membrane separations*, *Journal of the American Chemical Society* **135**, 7545–7552 (2013).
- [62] T. Watanabe and D. S. Sholl, *Accelerating applications of metal-organic frameworks for gas adsorption and separation by computational screening of materials*, *Langmuir* **28**, 14114–14128 (2012).
- [63] E. Haldoupis, S. Nair, and D. S. Sholl, *Finding MOFs for highly selective CO₂/N₂ adsorption using materials screening based on efficient assignment of atomic point charges*, *Journal of the American Chemical Society* **134**, 4313–4323 (2012).
- [64] J. Pérez-Pellitero, H. Amrouche, F. Siperstein, G. Pirngruber, C. Nieto-Draghi, G. Chaplais, A. Simon-Masseron, D. Bazer-Bachi, D. Peralta, and N. Bats, *Adsorption of CO₂, CH₄, and N₂ on zeolitic imidazolate frameworks: Experiments and simulations*, *Chemistry: A European Journal* **16**, 1560–1571 (2010).
- [65] J. Zang, S. Nair, and D. S. Sholl, *Prediction of water adsorption in copper-based metal-organic frameworks using force fields derived from dispersion-corrected DFT calculations*, *Journal of Physical Chemistry C* **117**, 7519–7525 (2013).
- [66] L. Chen, L. Grajciar, P. Nachtigall, and T. Düren, *Accurate prediction of methane adsorption in a metal-organic framework with unsaturated metal sites by direct implementation of an ab initio derived potential energy surface in GCMC simulation*, *Journal of Physical Chemistry C* **115**, 23074–23080 (2011).
- [67] A. L. Dzubak, L.-C. Lin, J. Kim, J. A. Swisher, R. Poloni, S. N. Maximoff, B. Smit, and L. Gagliardi, *Ab initio carbon capture in open-site metal-organic frameworks*, *Nature Chemistry* **4**, 810–816 (2012).
- [68] R. Mercado, B. Vlaisavljevich, L.-C. Lin, K. Lee, Y. Lee, J. A. Mason, D. J. Xiao, M. I. Gonzalez, M. T. Kapelewski, J. B. Neaton, and B. Smit, *Force field development from periodic density functional theory calculations for gas separation applications using metal-organic frameworks*, *Journal of Physical Chemistry C* **120**, 12590–12604 (2016).

- [69] B. Chen, N. W. Ockwig, A. R. Millward, D. S. Contreras, and O. M. Yaghi, *High H₂ adsorption in a microporous metal-organic framework with open metal sites*, *Angewandte Chemie* **117**, 4823–4827 (2005).
- [70] W. Chen, S. Liang, Y. Guo, K. Cheng, X. Gui, and D. Tang, *Thermodynamic performances of [mmim]DMP/methanol absorption refrigeration*, *Journal of Thermal Science* **21**, 557–563 (2012).
- [71] C. Campbell, C. A. Ferreiro-Rangel, M. Fischer, J. R. B. Gomes, and M. Jorge, *A transferable model for adsorption in MOFs with unsaturated metal sites*, *Journal of Physical Chemistry C* **121**, 441–458 (2017).
- [72] A. K. Rappe, C. J. Casewit, K. S. Colwell, W. A. Goddard, and W. M. Skiff, *UFF, a full periodic table force field for molecular mechanics and molecular dynamics simulations*, *Journal of the American Chemical Society* **114**, 10024–10035 (1992).
- [73] J. J. Potoff and J. I. Siepmann, *Vapor-liquid equilibria of mixtures containing alkanes, carbon dioxide, and nitrogen*, *AIChE Journal* **47**, 1676–1682 (2001).
- [74] T. Duerinck, R. Bueno-Perez, F. Vermoortele, D. E. D. Vos, S. Calero, G. V. Baron, and J. F. M. Denayer, *Understanding hydrocarbon adsorption in the UiO-66 metal-organic framework: Separation of (un)saturated linear, branched, cyclic adsorbates, including stereoisomers*, *Journal of Physical Chemistry C* **117**, 12567–12578 (2013).
- [75] R. Bueno-Perez, A. Martin-Calvo, P. Gomez-Alvarez, J. J. Gutierrez-Sevillano, P. J. Merkling, T. J. H. Vlught, T. S. van Erp, D. Dubbeldam, and S. Calero, *Enantioselective adsorption of ibuprofen and lysine in metal-organic frameworks*, *Chemical Communications* **50**, 10849–10852 (2014).
- [76] J. Borycz, D. Tiana, E. Haldoupis, J. C. Sung, O. K. Farha, J. I. Siepmann, and L. Gagliardi, *CO₂ adsorption in M-IRMOF-10 (M = Mg, Ca, Fe, Cu, Zn, Ge, Sr, Cd, Sn, Ba)*, *Journal of Physical Chemistry C* **120**, 12819–12830 (2016).
- [77] A. Luna-Triguero, J. M. Vicent-Luna, T. M. Becker, T. J. H. Vlught, D. Dubbeldam, P. Gómez-Álvarez, and S. Calero, *Effective model for olefin/paraffin separation using (Co, Fe, Mn, Ni)-MOF-74*, *ChemistrySelect* (2017).
- [78] T. Pham, K. A. Forrest, D. M. Franz, Z. Guo, B. Chen, and B. Space, *Predictive models of gas sorption in a metal-organic framework with open-metal*

- sites and small pore sizes*, Physical Chemistry Chemical Physics **19**, 18587–18602 (2017).
- [79] H. Fang, P. Kamakoti, J. Zang, S. Cundy, C. Paur, P. I. Ravikovitch, and D. S. Sholl, *Prediction of CO₂ adsorption properties in zeolites using force fields derived from periodic dispersion-corrected DFT calculations*, Journal of Physical Chemistry C **116**, 10692–10701 (2012).
- [80] L.-C. Lin, K. Lee, L. Gagliardi, J. B. Neaton, and B. Smit, *Force-field development from electronic structure calculations with periodic boundary conditions: Applications to gaseous adsorption and transport in metal-organic frameworks*, Journal of Chemical Theory and Computation **10**, 1477–1488 (2014).
- [81] J. Borycz, L.-C. Lin, E. D. Bloch, J. Kim, A. L. Dzubak, R. Maurice, D. Semrouni, K. Lee, B. Smit, and L. Gagliardi, *CO₂ adsorption in Fe₂(dobdc): A classical force field parameterized from quantum mechanical calculations*, Journal of Physical Chemistry C **118**, 12230–12240 (2014).
- [82] M. A. Addicoat, N. Vankova, I. F. Akter, and T. Heine, *Extension of the universal force field to metal-organic frameworks*, Journal of Chemical Theory and Computation **10**, 880–891 (2014).
- [83] L. Vanduyfhuys, S. Vandenbrande, T. Verstraelen, R. Schmid, M. Waroquier, and V. Van Speybroeck, *QuickFF: A program for a quick and easy derivation of force fields for metal-organic frameworks from ab initio input*, Journal of Computational Chemistry **36**, 1015–1027 (2015).
- [84] J. Park, J. D. Howe, and D. S. Sholl, *How reproducible are isotherm measurements in metal-organic frameworks?* Chemistry of Materials **29**, 10487–10495 (2017).
- [85] H. Wu, W. Zhou, and T. Yildirim, *High-capacity methane storage in metal-organic frameworks M₂(dhtp): The important role of open metal sites*, Journal of the American Chemical Society **131**, 4995–5000 (2009).
- [86] K. Lee, J. D. Howe, L.-C. Lin, B. Smit, and J. B. Neaton, *Small-molecule adsorption in open-site metal-organic frameworks: A systematic density functional theory study for rational design*, Chemistry of Materials **27**, 668–678 (2015).
- [87] P. D. Dietzel, V. Besikiotis, and R. Blom, *Application of metal-organic frameworks with coordinatively unsaturated metal sites in storage and sep-*

- aration of methane and carbon dioxide*, Journal of Materials Chemistry **19**, 7362–7370 (2009).
- [88] R. Krishna and J. M. van Baten, *Investigating the potential of MgMOF–74 membranes for CO₂ capture*, Journal of Membrane Science **377**, 249–260 (2011).
- [89] K. Lee, W. C. I. III, A. L. Dzubak, P. Verma, S. J. Stoneburner, L.-C. Lin, J. D. Howe, E. D. Bloch, D. A. Reed, M. R. Hudson, C. M. Brown, J. R. Long, J. B. Neaton, B. Smit, C. J. Cramer, D. G. Truhlar, and L. Gagliardi, *Design of a metal-organic framework with enhanced back bonding for separation of N₂ and CH₄*, Journal of the American Chemical Society **136**, 698–704 (2014).
- [90] N. L. Rosi, J. Kim, M. Eddaoudi, B. Chen, M. O’Keeffe, and O. M. Yaghi, *Rod packings and metal-organic frameworks constructed from rod-shaped secondary building units*, Journal of the American Chemical Society **127**, 1504–1518 (2005).
- [91] P. D. C. Dietzel, Y. Morita, R. Blom, and H. Fjellvåg, *An in situ high-temperature single-crystal investigation of a dehydrated metal-organic framework compound and field-induced magnetization of one-dimensional metal-oxygen chains*, Angewandte Chemie **117**, 6512–6516 (2005).
- [92] P. D. C. Dietzel, B. Panella, M. Hirscher, R. Blom, and H. Fjellvåg, *Hydrogen adsorption in a nickel based coordination polymer with open metal sites in the cylindrical cavities of the desolvated framework*, Chemical Communications, 959–961 (2006).
- [93] S. Bhattacharjee, J.-S. Choi, S.-T. Yang, S. B. Choi, J. Kim, and W.-S. Ahn, *Solvothermal synthesis of Fe–MOF–74 and its catalytic properties in phenol hydroxylation*, Journal of Nanoscience and Nanotechnology **10**, 135–141 (2010).
- [94] P. D. C. Dietzel, R. Blom, and H. Fjellvåg, *Base-induced formation of two magnesium metal-organic framework compounds with a bifunctional tetratopic ligand*, European Journal of Inorganic Chemistry **2008**, 3624–3632 (2008).
- [95] R. Sanz, F. Martinez, G. Orcajo, L. Wojtas, and D. Briones, *Synthesis of a honeycomb-like Cu-based metal-organic framework and its carbon dioxide adsorption behaviour*, Dalton Transactions **42**, 2392–2398 (2013).

- [96] M. Dincă and J. Long, *Hydrogen storage in microporous metal-organic frameworks with exposed metal sites*, *Angewandte Chemie International Edition* **47**, 6766–6779 (2008).
- [97] D. Britt, H. Furukawa, B. Wang, T. G. Glover, and O. M. Yaghi, *Highly efficient separation of carbon dioxide by a metal-organic framework replete with open metal sites*, *Proceedings of the National Academy of Sciences* **106**, 20637–20640 (2009).
- [98] J. M. Simmons, H. Wu, W. Zhou, and T. Yildirim, *Carbon capture in metal-organic frameworks - A comparative study*, *Energy and Environmental Science* **4**, 2177–2185 (2011).
- [99] E. D. Bloch, W. L. Queen, R. Krishna, J. M. Zadrozny, C. M. Brown, and J. R. Long, *Hydrocarbon separations in a metal-organic framework with open iron(II) coordination sites*, *Science* **335**, 1606–1610 (2012).
- [100] S. J. Geier, J. A. Mason, E. D. Bloch, W. L. Queen, M. R. Hudson, C. M. Brown, and J. R. Long, *Selective adsorption of ethylene over ethane and propylene over propane in the metal-organic frameworks $M_2(\text{dobdc})$ ($M=\text{Mg}, \text{Mn}, \text{Fe}, \text{Co}, \text{Ni}, \text{Zn}$)*, *Chemical Science* **4**, 2054–2061 (2013).
- [101] Y. He, R. Krishna, and B. Chen, *Metal-organic frameworks with potential for energy-efficient adsorptive separation of light hydrocarbons*, *Energy & Environmental Science* **5**, 9107–9120 (2012).
- [102] P. Verma, X. F. Xu, and D. G. Truhlar, *Adsorption on Fe–MOF–74 for C1–C3 hydrocarbon separation*, *Journal of Physical Chemistry C* **117**, 12648–12660 (2013).
- [103] U. Böhme, B. Barth, C. Paula, A. Kuhnt, W. Schwieger, A. Mundstock, J. Caro, and M. Hartmann, *Ethene/ethane and propene/propane separation via the olefin and paraffin selective metal-organic framework adsorbents CPO–27 and ZIF–8*, *Langmuir* **29**, 8592–8600 (2013).
- [104] S. Chavan, J. G. Vitillo, E. Groppo, F. Bonino, C. Lamberti, P. D. C. Dietzel, and S. Bordiga, *CO adsorption on CPO–27–Ni coordination polymer: Spectroscopic features and interaction energy*, *Journal of Physical Chemistry C* **113**, 3292–3299 (2009).
- [105] Z. Bao, S. Alnemrat, L. Yu, I. Vasiliev, Q. Ren, X. Lu, and S. Deng, *Adsorption of ethane, ethylene, propane, and propylene on a magnesium-based metal-organic framework*, *Langmuir* **27**, 13554–13562 (2011).

- [106] H. Wu, J. M. Simmons, G. Srinivas, W. Zhou, and T. Yildirim, *Adsorption sites and binding nature of CO₂ in prototypical metal-organic frameworks: A combined neutron diffraction and first-principles study*, *Journal of Physical Chemistry Letters* **1**, 1946–1951 (2010).
- [107] W. L. Queen, C. M. Brown, D. K. Britt, P. Zajdel, M. R. Hudson, and O. M. Yaghi, *Site-specific CO₂ adsorption and zero thermal expansion in an anisotropic pore network*, *Journal of Physical Chemistry C* **115**, 24915–24919 (2011).
- [108] W. S. Drisdell, R. Poloni, T. M. McDonald, J. R. Long, B. Smit, J. B. Neaton, D. Prendergast, and J. B. Kortright, *Probing adsorption interactions in metal-organic frameworks using X-ray spectroscopy*, *Journal of the American Chemical Society* **135**, 18183–18190 (2013).
- [109] K. Tan, S. Zuluaga, Q. Gong, Y. Gao, N. Nijem, J. Li, T. Thonhauser, and Y. J. Chabal, *Competitive coadsorption of CO₂ with H₂O, NH₃, SO₂, NO, NO₂, N₂, O₂, and CH₄ in M–MOF–74 (M=Mg,Co,Ni): The role of hydrogen bonding*, *Chemistry of Materials* **27**, 2203–2217 (2015).
- [110] X. Kong, E. Scott, W. Ding, J. A. Mason, J. R. Long, and J. A. Reimer, *CO₂ dynamics in a metal-organic framework with open metal sites*, *Journal of the American Chemical Society* **134**, 14341–14344 (2012).
- [111] L.-C. Lin, J. Kim, X. Kong, E. Scott, T. M. McDonald, J. R. Long, J. A. Reimer, and B. Smit, *Understanding CO₂ dynamics in metal-organic frameworks with open metal sites*, *Angewandte Chemie* **125**, 4506–4509 (2013).
- [112] B. M. Wiers, M.-L. Foo, N. P. Balsara, and J. R. Long, *A solid lithium electrolyte via addition of lithium isopropoxide to a metal-organic framework with open metal sites*, *Journal of the American Chemical Society* **133**, 14522–14525 (2011).
- [113] Y. Hwang, D.-Y. Hong, J.-S. Chang, S. Jhung, Y.-K. Seo, J. Kim, A. Vimont, M. Daturi, C. Serre, and G. Férey, *Amine grafting on coordinatively unsaturated metal centers of MOFs: Consequences for catalysis and metal encapsulation*, *Angewandte Chemie International Edition* **47**, 4144–4148 (2008).
- [114] A. Demessence, D. M. D'Alessandro, M. L. Foo, and J. R. Long, *Strong CO₂ binding in a water-stable, triazolate-bridged metal-organic framework functionalized with ethylenediamine*, *Journal of the American Chemical Society* **131**, 8784–8786 (2009).

- [115] J. J. Gutiérrez-Sevillano, D. Dubbeldam, F. Rey, S. Valencia, M. Palomino, A. Martín-Calvo, and S. Calero, *Analysis of the ITQ-12 zeolite performance in propane-propylene separations using a combination of experiments and molecular simulations*, *Journal of Physical Chemistry C* **114**, 14907–14914 (2010).
- [116] D. Dubbeldam and K. S. Walton, *On the application of classical molecular simulations of adsorption in metal-organic frameworks*, in *Metal-Organic Frameworks: Materials Modeling towards Engineering Applications* (Pan Stanford, 2015) p. 53.
- [117] T. Pham, K. A. Forrest, A. Hogan, K. McLaughlin, J. L. Belof, J. Eckert, and B. Space, *Simulations of hydrogen sorption in rht-MOF-1: identifying the binding sites through explicit polarization and quantum rotation calculations*, *Journal of Materials Chemistry A* **2**, 2088–2100 (2014).
- [118] J. Cirera, J. C. Sung, P. B. Howland, and F. Paesani, *The effects of electronic polarization on water adsorption in metal-organic frameworks: H₂O in MIL-53 (Cr)*, *Journal of Chemical Physics* **137**, 054704 (2012).
- [119] J. G. McDaniel and J. R. Schmidt, *Robust, transferable, and physically motivated force fields for gas adsorption in functionalized zeolitic imidazolate frameworks*, *Journal of Physical Chemistry C* **116**, 14031–14039 (2012).
- [120] J. G. McDaniel, K. Yu, and J. Schmidt, *Ab initio, physically motivated force fields for CO₂ adsorption in zeolitic imidazolate frameworks*, *Journal of Physical Chemistry C* **116**, 1892–1903 (2012).
- [121] J. G. McDaniel, S. Li, E. Tylianakis, R. Q. Snurr, and J. R. Schmidt, *Evaluation of force field performance for high-throughput screening of gas uptake in metal-organic frameworks*, *Journal of Physical Chemistry C* **119**, 3143–3152 (2015).
- [122] J. L. Belof, A. C. Stern, M. Eddaoudi, and B. Space, *On the mechanism of hydrogen storage in a metal-organic framework material*, *Journal of the American Chemical Society* **129**, 15202–15210 (2007).
- [123] J. L. Belof, A. C. Stern, and B. Space, *An accurate and transferable intermolecular diatomic hydrogen potential for condensed phase simulation*, *Journal of Chemical Theory and Computation* **4**, 1332–1337 (2008).
- [124] K. A. Forrest, T. Pham, K. McLaughlin, J. L. Belof, A. C. Stern, M. J. Zaworotko, and B. Space, *Simulation of the mechanism of gas sorption in*

- a metal-organic framework with open metal sites: Molecular hydrogen in PCN-61*, Journal of Physical Chemistry C **116**, 15538–15549 (2012).
- [125] T. Pham, K. A. Forrest, R. Banerjee, G. Orcajo, J. Eckert, and B. Space, *Understanding the H₂ sorption trends in the M-MOF-74 series (M=Mg,Ni,Co,Zn)*, Journal of Physical Chemistry C **119**, 1078–1090 (2015).
- [126] D. M. Franz, Z. E. Dyott, K. A. Forrest, A. Hogan, T. Pham, and B. Space, *Simulations of hydrogen, carbon dioxide, and small hydrocarbon sorption in a nitrogen-rich rht-metal-organic framework*, Physical Chemistry Chemical Physics **20**, 1761–1777 (2018).
- [127] M. Ramdin, T. W. de Loos, and T. J. H. Vlucht, *State-of-the-art of CO₂ capture with ionic liquids*, Industrial & Engineering Chemistry Research **51**, 8149–8177 (2012).
- [128] R. D. Rogers and K. R. Seddon, *Ionic liquids - Solvents of the future?* Science **302**, 792–793 (2003).
- [129] Y. J. Kim, S. Kim, Y. K. Joshi, A. G. Fedorov, and P. A. Kohl, *Thermodynamic analysis of an absorption refrigeration system with ionic-liquid/refrigerant mixture as a working fluid*, Energy **44**, 1005 – 1016 (2012).
- [130] M. Freemantle, *An Introduction to Ionic Liquids* (The Royal Society of Chemistry, 2009).
- [131] H. Liu and E. J. Maginn, *A molecular dynamics investigation of the structural and dynamic properties of the ionic liquid 1-n-butyl-3-methylimidazolium bis(trifluoromethanesulfonyl)imide*, Journal of Chemical Physics **135**, 124507 (2011).
- [132] D. Zheng, L. Dong, W. Huang, X. Wu, and N. Nie, *A review of imidazolium ionic liquids research and development towards working pair of absorption cycle*, Renewable and Sustainable Energy Reviews **37**, 47–68 (2014).
- [133] V. R. Ferro, C. Moya, D. Moreno, R. Santiago, J. de Riva, G. Pedrosa, M. Larriba, I. Diaz, and J. Palomar, *Enterprise ionic liquids database (ILUAM) for use in aspen one programs suite with COSMO-based property methods*, Industrial & Engineering Chemistry Research **57**, 980–989 (2018).
- [134] S. Kim, N. Patel, and P. A. Kohl, *Performance simulation of ionic liquid and hydrofluorocarbon working fluids for an absorption refrigeration system*, Industrial & Engineering Chemistry Research **52**, 6329–6335 (2013).

- [135] M. R. Currás, P. Husson, A. A. H. Pádua, M. F. Costa Gomes, and J. García, *High-pressure densities of 2,2,2-trifluoroethanol + ionic liquid mixtures useful for possible applications in absorption cycles*, *Industrial & Engineering Chemistry Research* **53**, 10791–10802 (2014).
- [136] A. Yokozeki and M. B. Shiflett, *Ammonia solubilities in room-temperature ionic liquids*, *Industrial & Engineering Chemistry Research* **46**, 1605–1610 (2007).
- [137] C. M. Tenney, M. Massel, J. M. Mayes, M. Sen, J. F. Brennecke, and E. J. Maginn, *A computational and experimental study of the heat transfer properties of nine different ionic liquids*, *Journal of Chemical & Engineering Data* **59**, 391–399 (2014).
- [138] K. Seddon and J. Holbrey, *Ionic liquids*, *Clean Products and Processes* **1**, 223–236 (1999).
- [139] W. Shi and E. J. Maginn, *Molecular simulation of ammonia absorption in the ionic liquid 1-ethyl-3-methylimidazolium bis(trifluoromethylsulfonyl)imide ([emim][Tf₂N])*, *AIChE Journal* **55**, 2414–2421 (2009).
- [140] J. Kahlen, K. Masuch, and K. Leonhard, *Modelling cellulose solubilities in ionic liquids using COSMO–RS*, *Green Chemistry* **12**, 2172–2181 (2010).
- [141] A. A. Niazi, B. D. Rabideau, and A. E. Ismail, *Effects of water concentration on the structural and diffusion properties of imidazolium-based ionic liquid-water mixtures*, *Journal of Physical Chemistry B* **117**, 1378–1388 (2013).
- [142] B. D. Rabideau, A. Agarwal, and A. E. Ismail, *Observed mechanism for the breakup of small bundles of cellulose α and β in ionic liquids from molecular dynamics simulations*, *Journal of Physical Chemistry B* **117**, 3469–3479 (2013).
- [143] P. B. Sánchez, M. Traikia, A. Dequid, A. A. H. Pádua, and J. García, *Molecular understanding of pyridinium ionic liquids as absorbents with water as refrigerant for use in heat pumps*, *AIChE Journal* **7**, 405–410 (2017).
- [144] M. Ramdin, S. P. Balaji, J. M. Vicent-Luna, J. J. Gutiérrez-Sevillano, S. Calero, T. W. de Loos, and T. J. H. Vlugt, *Solubility of the precombustion gases CO₂, CH₄, CO, H₂, N₂, and H₂S in the ionic liquid [bmim][Tf₂N] from Monte Carlo simulations*, *Journal of Physical Chemistry C* **118**, 23599–23604 (2014).

- [145] W. Shi and E. J. Maginn, *Atomistic simulation of the absorption of carbon dioxide and water in the ionic liquid 1-n-hexyl-3-methylimidazolium bis(trifluoromethylsulfonyl)imide ([hmim][Tf₂N])*, *Journal of Physical Chemistry B* **112**, 2045–2055 (2008).
- [146] E. J. Maginn, *Molecular simulation of ionic liquids: current status and future opportunities*, *Journal of Physics: Condensed Matter* **21**, 373101 (2009).
- [147] N. Pardo, K. Vatopoulos, A. Krook-Riekkola, J. Moya, and A. Perez, *Heat and cooling demand and market perspective*, Tech. Rep. (European Commission, Joint Research Centre, Institute for Energy and Transport, 2012).
- [148] M. Seiler, A. Kühn, F. Ziegler, and X. Wang, *Sustainable cooling strategies using new chemical system solutions*, *Industrial & Engineering Chemistry Research* **52**, 16519–16546 (2013).
- [149] H. Poth, *Electron cooling: Theory, experiment, application*, *Physics Reports* **196**, 135–297 (1990).
- [150] S. A. Tassou, J. S. Lewis, Y. T. Ge, A. Hadawey, and I. Chaer, *A review of emerging technologies for food refrigeration applications*, *Applied Thermal Engineering* **30**, 263–276 (2010).
- [151] Y. Fan, L. Luo, and B. Souyri, *Review of solar sorption refrigeration technologies: Development and applications*, *Renewable and Sustainable Energy Reviews* **11**, 1758–1775 (2007).
- [152] W. Wu, H. Zhang, T. You, and X. Li, *Thermodynamic investigation and comparison of absorption cycles using hydrofluoroolefins and ionic liquid*, *Industrial & Engineering Chemistry Research* **56**, 9906–9916 (2017).
- [153] A. A. Kiss and C. A. Infante Ferreira, *Heat Pumps in Chemical Process Industry* (CRC Press, 2016) p. 422.
- [154] I. Dinçer and M. Kanoğlu, *Refrigeration Systems and Applications* (John Wiley & Sons, Ltd, 2010).
- [155] F. Ziegler, *State of the art in sorption heat pumping and cooling technologies*, *International Journal of Refrigeration* **25**, 450–459 (2002).
- [156] D. Kim and C. Infante Ferreira, *Solar refrigeration options - A state-of-the-art review*, *International Journal of Refrigeration* **31**, 3–15 (2008).

- [157] A. Sözen, D. Altıparmak, and H. Usta, *Development and testing of a prototype of absorption heat pump system operated by solar energy*, Applied Thermal Engineering **22**, 1847–1859 (2002).
- [158] Y. E. Yuksel, M. Ozturk, and I. Dincer, *Thermodynamic performance assessment of a novel environmentally-benign solar energy based integrated system*, Energy Conversion and Management **119**, 109–120 (2016).
- [159] M. Medrano, M. Bourouis, and A. Coronas, *Double-lift absorption refrigeration cycles driven by low-temperature heat sources using organic fluid mixtures as working pairs*, Applied Energy **68**, 173 – 185 (2001).
- [160] P. Srihirin, S. Aphornratana, and S. Chungpaibulpatana, *A review of absorption refrigeration technologies*, Renewable and Sustainable Energy Reviews **5**, 343–372 (2001).
- [161] L. Chen, M. Sharifzadeh, N. Mac Dowell, T. Welton, N. Shah, and J. P. Hallett, *Inexpensive ionic liquids: $[\text{HSO}_4]^-$ -based solvent production at bulk scale*, Green Chemistry **16**, 3098–3106 (2014).
- [162] J. Sun, L. Fu, and S. Zhang, *A review of working fluids of absorption cycles*, Renewable and Sustainable Energy Reviews **16**, 1899–1906 (2012).
- [163] L. Dong, D. Zheng, N. Nie, and Y. Li, *Performance prediction of absorption refrigeration cycle based on the measurements of vapor pressure and heat capacity of $\text{H}_2\text{O}+[\text{DMIM}]\text{DMP}$ system*, Applied Energy **98**, 326–332 (2012).
- [164] S. Kim and P. A. Kohl, *Theoretical and experimental investigation of an absorption refrigeration system using $\text{R134}/[\text{bmim}][\text{PF}_6]$ working fluid*, Industrial & Engineering Chemistry Research **52**, 13459–13465 (2013).
- [165] A. Yokozeki and M. B. Shiflett, *Vapor-liquid equilibria of ammonia + ionic liquid mixtures*, Applied Energy **84**, 1258–1273 (2007).
- [166] W. Chen, S. Liang, Y. Guo, X. Gui, and D. Tang, *Investigation on vapor-liquid equilibria for binary systems of metal ion-containing ionic liquid $[\text{bmim}]\text{Zn}_2\text{Cl}_5/\text{NH}_3$ by experiment and modified UNIFAC model*, Fluid Phase Equilibria **360**, 1–6 (2013).
- [167] W. Chen, S. Liang, Y. Guo, and D. Tang, *Thermodynamic analysis of an absorption system using $[\text{bmim}]\text{Zn}_2\text{Cl}_5/\text{NH}_3$ as the working pair*, Energy Conversion and Management **85**, 13–19 (2014).

- [168] E. Ruiz, V. Ferro, J. de Riva, D. Moreno, and J. Palomar, *Evaluation of ionic liquids as absorbents for ammonia absorption refrigeration cycles using COSMO-based process simulations*, *Applied Energy* **123**, 281–291 (2014).
- [169] A. Cera-Manjarres, *Experimental determination and modelling of thermo-physical properties of ammonia/ionic liquid mixtures for absorption refrigeration systems*, Ph.D. thesis, Universitat Rovira i Virgili (2015).
- [170] M. Wang and C. A. Infante Ferreira, *Absorption heat pump cycles with NH_3 - ionic liquid working pairs*, *Applied Energy* **204**, 819–830 (2017).
- [171] R. E. Critoph, *Activated carbon adsorption cycles for refrigeration and heat pumping*, *Carbon* **27**, 63–70 (1989).
- [172] J. T. McMullan, *Refrigeration and the environment - issues and strategies for the future*, *International Journal of Refrigeration* **25**, 89–99 (2002).
- [173] T. M. Becker, D. Dubbeldam, L.-C. Lin, and T. J. H. Vlucht, *Investigating polarization effects of CO_2 adsorption in MgMOF-74*, *Journal of Computational Science* **15**, 86–94 (2015).
- [174] S. Chu, *Carbon capture and sequestration*, *Science* **325**, 1599 (2009).
- [175] R. S. Haszeldine, *Carbon capture and storage: How green can black be?* *Science* **325**, 1647–1652 (2009).
- [176] B. Smit, J. R. Reimer, C. M. Oldenburg, and I. C. Bourg, *Introduction to Carbon Capture and Sequestration* (World Scientific, 2014).
- [177] J. M. Huck, L.-C. Lin, A. H. Berger, M. N. Shahrak, R. L. Martin, A. S. Bhowan, M. Haranczyk, K. Reuter, and B. Smit, *Evaluating different classes of porous materials for carbon capture*, *Energy & Environmental Science* **7**, 4132–4146 (2014).
- [178] H. S. Antila and E. Salonen, *Polarizable force fields*, in *Biomolecular Simulations* (Springer, 2013) pp. 215–241.
- [179] S. Rick and S. Stuart, *Potentials and algorithms for incorporating polarizability in computer simulations*, in *Reviews in Computational Chemistry* (Wiley Online Library, 2003) pp. 89–146.
- [180] T. A. Halgren and W. Damm, *Polarizable force fields*, *Current Opinion in Structural Biology* **11**, 236–242 (2001).

- [181] M. G. Martin, B. Chen, and J. I. Siepmann, *A novel Monte Carlo algorithm for polarizable force fields: Application to a fluctuating charge model for water*, *Journal of Chemical Physics* **108**, 3383–3385 (1998).
- [182] T. Pham, K. A. Forrest, W.-Y. Gao, S. Ma, and B. Space, *Theoretical insights into the tuning of metal binding sites of paddlewheels in rht-metal-organic frameworks*, *ChemPhysChem* **16**, 3170–3179 (2015).
- [183] P. Cieplak, J. Caldwell, and P. Kollman, *Molecular mechanical models for organic and biological systems going beyond the atom centered two body additive approximation: aqueous solution free energies of methanol and *n*-methyl acetamide, nucleic acid base, and amide hydrogen bonding and chloroform/water partition coefficients of the nucleic acid bases*, *Journal of Computational Chemistry* **22**, 1048–1057 (2001).
- [184] P. Cieplak and P. Kollman, *Monte Carlo simulation of aqueous solutions of Li^+ and Na^+ using many-body potentials. coordination numbers, ion solvation enthalpies, and the relative free energy of solvation*, *Journal of Chemical Physics* **92**, 6761–6767 (1990).
- [185] V. Lachet, A. Boutin, B. Tavitian, and A. Fuchs, *Computational study of *p*-xylene/*m*-xylene mixtures adsorbed in nay zeolite*, *Journal of Physical Chemistry B* **102**, 9224–9233 (1998).
- [186] J. Stone, Anthony, *The theory of intermolecular forces* (Oxford University Press, 1996).
- [187] A. J. Stone, *Intermolecular potentials*, *Science* **321**, 787–789 (2008).
- [188] S. L. Mayo, B. D. Olafson, and W. A. Goddard, *DREIDING: a generic force field for molecular simulations*, *Journal of Physical Chemistry* **94**, 8897–8909 (1990).
- [189] J. N. Israelachvili, *7 - Repulsive steric forces, total intermolecular pair potentials, and liquid structure*, in *Intermolecular and Surface Forces (Third Edition)*, edited by J. N. Israelachvili (Academic Press, San Diego, 2011) pp. 133–149.
- [190] T. Darden, D. York, and L. Pedersen, *Particle mesh ewald: An $n \cdot \log(N)$ method for ewald sums in large systems*, *Journal of Chemical Physics* **98**, 10089–10092 (1993).
- [191] D. Wolf, P. Keblinski, S. R. Phillpot, and J. Eggebrecht, *Exact method for the simulation of coulombic systems by spherically truncated, pairwise r^{-1} summation*, *Journal of Chemical Physics* **110**, 8254–8282 (1999).

- [192] C. J. Fennell and J. D. Gezelter, *Is the ewald summation still necessary? pairwise alternatives to the accepted standard for long-range electrostatics*, *Journal of Chemical Physics* **124**, 234104 (2006).
- [193] N. D. Spencer and J. H. Moore, *Encyclopedia of chemical physics and physical chemistry: Applications*, Vol. 3 (Taylor & Francis, 2001).
- [194] J. N. Israelachvili, *6 - Van der Waals forces*, in *Intermolecular and Surface Forces (Third Edition)*, edited by J. N. Israelachvili (Academic Press, San Diego, 2011).
- [195] R. H. Perry, D. W. Green, J. O. Maloney, M. M. Abbott, C. M. Ambler, and R. C. Amero, *Perry's chemical engineers' handbook*, Vol. 7 (McGraw-hill New York, 1997).
- [196] P. Atkins and J. Depaula, *Atkins' Physical Chemistry, 8th Edition* New York (Freeman, 2006).
- [197] X. He, L. Fusti-Molnar, G. Cui, and K. M. Merz, *Importance of dispersion and electron correlation in ab initio protein folding*, *Journal of Physical Chemistry B* **113**, 5290–5300 (2009).
- [198] R. J.-M. Pellenq and D. Nicholson, *Intermolecular potential function for the physical adsorption of rare gases in silicalite*, *Journal of Physical Chemistry* **98**, 13339–13349 (1994).
- [199] T. van Westen, T. J. H. Vlugt, and J. Gross, *Determining force field parameters using a physically based equation of state*, *Journal of Physical Chemistry B* **115**, 7872–7880 (2011).
- [200] C. S. Schacht, T. J. H. Vlugt, and J. Gross, *Using an analytic equation of state to obtain quantitative solubilities of CO₂ by molecular simulation*, *Journal of Physical Chemistry Letters* **2**, 393–396 (2011).
- [201] G. Kresse and J. Hafner, *Ab initio molecular dynamics for liquid metals*, *Physical Review B* **47**, 558 (1993).
- [202] S. Russell and A. Warshel, *Calculations of electrostatic energies in proteins: The energetics of ionized groups in bovine pancreatic trypsin inhibitor*, *Journal of Molecular Biology* **185**, 389–404 (1985).
- [203] H. Yu and W. F. van Gunsteren, *Accounting for polarization in molecular simulation*, *Computer Physics Communications* **172**, 69–85 (2005).

- [204] A. Warshel, M. Kato, and A. V. Pisliakov, *Polarizable force fields: History, test cases, and prospects*, *Journal of Chemical Theory and Computation* **3**, 2034–2045 (2007).
- [205] P. Cieplak, F.-Y. Dupradeau, Y. Duan, and J. Wang, *Polarization effects in molecular mechanical force fields*, *Journal of Physics: Condensed Matter* **21**, 333102 (2009).
- [206] P. E. M. Lopes, B. Roux, and A. D. MacKerell Jr., *Molecular modeling and dynamics studies with explicit inclusion of electronic polarizability: theory and applications*, *Theoretical Chemistry Accounts* **124**, 11–28 (2009).
- [207] P. J. Mitchell and D. Fincham, *Shell model simulations by adiabatic dynamics*, *Journal of Physics: Condensed Matter* **5**, 1031 (1993).
- [208] J. R. Schmidt, K. Yu, and J. G. McDaniel, *Transferable next-generation force fields from simple liquids to complex materials*, *Accounts of Chemical Research* **48**, 548–556 (2015).
- [209] S. O. Odoh, C. J. Cramer, D. G. Truhlar, and L. Gagliardi, *Quantum-chemical characterization of the properties and reactivities of metal-organic frameworks*, *Chemical Reviews* **115**, 6051–6111 (2015).
- [210] W. L. Jorgensen, J. D. Madura, and C. J. Swenson, *Optimized intermolecular potential functions for liquid hydrocarbons*, *Journal of the American Chemical Society* **106**, 6638–6646 (1984).
- [211] D. Dubbeldam, S. Calero, T. J. H. Vlugt, R. Krishna, T. L. M. Maesen, E. Beerdsen, and B. Smit, *Force field parametrization through fitting on inflection points in isotherms*, *Physical Review Letters* **93**, 088302 (2004).
- [212] D. Yu, A. O. Yazaydin, J. R. Lane, P. D. C. Dietzel, and R. Q. Snurr, *A combined experimental and quantum chemical study of CO₂ adsorption in the metal-organic framework CPO–27 with different metals*, *Chemical Science* **4**, 3544–3556 (2013).
- [213] B. Chen, J. J. Potoff, and J. I. Siepmann, *Adiabatic nuclear and electronic sampling Monte Carlo simulations in the Gibbs ensemble: Application to polarizable force fields for water*, *Journal of Physical Chemistry B* **104**, 2378–2390 (2000).
- [214] T. M. Nymand and P. Linse, *Ewald summation and reaction field methods for potentials with atomic charges, dipoles, and polarizabilities*, *Journal of Chemical Physics* **112**, 6152–6160 (2000).

- [215] A. Goj, D. S. Sholl, E. D. Akten, and D. Kohen, *Atomistic simulations of CO₂ and N₂ adsorption in silica zeolites: The impact of pore size and shape*, Journal of Physical Chemistry B **106**, 8367–8375 (2002).
- [216] J. A. Gee, J. Chung, S. Nair, and D. S. Sholl, *Adsorption and diffusion of small alcohols in zeolitic imidazolate frameworks ZIF–8 and ZIF–90*, Journal of Physical Chemistry C **117**, 3169–3176 (2013).
- [217] Y. Zeng, P. Z. Moghadam, and R. Q. Snurr, *Pore size dependence of adsorption and separation of thiophene/benzene mixtures in zeolites*, Journal of Physical Chemistry C **119**, 15263–15273 (2015).
- [218] R. D. Shannon, *Dielectric polarizabilities of ions in oxides and fluorides*, Journal of Applied Physics **73**, 348–366 (1993).
- [219] P. T. van Duijnen and M. Swart, *Molecular and atomic polarizabilities: Thole's model revisited*, Journal of Physical Chemistry A **102**, 2399–2407 (1998).
- [220] Y. Tu and A. Laaksonen, *The electronic properties of water molecules in water clusters and liquid water*, Chemical Physics Letters **329**, 283–288 (2000).
- [221] M. in het Panhuis, P. L. A. Popelier, R. W. Munn, and J. G. Ángyán, *Distributed polarizability of the water dimer: Field-induced charge transfer along the hydrogen bond*, Journal of Chemical Physics **114**, 7951–7961 (2001).
- [222] K. D. Bonin and V. V. Kresin, *Electric-dipole polarizabilities of atoms, molecules, and clusters* (World Scientific, 1997).
- [223] C. M. Baker and J. MacKerell, Alexander D., *Polarizability rescaling and atom-based thole scaling in the CHARMM drude polarizable force field for ethers*, Journal of Molecular Modeling **16**, 567–576 (2010).
- [224] C. R. Vosmeer, A. S. Rustenburg, J. E. Rice, H. W. Horn, W. C. Swope, and D. P. Geerke, *QM/MM-based fitting of atomic polarizabilities for use in condensed-phase biomolecular simulation*, Journal of Chemical Theory and Computation **8**, 3839–3853 (2012).
- [225] D. Dubbeldam, S. Calero, D. E. Ellis, and R. Q. Snurr, *RASPA: Molecular simulation software for adsorption and diffusion in flexible nanoporous materials*, Molecular Simulation **42**, 81–101 (2016).
- [226] D. Dubbeldam, A. Torres-Knoop, and K. S. Walton, *On the inner workings of Monte Carlo codes*, Molecular Simulation **39**, 1253–1292 (2013).

- [227] T. R. C. Van Assche, T. Duerinck, J. J. Gutiérrez Sevillano, S. Calero, G. V. Baron, and J. F. M. Denayer, *High adsorption capacities and two-step adsorption of polar adsorbates on copper-benzene-1,3,5-tricarboxylate metal-organic framework*, *Journal of Physical Chemistry C* **117**, 18100–18111 (2013).
- [228] K. Esselink, L. D. J. C. Loyens, and B. Smit, *Parallel Monte Carlo simulations*, *Physical Review E* **51**, 1560–1568 (1995).
- [229] L. Loyens, B. Smit, and K. Esselink, *Parallel Gibbs-ensemble simulations*, *Molecular Physics* **86**, 171–183 (1995).
- [230] T. J. H. Vlugt, *Efficiency of parallel CBMC simulations*, *Molecular Simulation* **23**, 63–78 (1999).
- [231] T. J. H. Vlugt, E. García-Pérez, D. Dubbeldam, S. Ban, and S. Calero, *Computing the heat of adsorption using molecular simulations: The effect of strong coulombic interactions*, *Journal of Chemical Theory and Computation* **4**, 1107–1118 (2008).
- [232] T. M. Becker, J. Heinen, D. Dubbeldam, L.-C. Lin, and T. J. H. Vlugt, *Polarizable force fields for CO₂ and CH₄ adsorption in M–MOF–74*, *Journal of Physical Chemistry C* **121**, 4659–4673 (2017).
- [233] J. J. McCarthy, *Climate change 2001: impacts, adaptation, and vulnerability: contribution of Working Group II to the third assessment report of the Intergovernmental Panel on Climate Change* (Cambridge University Press, 2001).
- [234] M. L. Parry, *Climate change 2007-impacts, adaptation and vulnerability: Working group II contribution to the fourth assessment report of the IPCC, Vol. 4* (Cambridge University Press, 2007).
- [235] C. Rosenzweig, D. Karoly, M. Vicarelli, P. Neofotis, Q. Wu, G. Casassa, A. Menzel, T. L. Root, N. Estrella, B. Seguin, P. Tryjanowski, C. Liu, S. Rawlins, and A. Imeson, *Attributing physical and biological impacts to anthropogenic climate change*, *Nature* **453**, 353–357 (2008).
- [236] C. D. Thomas, A. Cameron, R. E. Green, M. Bakkenes, L. J. Beaumont, Y. C. Collingham, B. F. N. Erasmus, M. F. de Siqueira, A. Grainger, L. Hannah, L. Hughes, B. Huntley, A. S. van Jaarsveld, G. F. Midgley, L. Miles, M. A. Ortega-Huerta, A. Townsend Peterson, O. L. Phillips, and S. E. Williams, *Extinction risk from climate change*, *Nature* **427**, 145–148 (2004).

- [237] S. Pacala and R. Socolow, *Stabilization wedges: Solving the climate problem for the next 50 years with current technologies*, *Science* **305**, 968–972 (2004).
- [238] R. J. Heinsohn and R. L. Kabel, *Sources and control of air pollution: Engineering principles* (Pearson, 1998).
- [239] G. Brasseur, J. Orlando, G. Tyndall, and N. C. for Atmospheric Research (U.S.), *Atmospheric Chemistry and Global Change*, Topics in environmental chemistry (Oxford University Press, 1999).
- [240] J. G. Speight, *Chapter 7 - Acid gas treating*, in *Handbook of Natural Gas Transmission and Processing*, edited by S. Mokhatab, W. A. Poe, and J. G. Speight (Gulf Professional Publishing, Burlington, 2006) pp. 261 – 294.
- [241] C. Janiak and J. K. Vieth, *MOFs, MILs and more: concepts, properties and applications for porous coordination networks (PCNs)*, *New Journal of Chemistry* **34**, 2366–2388 (2010).
- [242] D. D'Alessandro, B. Smit, and J. Long, *Carbon dioxide capture: Prospects for new materials*, *Angewandte Chemie International Edition* **49**, 6058–6082 (2010).
- [243] T. Schnabel, J. Vrabec, and H. Hasse, *Unlike lennard-jones parameters for vapor-liquid equilibria*, *Journal of Molecular Liquids* **135**, 170–178 (2007).
- [244] D.-Y. Peng and D. B. Robinson, *A new two-constant equation of state*, *Industrial & Engineering Chemistry Fundamentals* **15**, 59–64 (1976).
- [245] G. te Velde, F. M. Bickelhaupt, E. J. Baerends, C. Fonseca Guerra, S. J. A. van Gisbergen, J. G. Snijders, and T. Ziegler, *Chemistry with ADF*, *Journal of Computational Chemistry* **22**, 931–967 (2001).
- [246] E. J. Baerends, T. Ziegler, A. J. Atkins, J. Autschbach, D. Bashford, A. Bérces, F. M. Bickelhaupt, C. Bo, P. M. Boerrigter, L. Cavallo, and et al., *ADF 2013, SCM, Theoretical Chemistry*, (2013), Vrije Universiteit, Amsterdam, The Netherlands, <http://www.scm.com>.
- [247] A. D. Becke, *Density-functional thermochemistry. III. The role of exact exchange*, *Journal of Chemical Physics* **98**, 5648–5652 (1993).
- [248] C. Lee, W. Yang, and R. G. Parr, *Development of the colle-salvetti correlation-energy formula into a functional of the electron density*, *Physical Review B* **37**, 785–789 (1988).

- [249] S. H. Vosko, W. L., and N. M., *Accurate spin-dependent electron liquid correlation energies for local spin density calculations: a critical analysis*, Canadian Journal of Physics **58**, 1200–1211 (1980).
- [250] P. J. Stephens, F. J. Devlin, C. F. Chabalowski, and M. J. Frisch, *Ab initio calculation of vibrational absorption and circular dichroism spectra using density functional force fields*, Journal of Physical Chemistry **98**, 11623–11627 (1994).
- [251] S. Grimme, J. Antony, S. Ehrlich, and H. Krieg, *A consistent and accurate ab initio parametrization of density functional dispersion correction (DFT–D) for the 94 elements H–Pu*, Journal of Chemical Physics **132** (2010).
- [252] T. Ziegler and A. Rauk, *Carbon monoxide, carbon monosulfide, molecular nitrogen, phosphorus trifluoride, and methyl isocyanide as .sigma. donors and .pi. acceptors. a theoretical study by the hartree-fock-slater transition-state method*, Inorganic Chemistry **18**, 1755–1759 (1979).
- [253] T. Ziegler and A. Rauk, *A theoretical study of the ethylene-metal bond in complexes between copper(1+), silver(1+), gold(1+), platinum(0) or platinum(2+) and ethylene, based on the hartree-fock-slater transition-state method*, Inorganic Chemistry **18**, 1558–1565 (1979).
- [254] F. M. Bickelhaupt and E. J. Baerends, *Kohn-Sham density functional theory: Predicting and understanding chemistry*, in *Reviews in Computational Chemistry* (John Wiley & Sons, Inc., 2007) pp. 1–86.
- [255] T. M. Becker, L.-C. Lin, D. Dubbeldam, and T. J. H. Vlugt, *Polarizable force field for CO₂ in M–MOF–74 derived from quantum mechanics*, Journal of Physical Chemistry C **122**, 24488–24498 (2018).
- [256] H. Fang, P. Kamakoti, P. I. Ravikovitch, M. Aronson, C. Paur, and D. S. Sholl, *First principles derived, transferable force fields for CO₂ adsorption in na-exchanged cationic zeolites*, Physical Chemistry Chemical Physics **15**, 12882–12894 (2013).
- [257] J. Applequist, J. R. Carl, and K.-K. Fung, *Atom dipole interaction model for molecular polarizability. application to polyatomic molecules and determination of atom polarizabilities*, Journal of the American Chemical Society **94**, 2952–2960 (1972).
- [258] D. Dubbeldam, S. Calero, and T. J. H. Vlugt, *iRASPA: GPU-accelerated visualization software for materials scientists*, Molecular Simulation **44**, 653–676 (2018).

- [259] J. Wang, P. Cieplak, J. Li, T. Hou, R. Luo, and Y. Duan, *Development of polarizable models for molecular mechanical calculations I: Parameterization of atomic polarizability*, Journal of Physical Chemistry B **115**, 3091–3099 (2011).
- [260] J. Wang, P. Cieplak, J. Li, J. Wang, Q. Cai, M. Hsieh, H. Lei, R. Luo, and Y. Duan, *Development of polarizable models for molecular mechanical calculations II: Induced dipole models significantly improve accuracy of intermolecular interaction energies*, Journal of Physical Chemistry B **115**, 3100–3111 (2011).
- [261] J. Wang, P. Cieplak, Q. Cai, M.-J. Hsieh, J. Wang, Y. Duan, and R. Luo, *Development of polarizable models for molecular mechanical calculations. 3. Polarizable water models conforming to thole polarization screening schemes*, Journal of Physical Chemistry B **116**, 7999–8008 (2012).
- [262] J. Wang, P. Cieplak, J. Li, Q. Cai, M.-J. Hsieh, R. Luo, and Y. Duan, *Development of polarizable models for molecular mechanical calculations. 4. \downarrow an der Waals parametrization*, Journal of Physical Chemistry B **116**, 7088–7101 (2012).
- [263] S. Hamad, S. R. Balestra, R. Bueno-Perez, S. Calero, and A. R. Ruiz-Salvador, *Atomic charges for modeling metal-organic frameworks: Why and how*, Journal of Solid State Chemistry **223**, 144–151 (2015).
- [264] T. M. Becker, A. Luna-Triguero, J. M. Vicent-Luna, L.-C. Lin, D. Dubbeldam, S. Calero, and T. J. H. Vlugt, *Potential of polarizable force fields for predicting the separation performance of small hydrocarbons in M-MOF-74*, Physical Chemistry Chemical Physics **20**, 28848–28859 (2018).
- [265] M. M. J. A. Moulijn A. van Diepen. Comyns, Alan E., *Applied Organometallic Chemistry* (John Wiley & Sons, Ltd., Chichester, United Kingdom, 2013) p. 566.
- [266] J.-R. Li, R. J. Kuppler, and H.-C. Zhou, *Selective gas adsorption and separation in metal-organic frameworks*, Chemical Society Reviews **38**, 1477–1504 (2009).
- [267] R. B. Eldridge, *Olefin/paraffin separation technology: a review*, Industrial & Engineering Chemistry Research **32**, 2208–2212 (1993).
- [268] J. Gascon, W. Blom, A. van Miltenburg, A. Ferreira, R. Berger, and F. Kapteijn, *Accelerated synthesis of all-silica dd3r and its performance in*

- the separation of propylene/propane mixtures*, Microporous and Mesoporous Materials **115**, 585–593 (2008).
- [269] J. van den Bergh, C. Gücüyener, E. A. Pidko, E. J. Hensen, J. Gascon, and F. Kapteijn, *Understanding the anomalous alkane selectivity of ZIF-7 in the separation of light alkane/alkene mixtures*, Chemistry: A European Journal **17**, 8832–8840 (2011).
- [270] Y.-S. Bae, C. Y. Lee, K. C. Kim, O. K. Farha, P. Nickias, J. T. Hupp, S. T. Nguyen, and R. Q. Snurr, *High propene/propane selectivity in isostructural metal-organic frameworks with high densities of open metal sites*, Angewandte Chemie International Edition **51**, 1857–1860 (2012).
- [271] A. F. P. Ferreira, J. C. Santos, M. G. Plaza, N. Lamia, J. M. Loureiro, and A. E. Rodrigues, *Suitability of Cu-BTC extrudates for propane-propylene separation by adsorption processes*, Chemical Engineering Journal (2011).
- [272] K. Li, D. H. Olson, J. Seidel, T. J. Emge, H. Gong, H. Zeng, and J. Li, *Zeolitic imidazolate frameworks for kinetic separation of propane and propene*, Journal of the American Chemical Society **131**, 10368–10369 (2009).
- [273] J. Heinen, N. C. Burtch, K. S. Walton, C. Fonseca Guerra, and D. Dubbel-dam, *Predicting multicomponent adsorption isotherms in open-metal site materials using force field calculations based on energy decomposed density functional theory*, Chemistry: A European Journal **22**, 18045–18050 (2016).
- [274] M. Jorge, M. Fischer, J. R. B. Gomes, C. Siquet, J. C. Santos, and A. E. Rodrigues, *Accurate model for predicting adsorption of olefins and paraffins on MOFs with open metal sites*, Industrial & Engineering Chemistry Research **53**, 15475–15487 (2014).
- [275] M. Fischer, J. R. B. Gomes, M. Fröba, and M. Jorge, *Modeling adsorption in metal-organic frameworks with open metal sites: Propane/propylene separations*, Langmuir **28**, 8537–8549 (2012).
- [276] F. D. Lahoz-Martín, S. Calero, J. J. Gutiérrez-Sevillano, and A. Martín-Calvo, *Adsorptive separation of ethane and ethylene using isorecticular metal-organic frameworks*, Microporous and Mesoporous Materials **248**, 40–45 (2017).
- [277] C. D. Wick, M. G. Martin, and J. I. Siepmann, *Transferable potentials for phase equilibria. 4. united-atom description of linear and branched alkenes and alkylbenzenes*, Journal of Physical Chemistry B **104**, 8008–8016 (2000).

- [278] B. Liu, B. Smit, F. Rey, S. Valencia, and S. Calero, *A new united atom force field for adsorption of alkenes in zeolites*, Journal of Physical Chemistry C **112**, 2492–2498 (2008).
- [279] K. Lucas, *Molecular Models for Fluids* (Cambridge University Press, 2007).
- [280] M. S. Shah, J. I. Siepmann, and M. Tsapatsis, *Transferable potentials for phase equilibria. improved united-atom description of ethane and ethylene*, AIChE Journal **63**, 5098–5110 (2017).
- [281] M. P. Allen and D. J. Tildesley, *Computer Simulation of Liquids (Second Edition)* (Oxford University Press, 2017).
- [282] J. M. Stout and C. E. Dykstra, *Static dipole polarizabilities of organic molecules. ab initio calculations and a predictive model*, Journal of the American Chemical Society **117**, 5127–5132 (1995).
- [283] A. K. Rappe and W. A. Goddard, *Charge equilibration for molecular-dynamics simulations*, Journal of Physical Chemistry **95**, 3358–3363 (1991).
- [284] J. M. Castillo, T. J. H. Vlugt, and S. Calero, *Understanding water adsorption in Cu–BTC metal-organic frameworks*, Journal of Physical Chemistry C **112**, 15934–15939 (2008).
- [285] R. Babarao and J. Jiang, *Unraveling the energetics and dynamics of ibuprofen in mesoporous metal-organic frameworks*, Journal of Physical Chemistry C **113**, 18287–18291 (2009).
- [286] Y. F. Chen, R. Babarao, S. I. Sandler, and J. W. Jiang, *Metal-organic framework MIL-101 for adsorption and effect of terminal water molecules: From quantum mechanics to molecular simulation*, Langmuir **26**, 8743–8750 (2010).
- [287] J. J. Gutierrez-Sevillano, A. Caro-Perez, D. Dubbeldam, and S. Calero, *Molecular simulation investigation into the performance of Cu–BTC metal-organic frameworks for carbon dioxide-methane separations*, Physical Chemistry Chemical Physics **13**, 20453–20460 (2011).
- [288] T. M. Becker, M. Wang, A. Kabra, S. H. Jamali, M. Ramdin, D. Dubbeldam, C. A. Infante Ferreira, and T. J. H. Vlugt, *Absorption refrigeration cycles with ammonia-ionic liquid working pairs studied by molecular simulation*, Industrial & Engineering Chemistry Research **57**, 5442–5452 (2018).

- [289] C. Cadena, Q. Zhao, R. Q. Snurr, and E. J. Maginn, *Molecular modeling and experimental studies of the thermodynamic and transport properties of pyridinium-based ionic liquids*, *Journal of Physical Chemistry B* **110**, 2821–2832 (2006).
- [290] S. Figueroa-Gerstenmaier, M. Francova, M. Kowalski, M. Lisal, I. Nezbeda, and W. Smith, *Molecular-level computer simulation of a vapor-compression refrigeration cycle*, *Fluid Phase Equilibria* **259**, 195–200 (2007).
- [291] T. W. P. Smith, J. P. Jalkanen, B. A. Anderson, J. J. Corbett, J. Faber, S. Hanayama, E. O’Keeffe, S. Parker, L. Johansson, L. Aldous, C. Raucci, M. Traut, S. Ettinger, D. Nelissen, D. S. Lee, S. Ng, A. Agrawal, J. J. Winebrake, M. Hoen, S. Chesworth, and A. Pandey, *Third IMO GHG Study 2014*, Tech. Rep. (International Maritime Organization (IMO), London, 2014).
- [292] A. F. Ferreira, P. N. Simões, and A. G. Ferreira, *Quaternary phosphonium-based ionic liquids: Thermal stability and heat capacity of the liquid phase*, *Journal of Chemical Thermodynamics* **45**, 16–27 (2012).
- [293] R. Ge, C. Hardacre, J. Jacquemin, P. Nancarrow, and D. W. Rooney, *Heat capacities of ionic liquids as a function of temperature at 0.1 MPa. measurement and prediction*, *Journal of Chemical and Engineering Data* **53**, 2148–2153 (2008).
- [294] S. P. Verevkin, D. H. Zaitsau, V. N. Emel’yanenko, A. V. Yermalayeu, C. Schick, H. Liu, E. J. Maginn, S. Bulut, I. Krossing, and R. Kalb, *Making sense of enthalpy of vaporization trends for ionic liquids: New experimental and simulation data show a simple linear relationship and help reconcile previous data*, *Journal of Physical Chemistry B* **117**, 6473–6486 (2013).
- [295] A. Yokozeki, *Theoretical performances of various refrigerant-absorbent pairs in a vapor-absorption refrigeration cycle by the use of equations of state*, *Applied Energy* **80**, 383–399 (2005).
- [296] N. A. Manan, C. Hardacre, J. Jacquemin, D. W. Rooney, and T. G. A. Youngs, *Evaluation of gas solubility prediction in ionic liquids using COSMOthermX*, *Journal of Chemical & Engineering Data* **54**, 2005–2022 (2009).
- [297] Z. Lei, C. Dai, and B. Chen, *Gas solubility in ionic liquids*, *Chemical Reviews* **114**, 1289–1326 (2014).

- [298] D. Moreno, V. R. Ferro, J. de Riva, R. Santiago, C. Moya, M. Larriba, and J. Palomar, *Absorption refrigeration cycles based on ionic liquids: Refrigerant/absorbent selection by thermodynamic and process analysis*, *Applied Energy* **213**, 179–194 (2018).
- [299] E. W. Lemmon, M. L. Huber, and M. O. McLinden, *NIST standard reference database 23: Reference fluid thermodynamic and transport properties-REFPROP, version 9.1, national institute of standards and technology, standard reference data program, gaithersburg*, (2013).
- [300] R. Tillner-Roth, F. Harms-Watzenberg, and H. Baehr, *Eine neue fundamentalgleichung für ammoniak*, *DKV Tagungsbericht* **20**, 67–67 (1993).
- [301] K. E. Gutowski, B. Gurkan, and E. J. Maginn, *Force field for the atomistic simulation of the properties of hydrazine, organic hydrazine derivatives, and energetic hydrazinium ionic liquids*, *Pure and Applied Chemistry* **81**, 1799–1828 (2009).
- [302] L. Zhang and J. I. Siepmann, *Development of the trappe force field for ammonia*, *Collection of Czechoslovak Chemical Communications* **75**, 577–591 (2010).
- [303] W. Shi and E. J. Maginn, *Continuous fractional component Monte Carlo: An adaptive biasing method for open system atomistic simulations*, *Journal of Chemical Theory and Computation* **3**, 1451–1463 (2007).
- [304] F. Wang and D. P. Landau, *Efficient, multiple-range random walk algorithm to calculate the density of states*, *Physical Review Letters* **86**, 2050–2053 (2001).
- [305] M. Ramdin, S. P. Balaji, J. M. Vicent-Luna, A. Torres-Knoop, Q. Chen, D. Dubbeldam, S. Calero, T. W. de Loos, and T. J. H. Vlugt, *Computing bubble-points of CO₂/CH₄ gas mixtures in ionic liquids from Monte Carlo simulations*, *Fluid Phase Equilibria* **418**, 100–107 (2016).
- [306] M. Ramdin, Q. Chen, S. P. Balaji, J. M. Vicent-Luna, A. Torres-Knoop, D. Dubbeldam, S. Calero, T. W. de Loos, and T. J. H. Vlugt, *Solubilities of CO₂, CH₄, C₂H₆, and SO₂ in ionic liquids and selexol from Monte Carlo simulations*, *Journal of Computational Science* **15**, 74–80 (2016).
- [307] M. Lagache, P. Ungerer, A. Boutin, and A. H. Fuchs, *Prediction of thermodynamic derivative properties of fluids by Monte Carlo simulation*, *Physical Chemistry Chemical Physics* **3**, 4333–4339 (2001).

- [308] M. S. Kelkar, W. Shi, and E. J. Maginn, *Determining the accuracy of classical force fields for ionic liquids: Atomistic simulation of the thermodynamic and transport properties of 1-ethyl-3-methylimidazolium ethylsulfate ([emim][EtSO₄]) and its mixtures with water*, *Industrial & Engineering Chemistry Research* **47**, 9115–9126 (2008).
- [309] M. M. Ghahremanpour, P. J. van Maaren, J. C. Ditz, R. Lindh, and D. van der Spoel, *Large-scale calculations of gas phase thermochemistry: Enthalpy of formation, standard entropy, and heat capacity*, *Journal of Chemical Physics* **145**, 114305 (2016).
- [310] Y. Paulechka, A. Blokhin, G. Kabo, and A. Strechan, *Thermodynamic properties and polymorphism of 1-alkyl-3-methylimidazolium bis(triflamides)*, *Journal of Chemical Thermodynamics* **39**, 866–877 (2007).
- [311] P. Navarro, M. Larriba, E. Rojo, J. García, and F. Rodríguez, *Thermal properties of cyano-based ionic liquids*, *Journal of Chemical & Engineering Data* **58**, 2187–2193 (2013).
- [312] M. Wang, T. M. Becker, and C. A. Infante Ferreira, *Assessment of vapor-liquid equilibrium models for ionic liquid based working pairs in absorption cycles*, *International Journal of Refrigeration* **87**, 10–25 (2018).
- [313] M. J. Frisch, G. W. Trucks, H. B. Schlegel, G. E. Scuseria, M. A. Robb, J. R. Cheeseman, G. Scalmani, V. Barone, B. Mennucci, G. A. Petersson, H. Nakatsuji, M. Caricato, X. Li, H. P. Hratchian, A. F. Izmaylov, J. Bloino, G. Zheng, J. L. Sonnenberg, M. Hada, M. Ehara, K. Toyota, R. Fukuda, J. Hasegawa, M. Ishida, T. Nakajima, Y. Honda, O. Kitao, H. Nakai, T. Vreven, J. A. Montgomery, Jr., J. E. Peralta, F. Ogliaro, M. Bearpark, J. J. Heyd, E. Brothers, K. N. Kudin, V. N. Staroverov, R. Kobayashi, J. Normand, K. Raghavachari, A. Rendell, J. C. Burant, S. S. Iyengar, J. Tomasi, M. Cossi, N. Rega, J. M. Millam, M. Klene, J. E. Knox, J. B. Cross, V. Bakken, C. Adamo, J. Jaramillo, R. Gomperts, R. E. Stratmann, O. Yazyev, A. J. Austin, R. Cammi, C. Pomelli, J. W. Ochterski, R. L. Martin, K. Morokuma, V. G. Zakrzewski, G. A. Voth, P. Salvador, J. J. Dannenberg, S. Dapprich, A. D. Daniels, O. Farkas, J. B. Foresman, J. V. Ortiz, J. Cioslowski, and D. J. Fox, *Gaussian 09 Revision E.01*, Gaussian Inc. Wallingford CT 2009.
- [314] T. A. Halgren, *Merck molecular force field. I. Basis, form, scope, parameterization, and performance of MMFF94*, *Journal of Computational Chemistry* **17**, 490–519 (1996).

- [315] Y. U. Paulechka, G. J. Kabo, and V. N. Emel'yanenko, *Structure, conformations, vibrations, and ideal-gas properties of 1-alkyl-3-methylimidazolium bis(trifluoromethylsulfonyl)imide ionic pairs and constituent ions*, Journal of Physical Chemistry B **112**, 15708–15717 (2008).
- [316] *NIST computational chemistry comparison and benchmark database NIST standard reference database number 101 release 18, october 2016, editor: Russell d. johnson III <http://cccbdb.nist.gov/>, .*
- [317] I. Urukova, J. Vorholz, and G. Maurer, *Solubility of CO₂, CO, and H₂ in the ionic liquid [bmim][PF₆] from Monte Carlo simulations*, Journal of Physical Chemistry B **109**, 12154–12159 (2005).
- [318] L. E. Ficke, R. R. Novak, and J. F. Brennecke, *Thermodynamic and thermo-physical properties of ionic liquid + water systems*, Journal of Chemical & Engineering Data **55**, 4946–4950 (2010).
- [319] M. Fermeglia and I. Kikic, *Excess enthalpy calculations by means of equations of state*, Journal of thermal analysis **29**, 687–695 (1984).
- [320] M. Wang, T. M. Becker, B. A. Schouten, T. J. H. Vlugt, and C. A. Infante Ferreira, *Ammonia/ionic liquid based double-effect vapor absorption refrigeration cycles driven by waste heat for cooling in fishing vessels*, Energy Conversion and Management **174**, 824–843 (2018).
- [321] G. Shu, Y. Liang, H. Wei, H. Tian, J. Zhao, and L. Liu, *A review of waste heat recovery on two-stroke ic engine aboard ships*, Renewable and Sustainable Energy Reviews **19**, 385–401 (2013).
- [322] V. Ruiz, *Analysis of existing refrigeration plants onboard fishing vessels and improvement possibilities*, in *Second International Symposium on Fishing Vessel Energy Efficiency* (Vigo, Spain, 2012).
- [323] W. Salmi, J. Vanttola, M. Elg, M. Kuosa, and R. Lahdelma, *Using waste heat of ship as energy source for an absorption refrigeration system*, Applied Thermal Engineering **115**, 501–516 (2017).
- [324] MAN Diesel & Turbon LTD, *Thermo Efficiency System for Reduction of Fuel Consumption and CO₂ Emission*, Tech. Rep. (Copenhagen, 2014).
- [325] J. Fernández-Seara, A. Vales, and M. Vázquez, *Heat recovery system to power an onboard NH₃-H₂O absorption refrigeration plant in trawler chiller fishing vessels*, Applied Thermal Engineering **18**, 1189–1205 (1998).

- [326] T. Cao, H. Lee, Y. Hwang, R. Radermacher, and H. H. Chun, *Performance investigation of engine waste heat powered absorption cycle cooling system for shipboard applications*, *Applied Thermal Engineering* **90**, 820–830 (2015).
- [327] K. Herold, R. Radermacher, and S. Klein, *Absorption Chillers and Heat Pumps, Second Edition* (CRC Press, 2016).
- [328] M. Wang and C. A. Infante Ferreira, *Performance analysis of double-effect absorption heat pump cycle using NH_3 /ILs pairs*, in *Proc. of the 12th IEA Heat Pump Conference* (Rotterdam, NL, 2017).
- [329] B. Schouten, *Advanced NH_3 based absorption refrigeration cycles: Modelling of the ionic liquid based double-effect cycles*, *Master's thesis*, Delft University of Technology (2017).
- [330] J. N. Canongia Lopes and A. A. H. Pádua, *Molecular force field for ionic liquids III: Imidazolium, pyridinium, and phosphonium cations; chloride, bromide, and dicyanamide anions*, *Journal of Physical Chemistry B* **110**, 19586–19592 (2006).
- [331] D. Matkowska and T. Hofman, *High-pressure volumetric properties of ionic liquids: 1-butyl-3-methylimidazolium tetrafluoroborate, $[\text{C}_4\text{mim}][\text{BF}_4]$, 1-butyl-3-methylimidazolium methylsulfate $[\text{C}_4\text{mim}][\text{MeSO}_4]$ and 1-ethyl-3-methylimidazolium ethylsulfate, $[\text{C}_2\text{mim}][\text{EtSO}_4]$* , *Journal of Molecular Liquids* **165**, 161–167 (2012).
- [332] M. Tariq, A. P. Serro, J. L. Mata, B. Saramago, J. M. Esperança, J. N. Canongia Lopes, and L. P. N. Rebelo, *High-temperature surface tension and density measurements of 1-alkyl-3-methylimidazolium bistriflamide ionic liquids*, *Fluid Phase Equilibria* **294**, 131–138 (2010).
- [333] Y. U. Paulechka, A. V. Blokhin, and G. J. Kabo, *Evaluation of thermodynamic properties for non-crystallizable ionic liquids*, *Thermochimica Acta* **604**, 122–128 (2015).
- [334] C. A. Nieto de Castro, M. J. V. Lourenço, A. P. C. Ribeiro, E. Langa, S. I. C. Vieira, P. Goodrich, and C. Hardacre, *Thermal properties of ionic liquids and ionic fluids of imidazolium and pyrrolidinium liquids*, *Journal of Chemical & Engineering Data* **55**, 653–661 (2010).
- [335] E. W. Lemmon, M. L. Huber, and M. O. McLinden, *NIST reference fluid thermodynamic and transport properties-REFPROP*, (2013).

- [336] C. Vasilescu and C. A. Infante Ferreira, *Solar driven multi-effect sub-zero ammonia based sorption cycles*, in *Proceedings of the International Sorption Heat Pump Conference (ISHPC11)* (Padua, Italy, 2011) pp. 885–892.
- [337] Wartsila, *Wartsila 38 Project Guide*, Tech. Rep. (Wartsila Ship Power Technology, 2008).
- [338] B. E. Poling, J. M. Prausnitz, and J. P. O’Connell, *The properties of gases and liquids* (McGraw-Hill, 2001).
- [339] M. Arun, M. Maiya, and S. Murthy, *Performance comparison of double-effect parallel-flow and series flow water-lithium bromide absorption systems*, *Applied Thermal Engineering* **21**, 1273–1279 (2001).
- [340] C. Vasilescu and C. Infante Ferreira, *Solar driven double-effect absorption cycles for sub-zero temperatures*, *International Journal of Refrigeration* **39**, 86–94 (2014).
- [341] G. Petrecca, *Industrial Energy Management: Principles and Applications* (Springer Science & Business Media, Boston, MA, 1993).
- [342] Y. Cao and T. Mu, *Comprehensive investigation on the thermal stability of 66 ionic liquids by thermogravimetric analysis*, *Industrial & Engineering Chemistry Research* **53**, 8651–8664 (2014).
- [343] P. Liu, M. Wang, and Z.-M. Cheng, *Thermal stability and vapor-liquid equilibrium for imidazolium ionic liquids as alternative reaction media*, *Journal of Chemical & Engineering Data* **60**, 836–844 (2015).
- [344] W.-q. Feng, Y.-h. Lu, Y. Chen, Y.-w. Lu, and T. Yang, *Thermal stability of imidazolium-based ionic liquids investigated by tg and FTIR techniques*, *Journal of Thermal Analysis and Calorimetry* **125**, 143–154 (2016).
- [345] F. Heym, B. J. M. Etzold, C. Kern, and A. Jess, *Analysis of evaporation and thermal decomposition of ionic liquids by thermogravimetric analysis at ambient pressure and high vacuum*, *Green Chemistry* **13**, 1453–1466 (2011).
- [346] M. Villanueva, A. Coronas, J. García, and J. Salgado, *Thermal stability of ionic liquids for their application as new absorbents*, *Industrial & Engineering Chemistry Research* **52**, 15718–15727 (2013).
- [347] B. K. Sovacool, *Valuing the greenhouse gas emissions from nuclear power: A critical survey*, *Energy Policy* **36**, 2950–2963 (2008).

CURRICULUM VITAE

Tim Michael Becker was born on the 14th of February 1988 in Aachen, Germany. During his B.Sc. program, he worked as an intern at PTT Global Chemical Public Company Limited in Map Ta Phut, Thailand. His work concerned the modeling and improvement of the polystyrene production. He obtained his B.Sc. degree in Mechanical Engineering in 2012 from RWTH Aachen University. After finishing his B.Sc degree, Tim began a M.Sc. program at RWTH Aachen University. His master's thesis concerns the computational investigation of structural and adsorption properties of zeolites and was conducted at the University of California, Berkeley in the group of Prof.dr. Berend Smit.

He obtained his M.Sc. degree with distinction in Chemical Engineering in 2014. Subsequently, Tim started a Ph.D. project in the Engineering Thermodynamics group headed by Prof.dr.ir. Thijs Vlugt at Delft University of Technology. The work was supervised by Prof.dr.ir. Thijs Vlugt and Dr. David Dubbeldam and focused on the development of a polarizable force field for Metal-Organic Frameworks. Besides, he investigated the diffusion of non-ideal mixtures and the prediction of Ammonia/Ionic Liquid mixtures for heat pump cycles. The results of his research are presented in this thesis. In 2019, Tim started a position as Quantitative Analyst at Wattsight. Part of his occupation is to develop statistical models to predict energy production and prices.



Tim Michael Becker

LIST OF PUBLICATIONS

Publications included in this thesis:

1. **T. M. BECKER**, D. DUBBELDAM, L.-C. LIN, AND T. J. H. VLUGT; Investigating Polarization Effects of CO₂ Adsorption in MgMOF-74. *Journal of Computational Science*, 15 (2016) 86-94.
2. **T. M. BECKER**, J. HEINEN, D. DUBBELDAM, L.-C. LIN, AND T. J. H. VLUGT; Polarizable Force Fields for CO₂ and CH₄ Adsorption in M-MOF-74. *Journal of Physical Chemistry C*, 121 (2017) 4659-4673.
3. **T. M. BECKER**, M. WANG, A. KABRA, S. H. JAMALI, M. RAMDIN, D. DUBBELDAM, C. A. INFANTE FERREIRA, AND T. J. H. VLUGT; Absorption Refrigeration Cycles with Ammonia-Ionic Liquid Working Pairs Studied by Molecular Simulation. *Industrial & Engineering Chemistry Research*, 57 (2018) 5442-5452.
4. M. WANG, **T. M. BECKER**, B. SCHOUTEN, T. J. H. VLUGT, AND C. A. INFANTE FERREIRA; Ammonia/Ionic Liquid Based Double-Effect Vapor Absorption Refrigeration Cycles Driven by Waste Heat for Cooling in Fishing Vessels. *Energy Conversion and Management*, 174 (2018) 824-843.
5. **T. M. BECKER**, D. DUBBELDAM, L.-C. LIN, AND T. J. H. VLUGT; Polarizable Force Field for CO₂ in M-MOF-74 Derived from Quantum Mechanics. *Journal of Physical Chemistry C*, 122 (2018) 24488-24498.
6. **T. M. BECKER**, A. LUNA-TRIGUERO, J. M. VICENT-LUNA, L.-C. LIN, D. DUBBELDAM, S. CALERO, AND T. J. H. VLUGT; Potential of Polarizable Force Fields for Predicting the Separation Performance of Small Hydrocarbons in M-MOF-74. *Physical Chemistry Chemical Physics*, 20 (2018) 28848-28859.

Publications not included in this thesis:

1. M. RAMDIN, **T. M. BCKER**, S. H. JAMALI, M. WANG, AND T. J. H. VLUGT; Computing Equation of State Parameters of Gases from Monte Carlo Simulations. *Fluid Phase Equilibria*, 428 (2016) 174-181.

2. A. LUNA-TRIGUERO, J. M. VICENT-LUNA, **T. M. BECKER**, T. J. H. VLUGT, D. DUBBELDAM, P. GÓMEZ-ÁLVAREZ, AND S. CALERO; Effective Model for Olefin/Paraffin Separation using (Co, Fe, Mn, Ni)-MOF-74. *ChemistrySelect*, 2 (2017) 665-672.
3. S. H. JAMALI, M. RAMDIN, **T. M. BECKER**, A. TORRES-KNOOP, D. DUBBELDAM, W. BUIJS, AND T. J. H. VLUGT; Solubility of Sulfur Compounds in Commercial Physical Solvents and an Ionic Liquid from Monte Carlo Simulations. *Fluid Phase Equilibria*, 433 (2017) 50-55.
4. S. H. JAMALI, M. RAMDIN, **T. M. BECKER**, S. K. RINWA, W. BUIJS, AND T. J. H. VLUGT; Thermodynamic and Transport Properties of Crown-Ethers: Force Field Development and Molecular Simulations. *Journal of Physical Chemistry B*, 121 (2017) 8367-8376.
5. M. WANG, **T. M. BECKER**, AND C. A. INFANTE FERREIRA; Assessment of Vapor-Liquid Equilibrium Models for Ionic Liquid Based Working Pairs in Absorption Cycles. *International Journal of Refrigeration*, 87 (2018) 10-25.
6. M. RAMDIN, S. H. JAMALI, **T. M. BECKER**, AND T. J. H. VLUGT; Gibbs Ensemble Monte Carlo Simulations of Multicomponent Natural Gas Mixtures. *Molecular Simulation*, 44 (2018) 377-383.
7. S. H. JAMALI, L. WOLFF, **T. M. BECKER**, A. BARDOW, T. J. H. VLUGT, AND O. A. MOULTOS; Finite-Size Effects of Binary Mutual Diffusion Coefficients from Molecular Dynamics. *Journal of Chemical Theory and Computation*, 14 (2018) 2667-2677.
8. L. WOLFF, S. H. JAMALI, **T. M. BECKER**, O. A. MOULTOS, T. J. H. VLUGT, AND A. BARDOW; Prediction of Composition-Dependent Self-Diffusion Coefficients in Binary Liquid Mixtures: The Missing Link for Darken-Based Models. *Industrial & Engineering Chemistry Research*, 57 (2018) 14784-14794.
9. S. H. JAMALI, L. WOLFF, **T. M. BECKER**, M. DE GROEN, M. RAMDIN, R. HARTKAMP, A. BARDOW, T. J. H. VLUGT, AND O. A. MOULTOS; OCTP: A Tool for On-the-Fly Calculation of Transport Properties of Fluids with the Order-n Algorithm in LAMMPS. *Journal of Chemical Information and Modeling*, 59 (2019) 1290-1294.

ACKNOWLEDGEMENTS

When I started my Ph.D., I could not have imagined how fast the time would pass. Even though the time seemed to have passed very quickly, or maybe because of this fact, it was a very eventful period with many happy, but also many challenging moments. Many of these challenges I faced together with friends and colleagues and for their support I am deeply thankful.

First of all, I thank my promoter Prof. Thijs Vlugt. Thank you for your guidance, for the freedom to focus on the projects I enjoyed the most, for always being approachable, and for always responding really quickly. I also thank my copromoter Dr. David Dubbeldam. I appreciate our discussions, your feedback has always been valuable, and thank you for answering all technical questions related to RASPA. Besides my promoters, I would like to thank the other members of my committee for reviewing and accepting my thesis. My special thanks go to Prof. Sofia Calero and Prof. Berend Smit who provided me with the opportunity to visit their research groups. I also want to mention three additional mentors who helped me getting started with molecular simulation and from whom I learned a lot: Prof. Li-Chiang Lin, Prof. Ahmed Ismail, and Prof. Brooks Rabideau.

During my Ph.D., I had the pleasure to collaborate with wonderful co-workers. Most of all, I thank Meng, Seyed, and Mahinder. Without you, my research would have been much less successful. But even more important, our work together always kept me enthusiastic and motivated. I am very grateful for our discussions, our joined work, and your friendship. In addition, I thank Dr. Carlos Infante Ferreira, Ludger, Jurn, Azahara, and José Manuel for our great and successful collaborations. Finally, I thank Prajakta and Abhishek who supported me during their master's thesis projects.

To keep on going, it was very important to have friends around me who supported me. You helped me by discussing my research and made me see my work from a different angle. However, more importantly, you helped me to relax and recover. I could not have done it without you: Remco, Sebastian, Metin, Julia, Dion, Sergio, Weiwei, Wenli, Christos, Tomasz, Dominik, João, Gustavo, Rene. I really enjoyed and appreciate our time together. Moreover, thanks to all the other friendly people at P&E, at TU Delft, and in Delft in general.

Last but not least, I thank my parents, my sister, and my grandparents for always supporting me. I could not have done it without you and I dedicate this thesis to you!